INFORMATION TO USERS

This manuscript has been reproduced from the microfilm master. UMI films the text directly from the original or copy submitted. Thus, some thesis and dissertation copies are in typewriter face, while others may be from any type of computer printer.

The quality of this reproduction is dependent upon the quality of the copy submitted. Broken or indistinct print, colored or poor quality illustrations and photographs, print bleedthrough, substandard margins, and improper alignment can adversely affect reproduction.

In the unlikely event that the author did not send UMI a complete manuscript and there are missing pages, these will be noted. Also, if unauthorized copyright material had to be removed, a note will indicate the deletion.

Oversize materials (e.g., maps, drawings, charts) are reproduced by sectioning the original, beginning at the upper left-hand corner and continuing from left to right in equal sections with small overlaps.

Photographs included in the original manuscript have been reproduced xerographically in this copy. Higher quality 6" x 9" black and white photographic prints are available for any photographs or illustrations appearing in this copy for an additional charge. Contact UMI directly to order.

ProQuest Information and Learning
300 North Zeeb Road, Ann Arbor, MI 48106-1346 USA
800-521-0600

UMI®

MEASURING LEAD, MERCURY, AND URANIUM BY IN VIVO X-RAY FLUORESCENCE

by

Joanne M. O'Meara, B.Sc.

A thesis submitted to the Faculty of
Graduate Studies in partial fulfillment of
the requirements for the degree:

Doctor of Philosophy

McMaster University

1999

MEASURING Pb, Hg, AND U BY IN VIVO X-RAY FLUORESCENCE

DOCTOR OF PHILOSOPHY (1999)
(Physics and Astronomy)

McMaster University
Hamilton, Ontario

TITLE: Measuring Lead, Mercury, and Uranium by *in vivo* X-ray Fluorescence

AUTHOR: Joanne M. O'Meara, B.Sc. (McMaster University)

SUPERVISOR: Dr. David R. Chettle

NUMBER OF PAGES: xii, 219

ABSTRACT

X-ray fluorescence (XRF) has been demonstrated to be a useful technique for measuring trace quantities of heavy metals in various tissues within the body. This thesis investigates a means of improving the measurement of lead in bone, as well as increasing the existing sensitivity of measuring kidney mercury content. The XRF measurement of uranium is also explored.

This work assesses the feasibility of a normalisation method for the ^{57}Co/90° system, in relating detected signal to the lead content of the sample. The feasibility of normalisation has been shown, which reduces subject dose and improves system transportability, as well as removes subjectivity, by eliminating the need for acquiring planar x-ray images of the measurement site.

In the measurement of renal mercury concentrations, a gain in sensitivity by increasing the x-ray tube operating voltage of the current system is investigated. It was found that 250 kV, rather than 175 kV, and a titanium rather than uranium filter, results in a 2.5 ± 0.2 times gain in sensitivity. This potential improvement could have profound clinical implications for the accuracy of occupational monitoring, and for assessing whether there is a quantitative relationship between biological fluid levels and mercury content in this critical organ.

The XRF measurement of bone uranium content is also explored. Both source-excited and polarised systems have been developed, however, the sensitivity is currently beyond that which is useful for occupational monitoring of exposure to this toxin. The particular case of measuring uranium in survivors of "Friendly Fire" incidents (from Operation Desert Storm) is investigated, and the first detectable quantity of uranium has been observed in a member of this cohort, with the XRF system designed and built during the course of this work.

ACKNOWLEDGEMENTS

Acknowledging the support I have received during the course of this work, I find that a natural division exists: those who primarily provided intellectual encouragement, and those who have given me constant moral support. While this division is somewhat blurry in many cases, this provides me with a straightforward means of ensuring that everyone who has helped me is recognised here.

First, in the category of intellectual support, the primary recognition must go to David Chettle. David has mentored me since I first worked for him as a somewhat "green" summer student - straight out of my first undergraduate year. It is difficult to describe the profound impact David has had on my growth as a scientist; suffice it to say that I honestly do not believe I would have even considered doing a Ph.D. if we had not met. Thank you for everything.

Many other wonderful members of the McMaster community have contributed to the work described in these pages. A special thanks is deserving to my supervisory committee, Drs. Fiona McNeill, Bill Prestwich, and Colin Webber. Fiona was always available to discuss XRF on the Phoenix patio, Bill had infinite patience in answering any question, and Colin brought insight and humour to all committee meetings. I would also like to thank the accelerator crew, Jim Stark, John Cave, and Marek Kiela for astounding me with their speed in completing tasks. In addition, Jim Garrett was extremely helpful in manufacturing both uranium shrapnel fragments and the uranium filter needed for the polarised Hg measurements. Jimmy Börjesson deserves a special thanks for all his help in the preliminary stages of the polarised system while on a work term here with us from Malmö, Sweden. I would also like to extend a hearty thank you to all my colleagues who volunteered for *in vivo* bone uranium measurements. Last but certainly not least, when acknowledging those who have been invaluable support to me at McMaster, the ladies in the Department of Physics and Astronomy office must be included. Wendy Malarek, Jackie Collin, Cheryl Johnston and Rosemary McNeice always greet me with a smile, no matter what university red tape I happen to be tangled up in!

As for moral support, many of the people listed above also fall into this category. However, it is hard to imagine the past four years without the constant love, understanding, support, and encouragement from Carl, who is always capable of lifting my spirits. In addition, fellow graduate students Rebeccah Marsh, Rob Hunter, Rebecca Murphy, Gordon Chan and Colleen Caney could always be counted on for diversions when the thesis was getting to be a bit much. In a similar vein, organising Spicy Camel Dish (GSA 3-pitch softball) for three summers was a great way of getting out of the lab and into the sunshine. Thanks to all past and present Camels for making it a joy to co-ordinate the team. Outside the university walls, Sinéad, Fin, Emma and Jack were terrific at reminding me that there is a world away from campus. Finally, last but definitely not least, I am truly grateful for the limitless love and support of my family. The energy and warmth of home was a wonderful refuge! This thesis is dedicated to my family, and to the memory of my faithful four-legged companion, Chelsea. She contributed significantly to my peace of mind over the past four years, and was a loyal friend for 11 short years. It was a great pleasure to wander the trails around Cootes Paradise with Chels whenever a particularly challenging problem arose.

TABLE OF CONTENTS

Abstract iii

Acknowledgements iv

Table of Contents vi

List of Figures x

List of Tables xii

Chapter 1: Introduction 1

- 1.1 Non-invasive elemental analysis 1
  - 1.1.1 Nuclear methods 2
    - a) Neutron activation analysis 2
    - b) Whole-body counting 3
    - c) Nuclear resonance scattering 4
    - d) Magnetic resonance spectroscopy 4
  - 1.1.2 Atomic methods 6
    - a) Absorptiometry 6
    - b) X-Ray Fluorescence 8
- 1.2 Metal kinetics 9
    - a) Lead 9
    - b) Uranium 13
    - c) Mercury 16
- 1.3 Heavy metal health effects 21
    - a) Lead 21
    - b) Uranium 23
    - c) Mercury 25

1.4 Occupational monitoring procedures 27

a) Lead 27

b) Uranium 28

c) Mercury 30

Chapter 2: Experimental Methods 33

2.1 Source of excitation photons 34

2.1.1 Source-excited x-ray fluorescence 34

a) Lead measurement system 38

b) Uranium measurement system 42

2.1.2 Polarised x-ray fluorescence 45

2.2 Detection systems 52

2.3 Phantom design and preparation 54

Chapter 3: Monte Carlo Methods 58

3.1 Monte Carlo techniques 58

3.2 Monte Carlo simulations of source-excited XRF 59

3.2.1 Model geometry 61

3.2.2 Model variables 63

3.2.3 Photon tracing 64

3.2.4 Compton scatter modelling 69

3.2.5 Detector response 72

3.2.6 Program output 73

3.2.7 Comparison with experiment 74

3.3 Monte Carlo simulations of polarised XRF 80

3.3.1 X-ray tube output modelling 82

3.3.2 Polariser output modelling 86

3.3.3 Sample output modelling 94

3.3.4 Detector response modelling 97

Chapter 4: Pb Investigations 100
4.1 Motivation of study 100
4.2 Materials and methods 105
4.3 Results 109
4.4 Clinical implications 114

Chapter 5: U Investigations 116
5.1 Motivation of study 116
5.2 Source-excited XRF 118
5.2.1 System description 118
5.2.2 Legitimacy of normalisation in bone-U measurements 119
5.2.3 Phantom measurements of bone-U concentrations 123
5.2.4 *In vivo* measurements of bone-U concentrations 125
5.2.5 Phantom measurements of U shrapnel 127
5.2.6 *In vivo* measurements of U shrapnel 130
5.2.7 Dosimetry 132
5.2.8 Clinical implications 132
a) Bone-U measurements 132
b) U shrapnel measurements 133
5.3 Polarised XRF 134
5.3.1 System description 135
a) Tube voltage and current 135
b) Polariser material, thickness, and collimation 140
c) Filtration 146
5.3.2 Phantom measurements 148
5.3.3 Dosimetry 150
5.3.4 Clinical implications 156

Chapter 6: Hg Investigations 158
6.1 Motivation of study 158

6.2 System description 159
- a) Tube current and voltage 160
- b) Polariser material, thickness, and collimation 160
- c) Filtration 163

6.3 Phantom measurements 172

6.4 Dosimetry 177

6.5 Clinical implications 182

Chapter 7: Conclusions 184

7.1 Lead 184

7.2 Uranium 185

7.2.1 Source-excited XRF 185
- a) Bone-U measurements 185
- b) U shrapnel measurements 186

7.2.2 Polarised XRF 187

7.3 Mercury 188

7.4 Potential advances 189

7.4.1 New photon sources 189

7.4.2 New detection systems 193

7.4.3 New spectroscopy systems 206

7.4.3 New analysis methods 208

References 212

LIST OF FIGURES

Number *Page*

1.1 Mass attenuation coefficient of iodine *versus* energy 7

1.2 Metabolic model for lead 11

1.3 Metabolic model for uranium 15

1.4 Metabolic model for inorganic mercury 19

2.1 The effect of momentum broadening on scattered energy 36

2.2 ^{109}Cd/backscatter detected Pb spectrum 39

2.3 ^{57}Co/90° detected Pb spectrum 41

2.4 ^{57}Co/backscatter detected U spectrum 45

2.5 Schematic of polarised XRF set-up 47

2.6 Schematic representation of polarisation 49

3.1 Flowchart to outline Monte Carlo simulation 61

3.2 Schematic of geometry in source-excited simulation 63

3.3 Comparison of simulated and experimental source-excited spectra 75

3.4 Comparison of simulated and experimental W tube output 84

3.5 Comparison of simulated and experimental Mo tube output 85

3.6 Schematic of geometry in polariser simulation 86

3.7 Comparison of simulated and experimental polariser output 91

3.8 Comparison of simulated and experimental polariser output 92

3.9 Schematic of geometry in sample simulation 95

3.10 Comparison of simulated and experimental sample output 99

4.1 Irradiated field of view in ^{57}Co/90° Pb system 108

4.2 Simulated Pb x-ray to coherent ratio *versus* bone radius 110

4.3 Simulated Pb x-ray to coherent ratio *versus* tissue thickness 110

4.4 Experimental Pb x-ray to coherent ratio *versus* bone radius 113

4.5 Experimental Pb x-ray to coherent ratio *versus* tissue thickness 114

5.1 Schematic of ^{57}Co/backscatter U set-up 119

5.2 Simulated U x-ray to coherent ratio *versus* tissue thickness 121

5.3 Simulated U x-ray to coherent ratio *versus* bone radius 122

5.4 Bone-U calibration lines 125
5.5 Bone-U *in vivo* measurement results 126
5.6 Schematic of U-shrapnel phantom 128
5.7 U x-ray intensity *versus* depth in shrapnel phantom 129
5.8 *In vivo* U XRF spectrum from "Friendly Fire" survivor 131
5.9 Schematic of experimental polarised system 138
5.10 Photon yield *versus* atomic number of polariser 141
5.11 Degree of polarisation *versus* atomic number of polariser 141
5.12 Mean spectral energy *versus* atomic number of polariser 142
5.13 U signal and background *versus* polariser thickness 145
5.14 U sensitivity *versus* polariser thickness 145
5.15 Polarised U spectrum 149
5.16 Skin dose distribution from polarised system 153
5.17 Skin dose data and empirical fit *versus* distance from beam centre 155
6.1 Hg signal and background *versus* polariser thickness 162
6.2 Hg sensitivity *versus* polariser thickness 162
6.3 Throughput rate and FWHM *versus* incident fluence 165
6.4 Throughput rate and FWHM *versus* filter thickness 166
6.5 Hg sensitivity and system dose *versus* filter thickness 171
6.6 Hg MDL *versus* depth in torso 174
6.7 Schematic of dosimeter arrangement 179
6.8 Dose distribution in phantom from Hg polarised system 180
7.1 Incident and Ge-detected spectra (full energy range) 197
7.2 Incident and Ge-detected spectra (0 to 30 keV range) 197
7.3 Incident and Ge-detected spectra (90 to 125 keV range) 198
7.4 Ge- and Pb-detected spectra (full energy range) 199
7.5 Ge- and Pb-detected spectra (0 to 30 keV range) 199
7.6 Two Pb-detected spectra (0 to 30 keV range) 201
7.7 Two Pb-detected spectra (30 to 60 keV range) 201
7.8 Two Pb-detected spectra (90 to 125 keV range) 202

LIST OF TABLES

Number *Page*

1.1 Lead content in tissues and organs 12
1.2 Mercury content in tissues and organs 20
1.3 Mercury concentrations in Hg miners and controls 21
1.4 Blood-lead levels associated with health effects 23
2.1 Lead K-shell x-ray characteristics 38
2.2 Characteristics of possible isotopic sources for Pb XRF 40
2.3 Characteristics of possible isotopic sources for U XRF 43
2.4 Uranium K-shell x-ray characteristics 43
3.1 Quantitative comparison of Monte Carlo and experiment 76
5.1 Regression analysis of source-excited bone-U calibration 124
5.2 Properties of Rando® phantom material 127
5.3 Attenuation coefficients of various filter materials 148
5.4 Regression analysis of polarised bone-U calibration lines 150
5.5 Comparison of source-excited and polarised U sensitivities 156
6.1 Regression analysis of polarised Hg calibration lines 175
6.2 Comparison of MDL's from various Hg measurement systems 176
6.3 Properties of tissue-equivalent material for dose measurements 179
6.4 Dose rates of various Hg measurement systems 181
7.1 Quantitative comparison of Ge and Pb detection systems 203
7.2 Comparison of mean $K\alpha_1$ areas detected by Ge and Pb 204

Chapter 1

INTRODUCTION

1.1 Non-invasive Elemental Analysis

There are many situations in which the medical community gains significant diagnostic power through elemental analysis in tissues or organs of a patient. For example, the ability to measure total body protein by assessing the quantity of nitrogen in the patient is of great importance for studying protein depletion and repletion after surgery. The measurement of total body nitrogen can also aid in the recognition and knowledge of early malnutrition and kidney failure, as both these conditions have associated protein depletion. Many other examples may be cited of the importance of measuring the amount of major elemental constituents of the human body, such as nitrogen, carbon, oxygen, hydrogen, calcium, phosphorus, sodium, and potassium. However, in the field of occupational health, there is considerable interest in quantifying the presence of trace elements in the body, such as lead, mercury, cadmium, and uranium. By monitoring the quantities of these toxic elements in subjects with occupational exposure, safe working environments can be achieved and intervention mechanisms can be put in place to ensure the risk to workers' health is minimised.

Whether measuring major elemental constituents or trace elements in human subjects, there are certain constraints on the technique chosen. In all cases, the ability to measure the element of interest in a particular tissue or organ with as little discomfort for the subject as possible is the main goal. This issue of comfort implies that for clinical feasibility, the measurement should be non-invasive, which we define here as requiring no tissue extraction (biopsy) and no introduction of foreign objects (probes) directly into the measurement site. Furthermore, the measurement should require minimal time and should not introduce unnecessary additional health issues, such as that which may arise from an excessive radiation dose associated with the procedure. Such non-invasive elemental analysis techniques can generally be divided into two categories: those relying on nuclear properties of the elements under investigation, and those based on atomic properties.

1.1.1 Nuclear methods

a) Neutron Activation Analysis (NAA)

NAA is based on the activation of a particular isotope by the interaction with an incident neutron. The product of this reaction is the formation of an excited nuclear state or a radioactive isotope of this, or another, element. By measuring the γ-ray emission from the excited state or following the subsequent β decay of the radioactive product, the quantity of the parent isotope present in the sample can be measured. NAA techniques and applications *in vivo* have been reviewed extensively elsewhere, Chettle & Fremlin, 1984, Beddoe & Hill, 1985, Cohn & Parr, 1985.

For NAA to be useful in medical applications, many factors must be considered. Of primary concern is the magnitude of the neutron absorption or scattering cross section as well as the energy and intensity of the γ ray emitted and the half-life of the decay. In order to generate a measurable signal in minimal irradiation time, the neutrons must interact with the isotope of interest with a reasonable cross section and yield a γ ray of sufficient energy to penetrate the sample. NAA has been used to measure total body concentrations of many of the major elements such as hydrogen, nitrogen, oxygen, sodium, magnesium, phosphorus, chlorine, and calcium (Sutcliffe 1996). NAA has also been applied to the measurement of certain toxic trace elements such as cadmium (Thomas *et al.*, 1979), mercury (Smith *et al.*, 1982), aluminium (Pejović-Milić *et al.*, 1998), and manganese (Arnold *et al.*, 1999).

b) Whole-Body Counting

Whole-body counting relies on the detection of radiation from naturally occurring radionuclides in the body. Therefore, this technique is confined to the *in vivo* measurement of total body potassium, as potassium is the only element in the body of sufficient quantity with a naturally occurring γ-ray emitting radioisotope, ^{40}K. Total body potassium (TBK) is determined by counting the 1.46 MeV γ rays emitted following the β decay (electron capture) of ^{40}K in a low-background whole-body counter.

A similar approach has also been applied to monitoring exposure to uranium and plutonium. The γ-ray signals specific to the decay chains of these elements are counted, and their signal strength is then related to exposure by comparisons with calibration standards. However, γ-ray intensities depend on both the mass of the element present and its location within the body. Whole-body or partial-body counting therefore only provides a quantitative estimate of content when calibration standards are constructed that model accurately both the element level and the distribution.

c) Nuclear Resonance Scattering

Certain elements in the body that are difficult to measure by neutron activation and do not have naturally occurring radioisotopes, such as iron and copper, can be measured by nuclear resonance scattering. This technique uses incident γ rays to excite the isotope of interest to a state that subsequently decays to the ground state by emission of characteristic γ rays. The difficulty with nuclear resonance scattering, however, is that the incident γ rays must be within approximately 1 eV of the energy of the excited state of the nucleus in order to cause excitation. Therefore, a radionuclide is required that happens to emit γ rays with an energy that corresponds to one of the excited states in the nucleus to be measured. Alternatively, a nuclide that decays to an excited state of the nucleus under investigation may also be used, however, various methods must be used to correct for energy losses arising from nuclear recoil during γ–ray absorption and emission (Vartsky *et al.*, 1979). Nuclear resonance scattering may soon benefit from the rapid development of synchrotron light sources at higher photon energies, as synchrotron facilities are powerful sources of tuneable monoenergetic photon beams but are currently operated at lower energies than required for these applications.

d) Magnetic Resonance Spectroscopy

When a human body is placed in a strong magnetic field, any nuclei with unpaired nucleons, such as ^{1}H, ^{13}C, ^{19}F, ^{23}Na, ^{31}P, and ^{39}K, tend to align their magnetic moment with or against this field vector. While only a small fraction of these nuclei are thus aligned, there is a sufficient number to result in a measurable response to a changing magnetic field tuned to the frequency at which these nuclei precess in the static applied field (Sutcliffe, 1996).

Since each isotope precesses at a unique frequency, tuning the sampling magnetic field to a particular frequency allows for the measurement of the amount of a specific isotope present in the sample.

Magnetic resonance spectroscopy has one significant advantage over the other possible nuclear methods for measuring these isotopes. There is no radiation dose, so repeated measurements are not limited by this factor. The majority of human studies to date have been measurements of ^{31}P, as these measurements provide a valuable means of monitoring the cellular energy balance due to the use of high-energy phosphate bonds to store energy (Leach, 1988). Due to perturbations of the local magnetic field arising from the environment in which the isotope is located, the precession frequency shifts slightly based on the chemical bonds in which the ^{31}P is involved. Therefore, magnetic resonance spectroscopy results in spectra with peaks in precession frequency corresponding to adenosine triphosphate (ATP), the major source of energy in the body; phosphocreatine (PCr), which provides a readily accessible short-term supply of energy; and inorganic phosphate, which is a product of ATP breakdown. These spectra provide a wealth of information in terms of understanding cellular metabolism, studying the effect of exercise on metabolism (Taylor *et al.*, 1983), and have also proved valuable in the study of muscular weakness and dystrophies (Arnold *et al.*, 1984). There is also considerable interest in the use of magnetic resonance spectroscopy for monitoring tumour metabolism as a method of measuring response to therapy.

1.1.2 Atomic methods

a) Absorptiometry

Absorptiometry utilises the rapid change in the photon absorption coefficient for a given element at a specific energy, known as an edge. This edge energy corresponds to the energy required to eject an electron from a bound shell; when this occurs in the K shell, the energy is referred to as the K edge of that particular element, and so on. When the energy of an incident photon is just above the required energy to eject an electron, there is a significantly higher probability that the photon is absorbed compared with a photon with energy just below this edge. Figure 1.1 demonstrates the magnitude of this change in absorption probability in iodine.

Differential absorption can therefore be measured at two photon energies, one on either side of the K edge of the element of interest. The difference in the absorption through the sample at these energies will depend on the amount of this element present. Furthermore, since the edge energy is unique to each element, the absorption through the sample at these energies will only change significantly due to the presence of a specific element; all other elements have absorption coefficients that are relatively unchanged between these two energies. Absorptiometry has been applied in the measurements of iodine in the thyroid (Jacobson, 1964) and antimony in the lungs (McCallum *et al.*, 1970). The clinical success of absorptiometry requires that the K edge of the element is sufficiently high in energy that the incident photons have acceptable penetration capabilities *in vivo*. Since the edge energy increases with increasing atomic number Z, absorptiometry is limited to elements with Z greater than approximately 40. In addition, due to the magnitude of the change in absorption cross section at an edge, as shown in figure 1.1, absorptiometry would not be expected to measure the presence of trace elements in the sample, even if the Z of the element is sufficiently high. Furthermore, this technique is limited by the availability of discrete photon emissions at energies just above and below the edge under investigation. This limitation may become less of a constraint in the near future, with the advent of synchrotron radiation sources at these energies.

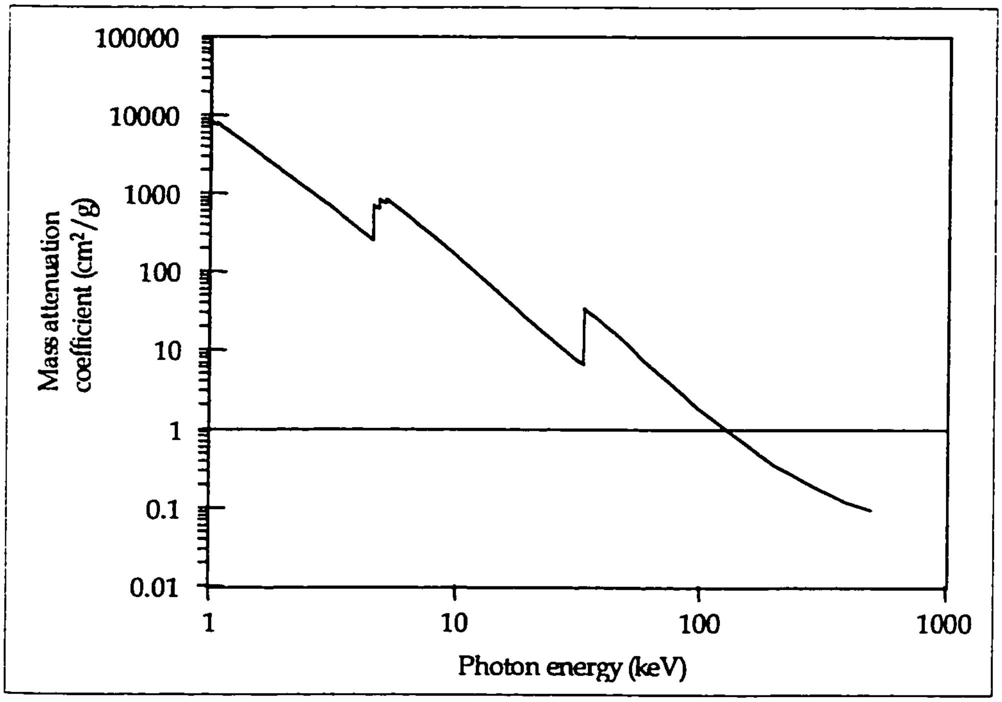

Figure 1.1: Log-log plot of mass attenuation coefficient as a function of photon energy for iodine. Note the edge features at 5 keV and 33 keV. These are the L and K shell edges respectively.

b) X-ray Fluorescence (XRF)

XRF is a process that involves the excitation of the atom by incident radiation, followed by the emission of an x-ray in order to return to the atomic ground state. When a photon of energy greater than a particular shell edge of the element under investigation is incident on the atom, one of the possible interactions that can occur is the photoelectric effect. In this interaction, an electron in that shell is ejected and the atom is left in an excited state. To return to its ground state, another electron from an outer shell falls into the vacancy created, and the atom emits a photon or one or more Auger electrons with energy corresponding to the difference in shell binding energies. Since the electron energy levels of each element are unique, the photons emitted in this process have characteristic energies that enable the elemental identification of the atom with which the photon interacted. By calibration methods that will be discussed in detail in later sections of this thesis, the number of these x-rays detected can be related to the amount of the element present in the sample.

As with absorptiometry, there is a practical limit to the atomic number of the elements that can be successfully measured *in vivo* with XRF. Since the incident photon energy must be greater than the K edge of the element under investigation, and the x-rays emitted are within a few keV of this edge, this threshold must be sufficiently high such that both the incident photons and emitted x-rays have acceptable penetration capabilities in tissue. Since the edge energy increases approximately with the square of the atomic number, this penetration requirement results in a practical limit of Z greater than approximately 40. This requirement of high atomic number elements also ensures that there is a high percentage of x-rays emitted per shell vacancy compared with Auger electrons, as this percentage, the fluorescence yield ω, also increases rapidly with Z.

Several elements have been successfully measured *in vivo* with XRF, particularly toxic metals with high Z, such as cadmium (Christoffersson and Mattsson, 1983), mercury (Börjesson *et al.*, 1995), gold (Shakeshaft and Lillicrap, 1993), lead (Ahlgren *et al.*, 1976; Somervaille *et al.*, 1985) and platinum (Jonson *et al.*, 1988). This thesis is an investigation of XRF applications in the measurements of uranium (O'Meara *et al.*, 1997), lead (O'Meara *et al.*, 1999; O'Meara *et al.*, 1998a), and mercury. It should be noted that *in vivo* XRF applications have been developed utilising L shell excitations, mainly in the measurement of lead (Wielopolski *et al.*, 1983; Rosen *et al.*, 1989; Wielopolski *et al.*, 1989). However, this work focuses on the use of K shell excitations only in the measurement of the three metals mentioned above.

1.2 Metal Kinetics

a) Lead

To understand the behaviour of a substance upon entry to as complex a system as the human body, simplified models are often introduced. In modelling the kinetics of a substance, compartmental models are used in order to provide a mathematical description of the transport of the substance within and through the body. Each compartment, as shown in figure 1.2, represents an anatomical or physiological system in the body, in which it is assumed that the substance in question is homogeneously distributed and well-mixed. Transport from one compartment to another is assumed to be exponential with a characteristic rate constant. For example, the arrow indicated in figure 1.2, from the compartment labelled "kidneys" to the compartment labelled "urine", represents a transfer of this substance with a particular rate constant, λ. If this were the only arrow originating from the kidney compartment, this transfer would result in the concentration C of this substance in the kidney being described mathematically as an exponential loss in time:

$$C(t) = C_o \cdot e^{-\lambda t} \qquad [1.1]$$

where C_o is the concentration at time t=0. However, since there is additional transfer of this substance to and from other compartments, this expression is not complete.

A number of metabolic models have been proposed to describe the kinetics of lead in the body. While each model differs slightly from the next in terms of the particular model parameter values assigned, generally they include compartments for whole blood, plasma, cortical and trabecular bone, as shown in figure 1.2. In addition, each model includes one or more other compartments, either incorporating many organs into one generic compartment simply labelled “soft tissue”, or modelling organs such as the kidneys, liver, and brain as separate compartments from this generic “soft tissue” component as shown in figure 1.2. Among the various models, these differences arise due to the detail with which physiological knowledge is incorporated into the compartmental divisions. For example, along with the variation in soft tissue compartments included, the modelling of the bone compartments can differ significantly from model to model, and accuracy depends on the incorporation of age variations in bone formation and resorption, as well as diffusion of lead in quiescent bone. (Note: for a more detailed discussion of the metabolic modelling of lead, see Fleming 1998, the main source of information for this section.) For our purposes, however, the sites of lead uptake and retention due to exposure is the issue of concern. This will allow for the design of measurement systems such that the concentration of lead is measured *in vivo* within the organs or tissues of major retention, as well as in organs of concern with respect to toxic effects.

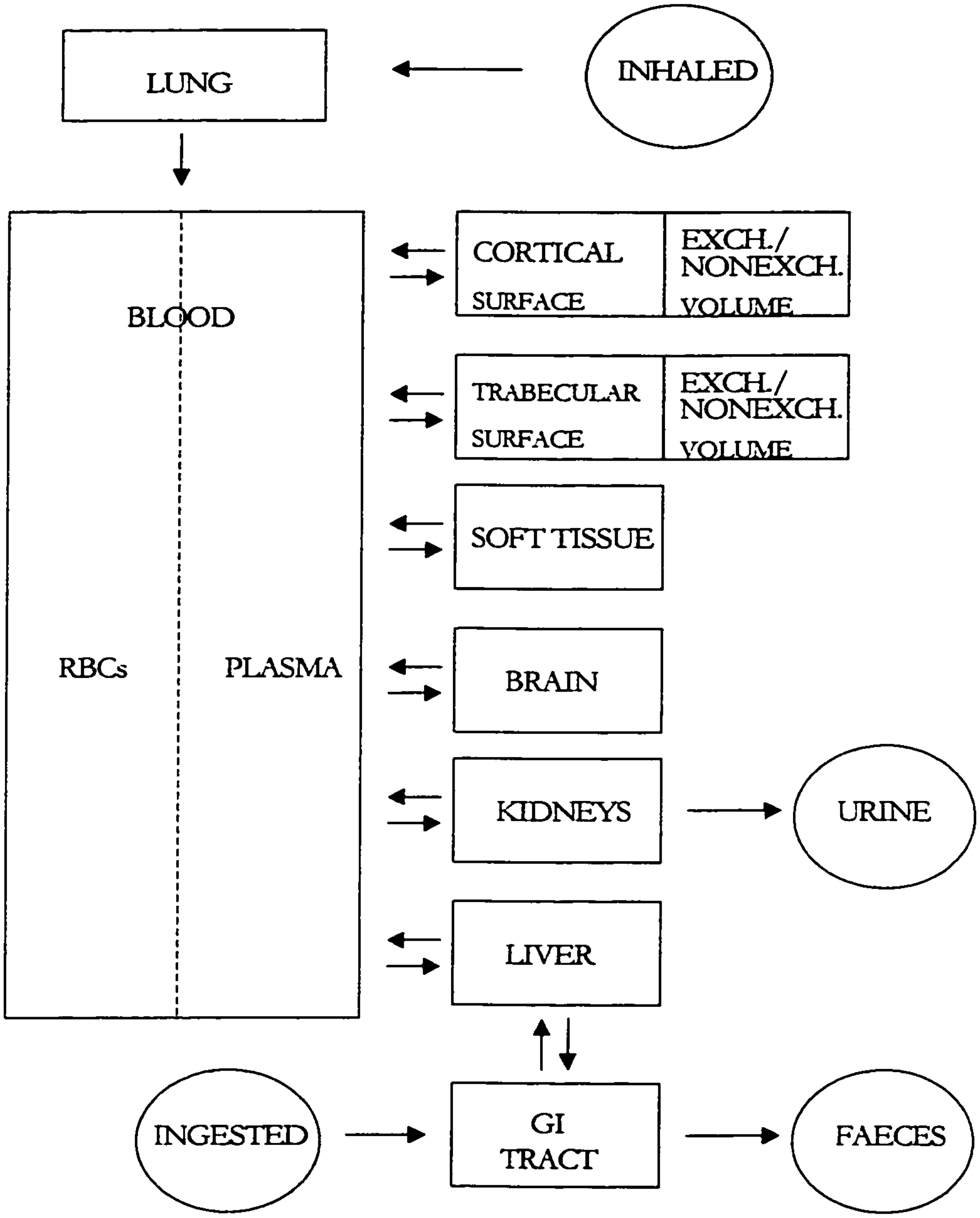

Figure 1.2: Generic metabolic model of lead – modified from Fleming, 1998.

Based on these models, it is clear that there are many organs in which lead is retained. However, based on autopsy results (Barry, 1975), the relative equilibrium concentrations in these organs is such that greater than 90% of the total lead body burden is contained within the bone compartments. These autopsy studies have also demonstrated that bone-lead concentrations increase with age, which suggests that lead is well retained in this compartment. Therefore, it is expected that bone-lead concentrations reflect cumulative lead exposure, and could reach levels that are measurable *in vivo* with x-ray fluorescence. Since the remaining minor portion of the lead burden is shared among many organs and tissues, it is not expected that levels in any other site would normally be sufficient for *in vivo* measurements. See table 1.1 for a summary of lead levels measured in autopsy samples.

Tissue	Number of samples	Mean (ppm wet weight)	Standard deviation (ppm wet weight)
Bone: petrous temporal	30	33.7	22.3
Bone: tibia	60	23.4	16.0
Bone: calvarium	31	20.2	16.0
Bone: rib	60	8.85	5.81
Liver	58	1.03	0.62
Kidney: cortex	59	0.78	0.38
Kidney: medulla	59	0.50	0.25
Pancreas	58	0.37	0.26
Spleen	59	0.23	0.25
Thyroid	55	0.19	0.23
Blood	53	0.20	0.12
Brain: cortex	58	0.10	0.14
Brain: Basal ganglia	34	0.09	0.04
Heart	59	0.07	0.05
Muscle	35	0.05	0.04

Table 1.1: Concentration of lead in tissues and organs of individuals with no known occupational exposure to lead. Modified, from Laird, 1983.

b) Uranium

A number of mathematical models have been developed that relate body uranium content to intake, *e.g.* ICRP 30 (1979). In general, these models are based on animal experiments, early human experiments, and estimates based on autopsy measurements requiring some assumptions regarding daily uranium intake (Wrenn *et al.*, 1985). Figure 1.3 summarises the metabolic model for uranium, ingested or inhaled, as proposed by Health and Welfare Canada (1987). While this form of metabolic model has been criticised for not being easily adapted to conditions of environmental exposures (Wrenn et al., 1985), it is generally considered acceptable in occupational exposure cases. More complicated models have been proposed, see for example Leggett, 1994, however figure 1.3 captures the essence of the uranium distribution in sufficient detail for our purposes. The model shown in figure 1.3 indicates that there is a rather complex path between uranium inhalation/ingestion and uranium storage. A further complication in this model is that the various compartmental rate constants in the lung section depend on the inhalation class of the uranium compound. This is based on the observation that different chemical and physical forms of uranium have different behaviours when inhaled. However, for the purposes of this thesis, the issue of concern is the distribution in the body once the uranium has entered the transfer compartment (the blood).

From figure 1.3, it is evident that the three main compartments to consider in discussing uranium retention are bone, kidney, and soft tissue. The bone is the compartment of long-term retention, as ~ 2% of the uranium in the transfer compartment is stored in bone with a biological half-life of ~ 5000 d (~ 14 years). As with lead retention, this compartment is therefore a reflection of cumulative exposure to this metal, and may be a source of continuous endogenous exposure well after exogenous exposure is terminated. Therefore, measurements in this tissue could provide useful information for occupational monitoring (see section 1.4 b)). The kidney is also a potentially useful site for measuring uranium concentrations *in vivo*. Figure 1.3 shows that ~ 12% of the uranium in the blood enters the kidney compartment. The vast majority of this 12% is eliminated with a ~ 6 d half-life, while a small fraction is retained in the kidney with a half-life of ~ 1500 d. Since kidney damage is a major concern in uranium exposure, see section 1.3 b), measurements of uranium in the kidney could be used in ensuring the health of those exposed in their work environment. Lastly, ~ 12% of the uranium in the transfer compartment is taken up by all other soft tissues. It is therefore not expected that any other tissue/organ is a candidate for *in vivo* measurements as 12% of the amount in the blood stream, distributed over all soft tissue except the kidneys, is not expected to yield measurable concentrations.

These compartments of uranium uptake and retention are necessarily a simplification of the true distribution of uranium from the bloodstream. Furthermore, the biological half-lives and fractions entering each compartment tend to vary from model to model based on author preference and the kind and quality of biological data available (Wrenn *et al.*, 1985). However, for the purposes of this study, the model depicted in figure 1.3 is sufficient for understanding the major sites of long-term and short-term uranium retention. This model of uptake and retention from the blood is assumed to be independent of the mechanism of entry to the transfer compartment, *i.e.* either inhalation or ingestion. It can therefore be assumed that this model of uranium retention also may be applied in cases of unconventional uranium exposure, such as the subcutaneous deposition of uranium fragments. The importance of the validity of this assumption will become clear in later sections of this thesis.

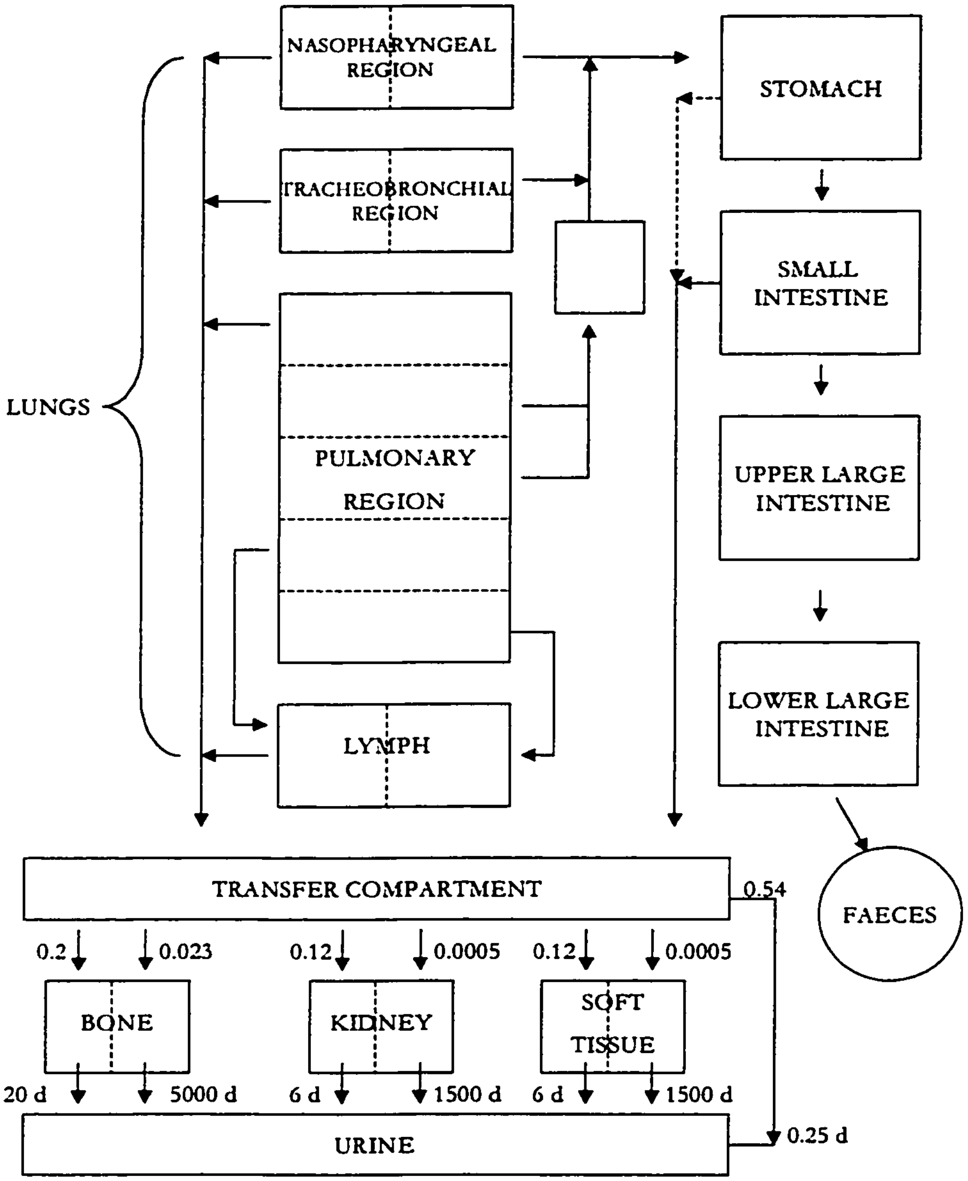

Figure 1.3: Metabolic model for uranium – from Health & Welfare Canada (1987).

c) Mercury

In contrast to lead and uranium, there are limited data available with which to construct metabolic models for mercury. Furthermore, as with uranium, the absorption and distribution of mercury in the body is a strong function of the particular chemical and physical form under consideration. For the purposes of this thesis, however, it is sufficient to focus attention on the kinetics associated with the inhalation of metallic or elemental mercury vapour, as this is the most important route for absorption of mercury in industry (Nordberg & Skerfving, 1972).

Based on the limited animal and human data available, a generic compartmental model for the kinetics of inorganic mercury is shown in figure 1.4. In general, approximately 80% of the elemental mercury vapour is absorbed in the lungs. This compartment may well be a vast oversimplification of the kinetics in the lung, and this may be better represented by a model similar to that of uranium, shown in figure 1.3. However, no direct measurements of detailed pulmonary deposition have been reported (Nordberg & Skerfving, 1972), therefore this simplified model is used. In contrast to the model of lead kinetics shown in figure 1.2, the mercury kinetic model includes the pathway of exhalation from the lungs. This is based primarily on animal data, in which it has been observed that a fraction of both inhaled and injected mercury vapour is exhaled shortly after administration (Nordberg & Skerfving, 1972). In addition to inhalation of vapour, the absorption pathway through ingestion is included in figure 1.4. The inclusion of this pathway, however, is more for the purposes of completeness, as most animal studies, as well as early human investigations, have demonstrated that the absorption of metallic mercury through the gastrointestinal tract is essentially negligible. However, elimination through faeces has been observed both in workers exposed to mercury vapour and subjects injected with Hg^{2+}(Nordberg & Skerfving, 1972). Therefore, the exchange between the blood, liver, and GI tract is included in this model to allow for this removal pathway.

Regardless of the pathway for absorption, once in the transfer compartment, elemental mercury (Hg^0) vapour is oxidised to mercuric mercury (Hg^{2+}) quite rapidly. However, a fraction of Hg^0 dissolves directly in the blood and is believed to remain in this form for a sufficient amount of time to travel at least one complete circulation through the body. It is this dissolved Hg^0 that can readily penetrate biological membranes, including the blood-brain barrier. With time, however, more of the Hg^0 is oxidised and is typically found in the plasma bound to different proteins. Only a very small fraction of this Hg^{2+} is found in a "free", ultrafiltrable form within the plasma. With these variations in the oxidation state of mercury with time, the relative ease of transfer from the blood to various other compartments will also vary with time after exposure. Furthermore, the ratio of mercury in the red blood cells (RBC's) to the concentration in the plasma varies with time, which further complicates the model of transfer from blood to organs and tissues. Nevertheless, certain generalisations can be made regarding the distribution within organs and tissues based on animal and human data.

The compartments shown in figure 1.4, representing the organs to which the mercury tends to be distributed from the blood, are chosen based on the trends observed in various studies, for example, Nordberg & Skerfving, 1972, Kosta *et al.*, 1975, and Matsuo *et al.*, 1989. In most of these reports, the highest concentration of mercury is generally found in the kidneys. The liver, spleen and thyroid are often the next three highest sites of accumulation. Although recognised as the 3rd and 4th highest sites of mercury concentration, the spleen and thyroid have been grouped as one compartment in figure 1.4, along with other organs that have shown measurable mercury levels in these studies, such as the pituitary. These organs have all shown similar mercury concentrations when any other organs than kidney, brain and liver are specifically mentioned, see tables 1.2 and 1.3. Therefore, it was felt that these could be grouped together due to their similar levels, which are significantly lower than the mercury concentrations seen in the major sites of accumulation, the kidney and the liver. However, there is no information available regarding the rates of exchange in these organs, therefore it is unknown whether the kinetics can accurately be represented as one compartment. It is interesting to note that, in contrast to both lead and uranium, there is no evidence that significant quantities of mercury accumulate in bone tissue.

The mercury levels in the kidneys are not believed to be uniformly distributed (Nordberg & Skerfving, 1972). The concentrations in this organ are important, as the kidney and the brain are considered to be the critical organs in terms of the toxicological effects of mercury. Furthermore, levels in the brain are thought to reflect cumulative exposure to mercury, as autopsy samples taken many years after the termination of exposure have shown considerable mercury levels in various regions of the brains of these workers (Nordberg & Skerfving, 1972). In addition, concentrations of inorganic mercury in the cerebrum have been shown to increase with age (Matsuo *et al.*, 1989), further evidence that this is a site of long-term retention.

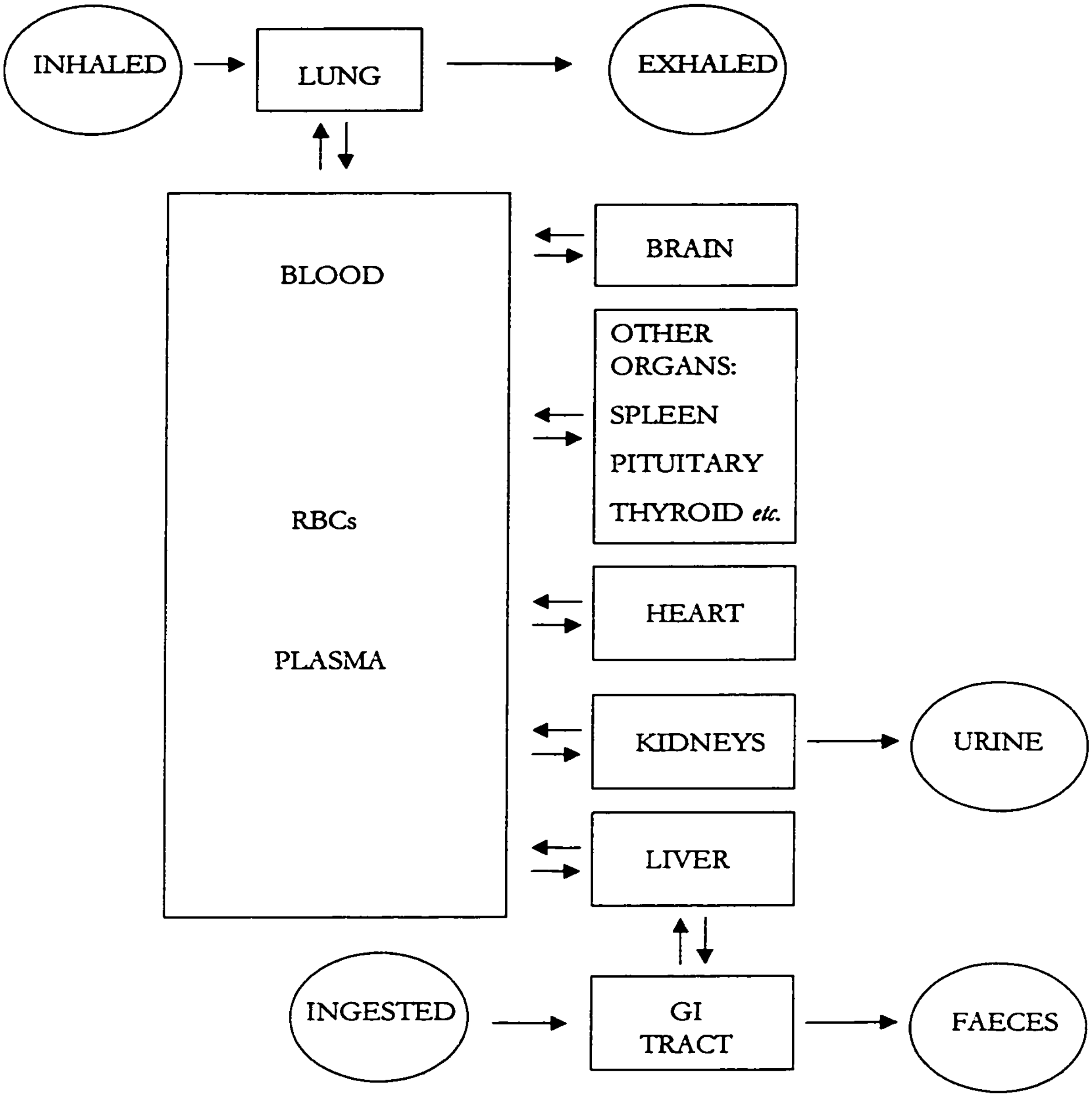

Figure 1.4: Generic metabolic model for inorganic mercury. Based on data summarised in Nordberg & Skerfving, 1972.

Matsuo *et al.* also demonstrate that concentrations in the heart increase with age, suggesting that the heart may also be a site of slow elimination of mercury. For this reason, although levels are similar to those of the spleen, thyroid, and pituitary as shown in tables 1.2 and 1.3, the heart is represented as a separate compartment in figure 1.4.

Based on these studies, some conclusions can be made. The critical organs for toxicological damage, the kidneys and the brain (see section 1.3 c)), are the primary organs of interest in terms of measuring mercury concentrations *in situ*. In terms of the feasibility of these measurements, it is somewhat fortuitous that the kidneys are one of the sites of the greatest mercury concentrations in the body. In addition, there are indications that the mercury concentrations in the brain may be an index for assessing cumulative exposure. However, levels in the brain are often much lower than those measured in the kidneys, see tables 1.2 and 1.3, and *in vivo* measurements in this site are more complicated due to shielding from the skull. *In situ* assessments of cumulative exposure may still be feasible, however, as one study has suggested that the heart may be an additional site of long-term retention, Matsuo *et al.*, 1989.

Organ	Mean (S.D.) in ng/g	Number of samples
Cerebrum	54 (1.7)	28
Cerebellum	69 (1.8)	25
Kidney – cortex	548 (2.2)	43
Kidney – medulla	339 (2.0)	32
Heart	41 (1.9)	33
Spleen	42 (1.7)	39
Liver	479 (2.0)	32

Table 1.2: Levels of mercury in various organs based on autopsy measurements. These are in individuals with no known occupational exposure, from Matsuo *et al.*, 1989.

Organ	Levels in miners Mean (S.D.) in µg/g	Levels in controls Mean (S.D.) in ng/g	Number of samples
Brain	0.7 (0.64)	4.2 (2.6)	5
Kidney	8.4 (4.9)	140 (160)	7
Thyroid	35.2 (28.5)	30 (37)	16
Pituitary	27.1 (14.9)	40 (26)	6
Liver	0.26 (0.25)	30 (17)	8

Table 1.3: Mercury concentrations in mercury miners and non-exposed controls, from Kosta *et al.*, 1975. Note that the occupational levels are given in µg/g whereas the unexposed levels are given in ng/g.

1.3 Heavy Metal Health Effects

a) Lead

It has long been known that exposure to lead can result in adverse health effects. Primarily, lead exposure results in damage to the nervous system, the kidneys, the reproductive system, and inhibits the production of heme. Furthermore, there is some evidence that lead exposure may increase the risk of some types of cancer. The health effects of lead exposure have been discussed in greater detail by Fleming, 1998, and Laird, 1983. The main health concerns are summarised below based on these discussions.

In the nervous system, the main symptom of low-level lead exposure in adults is reduced nerve conduction velocities. At higher exposure levels, the classic symptoms of lead poisoning arise from polyneuritis of sensory and motor nerves, which results in loss of motor function and can be manifested in wrist drop. In children, low-lead exposures are a concern, as elevated blood-lead levels in the umbilical cord have been associated with low scores on the Mental Development Index of Bayley, administered over the first two years of childhood. Table 1.4 summarises the blood-lead levels generally associated with these various detrimental effects on the nervous system.

During pregnancy, there are additional health concerns for the foetus when the mother is exposed to lead. One study has shown that umbilical cord blood-lead levels greater than 15 μg/dl can result in a modest decrease in foetal growth. It should be noted that these findings contradict those of another study and, therefore, the observation of a relationship between lead exposure and reduced foetal development has not clearly been demonstrated. However, a clear effect of lead exposure on the male reproductive system has been observed; with blood-lead greater than 60 μg/dl there is some indication of reduced sperm count and altered testicular function.

In the kidneys, lead affects the cells lining the proximal tubules, the portion of the kidneys associated with water and nitrogenous waste processing. Early kidney damage is difficult to detect, as the kidneys are known to have significant reserve capacity. Studies have shown that blood-lead levels greater than 60 μg/dl result in observable effects on the kidneys, such as chronic-lead nephropathy. This diseased state may lead to kidney failure in subjects exposed to such high-lead levels.

In addition to adverse effects on the nervous system, the reproductive system, and the kidneys, studies have shown that lead exposure inhibits the synthesis of heme. Lead exposure is believed to inhibit heme synthesis by impairing various enzymes required in the production process, and this can occur at rather low exposure levels. Therefore, enzymatic activity can be a very sensitive index of lead exposure, and this has been used to screen children for risk of lead intoxication. This reduction in heme can often result in anaemia, but in occupationally exposed individuals this anaemia is often mild and may go unrecognised. Blood-lead levels required for significant reductions in haemoglobin in adults and children are summarised in table 1.4.

Finally, some animal studies, with high lead doses, suggest that lead may be a renal carcinogen. This limited information suggests that lead may promote renal cancer caused by other organic compounds. It should be noted though that studies of occupationally exposed groups have not been conclusive, as some have observed an increase in the incidence of renal cancer while others have not observed this effect.

	Adults		Children	
System Affected	Blood-Lead Level	Effect	Blood-Lead Level	Effect
Nervous system	120 µg/dl 40 µg/dl	Encephalopathy Reduced nerve conduction velocities	10 µg/dl (umbilical cord)	Low scores on Mental Development Index
Reproductive system	60 µg/dl 15 µg/dl (umbilical cord)	Reduced sperm count Decreased foetal growth	N/A	
Kidneys	60 µg/dl	Chronic lead nephropathy	N/A	
Heme synthesis	50 µg/dl	Reduced haemoglobin	25 µg/dl	Reduced haemoglobin

Table 1.4: Summary of blood-lead (and umbilical-cord lead) levels at which various adverse health effects are observed; based on Fleming, 1998 and Laird, 1983.

b) Uranium

In the case of health effects due to uranium exposure, the situation is either simpler, or merely less documented, than in the case of lead exposure. In general, literature summarising the toxicity of uranium focuses on effects on the kidneys only. In some studies, however, the potential carcinogenic behaviour of uranium has also been investigated. While this list of suspected detrimental health effects is shorter than that previously discussed for lead, there is some evidence of considerable variability in uranium toxicity with species, chemical form, and exposure pattern (Leggett, 1989), thereby creating complications for industry with respect to establishing safe working levels and monitoring procedures. Nevertheless, extensive literature reviews have been written, summarising the available knowledge of uranium toxicity, to aid in the development of monitoring procedures for occupationally exposed individuals. The following is a summary based on these reviews (Wrenn *et al.*, 1985; Leggett, 1989; Leggett, 1994).

A quantitative relationship between uranium intake and kidney damage has been measured in several species. Based on animal studies, it has been shown that the proximal renal tubules are killed by high acute or lower chronic dosages of soluble uranium, administered by any route. In these studies, the animal can survive if the dosage is not sufficient to destroy a critical mass of the kidney. While lost tubules can be replaced, the new cells are often not structurally identical to the old cells, and not all damaged cells are replaced. From these studies, it has been concluded that uranium-induced kidney damage is a non-stochastic effect with a threshold level; below a critical uranium concentration the metal remains as a soluble complex in the filtrate and does not react with the tubule cells. Above this threshold, kidney damage may occur gradually as more tubules are lost than are successfully replaced. Typically renal reserve is sufficiently large to prevent irreversible kidney damage in occupationally exposed workers, and generally only transient kidney dysfunction has been observed in these populations. However, if uranium exposure is high for a long enough time, it is believed that damage may accumulate to a level that compromises function. The threshold of irreversible kidney damage is believed to be 1 to 3 μg/g of uranium in the kidney.

While uranium has been demonstrated to be a highly toxic substance in terms of kidney damage, concerns are often raised regarding its potential for cancer induction, as naturally-occurring isotopes of uranium are radioactive. However, no radiobiological effects from ingested or injected natural uranium have been observed in either occupationally-exposed populations or in experimental animals. It should be noted, though, that bone cancer has been induced in animals, by injection or inhalation of soluble compounds of high specific-activity uranium isotopes, ^{232}U or ^{233}U. In addition, lung cancer has been induced in rats and dogs (but not in monkeys) by the continuous inhalation of large amounts of highly insoluble UO_2 over 2 to 5 years. Therefore, uranium exposure limits are set with respect to the chemical toxicity to the kidneys as well as the risk of lung cancer, and the question of whether radiological or chemical toxicity is limiting depends on the isotopic mixture, the chemical form, solubility, and the mode of exposure.

c) Mercury

As with uranium, the health effects of mercury depend on the amount, duration of exposure, mode of intake, as well as the chemical and physical form of this toxic metal. For the purposes of this thesis, however, it is sufficient to focus attention on the toxic effects associated with the inhalation of metallic or elemental mercury vapour, as this is the most important route for absorption of mercury in industry (Nordberg & Skerfving, 1972). The following is largely a summary based on mercury toxicity descriptions from Armstrong, 1991, and WHO, 1976.

In the case of high level acute exposures to inorganic mercury vapour, the lungs are the critical organs. Symptoms of acute exposure include chest pain and inflammation of the lung tissue, as well as emphysema and haemorrhage. Such high levels of exposure to mercury vapour may lead to respiratory failure and death. In addition, there can be some associated detrimental effects to the central nervous system as well as to the kidneys, however, these are rather small in comparison to the effects on the respiratory system.

When individuals are exposed to significant mercury levels over a longer period of time, the main health concern shifts to the kidneys. Much like the effects of lead and uranium, it is believed that high levels of mercury exposure result in glomerular and tubular damage, requiring severe damage to occur before function is compromised. The substantial reserve capacity of the kidneys is likely responsible for the rarity of observing significant damage in occupationally-exposed populations.

Finally, in cases of low-level, long-term mercury exposure, the accumulation of mercury in the brain becomes the greatest cause for concern. Early signs of detrimental health effects to the brain include tiredness, frequent headaches, nausea, and diarrhoea. With further exposure to mercury, tremors in the fingers, lips and eyelids become evident. This can be accompanied by depression, memory loss, and insomnia. With prolonged exposure to lower levels of mercury vapour, severe behavioural changes have been observed.

It should be noted, however, that with the exception of prolonged exposure to extremely high concentrations of mercury vapour, all the aforementioned detrimental health effects are generally considered to be reversible once the exposure is stopped.

1.4 Occupational Monitoring Procedures

a) Lead

As lead is known to cause several detrimental health effects, occupational monitoring has become standard practice within companies in which workers are exposed to lead. For many years, blood samples have been collected on a regular basis and the lead content has been assessed. In addition, occasionally companies will require urine samples to be measured for lead concentration. In routine occupational monitoring, blood-lead levels over the course of an employee's entire work history are used as a measure of cumulative exposure to this toxin, as one individual measurement is merely a reflection of current or recent lead exposure. This time-weighted integrated blood-lead level, referred to as the CBLI (Cumulative Blood-Lead Index), is used as an index for industry to ensure workers' health is not compromised. However, for this to be an effective index of cumulative exposure due to the work environment, the CBLI has to be adjusted for the pattern of exposure to lead for a given worker. In addition, corrections must be made for any release of lead from bones into the blood (endogenous exposure). Detailed data must be kept for each worker in order to calculate an accurate CBLI (Börjesson, 1996).

An alternative to assessing cumulative lead exposure by calculating the CBLI is the measurement of lead directly in the site of long-term retention in the body, namely, the skeleton. As lead is stored in the bone with a half-life of several years, measurements directly in this tissue should provide a more direct indication of cumulative exposure and, therefore, a more direct index for health monitoring. Lead measurements in the bone would not require corrections for endogenous lead releases due to bone turnover, as this is inherently accounted for in the measurement. Furthermore, one measurement is sufficient to assess cumulative exposure, without requiring the integration of results over many years as is the case with the CBLI calculation. In addition, measurements of bone-lead could provide complementary data for interpreting the kinetics of lead in the human body, as well as a direct indication of the risk of future endogenous exposure. For these reasons, non-invasive *in vivo* x-ray fluorescence measurements of bone-lead have been gaining popularity in the field of occupational health.

b) Uranium

As discussed in 1.3 b), occupational uranium exposure limits are set with respect to the chemical toxicity to the kidneys as well as the risk of lung cancer. The question of whether radiological or chemical toxicity is limiting depends on the isotopic mixture, the chemical form, and the mode of exposure. Therefore, Health and Welfare Canada recommend that either lung scans or urinalysis be performed to monitor workers based on the particular parameters of uranium exposure in a given situation (Health & Welfare Canada, 1987). In some cases, if the isotopic mixture, chemical form, or exposure mechanism is unknown or variable, both lung scans and urinalysis should be implemented. Lung scans are useful in assessing the risk of lung cancer, as these measurements are directly in the critical organ. However, assessing risk of chemical damage through urinalysis is not the ideal approach.

As there are essentially no practical alternatives, urinalysis has been used as an index of uranium exposure for many years. However, estimates of the time-dependent uptake of uranium to blood based on urinary uranium levels often involve substantial uncertainty (Leggett, 1994). For example, uranium excretion rates are known to vary considerably during the day, and day to day, in a given individual. One study demonstrated that the rate of urinary uranium excretion can fall by an order of magnitude or more between the end of one work day and the beginning of the next in workers exposed to UO_2F_2 in air (Leggett, 1994). Another study (Chase, 1989) found considerable variation in uranium excretion rates among workers exposed to the same concentrations of uranium in air. The Chase report cited another paper (Spitz *et al.*, 1984) as the motivation of his work, as Spitz *et al.* had concluded that uranium urinalysis bioassay results were too variable to serve as a reliable monitoring tool for determining whether mill workers had been exposed to airborne uranium. It should be noted that there is some evidence that this variability can be reduced by normalising the absolute quantity of uranium in the urine sample to the amount of creatinine present (Karpas *et al.*, 1998). However, the Karpas *et al.* study did not compare the normalised uranium levels in urine to air concentrations. Therefore, it is not possible to conclude whether this normalisation procedure establishes urinary uranium as a useful index for monitoring airborne exposure.

In addition to intra- and inter-subject variations in uranium excretion rates, there is some evidence that biokinetics in the kidneys depends on the amount of uranium exposure (Leggett, 1994). The time-dependent transfer of uranium to urine in kinetic models is primarily based on data from three human studies in which relatively large amounts of uranium were injected. It is not clear that the current practice of using derived model rates of excretion per unit intake in occupational settings, where uranium exposures are at lower levels, is valid. Indeed, the study by Chase (1989) found that the observed average rate of excretion per unit uranium concentration in air was approximately three times higher than the rate predicted by an internal dosimetry model. Therefore, using urinary uranium levels to assess exposure may be confounded by both intra- and inter-subject variations in excretion rates per unit exposure, as well as the doubts about the validity of the assumption that excretion rates per unit exposure are independent of the magnitude of the exposure itself.

Although there are potential difficulties involved in interpreting urinary uranium levels as a marker of chemical toxicity, this is currently the only feasible measure available in occupational monitoring. Ideally, a non-invasive mechanism that measures uranium levels directly in the kidney would provide industry with a direct assessment of renal health. However, as discussed in 1.3 b), threshold levels of 1 to 3 μg/g of uranium in the kidneys may give rise to renal damage. It is questionable whether any of the non-invasive methods discussed in section 1.1 would be sufficiently sensitive to measure uranium in the kidneys at levels less than this threshold. Alternatively, since renal damage may be a cumulative effect, measurements of uranium in bone, the site of long-term retention, could provide a useful index to aid in monitoring workers. In addition, *in vivo* measurements of uranium in the bone could give valuable insight into uranium kinetics, which may be particularly important in the unique case of the subcutaneous implantation of uranium-containing metallic fragments. Furthermore, as with lead measurements in the bone, non-invasive assessments of bone-uranium could provide a measure of the risk of future endogenous exposure.

c) Mercury

As with lead and uranium, occupational monitoring for mercury exposure is comprised of blood and urine sampling. However, the mercury concentrations in these biological fluids are influenced by the most recent exposure. Furthermore, as with uranium, urinary mercury concentrations are notoriously difficult to interpret due to significant variations over the course of a workday as well as from day-to-day (Sällsten *et al.*, 1990). In addition, the interpretation of blood levels is confounded by the presence of methyl-mercury from environmental exposures, primarily through the ingestion of contaminated fish (Barregård, 1993).

Biological monitoring is most useful when levels in the biological fluids can be used to predict the absorbed dose, body burden, and concentrations in the critical organs. This is not yet the case for mercury vapour or other forms of inorganic mercury to which workers are exposed. Urinary mercury is probably proportional to the concentration of mercury in the kidney, but quantitative data are limited. In addition, even less is known to relate levels in blood and urine with levels in organs at higher exposures, when toxic effects may begin to affect the kinetics (Barregård, 1993). Therefore, non-invasive measurements of mercury directly in the kidneys would be extremely beneficial as an occupational monitoring method, as these measurements would not require assumptions regarding the relationship between kidney-mercury and urinary-mercury levels. As mentioned in section 1.2 c), the kidneys are the major site of mercury accumulation, therefore it is conceivable that levels in this organ will be sufficiently high for *in vivo* measurements to be feasible. However, unlike lead and uranium, the ability to measure mercury in a site of long-term retention, in order to assess cumulative exposure, is not straightforward. In the case of mercury kinetics, the brain is believed to be the site of long-term retention, and there is little evidence of significant mercury levels in the skeleton. As discussed in section 1.2 c), measurements in the brain are not particularly feasible due to the attenuation effects of the skull and the expectation of relatively low levels of mercury in this organ, even in cases of occupational exposure.

Regardless of the difficulties associated with measuring mercury in a site of long-term retention, a non-invasive method of assessing kidney-mercury levels would be useful to occupational monitoring as a direct probe of toxin levels in a critical organ. In addition, kidney-mercury measurements would aid in establishing whether there is a clear, quantitative relationship between levels in biological fluids and mercury content in this critical organ. Furthermore, as with non-invasive *in vivo* measurements of lead and uranium, measuring mercury in the kidneys of occupational workers would provide valuable information to help researchers improve the understanding of the kinetics of this toxic element.

Chapter 2

EXPERIMENTAL METHODS

X-ray fluorescence, as described in section 1.1.2 b), is based on the excitation of characteristic x-rays from a particular target element. There are three main apparatus requirements necessary for *in vivo* x-ray fluorescence measurements, a source of photons to cause the emission of characteristic x-rays from the target element, a detector to record the number of characteristic x-rays emitted from the target as a result of this irradiation, and a means for calibration.

In designing an optimal *in vivo* x-ray fluorescence system, there is little optimisation possible in terms of the detection system used for each target element. For K x-ray fluorescence, hyper-pure germanium detectors and ultra-fast electronics are almost always the best choice. For L x-ray fluorescence, lithium-drifted silicon detectors are often used in place of hyper-pure germanium, as the silicon-based detectors have advantages over germanium in low-energy photon spectroscopy (Knoll, 1989). As a general rule, the choice of hyper-pure germanium or lithium-drifted silicon has been the main factor in optimising x-ray fluorescence detection systems, with obviously some consideration given to the optimal size of the detector itself.

Therefore, the optimisation of a system for a given target element largely involves the selection of the photon source for the excitation of the characteristic x-rays. The first choice is whether monoenergetic radionuclide γ-ray sources are used, referred to in this thesis as source-excited x-ray fluorescence, or polarised x-rays are used, typically generated with an x-ray tube and referred to in this thesis as polarised x-ray fluorescence. For each type of system, there are a number of factors to consider in the particular design of the excitation source.

2.1 Source of Excitation Photons

2.1.1 Source-Excited X-ray Fluorescence

Aside from the obvious influence of price and availability, there are two main considerations in selecting the radioisotopic source of γ-rays required to stimulate x-ray emission. The most important factor is that the γ-ray energy emitted must be greater than the K edge of the element of concern. (Note: this discussion of methodology applies equally to source-excited L-shell based XRF, however, the text will refer to K shell XRF explicitly for simplicity.) At energies just above the K edge, the K-shell photoelectric cross section is at its highest, which implies that photons with this energy have a high probability of undergoing photoelectric events when interacting with the target element. This requirement that the incident photon energy is just above the K edge ensures that maximum signal is generated per incident flux.

The second criterion for γ-ray source selection is concerned with the magnitude of the background in the characteristic x-ray energy region of the detected spectrum. With the target element concentrations *in vivo* expected to be on the order of a few μg/g or parts per million, the principal interaction of γ-rays within the sample is Compton scattering.

Compton scatter is an interaction between photons and matter in which, as a first approximation, we can consider the photon to be incident on a stationary, free electron. By requiring conservation of total energy and momentum in the collision, it can be shown that a photon scattered at an angle θ has a reduced energy E' of:

$$E' = \frac{E}{1 + E/_{m_o c^2} \cdot (1 - \cos\theta)} \qquad [2.1]$$

where E is the incident photon energy and $m_o c^2$ is the rest mass energy of the electron with which the photon collides. Therefore, Compton scatter results in a shift in photon energy that depends on both the incident energy E and the angle of scatter θ. This implies that the energy of the γ-rays that have been scattered by the sample into the detector depends on the photon energy emitted from the source and the source-subject-detector geometry. Since these scattered photons give rise to the most prominent feature in the spectrum, it is important to maximise the energy separation between this feature and the low intensity x-ray signals arising from the target element. This may be accomplished through careful consideration of both the incident photon energy selected and the source-sample-detector geometry.

It should be noted that although equation 2.1 implies that all photons of energy E scattered through an angle θ will have a precise energy of E', in practice there is a significant distribution in energy of the incident photons scattered into the detector. This arises due to three main physical phenomena. The first of these factors resulting in a distribution of scattered photon energies is referred to as momentum broadening or Doppler broadening. Recall that equation 2.1 was derived with the assumption that the electron is stationary. This is clearly not the case with bound atomic electrons, which have a distribution of momenta characteristic to the element and the particular shell occupied. Therefore, the collision between the photon and the electron is more accurately described as scatter from a moving object, and the reduced energy E' predicted in equation 2.1 is Doppler shifted about this value accordingly. Figure 2.1 demonstrates the effect of momentum broadening on the photon energy detected at 180°, with a 100 keV incident photon scattered from carbon.

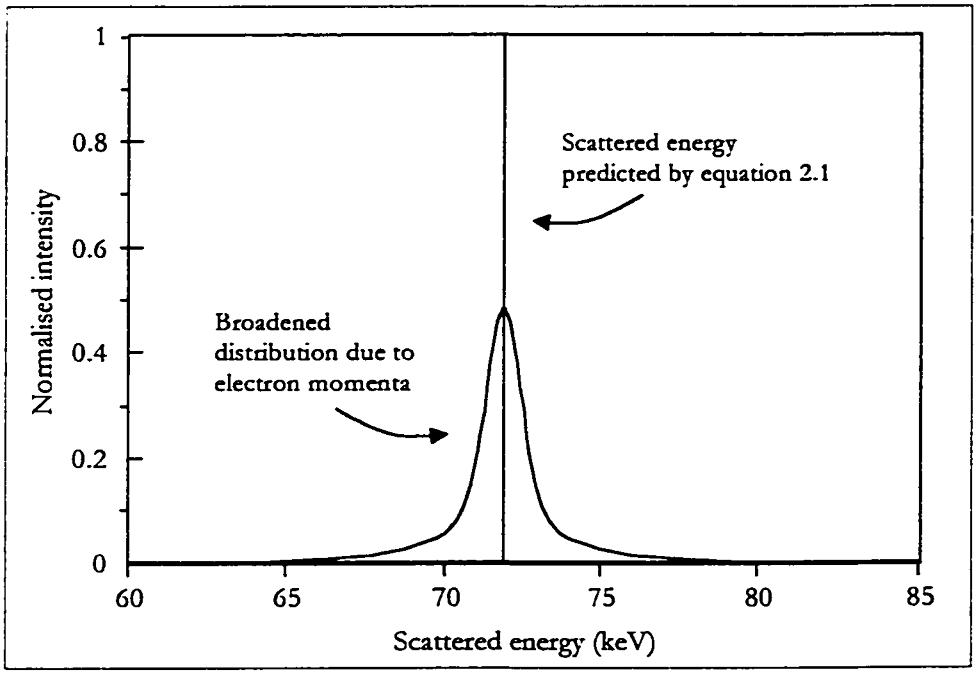

Figure 2.1: The effect of the finite momenta of the electrons on the energy of the photon scattered through a fixed angle. This calculation was done for a 100 keV incident γ-ray scattered through 180° from a carbon atom.

In addition to the broadening of the scattered photon energy arising from the finite momenta of the scattering electrons, the finite range of angles subtended by the detector gives rise to a distribution of detected photon energies. Clearly, if there is a range of angles θ through which the photon can scatter and still reach the detector, there will be a range of photon energies detected due to these interactions based on equation 2.1. Lastly, the various steps in energy deposition in the detector crystal, as well as the conversion of the energy deposited to a digital signal, result in one photon energy being recorded as a distribution; this is referred to as the detector response. However, the effects of the finite range of angles subtended by the detector and the detector response are typically less than the broadening of the monoenergetic line due to the electron momenta in the applications discussed in this thesis.

Since these three factors give rise to a significantly broadened Compton distribution, there can be considerable Compton intensity in the spectrum several keV in energy from the peak value predicted by equation 2.1. Therefore, it is important to maximise the difference in energy between this peak value and the energies of the characteristic x-rays to ensure the background under the signal is minimised. There is an additional concern with regards to the background under the characteristic x-rays. Momentum broadening and the finite angular acceptance of the system would be expected to result in a roughly symmetric Compton peak centred about the energy predicted in equation 2.1, using the mean angle of scatter into the detector for the value of θ. However, the detector response function results in a significant low-energy component, resulting in higher intensities in the lower-energy shoulder of the Compton distribution. Therefore, for a given separation between the Compton peak and the characteristic x-rays, a Compton peak at lower, as opposed to higher energy, than the x-rays results in less background under the signal and is therefore preferable. Optimising the position of the Compton distribution relative to the characteristic x-rays in the detected spectrum is accomplished through coupled selection of excitation photon energy and source-sample-detector geometry.

a) Lead measurement system

The K edge of lead is 88.005 keV (Lederer and Shirley, 1978) and therefore the first requirement for the source of γ-rays is that the main emission has an energy greater than, and preferably close to, this value to ensure maximum signal generation. The ideal candidate is ^{109}Cd, which emits a γ-ray at 88.035 keV as well as silver x-rays in the 22-25 keV range. These silver x-rays are approximately 30 times more intense than the 88 keV γ-ray and therefore must be shielded to reduce both the count rate in the electronics and unnecessary dose to the subject, as these low energy photons are not sufficiently energetic to give rise to lead x-ray signal. This can be readily achieved with a thin copper foil (Somervaille *et al.*, 1985).

X-ray line	Energy (keV)	Emission (relative to Kα_1) (%)
Kα_1	74.969	100
Kα_2	72.804	59.3
Kβ_1	84.936	22.2
Kβ_2	87.3	10.2
Kβ_3	84.45	11.6

Table 2.1: Lead K-shell x-ray characteristics, from Lederer & Shirley, 1978.

Lead x-rays have characteristic energies ranging from 72.8 keV to 87.3 keV (see table 2.1 for a complete list of x-ray energies and emission probabilities). With 88.035 keV γ-rays, equation 2.1 predicts that the peak in the Compton distribution will be detected at 65 keV when a source-sample-detector geometry of 180° (or backscatter geometry) is used. Since the scatter energy E' predicted by equation 2.1 increases with decreasing scatter angle, this geometry is the optimal arrangement to ensure maximal separation between the peak in the Compton distribution and the spectral region occupied by the detected lead x-rays. Therefore, a number of x-ray fluorescence systems have been designed with a ^{109}Cd source arranged in a backscatter geometry. The resulting detected spectrum from such a system is shown in figure 2.2.

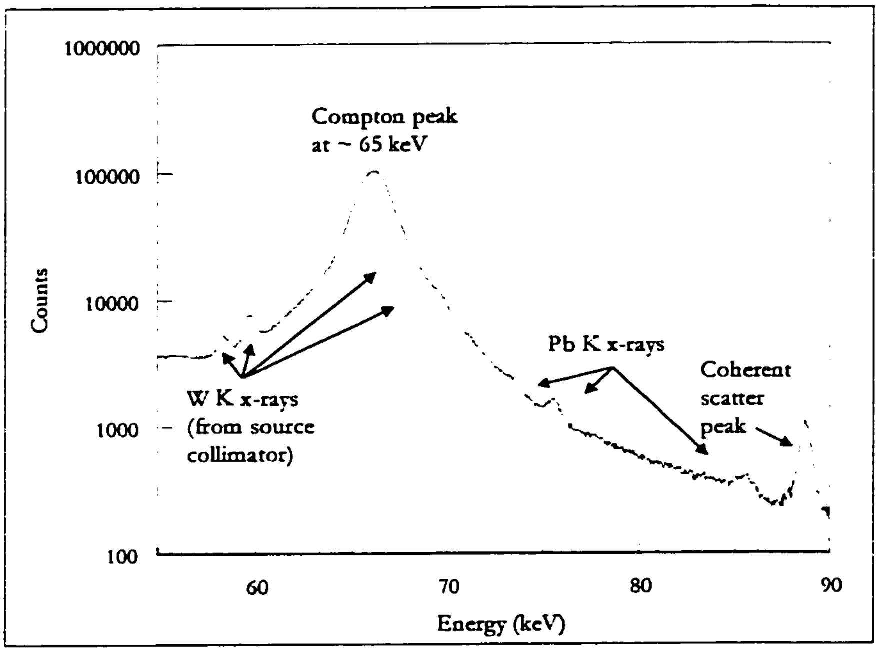

Figure 2.2: Detected spectrum from a 143 ppm Pb-doped plaster of Paris phantom, with a ^{109}Cd-backscatter geometry system. Note that the Compton peak is well separated and at a lower energy than the characteristic x-rays to ensure minimal background under the lead signal. The coherent scatter peak will be discussed in detail in subsequent sections.

While ^{109}Cd emits γ-rays at the ideal energy for maximum lead x-ray generation, and the Compton peak is both at lower energy and well separated from the characteristic x-ray region of the spectrum in a backscatter arrangement, until recently this source was extremely expensive and largely unavailable. Therefore, many lead x-ray fluorescence systems required a different radioisotope to excite the characteristic x-rays. The two most commonly cited possible sources are ^{57}Co and ^{153}Gd. Both these isotopes have been readily available for many years, and both have half-lives on the order of several hundred days, which implies that frequent replacement costs are not incurred. However, in terms of the criteria for selecting an appropriate γ-ray source for lead x-ray fluorescence, ^{57}Co is the preferred radioisotope. This is evident in a comparison of the peak energies of the Compton distributions for the two main geometries used in XRF systems, 90° and backscatter geometry. Table 2.2 summarises this comparison and includes the equivalent data for ^{109}Cd for completeness.

Isotope	Principal γ-ray energy (keV)	Photoelectric cross section of lead (cm^2g^{-1})	Energy of peak in Compton distribution (keV)	
			90° geometry	180° geometry
^{109}Cd	88.035	7.4	75	65
^{57}Co	122, 136	2.8	98, 107	83, 89
^{153}Gd	97, 103	5.7	81, 86	70, 73

Table 2.2: A comparison of the characteristics of the possible isotopic sources for lead x-ray fluorescence measurements.

It is clear from table 2.2 that ^{109}Cd will give rise to the most intense lead signal per unit incident flux, as the photoelectric cross section of lead is larger for this energy photon than the corresponding value for either ^{57}Co or ^{153}Gd. Based on this parameter, it would appear that ^{153}Gd is a better choice than ^{57}Co as a replacement for the expensive ^{109}Cd, as the photoelectric cross section of lead is approximately twice as large for ^{153}Gd photons compared with ^{57}Co. However, as is evident in table 2.2, both 90° and 180° geometry for ^{153}Gd result in the peaks in the Compton distributions having energies that are within the range of energies spanned by the lead x-rays. Since this distribution peak is many orders of magnitude larger than the x-rays, this factor of 2 increase in signal achieved with ^{153}Gd is more than lost by the significant increase in background under the x-ray peaks compared with ^{57}Co. For this reason, the earliest reported *in vivo* lead x-ray fluorescence system consisted of a ^{57}Co source in a 90° geometry (Ahlgren *et al.*, 1976, Ahlgren & Mattsson, 1979). As demonstrated in table 2.2, this geometry results in acceptable separation between the Compton peaks and the lead x-ray region. However, this does result in the x-rays being detected on the low energy shoulder of the Compton distribution, which is not ideal due to the asymmetry of the detector response function. Figure 2.3 illustrates a detected spectrum associated with the ^{57}Co-lead measurement system using a 90° geometry.

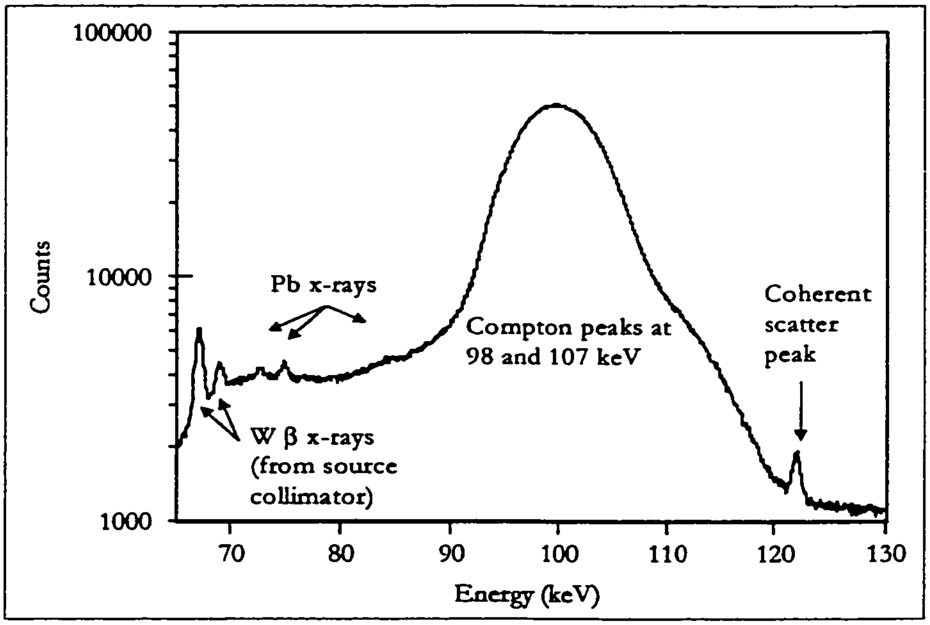

Figure 2.3: Detected spectrum from a ^{57}Co-lead measurement, arranged in a 90° geometry. The phantom contains 190 ppm Pb in plaster of Paris, which is surrounded by Perspex as a representation of overlying tissue. Note that there is acceptable separation between the Compton peaks and the lead x-ray region, however, unlike figure 2.2, these x-rays are now detected in the low energy tail of the Compton distribution.

Although the ^{109}Cd system results in higher precision measurements due to the increased signal and decreased background, ^{57}Co-based systems have not been entirely replaced. For example, ^{57}Co-based lead XRF systems have been used extensively around the world in assessing bone-lead concentrations in various study cohorts (Ahlgren *et al.*, 1980, Christoffersson *et al.*, 1984, Christoffersson *et al.*, 1986, Price *et al.*, 1984, Price *et al.*, 1992, Nilsson *et al.*, 1991, Schütz *et al.*, 1987a, Schütz *et al.*, 1987b, and Börjesson *et al.*, 1997). In addition, this system has recently been used to follow the effect of chelation on bone-lead concentrations in lead workers (Tell *et al.*, 1992 and Gerhardsson *et al.*, 1998).

b) Uranium measurement system

The K edge of uranium is 115.606 keV (Lederer and Shirley, 1978) and therefore the first requirement for the source of γ-rays is that the main emission has an energy greater than, and preferably close to, this value to ensure maximum signal generation. Based on this edge energy, tables of γ-ray energies from radioisotopes were consulted to identify possible candidates (Bowman & MacMurdo, 1974). The best possible choices, along with the corresponding peaks in the Compton distribution with 90° and backscatter configurations for the main emissions are tabulated in table 2.3.

Radioisotope	Half-life	Energies (keV) and strengths of main emissions	Energy of main Compton peak (keV)	
			90° geometry	Backscatter geometry
^{177m}Lu	155 d	115.9 (0.6%), 121.6 (5.9%), 147.1 (3.6%)	94.5, 98.2, 114.2	79.7, 82.4, 93.3
^{182}Ta	115 d	116.4 (0.6%), 152.4 (7.3%), 156.4 (2.7%)	94.8, 117.4, 119.7	80.0, 95.5, 97.0
^{243}Am	7950 y	74.7 (66%), 86.7 (0.4%), 117.8 (0.5%), 142.0 (0.1%)	65.2, 74.1, 95.7, 111.1	57.8, 64.7, 80.6, 91.3
^{110m}Ag	253 d	120.0 (0.11%), 132.6 (0.14%)	97.2, 105.3	81.6, 87.3
^{57}Co	270 d	122.1 (86%), 136.5 (11%)	98.5, 107.7	82.6, 89.0

Table 2.3: Characteristics of candidates for γ-ray sources for uranium K x-ray fluorescence.

For comparison, table 2.4 summarises the energies of the uranium K x-rays.

X-ray line	Energy (keV)	Emission (relative to Kα_1) (%)
Kα_1	98.439	100
Kα_2	94.665	61.9
Kβ_1	111.3	22.0
Kβ_2	114.5	12.3
Kβ_3	110.406	11.6

Table 2.4: Uranium K x-ray energies and emission probabilities, from Lederer & Shirley, 1978.

From table 2.4, it is clear that the photon source selected must not result in the main Compton peaks arising in the 94 to 114 keV energy range in the spectrum. Furthermore, as discussed previously, it is preferable to select the photon source and geometry such that the Compton distributions are detected at lower energies than the uranium x-rays. Based on the information in table 2.3, it would appear that ^{110m}Ag, ^{57}Co, ^{243}Am or ^{177m}Lu in backscatter geometry give rise to Compton distributions at lower, and reasonably distinct, energies than the x-ray region of the detected spectrum. ^{110m}Ag results in Compton peaks that are the furthest from the uranium x-ray energy range. However, these photon energies are emitted by ^{110m}Ag with a low emission yield, and there are a number of higher energy photons (on the order of several hundred keV) emitted with significantly greater intensity (Bowman & MacMurdo, 1974). These higher energy photons will give rise to potentially unacceptable subject absorbed dose and would be difficult to shield selectively, as is done with the silver x-rays emitted by the ^{109}Cd source used in *in vivo* lead x-ray fluorescence. These additional photons would also not be expected to result in significant uranium excitation as the photoelectric cross section at these higher energies is much reduced. Therefore, the higher energy photons emitted by ^{110m}Ag give rise to unnecessary dose, do not contribute significantly to the uranium signal generated, will unnecessarily increase the count rate in the detector to levels that are potentially difficult for the electronics to process, and would contribute to the Compton background. For these reasons, ^{110m}Ag does not appear to be an excellent choice for uranium K x-ray fluorescence.

The second choice, in terms of maximum energy separation of Compton peaks and uranium x-rays, is ^{57}Co in a backscatter geometry. Unlike ^{110m}Ag, the two photon energies listed in table 2.3 are the main γ-ray emissions from this isotope. Therefore there is no concern with respect to unnecessary additional dose or unnecessary increases in detector count rates as all photons emitted can contribute to the uranium signal generated. ^{57}Co appears to be the best choice for the radioisotopic γ-ray source needed to cause x-ray emission from uranium, as both ^{243}Am and ^{177m}Lu result in Compton distributions with peak values that are closer to the uranium x-ray energy region of the detected spectrum. Furthermore, ^{243}Am has major photon emissions that are not sufficiently energetic to contribute to uranium excitation. For these reasons, the source-excited K x-ray fluorescence system designed and built during the course of this work was based on the use of ^{57}Co in a backscatter geometry. Figure 2.4 illustrates a typical detected spectrum from this system.

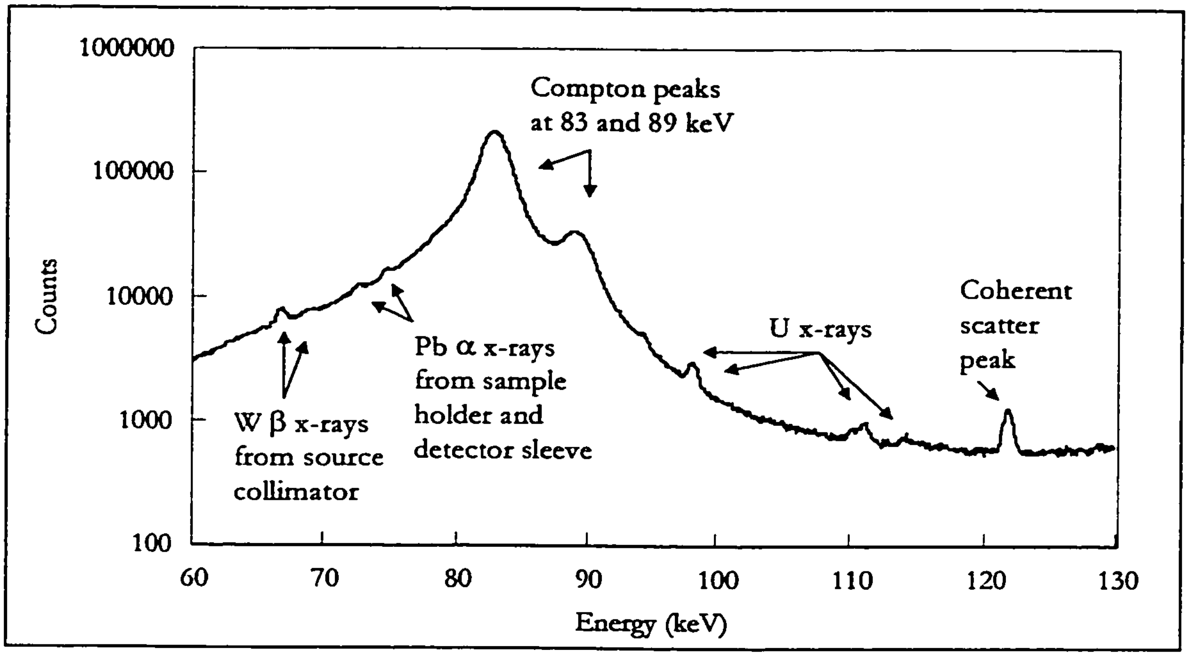

Figure 2.4: Typical detected spectrum obtained with the ^{57}Co backscatter geometry system to measure uranium concentrations. This particular spectrum was obtained with a plaster of Paris phantom containing 100 ppm of uranium. Note that the Compton peaks are well separated and at lower energies than the uranium x-ray region in the spectrum.

2.1.2 Polarised X-ray Fluorescence

As discussed in 2.1.1, one of the main considerations in designing an optimal source of excitation photons is the relative position of the peak in the background distribution and the target element x-rays in the detected spectrum. For each target element, the γ-ray energy and source-sample-detector geometry is optimised to ensure maximum energy separation between the signal and the peak in the background. In some cases, the limited availability of radioisotopic γ-ray sources and the fixed range of possible angles of scatter combine to result in an unacceptable proximity of the signal to the Compton peak. In these cases, other means of minimising the background in the x-ray energy region of the detected spectrum must be investigated in order to achieve reasonable sensitivity for measuring concentrations of trace elements. One such background reduction technique is the use of plane-polarised photons as the source of excitation of the characteristic x-rays of the target element.

The principle behind the use of plane-polarised x-rays as the excitation source is based on the differential Compton (or incoherent) scattering cross section for polarised radiation:

$$\left.\frac{d\sigma}{d\Omega}\right|_{incoherent} = \frac{r_o^2}{2}\cdot\left(\frac{\upsilon'}{\upsilon}\right)^2\cdot\left(\frac{\upsilon}{\upsilon'}+\frac{\upsilon'}{\upsilon}-2\sin^2\theta\cos^2\psi\right) \qquad [2.2]$$

where

r_o is the classical electron radius,

$h\nu$ is the energy of the incident photon (represented as E in equation 2.1),

$h\nu'$ is the scattered photon energy (represented as E' in equation 2.1),

θ is the angle of scatter, as defined in equation 2.1, and

ψ is the angle between the plane of incident polarisation and the scatter plane.

Based on equation 2.2, it is clear that the differential scattering cross section is at a minimum when ψ is 0° and θ is 90°. This implies that there is a direction in which a minimal intensity of Compton scattered photons is detected when a plane-polarised beam of photons is incident on a scattering sample. This direction corresponds to the direction of initial polarisation, as demonstrated in figure 2.5. Therefore, by positioning the detector such that it is aligned with the direction of initial polarisation of the excitation source, a minimum is expected in the intensity of the detected background.

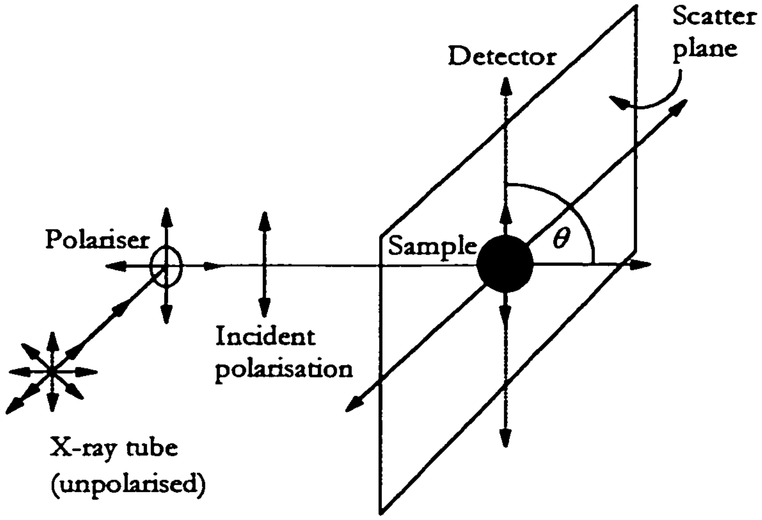

Figure 2.5: Schematic of the geometry used to position the detector in the direction of minimum Compton scatter with polarised photons as the excitation source. Based on equation 2.2, when the detector is positioned such that θ is 90° and ψ is 0°, the probability of scatter is significantly reduced. In this figure, unpolarised photons from a therapeutic x-ray tube are polarised before interacting with the sample through scatter from a polariser. This is described in more detail in the text.

This forms the basis of background reduction for applications in x-ray fluorescence measurements. A system is designed such that the subject is irradiated with polarised x-rays, and the detector is positioned such that the intensity of the scattered radiation is at a minimum. In contrast, the characteristic x-rays emitted from the target element have a near isotropic distribution, thereby resulting in a maximum in the signal to noise ratio when the system is so aligned. This technique has been used successfully by several researchers, e.g. Kaufman & Camp, 1974, who obtained a four-fold reduction in the Compton scatter peak detected.

Hence, the apparatus required for polarised x-ray fluorescence is markedly different from the simple requirements for source-based XRF. These systems require a source of polarised photons. In general, radionuclide and other conventional photon sources, such as x-ray tubes, emit unpolarised photons. Therefore, some mechanism must be utilised to polarise the beam before irradiating the sample. There are a variety of such methods available, however, for the energies of photons required in K x-ray fluorescence and the intensity of the beam needed, the technique favoured by the XRF field is that of Barkla scattering (Barkla, 1905). This approach seems to be the best method for improving the ratio of fluorescence to scattered radiation for low Z matrices (Ryon *et al.*, 1982, Heckel, 1995).

The method of polarising radiation through Barkla scattering is best understood through a simple classical analysis of Compton scatter. Consider the incident photon to be an electromagnetic wave of which the direction of the electric vector changes randomly with time, i.e. unpolarised radiation. Based on the properties of electromagnetic radiation, the direction of the electric vector is constrained to lie within the plane perpendicular to the direction of wave motion, or the plane perpendicular to the page based on figure 2.6. Therefore, at any given time the electric vector can be resolved into two components, one in the horizontal plane and one in the vertical plane, E_H and E_V respectively in figure 2.6.

In the right hand panel of figure 2.6, the resulting interaction between the electron and E_H is shown. When an electric vector oscillating in the horizontal plane approaches an electron, the electron essentially becomes a dipole, oscillating in the horizontal plane parallel to E_H. The dipole created through the interaction of the electron and the electric vector results in radiation emission. Radiation emitted from a dipole tends to have an electric vector oriented parallel to the dipole moment, and the radiation is therefore emitted in a plane perpendicular to this direction. This is demonstrated in figure 2.6; the electrons interacting with E_H establish a dipole in the horizontal direction, which in turn results in radiation emitted in the vertical plane. Similarly, electrons interacting with E_V establish a dipole in the vertical direction, which results in radiation emitted in the horizontal plane.

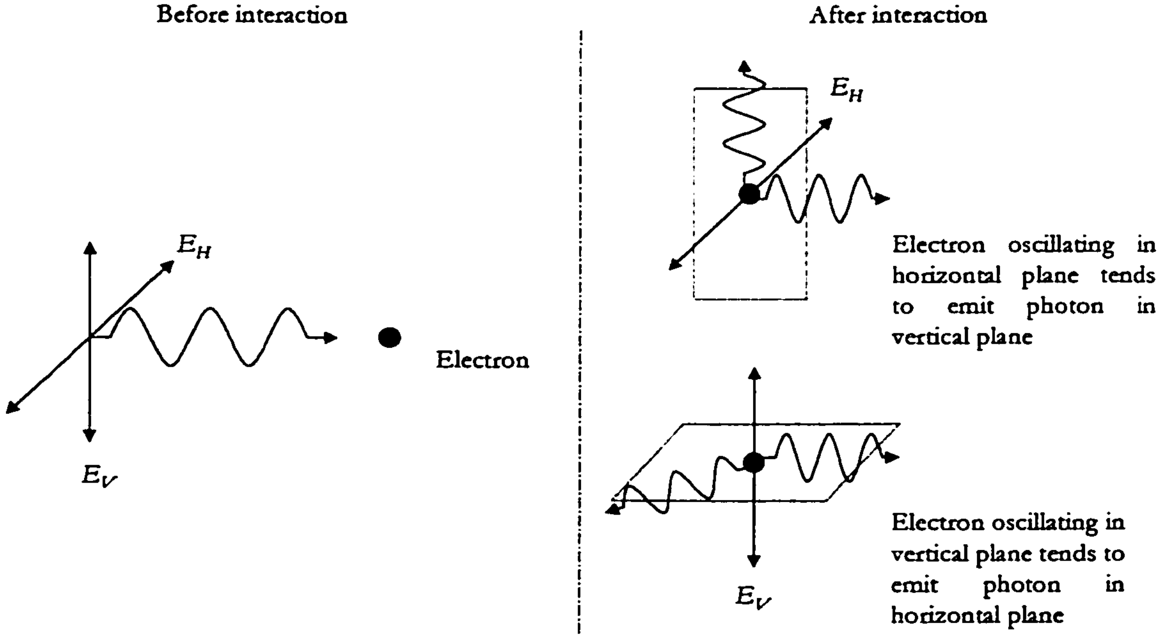

Figure 2.6: A schematic representation of the principle behind polarisation through Barkla scattering.

The key is that, classically, a dipole cannot radiate along its dipole direction. Therefore, any photons observed at $\theta = 90°$ in the horizontal plane, *i.e.* along the direction of E_H, must have been a result of interactions between the electron and electric vectors parallel to E_V and will therefore be polarised parallel to E_V. Similarly, any photons observed at 90° scatter angles in the vertical plane, *i.e.* photons observed in the direction of E_V, must have been due to scatter of E_H polarised photons, and will therefore be polarised parallel to E_H. This is a simple, classical description of the scattering of electromagnetic radiation by electrons and is therefore necessarily only an approximate account of these interactions. However, this description provides an adequate picture of the scattering process to allow for a visualisation of the method of polarisation through Barkla scatter.

The angle of scatter of the primary, unpolarised, radiation is of vital importance. If the purpose of this scatter is to generate a polarised beam, then extracting the scattered flux along the direction of E_H or E_V will serve this purpose. However, experimentally, in order to extract a reasonably high intensity polarised beam, the scatterer (polariser in figure 2.5) must subtend a significant solid angle. Therefore, scatter at angles other than 90° will occur, resulting in components of the extracted beam having electric vectors at angles to the vector associated with scatter at 90°, causing a decrease in the degree of polarisation of the secondary beam. Furthermore, a polariser of reasonable thickness is required to generate an intense secondary beam, resulting in a portion of the primary beam undergoing multiple scatter events. This, in general, also adds to the depolarisation of the secondary beam. Therefore, the optimal polariser solid angle and thickness must be selected as a compromise between polarisation and beam intensity. Finally, as an additional means of ensuring reasonable intensity of the polarised beam, radionuclide sources can not generally be produced with sufficient activity to serve as the primary beam. Therapy x-ray tubes are the preferred source of unpolarised radiation for generating polarised photons beams through Barkla scatter in these applications as several orders of magnitude of photon flux are lost in this polarisation process.

It is clear that there are a number of design parameters that must be optimised when considering polarised x-ray fluorescence measurements. For example, the energy distribution of the polarised beam is critical in terms of the ability to excite characteristic x-rays from the target element. The energy of this beam can be altered through selecting the operating voltage of the x-ray tube, the polariser material and thickness, as well as through the use of filters in the primary or secondary beam. As with source-based x-ray fluorescence, the ideal energy of the incident beam is just greater than the K edge of the target element and is such that the Compton distribution is well separated from the energy region of the detected characteristic x-rays. However, due to the requirement that the detector be positioned along the direction of initial polarisation to minimise scatter, the source-sample-detector angle can no longer be varied to achieve maximum Compton and x-ray separation. Nevertheless, there are a sufficient number of parameters that can be varied to optimise the secondary beam energy distribution, and hence the Compton scatter energy distribution detected at 90°. Of course, at the same time as optimising the secondary beam energy distribution, consideration must be made to the degree of polarisation of the beam, as this is influenced by the various parameters listed above. The best precision can be achieved by careful consideration of the trade-offs necessary for maximal secondary beam intensity, polarisation, and optimal energy distribution.

The particular design choices for measuring uranium and mercury *in vivo* with polarised x-ray fluorescence will be described in detail in subsequent chapters.

2.2 Detection systems

With the source of excitation photons selected, the next stage in the design process is the selection of the appropriate detection system. As discussed previously, the selection of this component is largely based on whether K- or L-shell x-rays are the signals being recorded from the target element.

As this work focuses on the K shell XRF measurement of lead, uranium and mercury only, the characteristic x-rays to detect are in the 65 to 115 keV energy range. In the detection of photons in this energy range, there are, at present, only two detector categories of major importance: inorganic scintillators, of which NaI(Tl) is the most popular, and germanium semiconductor detectors. Although there are many potential factors, the choice of a given application typically revolves around a trade-off between counting efficiency and energy resolution. NaI(Tl) detectors have the advantage that they are readily available in large sizes, which, together with a high density, can result in high efficiency for stopping incident photons. In addition, the reasonably high atomic number of iodine implies that a large fraction of all interactions in the detector result in complete energy absorption, and therefore photons are frequently recorded in the correct energy channel in the detected spectrum. However, the energy resolution of scintillators is poor. Good germanium systems will typically have energy resolutions of a few tenths of a percent compared with 5 to 10% for NaI(Tl). This improved energy resolution comes at a price, however, as the germanium detectors are generally smaller in size and have lower atomic number than NaI(Tl). The detection efficiencies of germanium crystals can be an order of magnitude lower than NaI(Tl) (Knoll, 1989).

The superior energy resolution is the overriding factor in the application of *in vivo* x-ray fluorescence. Not only does better resolution ensure the closely spaced characteristic x-ray peaks are separated, it also aids in the detection of weak lines when superimposed on a broad continuum (the Compton background distribution). Detectors with equal efficiency will result in equal areas under these peaks, but the detector with the better resolution will produce a narrow but tall peak that may then be more clearly observed above the statistical noise of the continuum. Therefore, the difference in detector efficiency between germanium and NaI(Tl) becomes important in choosing the detecting material. In these applications, the efficiency of germanium crystals is actually quite good. The germanium detector used in this work has an efficiency of 78% at 122 keV, implying that 78% of all 122 keV photons incident on the detector will deposit all energy in the crystal. Another figure often cited for detector efficiency is the peak to total ratio, which in these applications is 93% at 122 keV, implying that 93% of 122 keV photons that interact in the crystal will deposit all energy, which results in the photon being recorded correctly in the spectrum. Therefore, there is not a significant trade-off to consider between efficiency and resolution at these photon energies when selecting between germanium and NaI(Tl), as germanium has markedly better resolution and has sufficient efficiency. For these reasons, hyper-pure germanium detectors have been used in the design of the *in vivo* K-shell x-ray fluorescence measurements discussed in this thesis.

The particular germanium detector used in this work has a diameter of 50.5 mm, a thickness of 20 mm, and a resolution of 700 eV at 122 keV for a pulse shaping time of 1 μs. The detector output is passed through fast nuclear electronics, from the preamplifier directly attached to the germanium crystal, to the fast amplifier (Canberra Fast Spectroscopy Amplifier Model 2024), to the analogue to digital converter (Canberra Fast Analogue-to-Digital Converter Model 8077) where the intensity of the amplified signal from the detector is converted to a digital address. Due to high-count rates, pulse pile-up rejection is utilised to reduce background. The digital address is then used by the analysis software to increment the appropriate channel in the detected spectrum. The accumulating spectrum (photon counts versus photon energy) is displayed real time on a computer monitor.

2.3 Phantom design and preparation

Once the source of photons has been selected for optimal detection precision and the detector system has been set up, the design process is largely complete. However, in order to test the precision of this new system, a calibration must be performed using materials that simulate the subject for which this system was designed. This simulation of the eventual subject is referred to as a phantom, and the materials with which a phantom is made are dependent on the particular system being tested. Therefore, the final steps of design require careful consideration of the appropriate composition and dimensions of the phantoms required to calibrate the system.

Phantom materials are selected if they exhibit similar photon interaction cross sections to the respective tissues being modelled. For example, plaster of Paris ($CaSO_4 \cdot 2H_2O$) has a mass attenuation coefficient of 0.191 cm^2g^{-1} compared with 0.185 cm^2g^{-1} for bone, both at 100 keV (Berger, 1987). Therefore, plaster of Paris will exhibit similar attenuation of the incident fluence and characteristic x-rays as that observed in bone for this energy range. In addition, plaster of Paris is formed from a powder by adding water, and therefore using water with known amounts of added heavy metals results in a straightforward method for the construction of bone phantoms with known traces of the target element. However, there is a significant difference between the coherent scatter cross sections of these materials, 1.3 x 10^{-2} cm^2g^{-1} for plaster of Paris, and 1.1 x 10^{-2} cm^2g^{-1} for bone (Berger, 1987) at 100 keV. This is non-ideal, as many of the measurements of trace elements in bone use the coherent scatter signal as a normalisation factor. However, the difference in the coherent scatter cross sections is not expected to have any bearing on the legitimacy of calibrating with x-ray to coherent ratios per unit concentration derived from plaster of Paris phantoms, as this is more dependent on the angular distribution of the differential scattering cross section. Since plaster and bone exhibit similar angular distributions of coherent scatter, the difference in the total scattering cross section will merely require a correction of the *in vivo* detected x-ray to coherent ratios before calculating the metal concentration through calibration with ratios from plaster of Paris phantoms. For calibration purposes then in measuring metal content in bone, a set of plaster of Paris phantoms is made with a range of target element concentrations, with dimensions that reflect the bone at the site of measurement in the particular system.

In many x-ray fluorescence systems, measuring heavy metal concentrations in the kidney is the goal. In this case, a phantom must be designed that models both the soft tissue of the overlying torso, as well as the soft tissue of the kidney. As with choosing a material to simulate bone, relative attenuation coefficients are the main concern in choosing a soft-tissue-equivalent phantom material. In this regard, water is often chosen as the best phantom material, as water has a total mass attenuation coefficient of 0.171 cm^2/g where the corresponding value for soft tissue is 0.169 cm^2/g (Berger, 1987) at 100 keV. Therefore, water will exhibit similar attenuation of the incident fluence and characteristic x-rays to that observed in the torso and kidney at this energy range. In addition, known amounts of heavy metals can be introduced to a solution of water contained in a Perspex (Lucite, PMMA, $(C_5H_8O_2)_n$) bottle of appropriate dimensions to simulate the trace quantities of the target element in the kidney. This Perspex bottle can be positioned in a water bath at specific depths from the walls to simulate the kidney within the torso. Perspex is often used as the material of choice for the kidney sample as well as the water bath, as it also has similar attenuation properties to soft tissue at the relevant photon energies for this work, for example 0.164 cm^2/g at 100 keV (Berger, 1987). While water is the better simulation of soft tissue, the need for rigid walls is satisfied with this tissue-similar plastic. Unlike the simulation of bone, there is no need to consider the relative coherent cross sections in selecting a phantom material for kidney measurement systems, as the coherent scatter normalisation method is not used.

In one particular application in this thesis, Perspex is used as the soft tissue phantom material in simulating overlying tissue in measuring lead in the bone. When calibrations of heavy metal bone measurements are done, generally no overlying tissue is simulated in the phantom, as this is unnecessary when the normalisation method with coherent scatter is used. However, in one particular application, it was necessary to include a soft tissue phantom material overlying the plaster of Paris. In this case, the discrepancy between Perspex and soft tissue, in terms of interactions with the incident fluence, the characteristic x-rays, and the coherent scattered photons from the bone/plaster of Paris, can be justified in order to use a solid phantom material. This justification will be explored within the context of this particular application in greater detail in chapter 4, section 4.2.

Chapter 3

MONTE CARLO METHODS

3.1 Monte Carlo techniques

Monte Carlo methods are used to solve a wide variety of physical problems. Although Monte Carlo is a straightforward tool to simulate random processes, it can also be used for solving problems with no immediate probabilistic interpretation. The first uses of this method go far back in history, however, extensive applications came along with the use of modern computers in the late 1940s (Halton, 1970). These early investigations focussed on the use of Monte Carlo methods in solving particle transport problems, and this continues to be one of the areas of most extensive use (Lux and Koblinger, 1991).

In all applications, Monte Carlo methods are based on the construction of a stochastic model in which the expected value of a certain random variable (or a combination of several such variables) is equivalent to the value of a physical quantity to be determined. This expected value is then estimated by the average of several independent samples of this random variable. For the construction of the series of independent samples, random numbers following distributions of the variable to be estimated are used. Therefore, Monte Carlo calculations first require a stochastic model to be constructed. Then, in the actual implementation of the method, the user has to be able to select random numbers with various distributions (Lux and Koblinger, 1991).

In Monte Carlo methods applied to radiation transport, the physical process is stochastic in nature, and therefore, the most straightforward calculations are numerical simulations of the real physical events. When simulating physically stochastic processes, two expected values, that of the physical quantity and that of the average of random samples, must equal one another. Often, various methods are introduced, referred to as variance reduction techniques, in the sampling of distributions of such physical variables in order to increase the precision achieved per unit run-time of the simulation. With the further development of such variance reduction techniques and the rapidly increasing processing speeds of personal computers, complete simulations of complicated radiation transport problems are readily accessible. This proves an invaluable development tool for researchers, as the effect of any parameter in the design can be investigated with respect to the ultimate sensitivity of the measurement system, which, in many cases, would be extremely difficult, expensive and time-consuming to study experimentally. In addition, Monte Carlo simulations allow for a more complete understanding of the system itself, as the source of essentially any feature of the system output can be identified through the appropriate use of flags in the code.

3.2 Monte Carlo simulations of source-excited XRF

Over the past few years, there has been interest in using computational methods to model source-excited *in vivo* x-ray fluorescence (Todd *et al.*, 1991, He *et al.*, 1993, Tartari *et al.*, 1993, Wallace 1994). Monte Carlo simulations have been shown to be a useful tool in the design and construction of new applications of *in vivo* XRF. However, a complete simulation of source-excited *in vivo* x-ray fluorescence systems that model common interactions, such as

Compton scatter, with a sufficient level of detail for these purposes was not readily available and had not been fully reported in the literature before this work. The simulation developed during the course of this thesis was the first of its kind reported with a full account of correcting for the momentum broadening with every Compton scatter event in the sample from a theoretical basis (see section 2.1.1 for discussion of momentum broadening). In addition, this simulation is written such that the energy deposited in the detector crystal is simulated on a photon-by-photon basis, thus eliminating the need to rely on semi-empirical detector response functions (DRFs) or requiring an experimental assessment of the DRF for any detector used. Previous source-excited *in vivo* XRF simulations typically either rely on a semi-empirical DRF to compare simulations with experiment or use approximations in accounting for momentum broadening, if broadening is modelled at all. When broadening has been modelled, the algorithm used has not been clearly outlined. Therefore, this simulation has been reported in the literature (O'Meara *et al.*, 1998b) so that other researchers may similarly implement momentum broadening for in-house *in vivo* XRF simulations.

This simulation was written in FORTRAN 90, and is loosely based on the code originally reported by Todd *et al.*, (1991). The program can model any combination of heavy metal and radioisotopic source with the creation of the appropriate data files. This allows for the investigation of any of a number of current or future *in vivo* systems for measuring heavy metal concentrations. The overall simulation is summarised in flowchart form in figure 3.1. Figure 3.1a) shows the general sequence of steps in the Monte Carlo, while 3.1b) summarises, in more detail, the steps taken when a particular photon has hit the sample. It should be noted that separate programs have been written to model XRF measurements of trace elements in bone and XRF measurements of heavy metals in the kidney. However, the simulation of bone measurements will be the focus of the following sections, as the modelling of contrasting tissue media presents a slightly more complicated system in terms of photon propagation and interactions. The following discussion also holds for simulating the kidney as the target organ.

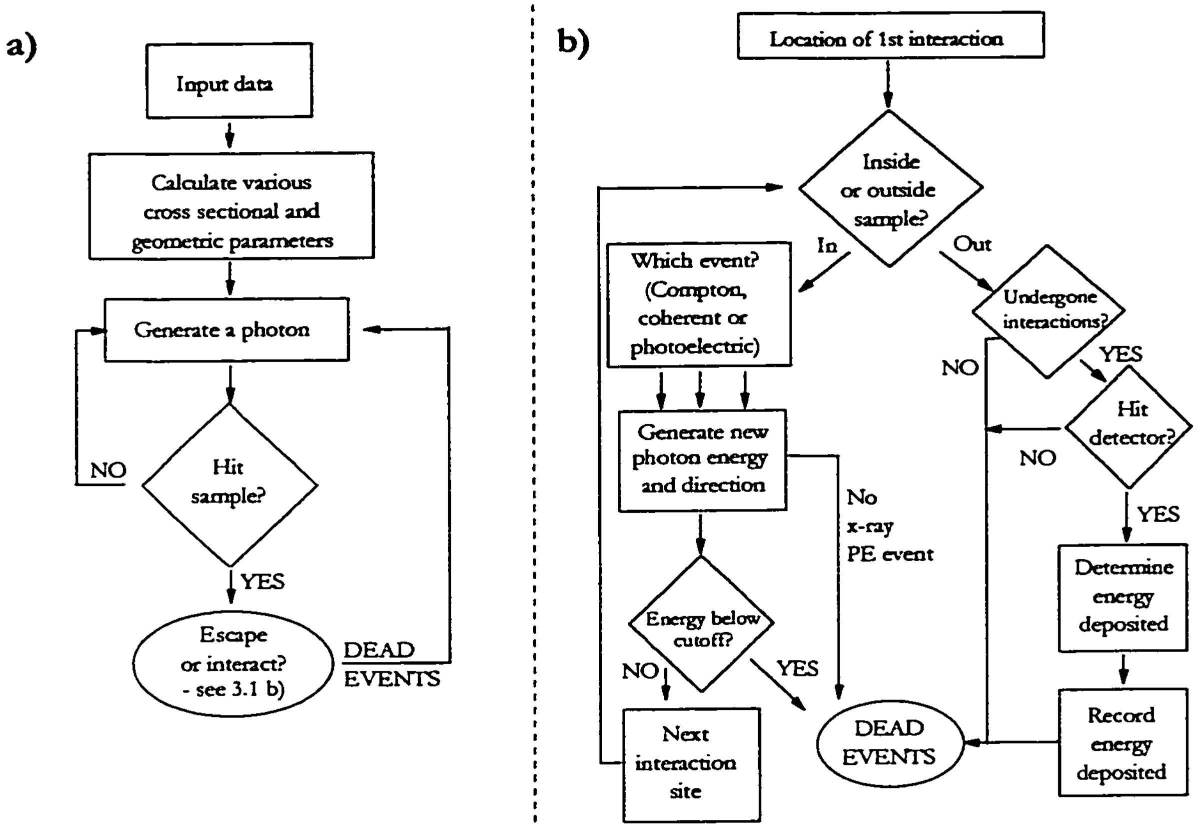

Figure 3.1a) General flowchart outlining the steps followed in the Monte Carlo simulation. Figure 3.1b) is an expansion of the "Escape or interact" step shown as the last stage in figure 3.1a). Once a photon has hit the sample, the steps outlined in more detail in figure 3.1b) are followed until the particular photon history is terminated as a dead event through the various possible mechanisms identified in 3.1b). Once terminated, the simulation generates the next photon and the cycle is repeated as shown in 3.1a).

3.2.1 Model geometry

The sample is represented as a system of cylinders as shown in figure 3.2. The bone is represented as a cylinder within a cylinder of soft tissue, both of variable radius. (Note: with the simulation of heavy metals in the kidney, the kidney is modelled as a cylinder of soft tissue within a larger cylinder of soft tissue to represent the torso. The kidney cylinder has a variable height within the torso cylinder, and unlike the bone cylinder discussed here, is not assumed to have the same height as the outer soft tissue cylinder for obvious reasons.) The bone cylinder can be positioned with a variable offset from the centre of the sample, in order to facilitate the modelling of either a shin, a finger, a thigh or other possible irradiation sites. When 90° geometries are simulated, the detector is positioned on-axis with the centre of the bone cylinder, regardless of its position within the soft tissue cylinder, as demonstrated in figure 3.2. This model is different from those reported by Wallace (1994) and Todd *et al.* (1991), as these earlier simulations represented the sample as systems of rectangles and squares. Although bone shafts and limbs tend to be somewhat elliptical in cross section, it is expected that our circular cylindrical geometry is more representative of the clinical sample shapes encountered during *in vivo* XRF measurements than the earlier geometries used.

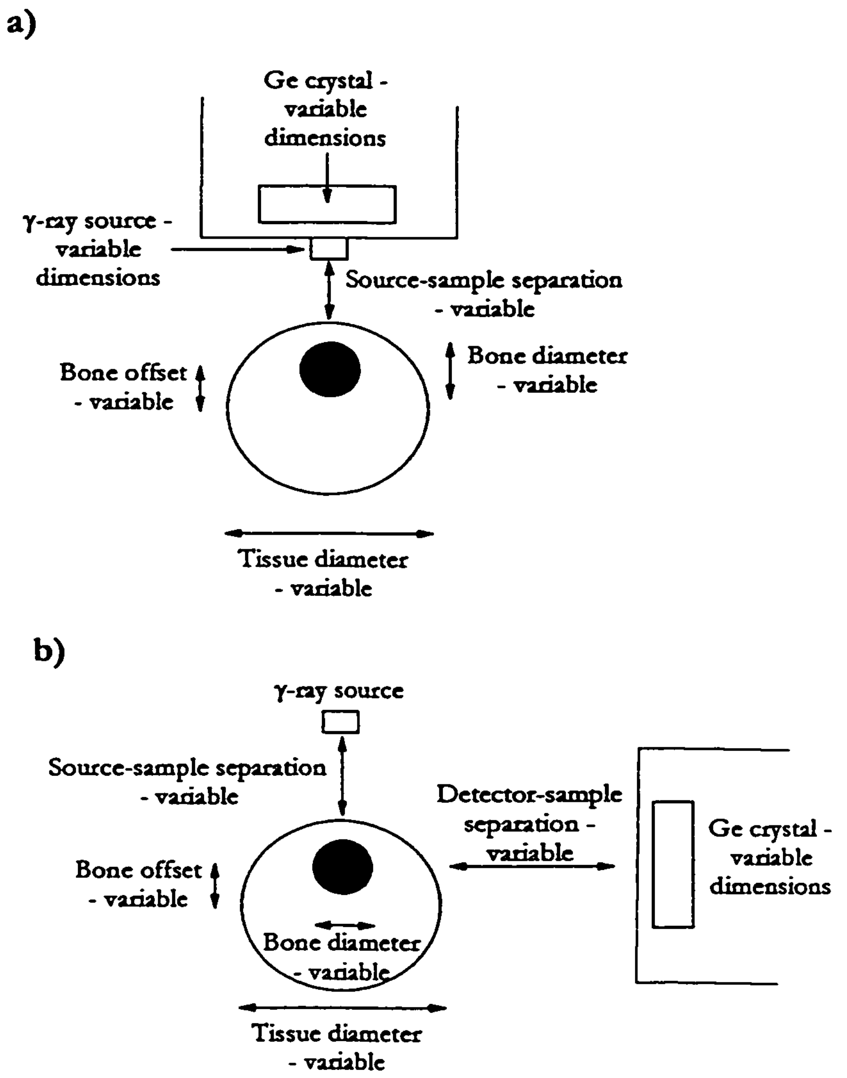

Figure 3.2. a) A schematic of the geometry used for simulating the 180° backscatter XRF systems. b) A schematic of the geometry used in the simulation of 90° scatter XRF systems. Note the alignment of the detector with the centre of the bone.

3.2.2 Model variables

This model allows for the choice of either 180° or 90° geometry, as is the case in the code reported by Todd *et al.* (1991). These represent the standard choices for *in vivo* XRF measurement systems. As mentioned in 3.2.1, the depth and size of the bone are specified by the user via an input data text file. This file also allows the user to set the distances from the sample to the source and the detector, the energy of the γ-ray emitted from the radioisotope being modelled as the source, the number of γ-rays to be traced, the concentration of heavy metal present in the bone, and the cut-off energy below which the γ-ray is no longer traced due to the improbability of subsequent detection. This file also contains the relevant information regarding the dimensions and interaction cross sections of the detector crystal to allow the modelling of energy deposited on an event-by-event basis. A separate data file is used to read in all the necessary information for the target element (*e.g.* lead, uranium *etc.*)

3.2.3 Photon tracing

The γ-rays are emitted with random direction, constrained by a specific source collimation. The geometry of the system is used to determine whether or not the γ-ray hits the sample. If the photon misses, the event is terminated, recorded as a miss, and the next γ-ray is emitted, as shown in figure 3.1a). For γ-rays that cross the sample surface, the distance to the first interaction is calculated based on the relevant attenuation cross section(s) μ, accounting for the different media encountered along the path of the photon. μ is the probability of photon interaction per unit path length through the medium, and the fraction of photons that do not interact traversing a distance x is given by:

$$\frac{I}{I_o} = e^{-\mu \cdot x} \qquad [3.1]$$

Therefore, if the photon is travelling through one medium only, the distance travelled before interacting can be estimated with a random number used to represent I/I_o through the expression:

$$\text{Distance} = -\frac{\ln(r)}{\mu(E)} \qquad [3.2]$$

where r is a random number, and μ is determined at the specific photon energy E, for the appropriate material, from tabulated values read in from data files. Equation 3.2 implies that if the random number is truly randomly generated, one half of these distance calculations will result in $x < ln(2)/\mu$, and one half of the distance calculations will result in $x > ln(2)/\mu$. So, for I_o incident intensity of photons with energy E, in a material with linear attenuation coefficient μ, one half of the intensity will have interacted within a distance $ln(2)/\mu$ of the sample boundary, which is the predicted intensity at this distance from equation 3.1. The spatial co-ordinates of the interaction site can then be determined by this distance travelled, given the present spatial co-ordinates and direction cosines of the photon. However, when there is more than one medium present, the distance travelled to the next interaction will depend on whether the photon path crosses the medium boundary, as different media have different values of μ for the same photon energy. Therefore, when modelling bone measurements, the distance to the next interaction is first calculated based on the μ value for the medium present at the current spatial location in the sample. The photon is then projected along its direction cosines to determine whether it crosses the bone/tissue boundary before its next interaction. If this is the case, then the distance to the next interaction must be recalculated to account for the different probabilities of interacting per unit path length in tissue and bone.

Once the new position of the photon has been determined, if the corresponding site for the next interaction is within the sample, the particular interaction is selected using a random number and the relevant photoelectric, Compton and coherent cross sections of either soft tissue or bone, as shown in figure 3.1b). As the total attenuation coefficient reflects the probability that some interaction takes place, the probability of each interaction can be represented separately as individual cross sections, *i.e.*, $\sigma_{Compton}$, $\sigma_{coherent}$, $\sigma_{p.e.}$ (where *P.E.* represents the photoelectric effect). The interaction cross sections of the materials modelled are generated by summing the elemental cross sections, given by Berger, 1987, weighted by the amount of each element present by mass. For tissues containing trace quantities of the target material, the cross sections of this element are also included in calculating the total interaction cross sections. Therefore, given that an event has occurred, the relative intensities of these individual cross sections provide a means for selecting the particular interaction that occurred:

If $r \leq \dfrac{\sigma_{P.E.}}{\sigma_{P.E.} + \sigma_{Compton} + \sigma_{coherent}}$ then a photoelectric event has occurred.

Otherwise, if $r \leq \dfrac{\sigma_{P.E.} + \sigma_{Compton}}{\sigma_{P.E.} + \sigma_{Compton} + \sigma_{coherent}}$ then a Compton event has occurred.

If neither of these conditions is satisfied, then, by process of elimination, the event must have been a coherent scatter (where r is a random number).

For interactions in the soft tissue region of bone simulations (or the torso region in kidney simulations), photoelectric events are treated as the termination of that particular γ-ray history, as the products of such an event will have effectively insufficient range to be detected or deposit energy elsewhere in the sample. Coherent events are treated as null interactions in soft tissue; no energy or direction change is assumed to occur due to the relatively small intensity and the rapid fall-off with angle of scatter of $d\sigma/d\Omega$ for this low Z material. While this is an approximation, it has been demonstrated that this is a valid assumption (see Somervaille *et al.*, 1985, figure 4a).) Compton events are modelled in a new manner compared with previous *in vivo* XRF simulations reported in literature, and this will be discussed in section 3.2.4.

Conversely, photoelectric events within the target organ can result in metal x-ray production, and coherent scatter events in bone can result in significant changes in direction of the photon. Photoelectric events in the bone region result in metal x-rays when all of the following criteria are satisfied:

i) The γ-ray has sufficient energy to undergo a K shell photoelectric event with the target element,

ii) The photoelectric event is determined to have occurred with the target element rather than another element in the bone. This can be determined using the relative photoelectric cross section of the target element, weighted by the concentration of the element present by weight, as this reflects the probability that the photoelectric event in bone occurred with this element. Therefore:

   If $r \leq \dfrac{concentration \cdot \sigma_{P.E.}(metal)}{\sigma_{P.E}(bone)}$ then the photoelectric event in bone has occurred with the target element (*r* is a random number).

iii) The photoelectric event with the target atom occurs in the K-shell, rather than one of the other filled electron shells in the atom. There is a certain probability that this is true, based on the magnitude of the K shell photoelectric cross section at the photon energy, relative to the total photoelectric cross section of the atom at this energy. From figure 1.1, the means of determining the K shell photoelectric cross section can be visualised by extrapolating the cross section at energies below the K edge to energies above the K edge. This extrapolation represents the contribution to the total cross section at energies above the K edge that arises from photoelectric events in other shells. The K shell cross section can then be determined as the difference between the total cross section and this extrapolated "other shell" contribution. Then,

If $r \le \dfrac{\sigma_{P.E.}(Kshell)}{\sigma_{P.E.}(total)}$, the photoelectric event with this element has occurred within the K shell; again, *r* is a random number.

This ratio of K shell to total P.E. cross section, is roughly 80% for lead and uranium for γ-rays with energies just above the K edge. Therefore, 80% of photoelectric events in these metals at these energies will occur in the K shell.

iv) The K shell photoelectric interaction with the target element results in the emission of an x-ray. As discussed in section 1.1.2 b), the result of the ejection of a K-shell electron can be either the emission of a characteristic x-ray or Auger electrons. The probability that an x-ray is emitted per K-shell vacancy, the fluorescence yield ω discussed in 1.1.2 b), gives a means of determining whether such a photon is emitted per event in the simulation. If $r \le \varpi_k$, then an x-ray, rather than Auger electrons, is emitted, where ω_k is on the order of 96% in lead and uranium, and *r* is a random number.

An additional random number is used to determine which K x-ray (α_1, α_2, β_1, β_2, or β_3) is produced based on tabulated relative intensities (Lederer and Shirley, 1978). The x-ray is given a random direction based on an isotropic distribution, and is then traced until it is either outside the sample (detected or otherwise), its energy is reduced through scatter events such that it falls below the low energy cut-off, or it undergoes a photoelectric event in soft tissue or bone. If no heavy metal x-ray is produced by a photoelectric event in the bone volume due to one or more of the above criteria not being satisfied, the γ-ray is terminated and the next photon is emitted.

Coherent scatter events in the bone are interactions between the incident photon and the entire atom. Coherent scatter differs from Compton scatter in that the photon interacts with a much more massive object, the entire atom, compared with one electron, and therefore the kinetics of the collision are different. Since the scattering object has more mass, the photon can be scattered through an angle θ, essentially without loss of energy. Therefore, in coherent scatter events, the only consideration is the new photon direction after the event, as the energy is assumed to remain the same. New direction cosines are generated using random numbers, where the differential cross section:

$$\frac{d\sigma}{d\Omega}=\frac{r_o^2}{2}\cdot\left(1+\cos^2\theta\right)\left|F(v^2)\right|^2 \qquad [3.3]$$

provides the probability distribution for selecting the scattered direction, using a method outlined by Chan and Doi (1988). In equation 3.3, r_e is the classical electron radius, θ is the angle of scatter and F is the atomic form factor as a function of v^2, which itself is dependent on both the photon energy and θ.

3.2.4 Compton scatter modelling

The main difference from earlier *in vivo* XRF codes reported in the literature is the inclusion of the phenomenon of momentum broadening of the scattered photon energy for a given scatter angle θ, as discussed in section 2.1.1. In this simulation, the distribution of electron momenta, referred to as the Compton profile for a particular element, is used to correct the energy of the scattered photon calculated under the assumption of a stationary scattering electron.

Before applying the correction for momentum broadening, the angle of scatter is first generated. As with coherent scatter, the angle θ is selected by sampling the probability distribution of scatter per unit solid angle, *i.e.* $d\sigma/d\Omega$, which in this case is given by the Klein-Nishina differential cross section for Compton scatter. The Klein-Nishina formula may be used with the assumption that the photon energy and angle of scatter are uniquely related through equation 2.1, as the double differential cross section, the probability of a photon scattering per unit solid angle ($d\Omega$) and per unit scattered energy ($d\omega'$), gives rise to the Klein-Nishina expression when integrated over $d\omega'$. This is only true with the assumption that all electrons may be excited; the validity of this will be addressed in section 3.2.7.

Sampling the angle of scatter θ from the Klein-Nishina expression is based on a combination of the direct sampling and rejection techniques as outlined by Lux and Koblinger (1991). This differs from the approach taken by Todd *et al.*, 1991, as it was found in this work that the Carlson method approximation used previously was not particularly accurate in selecting θ for these applications. The new direction cosines are determined and equation 2.1 is used to calculate the initial prediction for the energy of the scattered γ-ray, E_r.

The subroutine then uses a random number and the relative concentrations of the elements present in the medium at the location of scatter to determine the particular atom with which the γ-ray interacted. Once this element has been selected, its Hartree-Fock Compton profile is used to determine the effect of the finite momenta of the electrons on the scattered energy E_r. This profile is a probability density function of the projection of the electron momentum on the scattering vector, q, and has been tabulated by Biggs *et al.*, 1975, for all elements. This parameter q can be converted to a corresponding shift in the initial prediction of scattered energy E_r. However, the profile for this element must be truncated at the edge energy, corresponding to the incident photon energy minus the K edge energy of the element with which the photon interacted. This cut-off arises due to the requirement that the incident γ-ray transfers sufficient energy in the process to eject the electron. Truncating the total profile at this edge assumes that the contributions to the profile from the remaining electron orbitals are negligible for transfers of energy less than the K shell binding energy. This approach is taken as a means of simplifying the profile sampling for each scatter event. This may be a poor approximation with the higher-Z elements, such as calcium and phosphorus, found in the bone matrix. These elements comprise roughly 22 and 10% of the bone by weight respectively and it is unclear as to the extent to which these particular elements contribute to the total Compton scatter signal detected. Also, in using the elemental Hartree-Fock Compton profiles, there is an inherent assumption that profiles of free atoms could be used for elements in a molecular compound. Profiles generated in this manner are known to deviate from the experimentally measured molecular profiles (see, for example, Epstein *et al.*, 1973). However, as will be demonstrated in section 3.2.7, although there are approximations made, this simulation does compare well with experiment and is expected to provide an accurate tool for the purposes of XRF measurement system design and improvement.

With the appropriate elemental profile selected and truncated at the K edge energy, the q value can now be selected for a particular scatter event. This value is generated from the profile through a cumulative density function (*CDF*) approach. In the main part of the program, before the loop for simulating each γ-ray history, the elemental profiles are read in from the data file. These are then normalised and numerically integrated over the entire q range tabulated by Biggs *et al.*, 1975. This yields a *CDF* over a wide range of q values for each element. The cut-off q, corresponding to the minimum energy transfer requirement, is determined for the particular element that has been selected, and for the photon energy and scatter angle of the event. The appropriate elemental *CDF* is then evaluated at this maximum q, linearly interpolating between tabulated q values when necessary. This maximum cumulative density function value (CDF_{MAX}) is then used with a random number (r) to select the q value based on:

$$q = CDF^{-1}(r \cdot CDF_{\max}) \qquad [3.4]$$

where CDF^{1} is the inverse of the cumulative density function. This inverse function is obtained from the arrays of q and the *CDF* for the particular element involved in the scatter. The selected q value is then used to give the new scattered energy:

$$E' = \left(1 + \frac{2q\sin(\theta/2)}{137}\right)E_s \qquad [3.5]$$

where θ is the angle of scatter sampled from the Klein-Nishina formula, E_s is the scattered photon energy calculated from equation 2.1 using this value of θ, and q is sampled from the elemental profile as described above.

3.2.5 Detector response

In this simulation, unlike many of its predecessors, the detector efficiency is modelled on an event by event basis rather than convolving the simulation output with a "pseudo-detector response function" based on semi-empirical or experimental information. In this simulation, when it has been determined by geometry that a γ-ray has entered the detector crystal, that photon is then traced in the same manner as previously described for photon interactions in the sample. The end result is that the γ-ray is recorded in the simulated spectrum based on the total energy deposited in the germanium crystal, rather than the energy of the photon entering the crystal. However, this simulation does not model electron transport in the crystal and therefore may deviate from experimental spectra due to incomplete charge collection. Furthermore, the detector resolution response function has not been directly included in the simulation. This has generally not been necessary in practice as the Monte Carlo spectrum is often binned such that the change in energy between adjacent channels is greater than the full-width-half-maximum (FWHM) of the detector at even the highest energies examined. The detector resolution may be readily incorporated, however, by convolving the final detected spectrum with a Gaussian of variable width provided the detector resolution function has been assessed experimentally over the energy range of interest.

3.2.6 Program output

The program writes the results to two separate output files. The first gives information about various interactions in the system and lists energies deposited in both soft tissue and bone. This is important for dosimetric purposes. This file also contains the number of each type of characteristic x-ray detected, as well as the number of coherent photons counted with the full energy at which they were emitted from the source. These values are important in assessing the x-ray to coherent ratio for geometric variability, as will be discussed in more detail in chapter 4. The second output file contains a listing of the detected spectrum. To reiterate, the photons are counted in the energy channel corresponding to the energy deposited in the crystal, rather than assuming 100% efficiency and applying an empirical detector response function after the fact. This output file facilitates the testing of the program by comparison with corresponding experimental data.

3.2.7 Comparison with experiment

Figure 3.3 shows the comparison of the Monte Carlo simulation with the corresponding spectrum for a uranium plaster of Paris phantom obtained experimentally. The experimental spectrum was acquired with a hyperpure germanium detector, as described in section 2.2, with a 1 mCi ^{57}Co source mounted coaxially in front of the detector, in backscatter geometry, in a tungsten cup to shield the detector from direct photons from the source. The total diameter of the source in its mount is 16 mm. The 5.7 cm diameter, 9.8 cm high plaster of Paris phantom contained 100 μg uranium per gram of plaster and was positioned 10 cm from the source. The experimental spectrum shown in figure 3.3 is the difference between the total spectrum acquired with the phantom in place and the background spectrum obtained with the sample removed.

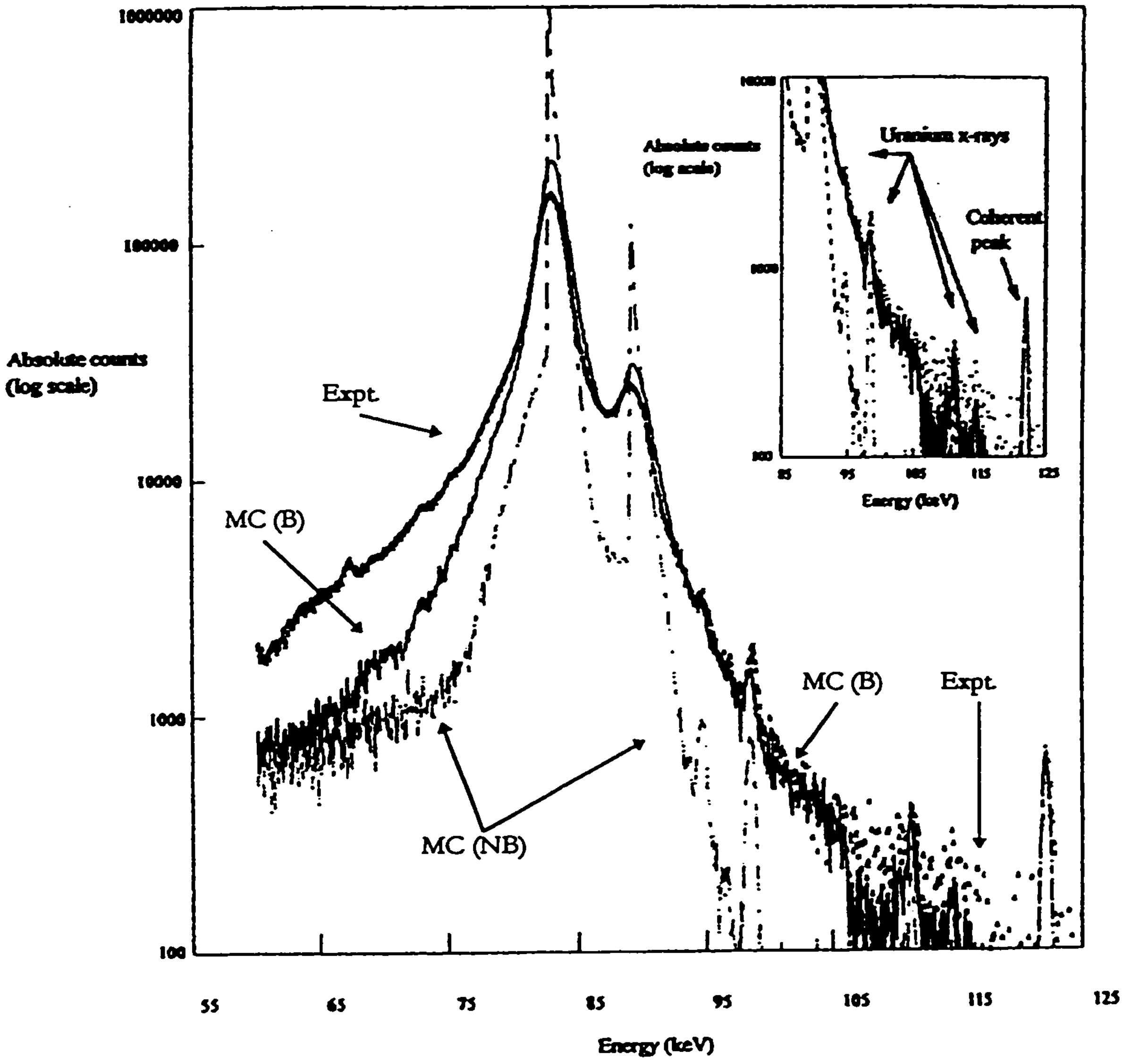

Figure 3.3: Comparison of Monte Carlo (MC (B) and MC (NB)) and experimental (Expt.) spectra for a uranium-doped plaster of Paris phantom. Note the effect of the inclusion of the broadening phenomenon, shown by MC (B) compared to MC (NB). The inset demonstrates the excellent agreement between the simulation with the profile modelled (MC (B)) and the experimental data (Expt.). A quantitative comparison of the various features is given in table 3.1.

The similarity between Monte Carlo and experiment is evident in a quantitative comparison between the areas of various components of the spectra, summarised in table 3.1.

It should be noted that the error bars and uncertainties in figure 3.3 and table 3.1 are based on standard counting statistics, although this admittedly underestimates the Monte Carlo uncertainty as it does not include any underlying uncertainties in all cross-sectional and geometric data entered as input into the simulation. Furthermore, these and all uncertainties in this thesis are 1σ unless otherwise stated. This numerical comparison is on a photon by photon basis; the results from the simulation have been scaled by the number of γ-rays emitted in the experimental measurement divided by the number of γ-rays traced in the simulation. There has been no normalisation of simulated to experimental spectra based on total area, or any other such parameter. Since the 122 keV and 136 keV γ-ray emission rates were measured directly for this particular ^{57}Co source in its collimator, the comparison on a per photon basis will not be influenced by factors such as self-absorption, absorption in the source window and scattering from the source backing.

Spectral feature	Monte Carlo	Experiment	% difference (expt-MC)/expt
$K\alpha_1$ x-ray area	$(8.8 \pm 0.4) \times 10^3$	$(10.6 \pm 0.6) \times 10^3$	16 ± 6
$K\beta_1$ x-ray area	$(2.2 \pm 0.2) \times 10^3$	$(2.3 \pm 0.3) \times 10^3$	3 ± 14
$K\beta_2$ x-ray area	$(0.70 \pm 0.09) \times 10^3$	$(0.6 \pm 0.2) \times 10^3$	-15 ± 43
Coherent area	$(7.3 \pm 0.3) \times 10^3$	$(7.6 \pm 0.6) \times 10^3$	4 ± 9
Compton area under x-rays (92.5 to 115.5 keV)	$(2.84 \pm 0.02) \times 10^5$	$(3.10 \pm 0.01) \times 10^5$	8.2 ± 0.7
Total Compton area (60.5 to 105.5 keV)	$(1.206 \pm 0.001) \times 10^7$	$(1.146 \pm 0.004) \times 10^7$	-5.2 ± 0.4
Low energy side of Compton (60.5 to 80.5 keV)	$(1.395 \pm 0.004) \times 10^6$	$(2.501 \pm 0.003) \times 10^6$	44.2 ± 0.2

Table 3.1: An absolute quantitative comparison of the areas of various spectral components. Apart from the Compton area, all features are in agreement. It should be noted that the uncertainties given on the Monte Carlo peak areas are based on Poisson statistics only. This does not account for the uncertainties on all the input data required for the simulation and is therefore an underestimate of the errors on these values.

Based on the results summarised in table 3.1, this simulation is an accurate model of the x-ray and coherent intensities when compared with the corresponding experimentally measured spectrum, in terms of absolute counts detected. Furthermore, although the Compton area values given in table 3.1 do not agree within uncertainty, there is good agreement, within 10%, with respect to the total Compton area, as well as the region under the x-ray and coherent peaks, as is evident in figure 3.3. However, the simulation is a significant underestimate of the experimentally determined Compton area in the low-energy tail of the Compton distribution. There are a number of possible explanations for this discrepancy. Difficulties arise in comparing experiment and simulation due to attempting to correct for scattering from the surroundings. The Monte Carlo simulation effectively models the sample as suspended in air. This is obviously not feasible to reproduce experimentally, and correcting for scatter from the sample support is non-trivial. Generally, an experimental spectrum is generated that is the difference between the sample with the support and the support alone. However, complicated effects arising from, for example, scatter from support to sample to detector, or scatter from support to detector from a region of the apparatus that was previously in the 'shadow' of the sample, may result in under- or over-subtraction of the spectrum. This may give rise to a low-energy scatter component that is not observed in the simulated spectrum. Also, in the 58 to 70 keV energy range, partially shown in figure 3.3, tungsten x-rays are observed experimentally due to returning photons interacting in the source collimator before detection. In addition, the experimentally measured source output is the full energy γ-ray intensity and does not account for the emission of photons less than this full energy arising from scatter in the source collimator, source backing, and the source itself. Therefore, these factors will result in an expected underestimation of the lower energy spectral region by the simulation, as observed.

Furthermore, the detector is modelled as an ideal germanium crystal of variable dimensions, effectively suspended in air. Again, this is not an accurate representation of the experimental system and the assumption that detector response can be modelled on the basis of photon energy deposition is inherently limited in accuracy. It has been shown (Kaufman *et al.*, 1982, Rindby *et al.*, 1982) that different detectors used in fluorescent excitation analysis exhibit wide variations in background counts in this low-energy region even when tested under identical conditions. It is generally proposed that the detection process itself gives rise to the background counts in this spectral region. Particular factors contributing to this phenomenon include the escape of photoelectrons, bremsstrahlung and characteristic x-rays created in the crystal, incomplete charge collection, as well as scatter of incident photons in the detector assembly before detection (Goulding *et al.* 1971, Heath 1971, Meixner 1974, Goulding and Jaklevic 1977, Seltzer 1981, Varley *et al.* 1981, Gonsior and Roth 1983). These studies emphasise that these factors, along with complications arising from pulse pile-up, result in considerable deviations in the detector response function from the expected function based on simple calculations of photon energy deposition and intrinsic resolution. Since our simulation does not account for all of these factors, the observed discrepancy in the 60 to 80 keV range of figure 3.3 is not unexpected. (Note: the experimental spectrum represented in figure 3.3 was acquired with less than 1% deadtime. This indicates that pulse pile-up is not expected to be a major contribution to the observed discrepancy.) Therefore, incomplete charge collection, electron escape from the detector and scatter in the detector assembly are all expected to give rise to the higher experimentally observed counts in this low-energy region. However, since this low-energy region is not significant in most *in vivo* spectra considered in this thesis, this discrepancy is not a major concern. Although the measured detector response function may provide a more accurate representation of the detected spectrum, for these applications it is felt that extensive detector response assessments are unnecessary as our more simplistic approach is accurate in the main spectral region of interest.

There is another possible reason for the observed disagreement between the Monte Carlo Compton feature and the corresponding experimental data. By using the Klein-Nishina formula to generate the angle of scatter in each event, the assumption is made that the electron with which the photon interacts is both free and stationary. The simulation has modelled the finite momentum of the electrons by incorporating the Compton profile in the determination of the final energy of the scattered photon, however, the assumption that the electrons are free partially remains in the model. It should be noted that binding effects are accounted for in modelling momentum broadening by truncation of the profile at the edge energy. In order to model bound electrons fully, the incoherent scattering function $S(\omega,\theta,Z)$ must be included in selecting the angle of scatter θ. However, as discussed elsewhere (O'Meara *et al.*, 1998b), the inclusion of the $S(\omega,\theta,Z)$ in generating θ does not result in a significantly more accurate simulation but does require 1.4 times more CPU time to follow the same number of photons in the sample.

It is because of many of these necessary approximations that *in vivo* XRF Monte Carlo simulations and experiment previously have not been compared on a photon-by-photon basis. Typically, spectra are normalised to unit area and the relative shapes and intensities are investigated. Therefore, although the total Compton area and the region under the x-ray and coherent peaks are not in complete agreement with experiment within uncertainty, the observed agreement within 5 to 10% is excellent since the attempt to compare spectra per photon emitted is known to be limited in its accuracy. Although there are inherent limitations with this simulation, it is felt that this code is a significant improvement on previous approaches reported fully in literature for modelling *in vivo* source-based XRF systems. This simulation avoids the need to investigate experimentally the detector response function of any detector used and includes Doppler broadening of the scattered photon energy from a theoretical basis with every Compton scatter event in the sample.

3.3 Monte Carlo simulations of polarised XRF

As discussed in section 2.1.2, polarised radiation has been used as a means of reducing the background under the characteristic x-rays in x-ray fluorescence spectra. In order to use the Monte Carlo simulations described in the preceding section as a design and optimisation tool for polarised *in vivo* XRF systems, certain modifications must be made to these programs. The major addition to the program is the modelling of the polarisation vector of each photon. As noted in section 2.1.2, the differential scattering cross section for Compton interactions is a function of the angle between the plane of incident polarisation and the scatter plane, ψ. This dependence is eliminated for unpolarised radiation, by averaging equation 2.2 over all ψ, yielding the Klein Nishina formula. However, when modelling Compton interactions of polarised photons, it is important to consider the direction of initial polarisation, as well as photon energy and direction cosines, when generating the new direction cosines and photon energy after scatter. In addition, the differential scattering cross section for coherent scatter interactions of polarised radiation is a function of the polarisation vector. Therefore, throughout the photon history, the program must continue to update the photon energy and direction cosines as described for source-excited XRF simulations, as well as the polarisation vector.

The other change to the simulations in order to model polarised XRF systems arises from the rather more complicated experimental set-ups involved compared with source-excited based XRF. As demonstrated schematically in figure 2.5, polarised systems require an x-ray tube, a polarising medium, as well as the sample and detector, and often include filters of various dimensions and compositions located either before the polariser or before the sample. Therefore, the complete simulation of these systems requires more stages of modelling than merely the emission of a γ-ray toward the sample, the tracing of the γ-ray in the sample, and the determination of whether this photon is detected, as is the case with source-excited simulations. Simulations of polarised systems are typically divided into separate stages, with the output of the preceding stage serving as the input to the next stage. In this work four separate programs have been developed, largely based on the simulations described in the preceding section with the addition of modelling the polarisation vector. These programs are designed to simulate i) the spectrum of photon energies emitted by the x-ray tube of variable voltage and anode material, ii) the interaction of these photons in the polariser of variable dimensions and material, iii) the interaction of the photons emitted at 90° to the primary beam from the polariser (through a collimator of variable aperture and length) in the sample, and iv) the interaction of the photons emitted from the sample, incident on the detector face, in the detector crystal.

It should be noted that, unlike source-excited based *in vivo* XRF systems, complete simulations of polarised *in vivo* XRF have been reported previous to this work (for example, Lewis, 1994, Lewis *et al.*, 1995, Ao *et al.*, 1997, Hugtenburg *et al.*, 1998, and Lewis *et al.*, 1998). These simulations include momentum broadening as well as photon polarisation monitoring, and in some cases also model photon interactions in the detector. In most cases, such models have made use of the commercially available Monte Carlo software, EGS4, as this particular Monte Carlo package has been recently extended to model photon polarisation (Namito *et al.*, 1993). However, EGS4 utilises a programming language that is unique and rather different from other languages. Therefore, it was felt that given the experience of writing in-house source-excited simulations, it would be more efficient to adapt the in-house code to model the polarised-based XRF systems rather than learn a new programming language. Furthermore, writing in-house simulations rather than directly implementing commercial software is considerably more conducive to understanding thoroughly the underlying physical principles behind the interactions in all stages of the measurement system.

3.3.1 X-ray tube output modelling

Previous Monte Carlo simulations have generated the photon energy spectrum based on the algorithm originally proposed by Birch and Marshall, 1979. In this work, it was found that the Birch and Marshall algorithm provided an accurate simulation of spectra from tungsten anode targets. However, when modelling molybdenum targets as a means of testing the code, it was found that although the Birch and Marshall algorithm for generating the characteristic x-rays from the anode material was accurate, the model proposed by Tucker *et al.*, 1991 was the better approach for generating the bremsstrahlung continuum portion of the x-ray tube spectrum.

In both cases, the user is prompted to enter the tube voltage, the anode angle (as this will affect the degree of attenuation of the photons in the anode itself), the energy bin widths to use for the output spectrum file, the window material and thickness, and the thickness and atomic number of any additional filters used (note: air attenuation can also be included). The program then writes the output spectrum to a file, which is named based on user input. For simplifying subsequent stages of the modelling of these systems, the bremsstrahlung spectrum is recorded as one array with the energy bin width specified by the user, while the characteristic anode x-rays are recorded as a second array, with the correct corresponding x-ray energies. It was found that the spikes created in the output spectrum when these two components were combined made subsequent selection of photon energies based on this spectrum somewhat difficult. Figure 3.4 demonstrates the agreement between this algorithm and tabulated x-ray tube spectra for tungsten anodes, while figure 3.5 demonstrates the agreement between simulated and experimental tube spectra for molybdenum anodes.

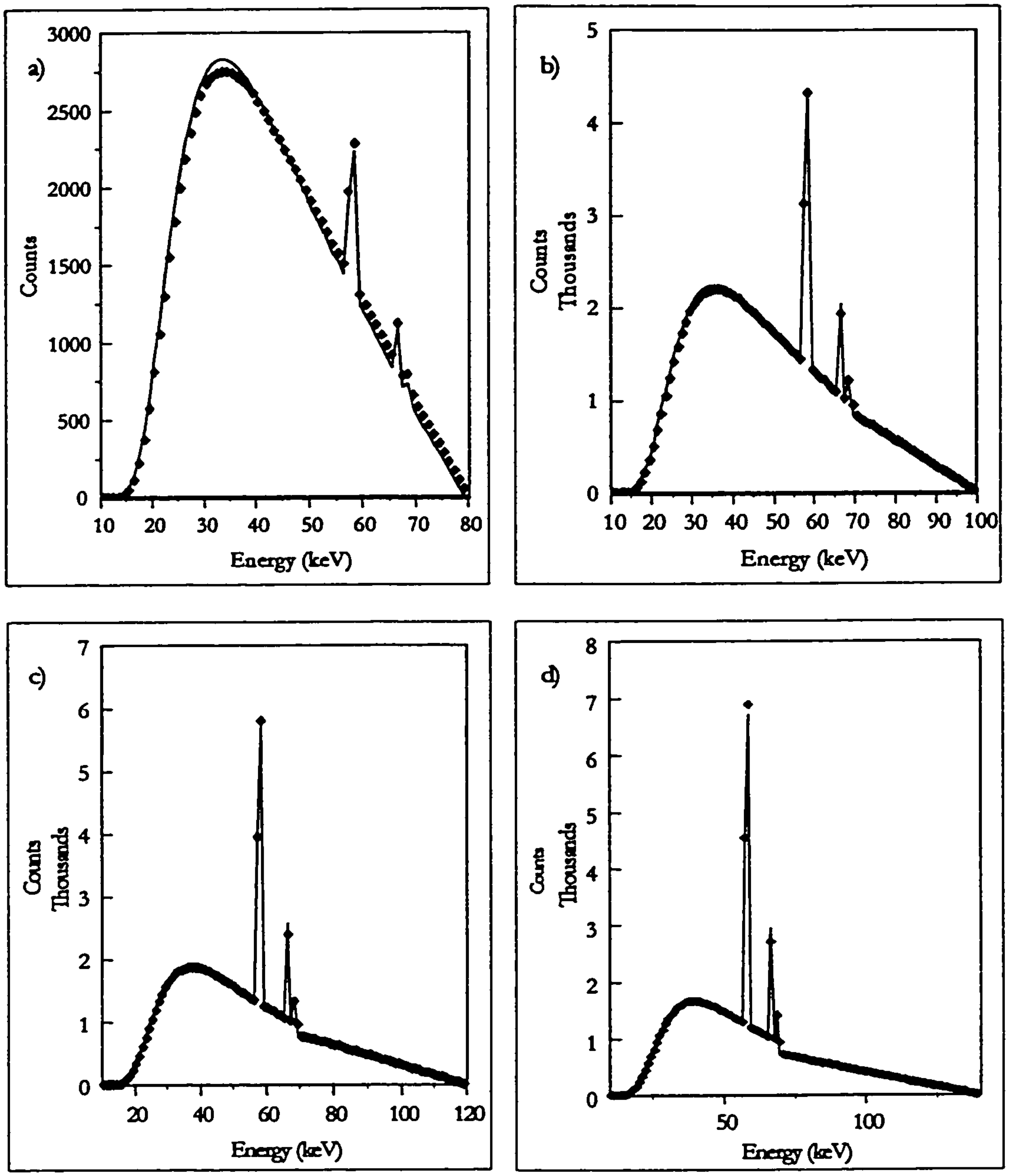

Figure 3.4: A comparison of the simulated tube spectral output from a tungsten anode with tabulated spectral data from Birch *et al.*, 1979. a) shows the comparison for 80 kV voltage, b) for 100 kV, c) for 120 kV and d) for 140 kV. All comparisons have corrected for 2.5 mm of inherent aluminium filtration. Tabulated data are shown as solid line while simulated data are shown as diamonds.

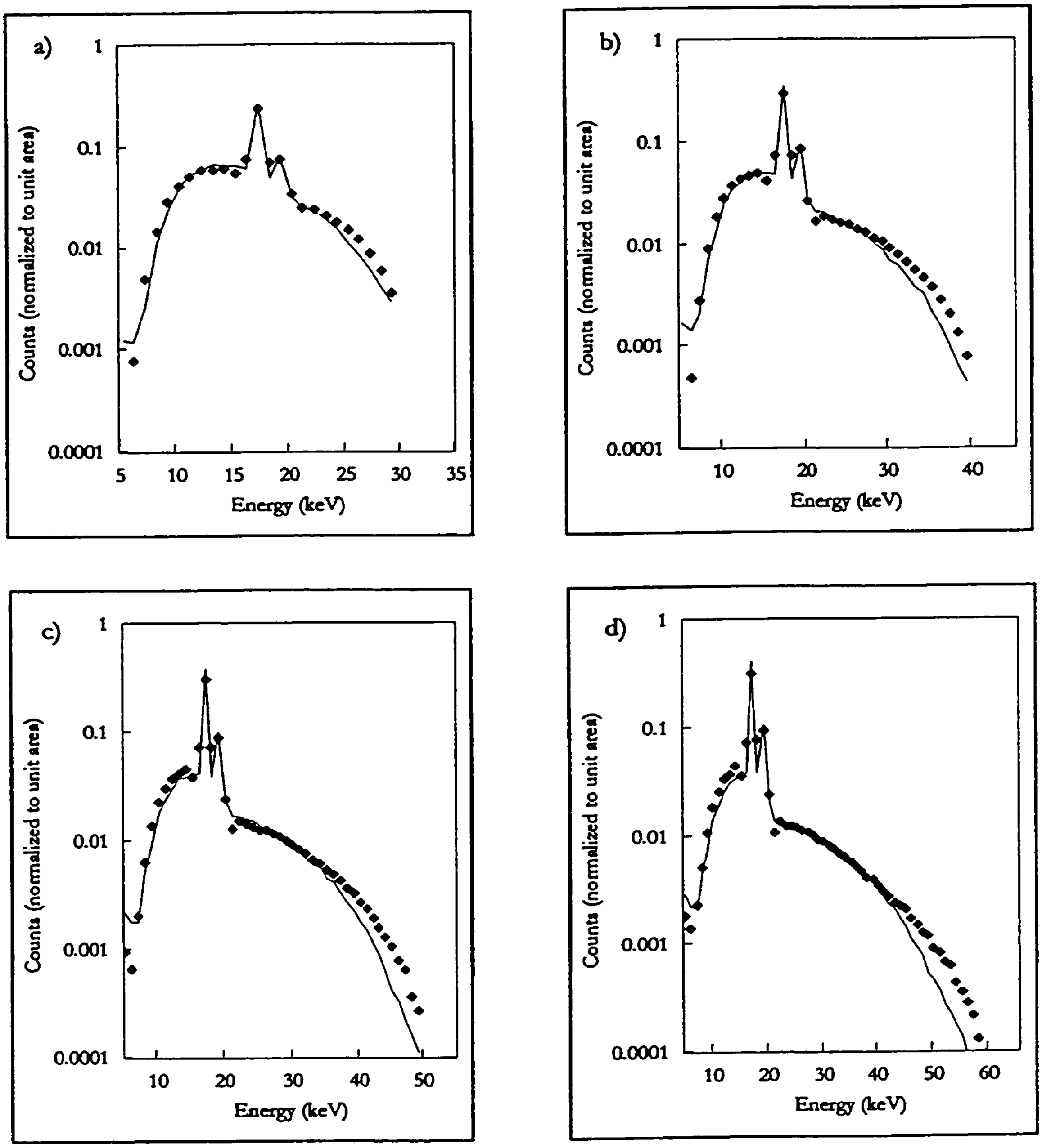

Figure 3.5: Comparisons of simulated x-ray tube spectral output and experimental data for a molybdenum anode. Comparisons at tube voltages of a) 30 kV, b) 40 kV, c) 50 kV, and d) 60 kV are shown. The anode is at an inclination of 6°, and the attenuation of a 0.0325 cm beryllium window and 237 cm of air between the tube and the detector is included. The experimental data, acquired by Dr. A. C. Todd *et al.* at Mount Sinai Medical Center, New York, are shown as solid lines while the generated spectra are represented by diamonds. It should be noted that the computed spectra are run through the detector response portion of the simulation in order to allow a direct comparison with these experimental data.

It is clear that, based on figures 3.4 and 3.5, there is acceptable agreement between simulation and the corresponding experimental data. With this agreement achieved, the next stage in the simulation could be developed and tested.

3.3.2 Polariser output modelling

The next stage in the Monte Carlo simulation of *in vivo* polarised XRF systems is the output from the polariser. The modelling of photon interactions in the polariser requires several input variables, for example, the polariser material, summarised by a list of elements with their corresponding percent abundance by weight, the polariser thickness, diameter, the incident beam diameter, the collecting collimator length and inner diameter and the angle of the polariser with respect to the incoming and outgoing beams. Figure 3.6 summarises the geometry of the system used, and specifies the geometry variables that are set by the user.

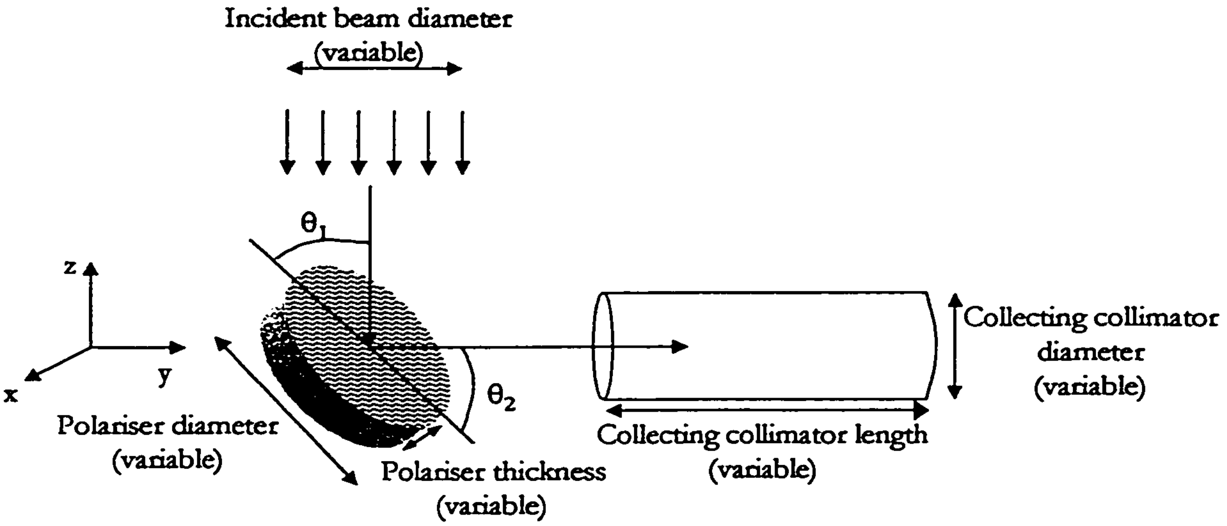

θ_1 - angle between incident beam axis and polariser surface
θ_2 - angle between outgoing beam axis and polariser surface
(both variable)

Figure 3.6: Schematic of the geometry used in the polariser output model. The variables that are specified by the user are indicated.

From figure 3.6, it is evident that there is considerable flexibility inherent in this code. A wide variety of polariser materials, dimensions and scatter geometries may be investigated by this stage of the simulation in order to identify the best combination of these variables in terms of the overall system sensitivity achieved.

Once these variables have been set through input data files, the simulation generates a photon with direction cosines along the negative z direction and with a polarisation vector randomly oriented in the x-y plane. The starting z spatial co-ordinate for each photon is the same, however, the x and y co-ordinates are chosen randomly such that there is a uniform distribution of emitted photons describing a circle of user-specified radius about the z axis denoted in figure 3.6. The photon energy is selected based on the output spectrum from the preceding stage of the simulation. First, the relative fractions of bremsstrahlung photons and characteristic x-rays recorded in the tube output file are used with a random number to determine to which group this particular history belongs. If the random number indicates that this is a bremsstrahlung photon, then the energy of this photon history is generated using a random number and a spline fit to the bremsstrahlung energy distribution recorded as the tube output. If the random number indicates that a characteristic x-ray was generated from the tube, another random number and the recorded relative intensities of these characteristic x-ray emissions from the tube are used to determine which x-ray was emitted. This then uniquely determines the photon energy emitted.

With the initial conditions determined, the photon is projected along its direction cosines (the negative z direction) toward the polariser. Given the initial distance of the photon from the z axis, the diameter of the polariser and the angle of inclination (θ_i) of the polariser to the incident beam, it is determined whether the photon crosses the polariser surface. If the photon misses the surface, it is recorded as a miss and the history is terminated. However, if the photon crosses the polariser surface, then the history must be followed to determine whether interactions occur, which may result in the re-direction of the photon into the collecting collimator. As with the photon tracing described in 3.2.3, the distance to the first interaction is determined based on the attenuation coefficient of the polariser material at the particular photon energy generated. If this distance is outside the polariser, the photon has been transmitted without interacting, is recorded as such, and the next photon history is generated. However, if the distance to the first interaction results in an event within the polariser, further steps must be taken in following this photon to its termination.

As with source-excited XRF simulations, when it has been determined that an interaction has occurred in the polariser, a random number is then used to determine which type of event has taken place. In these simulations, the polariser material is typically a low- to mid-Z element or matrix and therefore, as with tissue, it can be argued that the products of photoelectric events in the polariser have effectively insufficient range to emerge from the sample. Therefore, if it has been determined through a random number and the relative intensities of the photoelectric, Compton, and coherent cross sections that a photoelectric event has occurred, the photon is recorded as having undergone such a process and the history is terminated. However, if either Compton or coherent scatter occurs in the sample instead of photoelectric events, the new direction cosines, polarisation vector, and in the case of Compton scatter, the new photon energy, must be determined.

In the case of Compton scatter, the polar scattering angle θ, the angle between initial and final photon direction vectors $\mathbf{k}_0$ and $\mathbf{k}$ when $\mathbf{k}_0$ is aligned with the z axis, is selected based on sampling the Klein-Nishina formula, as outlined in 3.2.4. This scatter angle provides the initial prediction of the scattered photon energy through equation 2.1 and the momentum broadening is then accounted for as discussed in section 3.2.4. The main difference in modelling polarised photon Compton scatter arises in generating the azimuthal scattering angle, ψ, the angle between the plane of incident polarisation and the scatter plane when $\mathbf{k}_o$ is along the z axis and $\mathbf{e}_o$, the initial polarisation vector, is along the x axis. With unpolarised radiation, this angle ψ has a uniform distribution from 0 to 2π radians. However, when incident photons have a particular $\mathbf{e}_o$, there is a corresponding non-uniform distribution of the scatter angle ψ, which is, after all, the reason for using polarised radiation as the source of excitation for *in vivo* XRF. Therefore, once θ has been determined based on the Klein-Nishina formula, ψ is then generated with random numbers based on the differential incoherent scattering cross section for polarised radiation, equation 2.2, given this particular photon energy and polar scatter angle θ. With the scatter angles θ and ψ generated, the new direction cosines and polarisation vector must be determined. The algorithm developed by Namito *et al.*, (1993) is used for this purpose. Again, following the procedure outlined by Namito *et al.*, (1993), the new direction cosines and polarisation vector must be transformed back to the laboratory frame, as an initial transformation was required to align $\mathbf{k}_o$ with the z axis and $\mathbf{e}_o$ with the x axis for simplification of the interpretation of the angles θ and ψ.

An analogous procedure is used to determine the new direction and polarisation of the photon after coherent scatter. As discussed in section 3.2.3, coherent scatter results in a change in photon direction with essentially no loss in energy. With unpolarised radiation, the angle of scatter θ is generated by sampling equation 3.3 and ψ is assigned a value following a uniform distribution from 0 to 2π radians. With polarised radiation, as was the case with

Compton scatter, the differential scattering cross section for coherent scatter is explicitly a function of ψ and equation 3.3 becomes:

$$\left.\frac{d\sigma}{d\Omega}\right|_{coherent} = r_o^2(1-\sin^2\theta\cdot\cos^2\psi)\cdot\left|F(v^2)\right|^2 \qquad [3.6]$$

Given this expression, it is clear that the method of generating new direction and polarisation vectors for a photon after coherent scatter is essentially identical to the procedure for Compton scatter. First, θ is generated based on equation 3.3 under the transformation to the scatter frame, which aligns $\mathbf{k}_o$ with the z axis and $\mathbf{e}_o$ with the x axis. With this particular θ value, ψ is then selected based on equation 3.6, given θ and the photon energy. The new direction and polarisation vectors are calculated based on θ and ψ and transformed to the laboratory frame following the algorithms outlined by Namito *et al.* (1993).

With a new direction, polarisation vector, and in the case of Compton scatter, a new photon energy, the program continues to trace the photon until it is terminated. The declaration that the history is over may result from either the occurrence of a photoelectric event, the loss of sufficient energy in scatter events such that the energy falls below a cut-off value below which the photon is no longer traced, or the photon emerges from the sample. If the photon emerges from the sample, the direction vector, and the collecting collimator aperture and length are then used to determine whether the photon emerges from the collimator. If this history does result in transmission through the collecting collimator, the photon energy and polarisation vector are recorded in the output file to be used as input to the next stage. Once the history has been terminated, the next photon is generated until the required number of histories has been traced.

As the final step in the simulation, the user is asked if there is significant filtration to consider. The user may then enter the atomic number and thickness of any filters present at the end of the collecting collimator and these values are used to correct the emerging energy spectrum through equation 3.1, where x is the thickness specified and μ is the attenuation coefficient of the particular element indicated, for each photon energy bin. This approach is approximate, however, it is expected to yield a reasonable first approximation of the effect of filtration of the beam while maintaining reasonable CPU run-times. Figures 3.7 and 3.8 compare Monte Carlo simulated polariser output spectra with the corresponding experimental data for both tungsten and molybdenum target x-ray tubes.

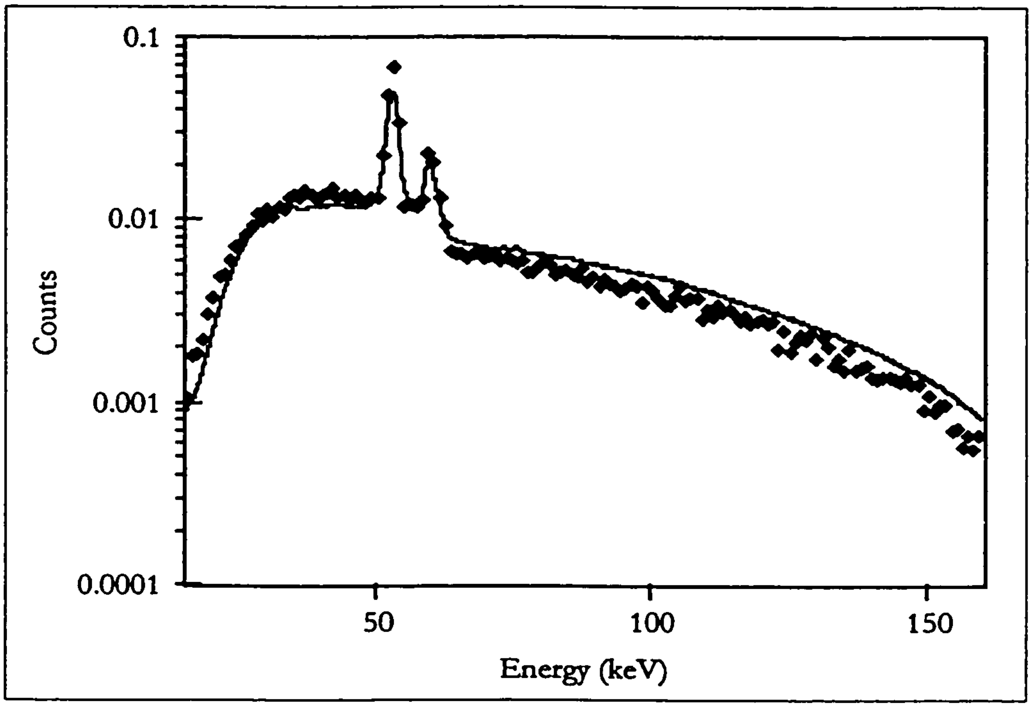

Figure 3.7: A comparison of the simulated polariser output from a tungsten anode x-ray tube, operating at 250 kV, with the corresponding experimental data. Mylar was used as the polariser. The computed spectra are run through the detector response portion of the simulation in order to allow a direct comparison with these experimental data. Simulation is shown as diamonds, and experimental data are represented by the solid line.

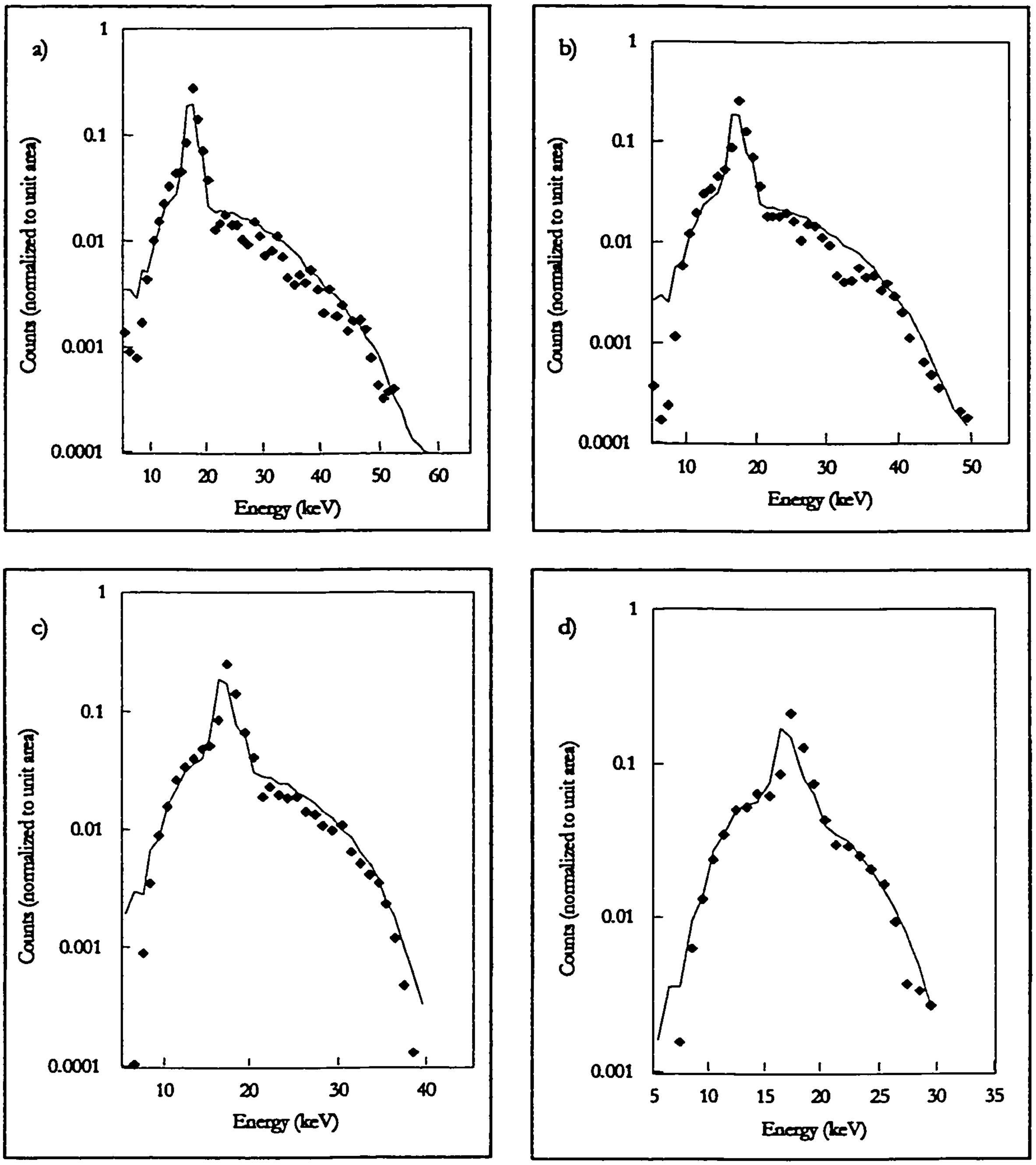

Figure 3.8: Comparisons of simulated polariser output and experimental data for a molybdenum anode x-ray tube. The polariser material is B_4C. a) shows the comparison for 60 kV tube voltage, b) shows the comparison for 50 kV tube voltage, c) tube voltage of 40 kV, and d) is the comparison made at 30 kV tube voltage. As in figure 3.5, experimental data are shown as a solid line and simulation is represented by diamonds.

It should be noted that there is some discrepancy between experiment and simulation at lower photon energies. This is likely attributable to one of two factors, incomplete background subtraction with the experimental data or incomplete modelling of photon interactions in the crystal, as discussed in section 3.2.7. It was emphasised that these factors are expected to result in the simulation underestimating the low energy region of the spectrum.

There is an additional potential source of this low energy discrepancy. The method for simulating the collimators involves a simplification that is expected to contribute to this deviation. It is assumed that only those photons with initial directions sufficient to emerge through the far end of the collimator will be incident on the next stage of the process. However, it is possible, experimentally, for photons to scatter from the inner wall of the collimator and emerge through the far end. These photons are not included in the simulation. Therefore, it is expected that, if there is a significant amount of such wall scatter events, the simulation will deviate from experiment. In particular, since these scatter events could result in the photon emerging with reduced energy, the experimental spectrum should have a higher normalised intensity in the lower energy regions.

As discussed in section 3.2.7, the presence of pile-up, and the use of pile-up rejection, in the experimental data will also further complicate the comparison between experiment and simulation. However, unlike the factors discussed above, pulse pile-up is expected to result in the simulation underestimating the high energy region, while the overall effect of the use of pile-up rejection on the spectral shape is not obvious. There appears to be some evidence of the effect of pile-up in figures 3.7 and 3.8, at the very high end of the spectra, where the experimental data are slightly higher than the corresponding simulated data.

Aside from these slight discrepancies, it is clear from figures 3.7 and 3.8 that there is acceptable agreement between simulation and the corresponding experimental data. With this agreement achieved, the next stage in the simulation could be developed and tested.

3.3.3 Sample output modelling

Four versions of this stage have been written, one to simulate measurements in bone, the second to simulate measurements in the kidney, the third models interactions in plaster of Paris, the common phantom material used to emulate bone mineral, and the fourth traces photons in an aqueous sample with a variable concentration of heavy metal content. With four different programs, there is considerable flexibility in terms of investigating system performance for a number of clinical applications. As with the discussion of source-excited XRF simulations, it is sufficient to discuss one particular model in detail, as the algorithms used in all cases are essentially identical, with some differences arising in the particular cross-sectional and geometric information required for each.

For each sample simulation, there are a number of input parameters required. In an input data file, the user specifies the distance between the incident beam collimator and the sample surface, and the diameter of this collimator. This file also contains the distance between the sample surface and the collecting collimator, as well as the diameter and length of this second collimator. Furthermore, the user specifies the sample dimensions, the low energy cut-off value, the heavy metal concentration by weight, the density of the sample material(s) and the necessary cross-sectional information for the elements involved. In the case of the simulations of bone and kidney measurements, there are two different regions in the sample and the dimensions and position of the bone or kidney within the sample must also be specified. Figure 3.9 shows the geometry used in these simulations and specifies the variables that can be set by the user.

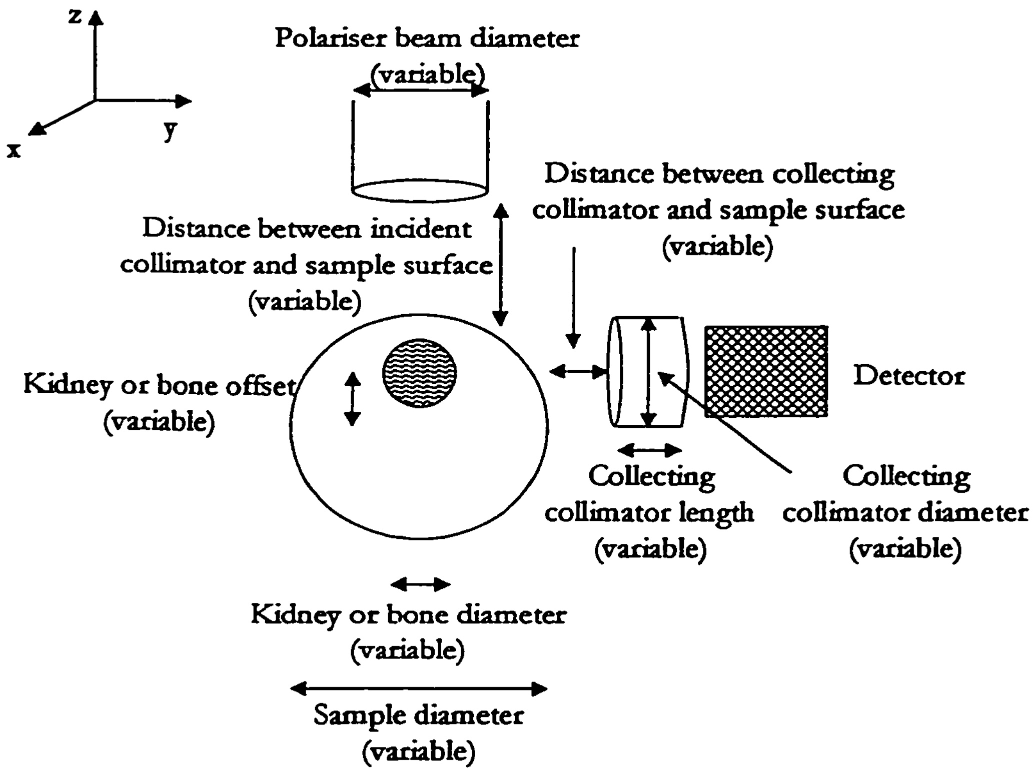

Figure 3.9: Schematic of the geometry used in modelling the sample output. When modelling aqueous solutions or plaster of Paris, the shaded region is not included and the collecting collimator is centred with respect to the sample.

With these parameters set, a photon is generated with a negative z direction, starting at a fixed distance from the sample in the z direction. The x and y co-ordinates are chosen randomly such that there is a uniform distribution of emitted photons describing a circle of user-specified radius about the z axis denoted in figure 3.9. The photon energy is selected based on the output spectrum from the preceding stage of the simulation as discussed in section 3.3.2. However, unlike the initial polarisation vector generated in the preceding simulation, in this case the polarisation vector is selected based on the distribution of vectors recorded as output from the polariser. The photon is then projected forward along the negative z direction to the surface of the sample. As before, the geometry of the sample and the incident photon position and direction dictates whether a particular photon crosses the sample surface. If the photon misses the sample, the history is recorded as such and the next photon is generated. However, if the photon crosses the sample surface, the previously outlined procedure of photon tracing is then undertaken.

In tracing polarised photons in the sample, the procedure outlined in section 3.2.3, with the modifications to modelling polarised Compton and coherent scattering as outlined in section 3.3.2, is all that is required. The only additional modification that must be made, which has not been required prior to this stage of the simulation, is the modelling of characteristic x-ray emission due to polarised photon interactions with the target element. When it has been determined that a characteristic x-ray is emitted, by requiring that the four criteria discussed in section 3.2.3 are satisfied, the appropriate photon energy is selected by the relative intensities of the various characteristic x-rays. This new photon is given a random direction based on an isotropic distribution and a new polarisation vector must be assigned. The only constraint on this polarisation vector is that it must be orthogonal to the new direction vector, and a polarisation vector is generated such that it has a random orientation in this plane.

As before, each photon is traced until it undergoes a photoelectric event in the sample that does not result in target element x-ray emission, its energy is reduced through scatter events such that it falls below the low energy cut-off, or it emerges from the sample. If it has been determined that the photon has been emitted from the sample, the photon direction vector and its location relative to the collecting collimator are used to determine whether the photon will cross the first face of the collimator. If this occurs, the length of the collimator and the direction cosines are used to determine if the photon emerges through the length of this collimator to reach the detector face. Photons that reach the detector face are recorded in an output spectrum file. The number of photons missing the collimator face and the number of photons crossing the first face but not the second are both recorded in an output file.

3.3.4 Detector response modelling

When the sample output simulation has run, the output spectrum must then be used as the input to the detector response model in order to be able to compare simulated spectra with the corresponding experimental data. Each photon is generated with energy selection based on the spectrum of photons getting through the collecting collimator in figure 3.9. Direction cosines are set such that the photon is generated with a direction parallel to the y axis in figure 3.9, under the assumption that the collimator has effectively created a parallel beam incident on the detector. This assumption is valid provided the collimator is long relative to its inner diameter. Alternatively, another program exists which generates photons with directions that diverge over the diameter of the detector crystal. With the photon energy and direction generated, each history is traced as discussed in section 3.2.5, with the end result being a detected spectrum that reflects the energy deposited in the crystal rather than the energy incident on the crystal. This avoids the need to do extensive experimental investigations of detector response for any crystal used.

Figure 3.10 demonstrates the agreement between the sample output simulation, in conjunction with the detector response model, and the corresponding experimental data. This figure was generated by running the x-ray tube output code for a tungsten anode, the polariser output simulation for an aluminium polariser, and the plaster of Paris sample simulation with 100 μg/g uranium present. It is clear that there is acceptable agreement between Monte Carlo and experiment. Nevertheless, the discrepancy at lower energy due to incomplete background subtraction, scatter in the detector assembly, and simplified modelling of both photon interactions in the crystal and collimation, is clearly evident. In fact, the difference between experiment and simulation appears to be more pronounced than that observed in figures 3.7 and 3.8. This may be attributable to the use of a shorter collimator in this stage, which implies that the simplified modelling of the collimator is a poorer approximation than when used in the previous stage. Based on this argument, one would expect the experimental data from this stage to have a more pronounced low-energy component *versus* the corresponding Monte Carlo data, compared to the simulations with a longer collimator. Since these spectra are normalised, a lower simulated spectrum at low energy results in a higher simulated spectrum at higher energy. However, as discussed above, pulse pile-up is expected to result in the simulation underestimating the high energy region. It would appear that this potentially countering influence of pulse pile-up has reduced the discrepancy in this region with the higher tube output, obtained by running at 250 kV compared with 175 kV, figure 3.10 b) *versus* 3.10 a). It should be noted that unlike the source-excited simulations, polarised XRF does not lend itself to comparing spectra on a per-photon basis. With x-ray tubes as the excitation source, it is extremely difficult to assess the source strength, as the intensity is such that direct measurements of the count rate are difficult. Furthermore, the intensity of the tube depends on the current on the cathode, and this can fluctuate significantly during the course of a measurement. Therefore, spectra in figures 3.4, 3.5, 3.7, 3.8, and 3.10 have all been normalised to unit area in order to compare Monte Carlo with experiment.

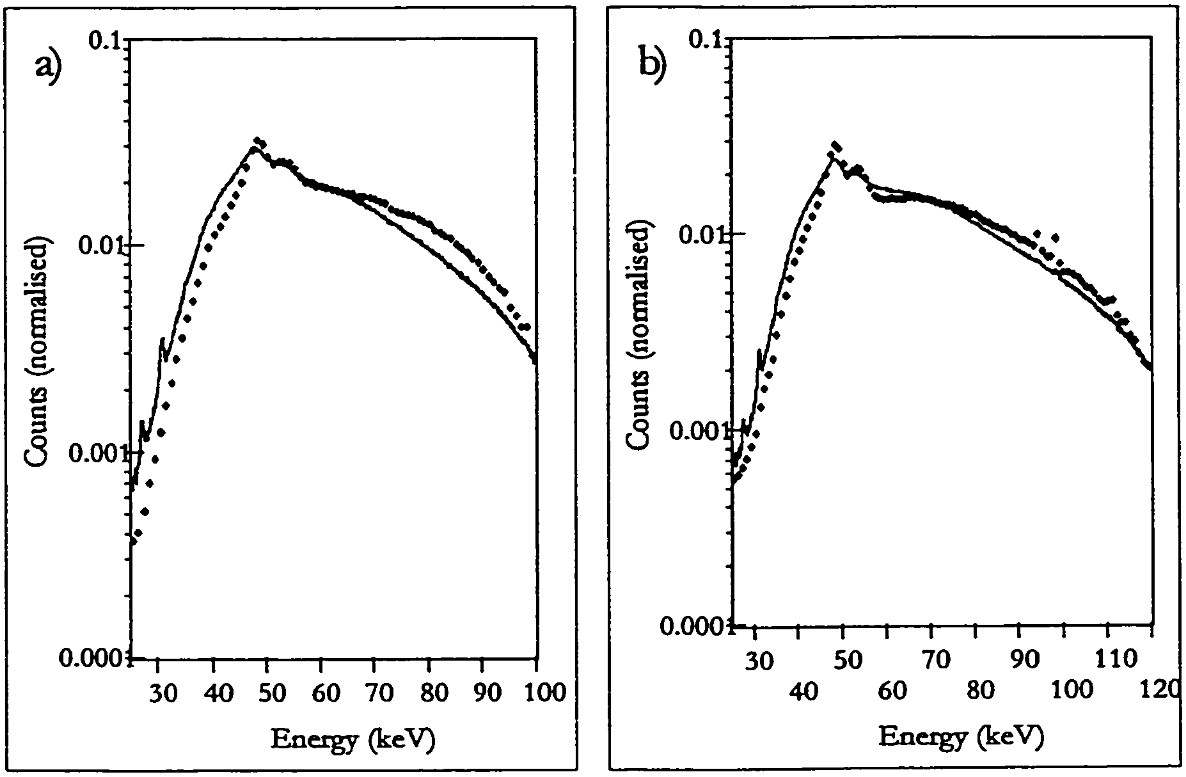

Figure 3.10: A comparison of Monte Carlo and experiment for the sample output. In this comparison, a tungsten anode tube has been used with an aluminium polariser and a uranium-doped plaster of Paris phantom. The Monte Carlo sample output spectrum has been run through the detector response code in order to be able to compare directly the spectral shape with the corresponding experimental data. a) shows the comparison with tube voltage of 175 kV, while b) demonstrates the comparison with tube voltage of 250 kV. As before, the simulation is shown as diamonds, and experimental data are represented by the solid line.

Chapter 4

Pb INVESTIGATIONS

4.1 Motivation of study

In section 2.1.1 a), design choices for the *in vivo* measurement of lead in bone through source-excited x-ray fluorescence were discussed. It was noted that two main systems have been designed and implemented for the estimation of skeletal concentrations of lead in both occupationally exposed subjects and the general population, in areas with elevated lead levels. The ^{57}Co XRF system uses two sources positioned in a 90° geometry with the sample and the detector, and is used to measure bone-Pb concentrations in the second phalanx of the forefinger (Ahlgren *et al.*, 1976). Such systems have been extensively used around the world in assessing bone-lead concentrations in various study cohorts (Ahlgren *et al.*, 1980, Christoffersson *et al.*, 1984, Price *et al.*, 1984, Christoffersson *et al.*, 1986, Schütz *et al.*, 1987a, Schütz *et al.*, 1987b, Nilsson *et al.*, 1991, Price *et al.*, 1992, Börjesson *et al.*, 1997, and Tartari *et al.*, 1997). In addition, this system has been used to follow the effect of chelation on bone-Pb concentrations in lead workers (Tell *et al.*, 1992 and Gerhardsson *et al.*, 1998). Subsequently, a system using a ^{109}Cd source positioned in a backscatter geometry with the sample and the detector was developed to measure lead in the tibia and calcaneus (Somervaille *et al.*, 1985). Both techniques quantify bone-Pb content based on the registered net counting rate of lead characteristic K x-rays; however, each system uses a different method for converting this net counting rate to a corresponding concentration. The use of different calibration techniques has resulted in the reporting of lead concentrations with slight differences in units; the ^{57}Co system gives lead concentrations in g lead per g wet bone whereas the ^{109}Cd system quotes lead concentrations in g lead per g bone mineral.

The complications in converting counting rate to lead concentration arise due to many factors. For a given lead concentration, the net counting rate of characteristic x-rays will vary due to interpatient variations in overlying tissue thickness, bone size, source-sample and detector-sample geometry, as well as the size and shape of any marrow space in the irradiated volume. In order to achieve an accurate bone-Pb measurement, these factors must be accounted for in the calibration procedure.

The ^{57}Co-based system accounts for bone size by taking two orthogonal planar x-ray images of the subject at the site of the XRF measurement. Phantoms of variable radius constructed from silica paraffin wax and bone ash with known amounts of lead, surrounded by silica paraffin wax to simulate overlying soft tissue, have been used to establish a relationship between the square of the bone diameter, the net counting rate of characteristic x-rays, and the lead content (Ahlgren *et al.*, 1979). Therefore, the measured bone diameter from the planar images and the net counting rate from the XRF measurement can be used with this calibration relationship to determine lead concentration.

The ^{109}Cd-based system makes use of additional information in the detected spectrum to correct for the factors that confound the conversion from x-ray counting rate to Pb concentration. It has been demonstrated (Somervaille *et al.*, 1985) that by normalising the x-ray counts with the coherent scatter signal predominately arising from the bone mineral, the resulting ratio is directly proportional to bone-Pb content and independent of these confounding factors. This method is preferable to the technique used in the ^{57}Co-based system, as it eliminates the need for transporting extensive additional equipment for acquiring x-ray images at on-site measurements in cases of occupational exposure. Perhaps of more importance in terms of concerns for the subject, the avoidance of planar x-ray images results in a significantly lower absorbed dose to the subject from the entire procedure. Furthermore, eliminating the use of planar imaging in favour of coherent normalisation would result in a more objective measurement system, as it removes the need for operator interpretation of the images. Currently, subjectivity may be introduced in calculating an average bone diameter from these images, as this parameter varies in both axial and transverse directions. Normalisation using features in the detected spectrum ensures the x-ray signal correction is based on the subject geometry precisely at the measurement site in the finger. In addition, coherent normalisation is expected to correct for intrapatient variability arising in longitudinal studies due to changes in subject positioning. While attempts are made to keep this to a minimum, there is currently no allowance made for this source of signal variation. However, as was extensively discussed by Somervaille *et al.* (1985), the coherent normalisation procedure is feasible in the ^{109}Cd-based system because it satisfies a specific set of criteria. This is not necessarily true for the ^{57}Co-based system.

In order for the x-ray to coherent ratio to be independent of overlying soft tissue thickness, source-sample and detector-sample geometry, and bone size, the x-rays and coherent signal must be produced (i) by the same incident fluence, (ii) in the same location in the sample, and (iii) with the same angular distribution. Furthermore, (iv) the two signals must be attenuated in the sample in a similar fashion. The first criterion is met with the ^{109}Cd-based system, as the energy of the γ-ray used is only 30 eV above the K edge of lead. Therefore, Compton scatter through an angle greater than 3.6° will result in a scattered γ-ray energy below this edge, based on equation 2.1, and thereby results in a photon that does not have sufficient energy to undergo K shell photoelectric events with lead atoms. It follows then that both the lead x-rays and the coherent scatter signal are produced by the fluence of uncollided ^{109}Cd γ-rays, as the coherent scatter photons detected with the full energy of emission are also necessarily produced by the scatter of uncollided γ-rays only.

With respect to the second criterion, it is known that the lead x-ray signal is produced in the bone matrix, as this is the site of long-term retention of this metal. The mass of lead in the overlying soft tissue is negligible compared to that in bone, therefore, no significant signal is generated in this tissue type. As for coherent scatter production, the strong Z dependence of the differential scattering cross section is an important property. Because of this strong Z dependence, the differential scattering cross section for coherent scatter in the backward direction is approximately 30 times larger in cortical bone than in soft tissue. Therefore, the coherent peak detected in the backward direction is primarily due to uncollided photon interactions within the bone matrix, *i.e.* in the same location as the site of lead x-ray production. Furthermore, both signals arise from the bone matrix with similar angular distributions, as the differential coherent scattering cross section is roughly isotropic in the backscatter direction. Lastly, since the energies of the two signals are similar, 88 keV in the case of the coherent signal and 72.8 to 87.3 keV for the lead x-rays, these photons are subject to similar attenuation losses in soft tissue and bone.

Conversely, the first criterion is not satisfied in the ^{57}Co-based system. In this case, the predominant γ-ray is 34 keV higher in energy than the lead K edge. Therefore, a significant fraction of Compton scattered photons are still sufficiently energetic to produce lead x-rays, and it is no longer true that both signals arise from the same uncollided fluence. The second criterion, that the two phenomena arise from the same location in the sample, remains satisfied with this system. The lead x-rays are still produced in the bone matrix, and at 122 keV, the differential scattering cross section for cortical bone is approximately 40 times larger than that of soft tissue at 90°. However, the differential coherent scattering cross section is not invariant over the detected range of scatter angles, 90 ± 15°, therefore the third criterion is no longer satisfied since the x-rays are produced with an isotropic distribution. Furthermore, there is a significant difference expected in attenuation of the two signals due to the larger discrepancy in energies between the lead x-rays and the coherent-scattered photons. For these reasons, coherent normalisation is not expected to result in an x-ray to coherent ratio that is independent of these parameters. It is for these reasons that coherent normalisation has not been used previously with *in vivo* Pb XRF measurements using the ^{57}Co-based system. However, it is possible that the reasons for not satisfying these criteria result in several cancelling factors that may give rise to an x-ray to coherent ratio invariant over a limited range of tissue thickness and bone size. Since the coherent normalisation procedure is preferable to the current calibration method in terms of lower subject dose, improved system transportability, and reduced subjectivity of measurement, it was deemed worthwhile to investigate the variation of the x-ray to coherent ratio with tissue thickness and bone size through experiment and Monte Carlo calculations for ^{57}Co-based systems.

4.2 Materials and Methods

The Monte Carlo simulation code used for investigating the feasibility of coherent normalisation has been described in detail in chapter 3. Five simulations were run with 3 mm, 3.5 mm, 4 mm, 4.5 mm, and 5 mm bone radii respectively, while the overlying tissue thickness was fixed at 6 mm. A set of five simulations was also run with a constant bone radius of 4 mm and overlying tissue thicknesses of 4.5 mm, 5.25 mm, 6 mm, 6.75 mm, and 7.5 mm respectively. These values were chosen based on the observed range of dimensions from planar x-rays of a cohort of 39 subjects previously measured with the ^{57}Co XRF system (data provided by J. Börjesson). Source-sample and detector-sample distances corresponding to typical values in clinical measurements were used. Due to the nature of the experimental apparatus, the distance from the source surface to the centre of the phantom (or finger) was modelled as a fixed quantity, and the distance from the surface of the detector to the surface of the sample was fixed for all simulations. Each run traced 9 x 10^8 photon histories, which required approximately 12 hours CPU time using a 266 MHz Pentium II processor. The numbers of K_{α_1} x-rays and coherent-scattered photons detected were recorded in an output file, allowing for the investigation of the behaviour of the ratio of these parameters for fixed lead content as a function of bone size and tissue thickness.

The same ranges of dimensions were used in constructing phantoms to test the coherent normalisation experimentally. Cylindrical phantoms, 10 cm in length, were constructed with an inner cylinder of plaster of Paris ($CaSO_4 \cdot 2H_2O$) doped to a lead concentration of 200 μg/g. This bone phantom of variable radius was then surrounded by a fixed thickness of Perspex (Lucite, PMMA, $(C_5H_8O_2)_n$) to simulate overlying soft tissue. Five such phantoms were made, with an additional four made with fixed bone radius and variable

Perspex layer thickness. The precise values of bone size and tissue thickness for these 9 phantoms are those used in the Monte Carlo simulations.

These phantom materials were selected as they exhibit similar photon interaction cross sections to the respective tissues being modelled, with the differences in coherent scattering properties of bone and plaster not expected to affect the legitimacy of the use of plaster in this particular application, as discussed in section 2.3. However, as noted in 2.3, there is a non-ideal discrepancy between Perspex and soft tissue, in terms of interactions with the incident fluence, the characteristic x-rays, and the coherent scattered photons from the bone/plaster of Paris.

Relative attenuation coefficients are generally the main concern in choosing a soft-tissue-equivalent phantom material. In this regard, the discrepancy between Perspex and soft tissue, 0.18 cm^{-1} and 0.16 cm^{-1} at 122 keV respectively (Berger, 1987), indicates that this phantom material is not a perfect model for these energy photons. However, these phantoms are designed to investigate coherent normalisation, and therefore the concern is more with respect to the relative attenuation of lead x-rays to coherent-scattered photons for Perspex *vs.* soft tissue. In this regard, the relative increase in the linear attenuation coefficient for Perspex at 75 keV (lead alpha x-rays) *vs.* 122 keV (coherent-scattered photons) is similar to that observed in soft tissue (0.21 cm^{-1} vs. 0.18 cm^{-1} for Perspex; 0.19 cm^{-1} vs. 0.16 cm^{-1} for soft tissue) (Berger, 1987). This indicates that Perspex is expected to demonstrate a similar change in the x-ray to coherent ratio with increasing thickness as that which would be observed in soft tissue. Furthermore, it should be noted that the Monte Carlo simulations were run with elemental compositions of soft tissue and bone (ICRP, 1975, Woodard, 1962) rather than

Perspex and plaster of Paris, and agreement between Monte Carlo and experiment would thereby provide additional evidence that these phantom materials are suitable for this purpose.

In preliminary experiments it was noted that a considerable fluence of 122 keV γ-rays from ^{57}Co was reaching the detector that did not arise from coherent scatter from the plaster of Paris. These photons arose from both direct transmission through the tin source holders as well as coherent scatter from the opposing source collimator, see figure 4.1. Therefore, it was necessary to shield the detector such that the 122 keV γ-rays detected could only result from coherent scatter in the sample, and two slabs of tungsten, 4 mm thick, were used for this purpose, shown in figure 4.1 as hatched areas. With these shields in place, it was observed experimentally that 98 to 100 % of the coherent scatter peak detected is attributable to interactions in the phantom/finger. The contribution from direct transmission and scatter from the sample holder was therefore considered to be insignificant and no further account of this was made in data analysis.

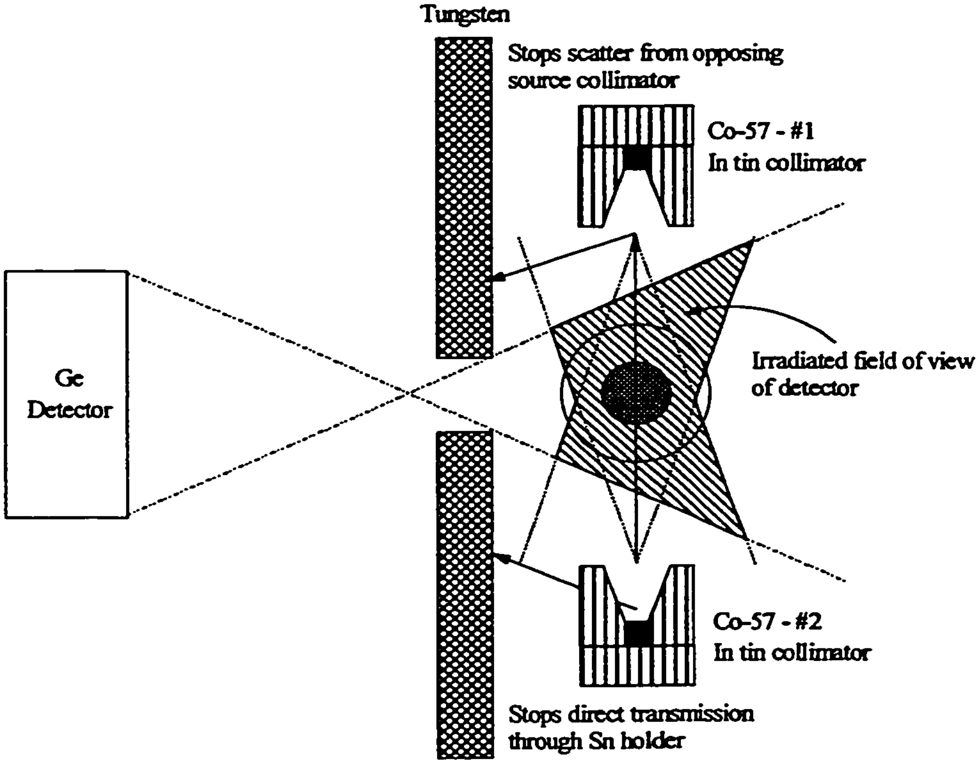

Figure 4.1: Irradiated field of view of the detector with the use of two tungsten slabs for shielding. These slabs, indicated by the hatched pattern in the figure, are necessary to reduce the direct transmission and scatter from the assembly of the 122 keV γ-rays from the source.

Each spectrum was acquired for 2 hours, with the detector at 7.5 cm from the phantom surface and the sources at 3.75 cm from the centre of the phantom, as shown in figure 4.1. Each phantom was measured three times. The detected spectra were then analysed with a non-linear least squares fit to determine the net counts of the lead K_{α_1} and K_{α_2} peaks as well as the coherent scatter peak area. The ratio of these areas was then investigated for variation with bone size or tissue thickness.

4.3 Results

Figures 4.2 and 4.3 demonstrate the x-ray to coherent ratios as functions of both bone radius and overlying tissue thickness as predicted by Monte Carlo simulations. Also plotted in these figures are the effects of bone size and tissue thickness on the absolute number of x-rays detected. It should be noted that both the x-ray to coherent ratio and the absolute number of x-rays detected have been normalised to a mean of unity such that these values can be plotted on the same scale; the resulting adjusted parameter is referred to as the Y value. It is evident from both figures that all of the x-ray to coherent ratios are within 5 % of the average ratio. Furthermore, it is clear from figure 4.2 that this coherent normalisation corrects for the observed increase of about a factor of 2 in the absolute number of x-rays detected per unit lead concentration with increasing bone size. However, figure 4.3 indicates that the absolute number of x-rays detected does not vary dramatically with increasing overlying soft tissue thickness. It is clear from these simulations that the absolute number of x-rays does not decrease significantly with increasing attenuating medium over this thickness range, which may be attributable to the relatively low attenuation coefficient for soft tissue for these energies, 0.17 to 0.18 cm^{-1} (Berger, 1987). Furthermore, as the tissue thickness increases, the solid angle subtended by the detector at the bone site changes due to the design of the experimental apparatus being modelled. This will also influence the absolute number of photons detected per unit lead concentration and per unit time. Since increasing overlying tissue thickness does not result in significant decreases to the absolute number of events detected, the coherent normalisation procedure does not result in a parameter with less variability than the absolute number of x-rays detected over these tissue thicknesses according to these simulations.

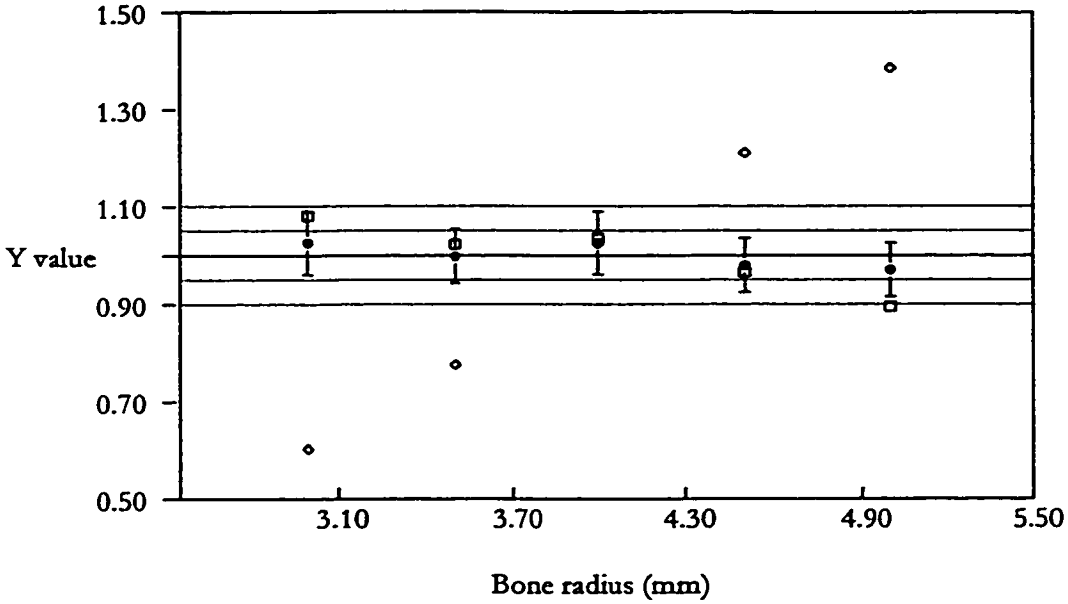

Figure 4.2: A plot of the x-ray to coherent ratio (Y) versus bone radius. The solid dots, ●, represent the ratio of $K_{\alpha 1}$ to coherent photons detected as predicted by the Monte Carlo simulation. For comparison, the absolute number of x-rays detected, diamonds, ◇, and the effect of normalising the absolute number of x-rays detected to the square of the bone diameter, open squares, □, are also plotted as a function of bone radius.

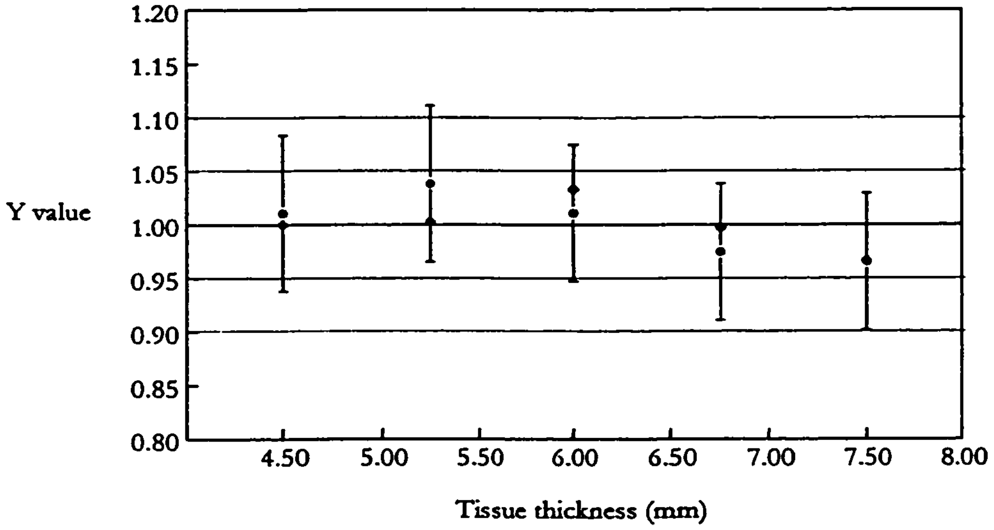

Figure 4.3: A plot of the x-ray to coherent ratio (Y) versus overlying tissue thickness based on Monte Carlo simulation. The symbols are as defined in figure 4.2.

Figures 4.4 and 4.5 illustrate the corresponding experimental data, plotted as the x-ray to coherent ratio as a function of bone size and overlying tissue thickness. Here the ratio plotted is the inverse variance weighted mean of three phantom measurements. It is clear that in both cases, only the extreme low end of the range of values tested results in a ratio that is greater than 5% from the mean, and the ratios observed at these extremes are both within 10 % of the mean, within uncertainty. At these extremes, the simulations predict that the ratios are within 5% of the mean. The discrepancy here is potentially attributable to a bias in the experimental geometry, as the smaller phantoms are difficult to align with the centre of the detector in the sample holder of this system. In general, the ratio should be insensitive to relatively small changes in alignment, however, the opening aperture of the tungsten shield, shown in figure 4.1, is quite narrow. For many of the phantoms, the alignment is not crucial, as the aperture is smaller than the bone diameter. However, for the smallest phantoms, the field of view of the detector contains some Perspex, as the phantom tends to sit low in the holder. This change in the composition of the field of view may result in the significant reduction in the x-ray to coherent ratio observed in figures 7.4 and 7.5. Therefore, the simulation findings for small bone radii and overlying tissue thicknesses may reflect the true behaviour of the ratio with these variables if the sample positioning were reproducible with all phantoms.

Figures 4.2 and 4.4 also demonstrate the effect of normalising the absolute number of x-rays detected to the square of the bone diameter, the current calibration procedure. It is clear that this method also corrects for the observed increase in the absolute number of x-rays detected with increasing bone size. However, based on the Monte Carlo data, the variability in the x-ray to diameter squared parameter is significantly larger than that of the x-ray to coherent ratio – having a standard deviation of 7% *versus* 2.5% respectively. The experimental data do not exhibit as dramatic a difference between the variability when normalising to the square of the diameter and when normalising with the coherent intensity – standard deviations of these experimental data are 7% and 8% respectively. This is likely attributable to the difficulties in reproducibly positioning small phantoms experimentally, as discussed above. However, it should be noted that the phantom bone diameters are known precisely and not measured with planar x-rays for these calculations. Therefore, any variance that may arise from measuring the diameter, as done *in vivo*, has not been included when comparing with the variance of the x-ray to coherent ratio.

It follows then that the x-ray to coherent ratio is within 5 to 10% of the mean over the entire range of bone radii and overlying tissue thicknesses tested experimentally and with simulations. This is an acceptable degree of variation to introduce to the measurement system, as this is significantly lower than the typical uncertainty of an individual *in vivo* XRF measurement. Furthermore, if the reproducible positioning of the sample could be improved for small objects, it is possible that this method results in a parameter that has less intrinsic variability than that introduced currently through corrections with the square of the bone diameter.

It should be noted that in both the experiments and the simulations it is apparent that the coherent normalisation procedure is somewhat unnecessary for correcting for variations with tissue thickness in the number of x-rays detected per unit lead concentration. It is clear from figures 4.3 and 4.5 that the observed absolute number of x-rays detected does not exhibit a clear trend with increasing tissue thickness, but rather fluctuates about an average value much like the x-ray to coherent ratio itself. However, the coherent normalisation procedure does reduce the variability in the number of x-rays detected for a fixed lead concentration over this range of tissue thicknesses based on the experimental data. The standard deviation of the absolute number of x-rays detected per unit lead concentration is 10% of the mean, whereas the standard deviation of the x-ray to coherent ratio is 6 % over the same range of tissue thicknesses. This reduction in the standard deviation may be attributable to the ratio correcting for various other factors in relating net counts to concentration, for example, slight changes in source-sample or source-detector geometry between experiments. This reduced variability suggests that using the x-ray to coherent ratio as the calibration parameter may result in reduced uncertainty in relating the net x-ray counting rate to concentration compared with a method that only corrects for bone size, as is the case currently.

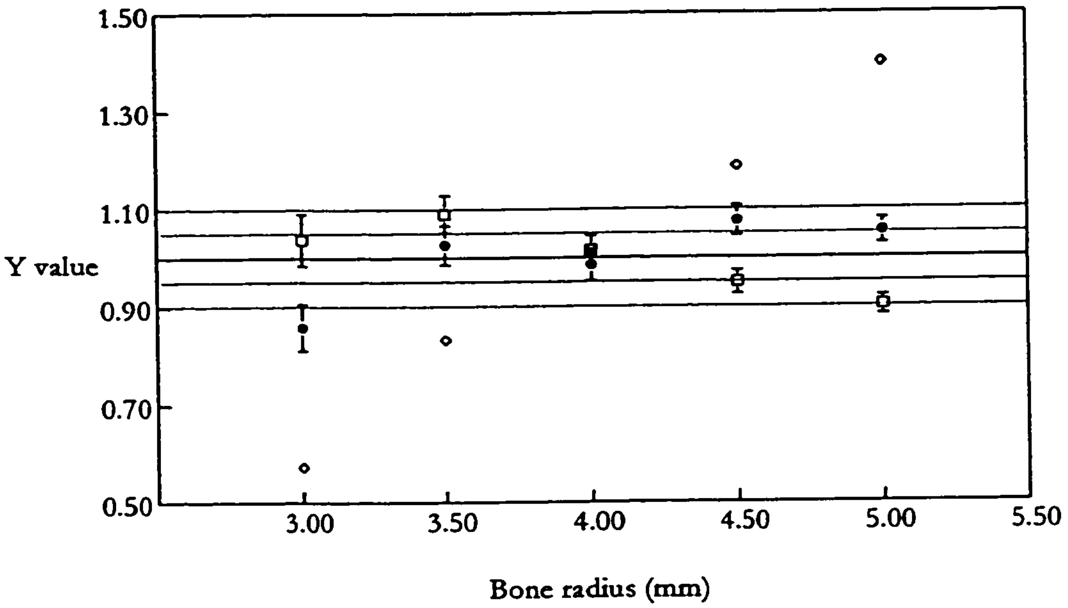

Figure 4.4: Experimentally measured x-ray to coherent ratio (Y) as a function of bone size. The symbols are as used in figures 4.2 and 4.3.

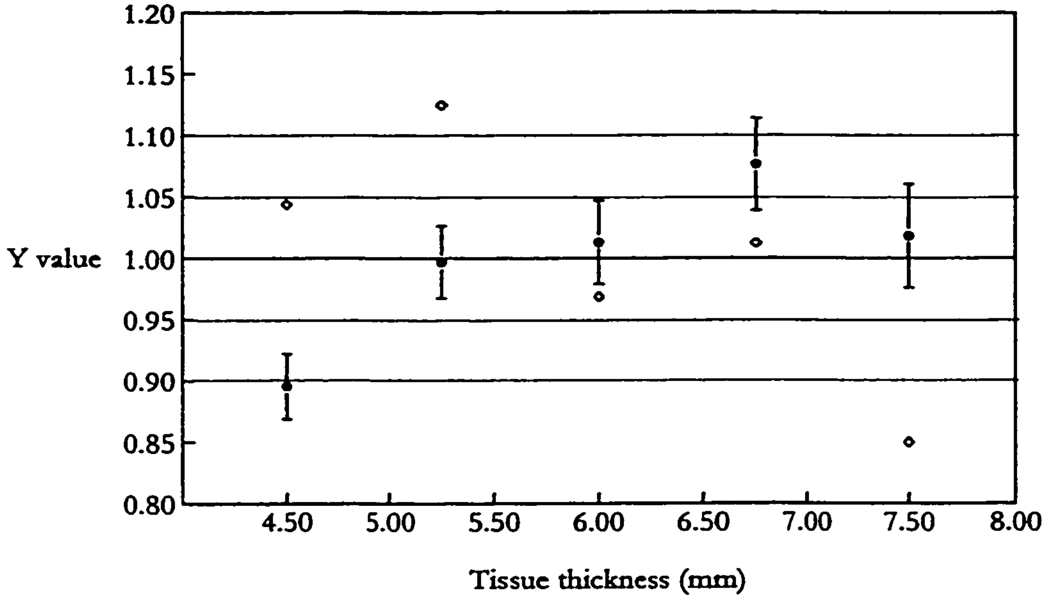

Figure 4.5: Experimentally measured x-ray to coherent ratios (Y) as a function of tissue thickness. The symbols are as used in figures 4.2, 4.3, and 4.4.

4.4 Clinical Implications

Based on Monte Carlo simulations and experiments, the absolute number of x-rays detected per unit concentration is a strong function of bone radius. However, these investigations demonstrate that the ratios of x-ray to coherent peak areas over an anatomically relevant range of bone radii are all within 5 to 10% of the mean ratio. Furthermore, this ratio has less variability with tissue thickness compared with the absolute number of x-rays detected, although this observation may arise from the ratio eliminating variations in x-rays detected due to slight changes in geometry between experiments. Therefore, both experiments and simulations indicate that the coherent normalisation procedure is feasible for correcting the observed net counting rate of lead x-rays in the ^{57}Co-based XRF *in vivo* measurements, to account for interpatient variations in bone size, and to some extent tissue thickness and variations in geometry. This eliminates the need for corrections based on the measured dimensions of the bone of each subject, which therefore avoids the acquisition of two planar images of the measurement site. This normalisation procedure thereby reduces subject dose and improves the transportability of the complete measurement system, as well as eliminates the subjectivity currently required in calculations based on these images.

Chapter 5

U INVESTIGATIONS

5.1 Motivation of study

In section 1.1, the motivation for developing non-invasive measurement systems to monitor occupational exposure to toxic elements was discussed in detail. Before this work, there had been no such system designed for monitoring uranium; typically workers exposed to this toxic metal are monitored with lung scans and urine samples. However, the complex metabolic pathway from uranium inhalation/ingestion to common sites of retention make accurate body burden assessment a difficult task. Therefore, this alone is more than sufficient motivation for assessing the feasibility of measuring uranium *in vivo* with XRF as a more accurate index of cumulative and target organ exposure than urine samples and lung scans, as discussed in detail in section 1.4 b).

However, a more immediate motivation was the initial impetus to this investigation. During the early months of 1991, the U.S. military was engaged in combat in the Persian Gulf, in Operation Desert Storm. At that time, a new anti-tank shell with a depleted uranium coat was used in military action for the first time. The depleted uranium encased shell had been proposed as an improvement to lead or stainless steel based shells, as the higher density of uranium results in greater range, truer flight, and greater penetrating power. In addition, the pyrophoric nature of uranium results in the shell igniting as it penetrates the tank wall, which leads to more effective elimination of personnel within the tank. The uranium shells proved to be most successful for the U.S. military in Operation Desert Storm, however, several U.S. tanks were inadvertently hit by these shells. While few personnel survived such "Friendly Fire" incidents, on the order of 35 soldiers returned from the Gulf with implanted shrapnel from such accidents that had not entirely been removed in field surgery. Veterans' Affairs was concerned for the health of these individuals, as it was possible that the remaining shrapnel contained uranium, which could pose a significant long-term health risk as a source of endogenous exposure to this toxic element. It was in the interest of the health of these soldiers to investigate the feasibility of XRF monitoring in trying to answer two key questions: do these fragments contain measurable quantities of uranium, and, if so, is this uranium being metabolised and therefore giving rise to a significant source of endogenous exposure?

Preliminary monitoring of this cohort suggested that the answer to these questions is yes – among these soldiers there were significant elevations of uranium in the urine, above that of the general population, for several years after Operation Desert Storm. This suggests that there is indeed ongoing exposure, which is likely attributable to uranium-containing fragments not removed in field surgery. In addition, one subject underwent a second surgical procedure, and it was observed that the urinary uranium levels decreased significantly after several metallic fragments were removed (unpublished). Therefore, it was deemed worthwhile to investigate the sensitivity of XRF measurements of uranium in bone for both occupational monitoring and for the particular application of monitoring survivors of "Friendly Fire" incidents, as a means to understand the biokinetics better, as well as to assess cumulative exposure. Furthermore, collaborators at Veterans' Affairs were interested in the application of XRF to the determination of the quantity of uranium in localised fragments, as all imaging modalities are merely able to locate metallic/dense fragments without providing any elemental assessment. XRF measurements to determine the concentration of uranium accumulating in the skeleton as well as to assess fragment composition would provide valuable information for developing strategies for treating these individuals, as well as any future cases that may arise with the continued use of these shells in combat.

5.2 Source-excited XRF

5.2.1 System description

In section 2.1.1 b), design considerations for source-excited *in vivo* XRF measurements of uranium were discussed. It was determined that the use of ^{57}Co in a backscatter geometry would result in the best signal to noise ratio in the energy region of the characteristic x-rays in the detected spectrum. Therefore, the experimental set-up was employed as shown in figure 5.1. A hyperpure germanium detector was used, 50.5 mm in diameter, 20 mm thick with a resolution of 700 eV at 122 keV for a pulse shaping time of 1 μs (Canberra, 1991). A 1 mCi ^{57}Co source was mounted coaxially in front. The detector was shielded from direct emission by a tungsten source holder with walls 5 mm thick, a bore length of 3.8 mm and an opening diameter of 6.75 mm. The detector output was passed through fast nuclear electronics and, because of high count rates, pulse pile up rejection was utilised to reduce background. The detector output was first passed through a pre-amp and was then relayed to the amplifier and ADC. The ADC output was sent to the MCA which allowed the spectrum to be displayed on the computer monitor as discussed in section 2.2.

The spectra were saved for further analysis. The samples were measured at a fixed distance from the source and irradiated for a fixed preset live time.

The degree of collimation of the beam at the sample is an additional factor in the sensitivity of the system. In order to maximise sensitivity, collimation and source-sample distance were selected such that the volume irradiated coincides with the volume viewed by the detector. This ensures minimal dose to the subject as well as reduces the energy range of the detected Compton scattered photons.

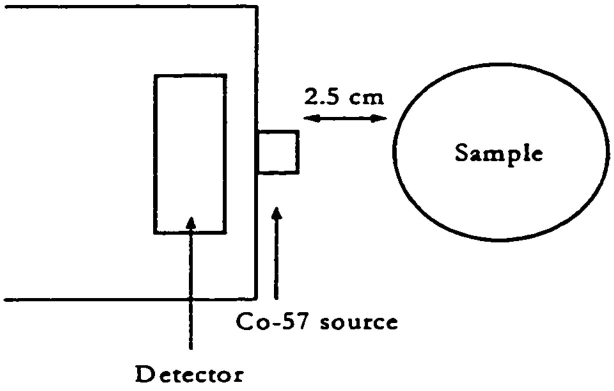

Figure 5.1: Experimental set-up of the ^{57}Co system for the *in vivo* measurement of uranium.

5.2.2 Legitimacy of normalisation in bone-U measurements

As discussed in the preceding chapter, the ^{109}Cd bone-Pb measurement system uses a method of normalisation to eliminate confounding factors when relating characteristic x-ray count rate to target element concentration present. This normalisation greatly simplifies the system, as information from the detected spectrum itself is used to correct the x-ray count rate for such factors as overlying soft tissue thickness and bone size. It was necessary to investigate the legitimacy of using this normalisation procedure with the ^{57}Co bone-U measurement system.

Recall that the legitimacy of normalisation requires the satisfaction of four criteria: the x-rays and coherent signal must be produced (i) by the same incident fluence, (ii) in the same location in the sample, and (iii) with the same angular distribution. Furthermore, (iv) the two signals must be attenuated in the sample in a similar fashion. With ^{57}Co, the primary photon energy is 122 keV, and at this energy the differential cross section for coherent scatter in the backward direction is approximately 40 times larger in cortical bone than in soft tissue. Therefore, the detected coherent intensity is primarily due to incident γ-rays interacting with bone, rather than soft tissue. However, this incident photon energy is 6.5 keV above the K edge of uranium. Based on equation 2.1, Compton scatter through less than 40° results in γ-rays with sufficient energy to excite uranium x-rays. Since the coherent scatter feature in the detected spectrum arises from uncollided photons only, this energy difference implies that the x-ray and coherent intensities detected are no longer necessarily arising from the same incident fluence. Furthermore, although the x-rays and coherent scattered photons are generated from the same location in the sample with similar angular distributions, the difference in energies (94 to 114 keV for the U x-rays compared with 122 keV for the coherent scattered photons) may result in differences in attenuation. Since all four criteria are not satisfied, it is not immediately clear that normalisation can be used with ^{57}Co-based U measurements in bone. Monte Carlo simulations were necessary to assess the validity of applying this normalisation to the uranium system.

As before, simulations were run for the uranium system with various values of overlying soft tissue thickness and bone size to assess the variation of the x-ray to coherent ratio. Figures 5.2 and 5.3 demonstrate these results. The error bars are based on setting uncertainties as the square root of counts detected in the Monte Carlo output. As is evident in figures 5.2 and 5.3, the ratio of the Kα_1 x-rays detected to the 122 keV coherent γ-rays detected remains constant for a wide range of overlying soft tissue and bone thickness. This indicates that the normalisation procedure is legitimate in the measurement of bone uranium using ^{57}Co in a backscatter geometry, eliminating the numerous geometric factors affecting the conversion of intensity of x-ray peaks to metal concentration.

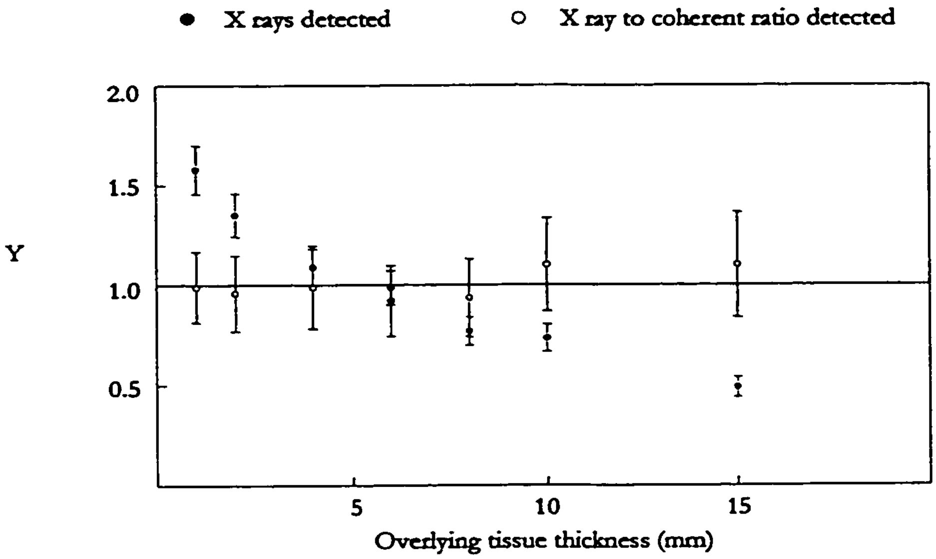

Figure 5.2: Monte Carlo output investigating the effect of overlying soft tissue on the Kα_1 to coherent ratio detected. The variable Y is the total number of x-rays detected (solid circles) or the x-ray to coherent ratio detected (open circles) normalised to a mean of unity.

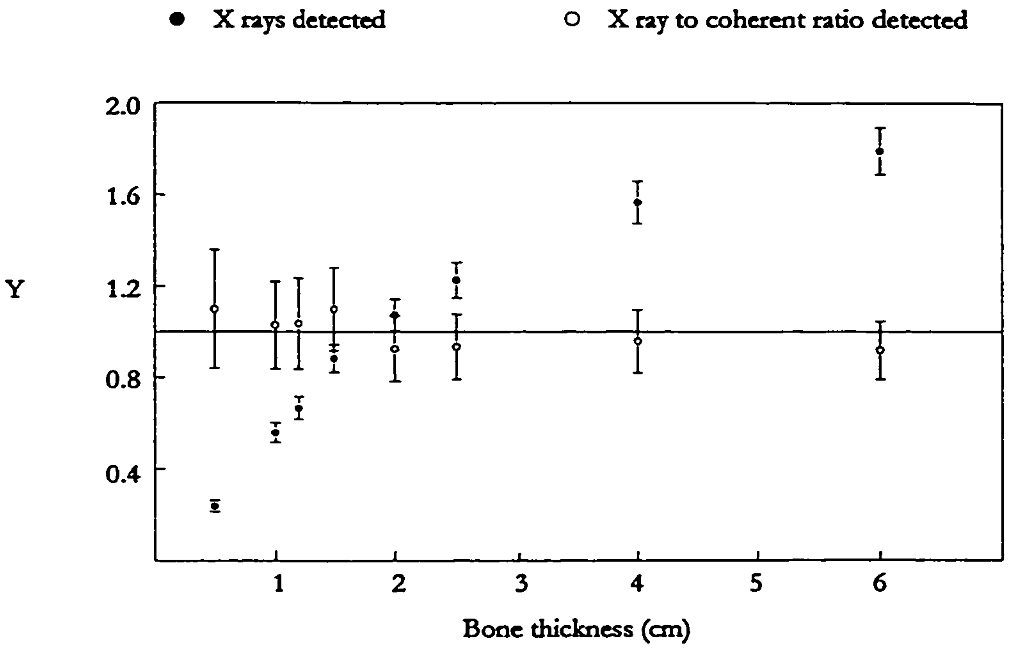

Figure 5.3: X-ray to coherent ratio detected as a function of bone thickness. Symbols and variables are as defined in figure 5.2.

The legitimacy of normalising the x-rays to the coherent peak is possibly an unexpected result. With a difference of 6.5 keV between the K edge of uranium and the incident photons of the ^{57}Co source, a large fraction of Compton scatter events can still allow for subsequent x-ray production. Therefore, since coherent scatter arises from uncollided photons only, the x-ray and coherent intensities detected are no longer due to the same incident flux. More explicitly, as the overlying soft tissue depth increases, the uncollided photon flux at the bone decreases, which results in a corresponding decrease in the coherent scatter events occurring with these γ-rays. At the same time, the Compton flux at the bone is increasing, which somewhat counters the decrease in x-ray production due to the attenuation of the uncollided beam. It is therefore expected that the ratio of the x-ray intensity to coherent intensity would increase with increasing overlying soft tissue. However, as the coherent photons and x-rays travel back to the detector, the lower energy x-rays have a higher probability for attenuation in the overlying tissue. In this respect, the differential attenuation of the 122 keV coherently scattered γ rays and the lower energy x-rays is such that it tends to counter the expected increase in x-ray to coherent ratio with increasing overlying tissue. Hence, although the major criterion for legitimate normalisation is that the x-rays and coherently scattered photons arise from the same photon flux, there are sufficient countering influences in this system that the ratio of x-ray to coherent intensities for a given concentration remains constant for a wide range of geometries.

5.2.3 Phantom measurements of bone-U concentrations

Six uranium doped plaster of Paris phantoms were prepared, ranging in concentration from 0 to 100 ppm. Each phantom was measured three times in random orientations to assess the uniformity of the uranium concentration. The spectra, see figure 2.4, were then analysed for x-ray and coherent peak intensities. Each spectrum was divided into four regions, alphas (1 and 2), from 92.8 to 102.6 keV, beta 1 and 3, from 108.4 to 113.5 keV, beta 2' and 2", from 112.7 to 116.1 keV, and the coherent region, from 120 to 124 keV. The first three regions were fit with a double exponential background to model the high energy tails of the two Compton peaks, and two Gaussians with linked amplitudes and positions. The coherent region, sufficiently separated in energy from the Compton peaks, was modelled with only one exponential background term and one Gaussian for the coherent peak. The non-linear least squares Marquardt method (in Bevington 1969) was applied to each region of each spectrum and the ratios of the intensities of $K\alpha_1$, $K\beta_1$, and $K\beta_2$ to the coherent intensity were plotted against uranium concentration, see figure 5.4.

Table 5.1 contains the results of regression analysis of these calibration lines.

X-ray/coherent	Slope +/- σ(slope) [ppm^{-1}]	Intercept +/- σ(intercept)	r value
$K\alpha_1$/coherent	0.0142 +/- 0.0004	0.01 +/- 0.05	1
$K\beta_1$/coherent	0.0031 +/- 0.0001	0.003 +/- 0.02	0.98
$K\beta_2$/coherent	0.0008 +/- 0.0002	-0.002 +/- 0.03	0.73

Table 5.1: Summary of regression analysis of 3 calibration lines for the uranium bone system.

The minimum detectable limit (MDL) based on each x-ray calibration line can then be calculated as:

$$\text{MDL} = 2^*(\sigma(\text{intensity for concentration} \Rightarrow 0))/\text{slope} \qquad [5.1]$$

This is a common definition of lower limit of detection, set as the concentration that gives rise to an x-ray peak intensity (normalised to the coherent) that is twice the standard deviation in that measured concentration, in the limit of low uranium concentration. With the slopes listed above and the uncertainties in the x-ray to coherent ratios for the blank phantom spectra, this gives a combined MDL of 4 ppm in plaster of Paris phantoms.

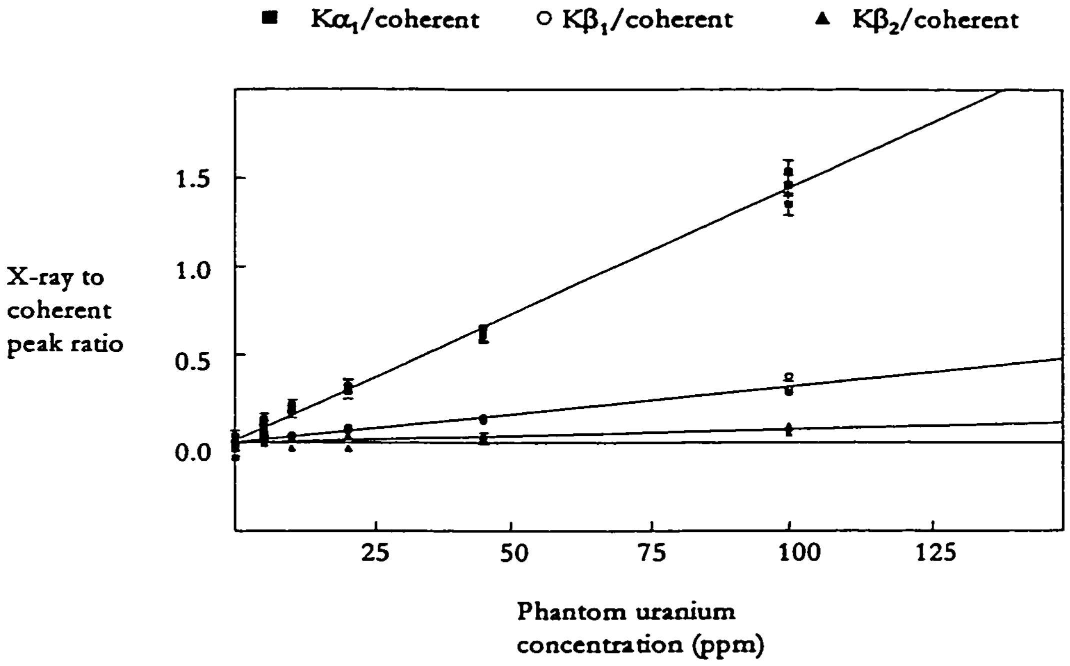

Figure 5.4: Calibration lines established with the uranium plaster of Paris phantoms. The slope and intercept of each line can then be used to determine uranium concentration from a measured x-ray to coherent ratio *in vivo*.

5.2.4 In vivo measurements of bone-U concentrations

Once the detection limit has been established in plaster of Paris phantoms, it is necessary to assess the sensitivity of the system *in vivo*. Preliminary studies involving the measurement of non-occupationally exposed volunteers were conducted. The subject was seated with the source positioned 2.5 cm from the skin surface, at a height corresponding to the middle of the tibia. The leg was secured at the base of the knee and at the ankle to discourage movement during the measurement. The spectrum was acquired for 45 minutes (live time) and then analysed with the non-linear routine designed for the phantom spectra. The x-ray to coherent ratios were determined and converted to a corresponding x-ray to coherent ratio in plaster of Paris, a correction necessary due to the difference between bone mineral and plaster in differential coherent cross section in the backward direction. The corrected ratios were then used with the calibration lines to determine the corresponding concentrations. Each subject then had a mean concentration calculated that is an inverse variance weighted mean of the three concentrations derived from the three separate x-ray ratios and calibration lines. Figure 5.5 demonstrates the results of the mean concentrations of 10 subjects, male and female, ranging in age from 22 to 49 years, 9 with no known occupational exposure to uranium, and one with 10 years experience working with uranium in a university setting.

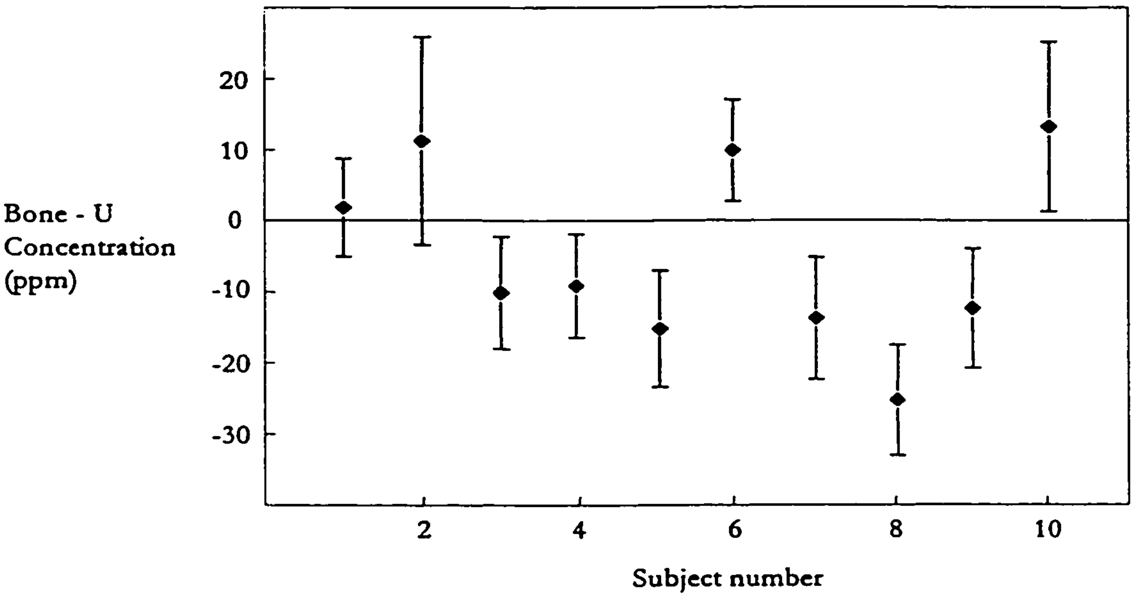

Figure 5.5: *In vivo* measurement results. Mean uranium concentrations are determined as the inverse variance weighted mean of concentrations calculated using the calibration lines shown in figure 5.4.

The average concentration of these volunteers is -4.0 μg U/g bone mineral with a standard deviation of 13 μg U/g bone mineral. The average uncertainty of the mean concentration for this group is approximately 9 μg U/g bone mineral. This is a useful measure of the precision of the *in vivo* system and suggests that the minimum detectable limit is on the order of 20 μg U/g bone mineral for this system. These investigations, both phantom and *in vivo*, have been reported in detail elsewhere, O'Meara *et al.*, 1997.

5.2.5 Phantom measurements of U shrapnel

A specially designed phantom was built for this work, in order to simulate the deposition of uranium fragments in soft tissue in various geometries. The phantom material was constructed from tissue-equivalent plastic cast into six circular sections, each approximately 40 mm thick, having a diameter of 150 mm. The elemental composition of this material, commercially manufactured by The Phantom Laboratory, Salem, New York, is listed in table 5.2, and is designed to simulate the photon interaction properties of soft tissue at these energies. Compared to actual tissue, this material has less oxygen and more carbon; the resulting deficit in atomic number is compensated by the minor quantity of antimony.

Element	**Percentage by weight**
Carbon	67.78
Oxygen	20.31
Hydrogen	9.18
Nitrogen	2.50
Antimony	0.22
Effective atomic number	7.6
Electron density	3.2781×10^{23} e/g
Physical density	0.997 g/cm^3

Table 5.2: Properties of Rando®, tissue-equivalent plastic used in simulating soft tissue for the investigation of XRF measurements of uranium fragments.

The sections are fastened by a bone phantom, cylindrical in shape, that can be thread through the tissue sections at the centre or at a position that is 55 mm offset from the centre, as shown in figure 5.6 a). This is to allow for the simulation of limbs with either central or offset bone location, *i.e.* a femur or a tibia. Each section has a specific distribution of drilled channels into which tissue equivalent Rando® plastic plugs can be placed, figures 5.6 b), c), and d). These plugs were used to position the uranium pellets manufactured for this project, ranging in mass from 8 to 60 mg. Figure 5.6 shows a schematic of these tissue-equivalent phantom sections.

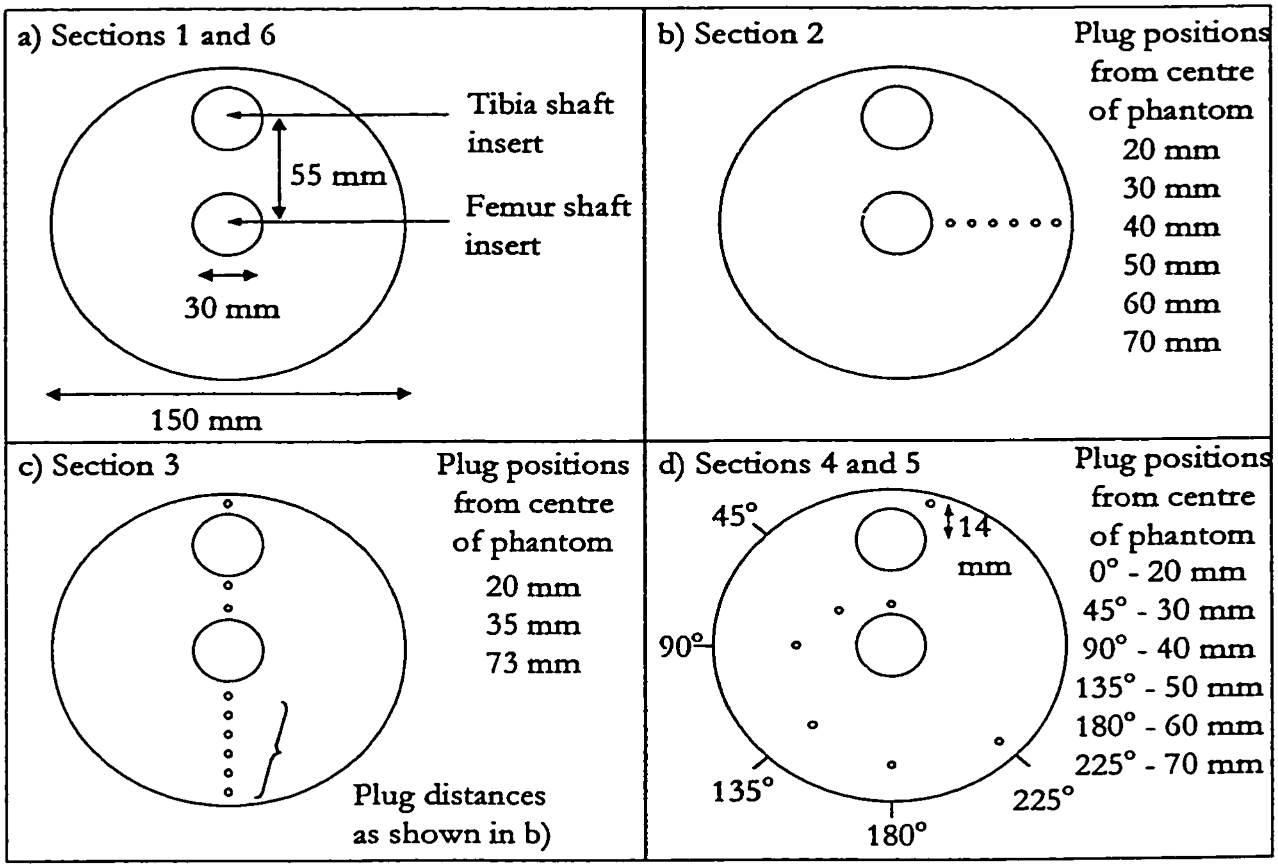

Figure 5.6: Schematic of the six tissue-equivalent sections used to simulate uranium fragment deposition in limbs.

The phantom was then irradiated with the system described in section 5.2.1, and the spectra were analysed to determine the intensity of x-rays detected in a one hour period.

Note that these x-ray intensities are not normalised to the corresponding coherent scatter intensity, as the coherent scatter peak detected will largely arise from any bone tissue present in the sample and not the uranium fragment itself. Figure 5.7 illustrates the results of the measurement of x-ray intensity for two pellets, 32.5 and 62.5 mg respectively, positioned from 5 to 55 mm beneath the surface of the phantom, in the plug locations shown in figure 5.6 c). It is apparent that there is a rapid decrease in the signal intensity as the overlying tissue thickness increases. It is also apparent that the fragments are observable with as much as 3 to 4 cm of overlying tissue masking the signal. Therefore, XRF is a feasible method of qualitatively assessing whether or not fragments contain uranium, provided the shrapnel is within 3 to 4 cm of the surface, with a measurement time on the order of 1 hour.

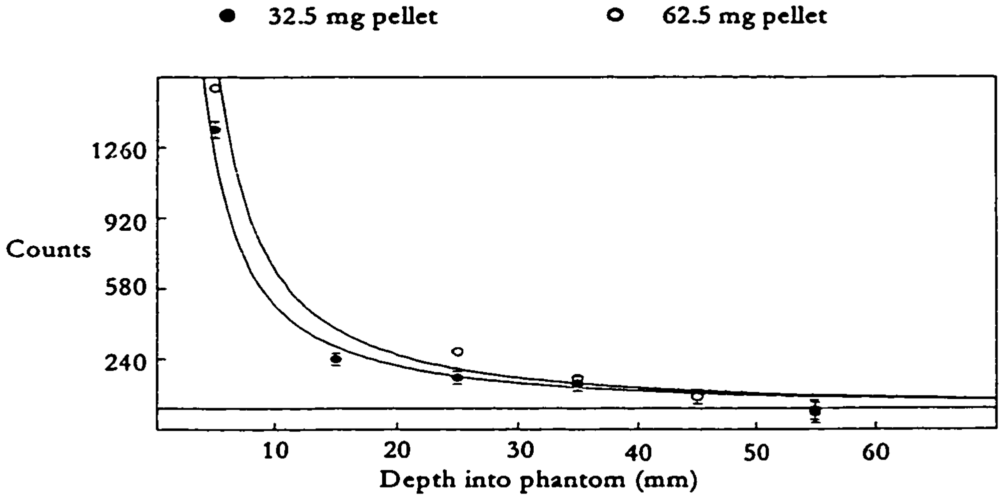

Figure 5.7: X-ray intensity from uranium fragments as a function of depth in section 3 shown in figure 5.6. Note that the large difference in uranium mass does not result in a correspondingly large difference in the x-ray intensity at any depth.

However, figure 5.7 also illustrates an important observation. The x-ray intensity observed does not appear to have a strong relationship with the mass of the fragment. It is believed that this is due to self-attenuation; the larger fragment does not result in a proportionally larger number of x-rays observed because the increase in size associated with this increase in mass results in more x-rays being attenuated before leaving the surface. It has been suggested that the number of x-rays detected is more likely to depend on the actual mass per unit surface area of the fragment. Because there is no clear relationship between x-ray intensity and fragment mass, there is no straightforward manner of calibration to allow XRF to assess quantitatively the amount of uranium identified in the subcutaneous fragment.

5.2.6 In vivo measurements of U shrapnel

Measurements were conducted of one "Friendly Fire" subject in September, 1996. This subject was known to have no fragments in the right lower leg, while the left lower leg was known to have contained numerous metallic fragments, based on radiographs. Bone-U measurements were conducted in the right tibia and calcaneus, and two measurements were made on the left tibia, at two locations separated by 5 cm vertically. Three of these four measurements resulted in concentrations that were not above the detection limit. However, the fourth measurement, one of the assessments of the left tibia, resulted in an equivalent concentration of 86 ± 14 ppm. Figure 5.8 shows the detected spectrum from this first ever reported *in vivo* measurement of uranium with XRF. This non-zero equivalent bone concentration is likely due to signal arising from a uranium-containing fragment within the soft tissue region above the tibia site under investigation. This seems the most reasonable source of the signal, as the other three measurements of bone concentration were not significantly different from zero, including a measurement of the same bone only a few centimetres below the site in question. Furthermore, there was some scar tissue on the surface of the skin at this location, and the left leg was known to have contained shrapnel from the Gulf War injuries. Additional attempts to identify uranium fragments in this subject did not indicate any presence of this metal, however, these investigations were limited by time and the choice of location within the left leg based on the subject's memory only (radiographs were unavailable at the time of the study). These investigations of uranium shrapnel with XRF have been reported elsewhere in detail, O'Meara *et al.*, 1998c.

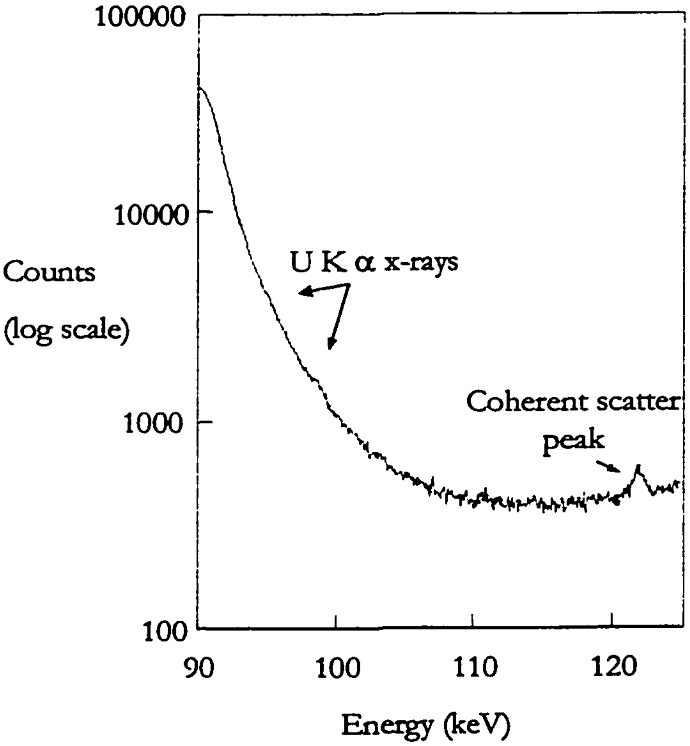

Figure 5.8: First ever reported *in vivo* U XRF measurement. The spectrum shown here was detected from one of the "Friendly Fire" subjects known to have metallic shrapnel implanted due to Operation Desert Storm, and known to have an endogenous source of uranium exposure based on urine monitoring.

5.2.7 Dosimetry

Due to the marked similarities with the bone lead system, an estimate of the effective dose can be made by correcting the lead system dose for γ-ray energy and source intensity. The effective dose from a typical lead exam has been accurately determined to be 35 nSv in a half hour measurement (Todd *et al.*, 1992). Todd *et al.* used a 2.2 GBq ^{109}Cd source, compared to the 37 MBq ^{57}Co source used here; so the photon fluence rate was 2.2 times higher for the lead system, allowing for the different branching ratios of the photons emitted by these sources. However, because of the different photon energies, the lead system energy fluence rate is only 1.6 times higher than that for uranium. Also, a larger fraction of the lower energy photons, used for the lead measurement, is absorbed, the ratio of mass energy absorption coefficients being 1.17. Lastly, these bone uranium measurements take 45 minutes compared to the 30 minutes used for bone lead. Combining these factors leads to an effective dose of 30 ± 5 nSv for a bone uranium assessment.

5.2.8 Clinical implications

a) Bone-U measurements

Studies of uranium levels in bone measured from autopsy samples of both occupational and non-occupational groups (Wrenn *et al.* 1985, Leggett 1994, Dang *et al.* 1995) indicate that typical levels are in the sub-μg U/g bone ash and ng U/g bone ash ranges respectively. Non-occupational groups from 20 studies worldwide range in bone uranium concentrations from 0.8 to 20 ng U/g bone ash, with a mean value of 8 ng U/g bone ash, whereas the occupationally exposed subjects (sample size of 8 workers) ranged in concentration from 0.05 to 1.8 μg U/g bone ash (note: bone ash and bone mineral are effectively equivalent).

Based on these few data from uranium workers, it is difficult to conclude whether this system is sufficiently precise for use in monitoring occupationally exposed individuals. The indication, however, is that the typical concentration in both non-exposed subjects and uranium workers is well beyond the current capabilities of this system, having a minimum detectable limit on the order of 20 μg/g. It is even more difficult to conclude whether this system is sufficiently precise for the particular application of measuring bone uranium concentrations arising from "Friendly Fire" incidents during Operation Desert Storm, as very little is known about the kinetics of subcutaneous uranium fragments. However, although the observed urinary excretion levels in this group are significantly higher than typical levels for the general population, based on the kinetic models described in section 1.2 b), it is unlikely that their bone uranium concentrations will exceed the higher end of the range of values observed in occupational workers for several years. These estimated concentrations have been supported by the preliminary measurements of one of the members of the "Friendly Fire" cohort, as three measurements of bone uranium resulted in concentrations that were not above the detection limit. Therefore, it seems that the expected concentrations in both uranium workers and this unique group of exposed individuals are currently beyond the capabilities of this system. Future avenues for improving system sensitivity will be discussed in detail in chapter 7.

b) U shrapnel measurements

Initial measurements with a member of this "Friendly Fire" cohort serve to summarise the clinical capabilities of the XRF system in assessing subcutaneous shrapnel. Three measurements were made attempting to identify uranium in subcutaneous fragments.

Of these three measurements, only one resulted in a measurable quantity of uranium being detected. It was concluded that this non-zero measurement was in fact the localisation of a uranium-containing fragment. This first measurement of a member of the cohort illustrates that XRF is capable of qualitatively identifying the presence or absence of uranium in subcutaneous fragments. However, based on phantom work, because there is no clear relationship between x-ray intensity and fragment mass, there is no straight forward manner of calibration to allow XRF to assess the amount of uranium identified in the subcutaneous fragment quantitatively. Future work may involve assessing the extent to which calibration is feasible for determining an effective mass per unit surface area based on x-ray intensity and an estimate of fragment depth.

5.3 Polarised XRF

As discussed in chapter 2, the use of polarised photons has been successfully implemented as a means of improving the XRF *in vivo* detection limit of some heavy metals. Therefore, polarised XRF was investigated as a means of improving the sensitivity achieved with the ^{57}Co-based U system described in section 5.2. From discussions in section 2.1.2, it is clear that there are a number of design parameters that must be optimised when considering polarised x-ray fluorescence measurements. For example, the energy distribution of the polarised beam is critical in terms of the ability to excite characteristic x-rays from the target element. The energy of this beam can be altered through selecting the operating voltage of the x-ray tube, the polariser material and thickness, as well as through the use of filters in the primary or secondary beam. As with source-based x-ray fluorescence, the ideal energy of the incident beam is just greater than the K edge of the target element and is such that the Compton distribution is well separated from the energy region of the detected characteristic x-rays. However, due to the requirement that the detector be positioned along the direction of initial polarisation to minimise scatter, the source-sample-detector angle can no longer be varied to achieve maximum Compton and x-ray separation. Nevertheless, there are sufficient parameters that can be varied to optimise the secondary beam energy distribution, and hence the Compton scatter energy distribution detected at 90°. Of course, at the same time as optimising the secondary beam energy distribution, the degree of polarisation of the beam must also be considered, as this is influenced by the various parameters listed above. The best precision can be achieved by careful consideration of the trade-offs necessary for maximal secondary beam intensity and polarisation, as well as the optimal energy distribution. The main design parameters to consider, a) tube voltage and current, b) polariser material, thickness and collimation, and c) filtration, will be addressed separately below.

5.3.1 System description

a) Tube voltage and current

With a K edge energy of 115.6 keV, the system design for uranium necessarily requires a relatively high energy photon distribution for optimal x-ray excitation. Throughout these studies, the x-ray tube used as the source of such photons is a Phillips RT 250 (III) Depth Therapy Generator. As the name implies, this system is designed for cancer therapy treatments, and has fixed voltage settings of 75 kV, 125 kV, 175 kV and 250 kV. These voltages can be run with a maximum cathode current of 20 mA for all voltages except 250 kV, at which the tube can be operated at a maximum of 15 mA. Since this system is no longer being used for its designed purpose, some modifications were necessary. The main change was the addition of shielding. When x-ray tubes are used in therapy, tube housing is built such that the leakage radiation at 1 meter from the target does not exceed 1 R (1 Roentgen – equivalent to 260 μC/kg, a measure of the exposure/dose associated with this radiation) in one hour when operated at maximum current and voltage (Cember, 1992). In therapy, this is an acceptable additional exposure to the patient, given that therapy sessions are typically only on the order of several minutes and the subject is exposed to considerably higher dose at the site of treatment. However, the dose associated with such leakage radiation is not acceptable for our purposes, and would give rise to photon fluence rates incident on the detector that could cause significant count rate problems.

A conservative estimate was made of the photon fluence rate associated with an exposure rate of 260 μC/kg per hour at 1 m from the target with the tube operating at 250 kV. From this estimate, it was determined that several orders of magnitude reduction in fluence would be required in order to yield acceptable subject dose for a typical measurement, as well as to shield the detector from excessive fluence not arising from the subject. In order to achieve this reduction, 4 cm of lead were required as leakage shielding. With this quantity of shielding, the subject would receive on the order of 1×10^{-15} C/kg in a one hour measurement from leakage radiation, which is considerably lower than the limit of 3 μC/kg in a one week period for general public exposure, the limit used when conventional shielding of x-ray units is considered. In addition, 4 cm of lead is expected to reduce the leakage photon fluence rate incident on the detector to 1 photon per hour.

A lead box was constructed to surround the x-ray tube used in this study. It was deemed worthwhile to enclose the polariser with the x-ray tube in this shielding box, to eliminate the possibility of scattered photons from the polariser, not directed toward the subject, giving rise to further unnecessary dose and count rate problems. In order to make the design flexible, the box was divided into two sections, the upper chamber containing the x-ray tube and the lower chamber containing the polariser. The two chambers are separated by a lead shelf that is 4 cm thick, and a copper collimator, 10 cm long with an inner diameter of 2 cm and an outer diameter of 10 cm penetrates through this shelf to direct the tube output onto the polariser below. The particular choice of collimator length and aperture will be discussed in greater detail in section 5.3.1 b). Figure 5.9 demonstrates the tube, polariser and lead box design schematically. Each chamber has a portal-style aperture on each side to allow limited access to the tube for minor maintenance, and complete access to the lower chamber to allow the polariser to be changed and filters to be inserted in the primary beam. Pertinent dimensions are shown in figure 5.9.

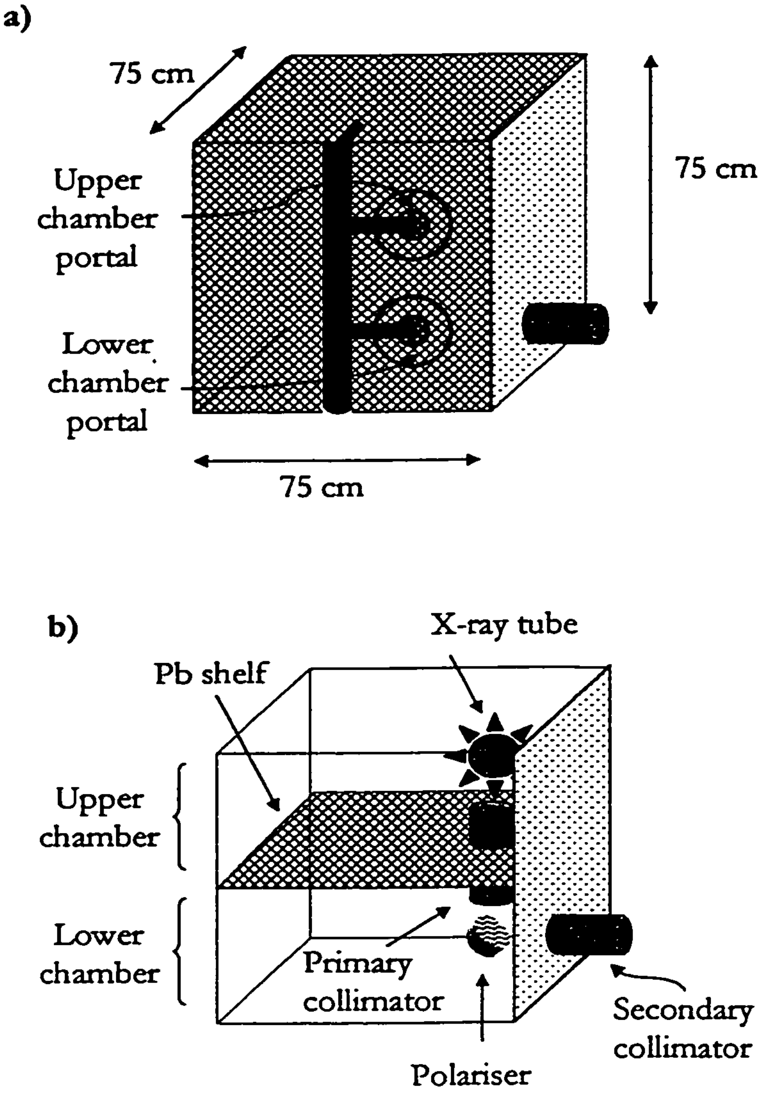

Figure 5.9: Schematic diagram of lead box. Figure 5.9 a) shows the pertinent dimensions and the upper and lower access portals on one side of the box. Figure 5.9 b) shows the arrangement inside the box, illustrating the relative orientation of the x-ray tube, collimators and polariser.

With these modifications made, the system was ready for testing. The first parameters to consider are the tube voltage and current at which to operate. The current is a straightforward parameter to optimise, as this variable influences the intensity of the photon beam emitted by the x-ray tube. Typically, the system is run with the current at its maximum to ensure maximal tube output. If this photon rate is too intense for the detector and electronics or gives rise to an unacceptable subject dose, it is preferable to filter the beam, rather than decrease the current. Filtration is the superior approach as it preferentially reduces the low energy photons that do not give rise to characteristic x-rays, whereas decreasing the current reduces the intensity at all photon energies equally. Therefore, this system was operated at ~20 mA for all tube voltages except 250 kV, at which voltage the tube was operated at ~15 mA.

The tube voltage is also a straightforward choice when designing a system to measure uranium. Because of the high K edge of this element, it is necessary to operate the tube at its highest voltage possible, in this case 250 kV, in order to generate a significant number of photons with sufficient energy to excite uranium atoms in the sample. From figures 3.4 and 3.5, it is clear that the majority of photons emitted by the x-ray tube are considerably lower in energy than the maximal tube output based on the voltage across the anode and cathode. Furthermore, the beam is scattered through 90° before irradiating the sample, thereby reducing the overall energy based on equation 2.1. Therefore, a tube voltage setting of 250 kV is the preferred choice, as even a setting of 175 kV will result in relatively few photons with sufficient energy to excite uranium. 75 kV is clearly not expected to give rise to any uranium K x-rays, and the spectrum generated at 125 kV, scattered through 90°, is also not particularly useful. In addition to having a higher energy photon distribution, the higher voltage setting also results in an overall increase in total tube output. As discussed with respect to the tube current, it is better to run with the highest possible tube output and filter if necessary to reduce dose and detector count rate in order to achieve the best sensitivity.

b) Polariser material, thickness, and collimation

With the tube voltage set at 250 kV, and the current close to 15 mA, the next parameters to consider involve the polarisation stage of the system. The ideal polariser material is one in which Compton scatter is the predominant interaction to ensure the highest yield per incident fluence rate. Therefore, low Z materials are often used (for example, aluminium polarisers reported by Christoffersson and Mattsson, 1983, Börjesson *et al.*, 1995), as these polariser materials result in fewer photons lost in photoelectric interactions. It has also been proposed, however, that higher Z materials, for example copper, would be the better choice. Such higher Z materials would scatter considerably fewer low energy photons, thereby yielding a more useful incident energy distribution (Lewis, 1994). Therefore, polariser material was investigated with Monte Carlo simulation to compare total yield, energy distribution, and degree of polarisation achieved with B_4C, aluminium, copper, and tin.

From these simulations, it was clear that B_4C and aluminium result in the highest yield per incident fluence, but copper results in a photon energy distribution characterised by the highest mean energy. Copper also gives rise to the highest degree of polarisation, as this higher Z material has a reduced probability of multiple scatter events, although the polarisation differences are not substantial. Overall, tin is a poor choice, as its significant photoelectric cross section results in characteristic x-rays being a substantial component of the spectrum, thereby reducing the mean photon energy incident on the sample and decreasing the polarisation. Figures 5.10, 5.11, and 5.12 summarise the simulation findings, plotted as total photon yield, polarisation, and mean spectral energy *versus* atomic number respectively.

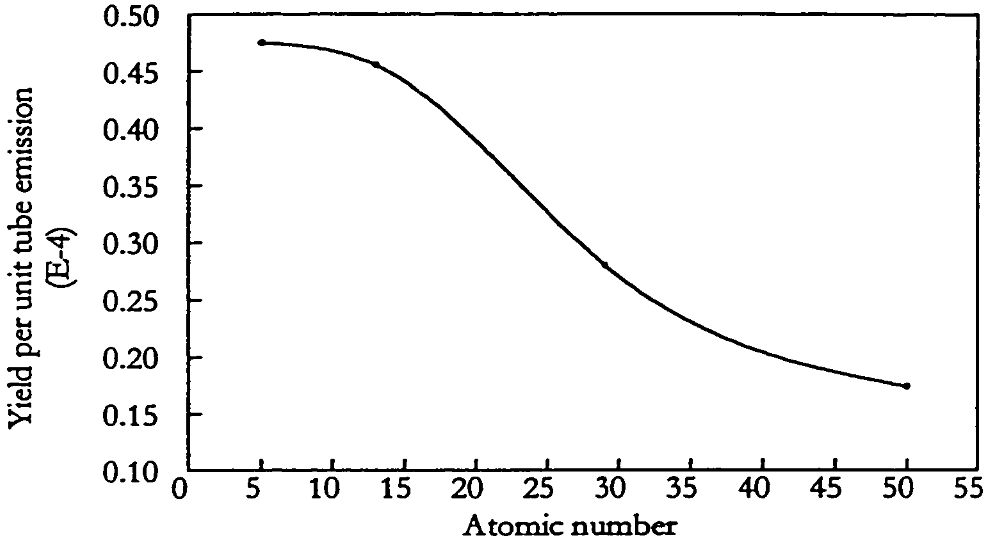

Figure 5.10: Total photon yield per unit tube emission as a function of the atomic number of the polariser. All polarisers were simulated with the same g/cm² thickness.

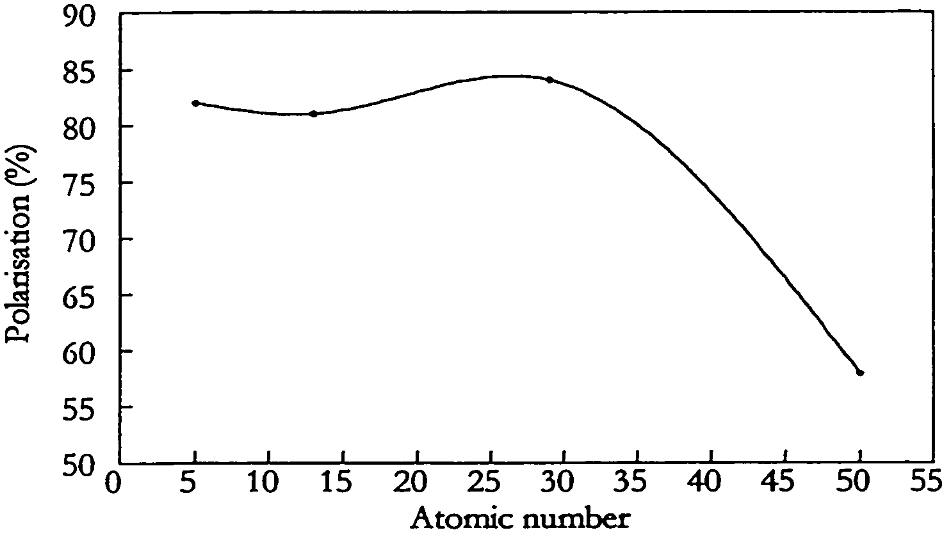

Figure 5.11: Degree of polarisation as a function of atomic number of the polariser. All polarisers were simulated with the same g/cm² thickness.

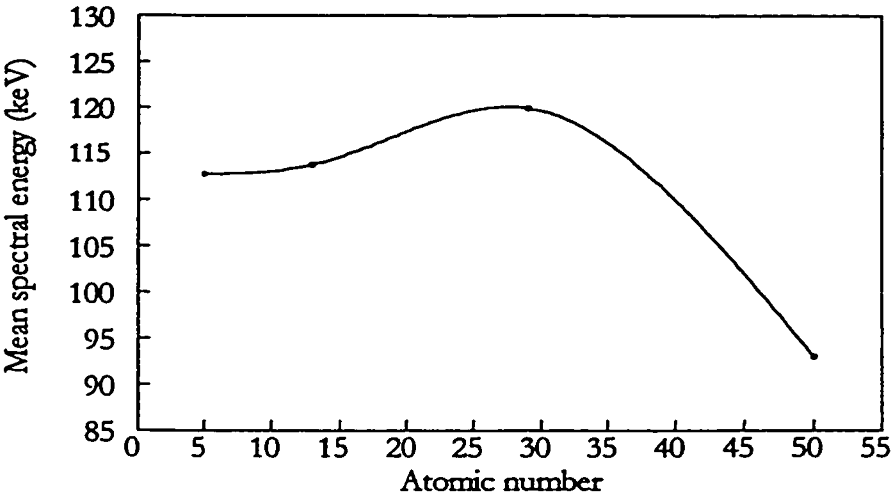

Figure 5.12: Mean spectral energy as a function of atomic number of the polariser. All polarisers were simulated with the same g/cm^2 thickness.

Based on these simulations, it was decided that the first design would use an aluminium polariser. Although copper results in a higher energy photon spectrum incident on the sample, and a slightly higher degree of polarisation, the larger photon yield from aluminium is preferable. As discussed for optimising the tube current, it was deemed worthwhile to use the polariser material associated with the greatest yield. This ensures that the absolute greatest number of photons are incident on the sample, thereby giving rise to the greatest characteristic x-ray signal generated. If this arrangement results in an unacceptable subject dose, or excessively high count rates in the detector/electronics, then filtration can be optimised to tailor the photon energy distribution. Since there was little difference between aluminium and B_4C, aluminium was chosen simply as it was readily available. One might argue that increasing the thickness of copper used in these comparisons would give rise to similar yields as those obtained with aluminium and B_4C, thereby indicating that an increased thickness of copper would be the best choice. However, as will be discussed below, increasing the thickness results in a decrease in polarisation, such that for a similar photon yield the polarisation could be worse. Future polarised systems at McMaster may well investigate the effects of replacing the aluminium with a copper polariser.

As discussed in section 2.1.2, the polariser solid angle and thickness must be selected as a compromise between polarisation and beam intensity. Again, Monte Carlo simulation is a powerful tool for assessing the optimal values for these parameters. In the case of the polariser solid angle, however, the design chosen is based on preceding polarised XRF systems.

The use of a 20 cm long, 2 cm inner diameter copper collimator was adopted based on the specifications given for the cadmium, platinum, gold and mercury systems, originally designed by Christoffersson *et al.*, 1983, Jonson *et al.*, 1988, and Börjesson *et al.*, 1995. Ideally, the optimal design should be selected based on the minimum detectable limit as a function of aperture angle. As the angle increases, it is expected that the total photon fluence incident on the sample will increase, however, the degree of polarisation will decrease. Such simulations were not investigated *a priori*, as the accuracy of the simulations could not be tested with experiment until the preliminary system was built. Therefore, the aperture angle used in previous systems was adopted. In future developments of this system, the aperture angle may be investigated as a means of improving the system sensitivity, now that the Monte Carlo simulations have been demonstrated to reflect accurately the corresponding experimental data (see chapter 3). Nevertheless, the logistics of changing this aperture angle are not trivial given the design of the shielding box.

With the selection of tube voltage, current, polariser material, and aperture angle, the optimal thickness of the polariser was then investigated with Monte Carlo. As with the aperture angle, there is an inherent trade-off between count rate and polarisation when considering the best thickness to use. As shown in figure 5.13, as the thickness is increased, the increase in incident fluence results in an increase in uranium signal detected. However, as the aluminium thickness increases, the probability of multiple scatter events increases. This results in a decrease in polarisation, which is reflected by an increasing background under the uranium x-rays in the detected spectrum, demonstrated in figure 5.13. Since the sensitivity is inversely proportional to the square root of the background and directly proportional to the signal, figure 5.14 shows the behaviour of the ratio of these variables with increasing thickness. It is clear that there is little change in this ratio over the range of thicknesses simulated. However, the 1 cm aluminium polariser gives rise to the highest sensitivity overall. Therefore, a 1 cm aluminium polariser was used in all subsequent optimisation simulations, as well as the final experimental arrangement.

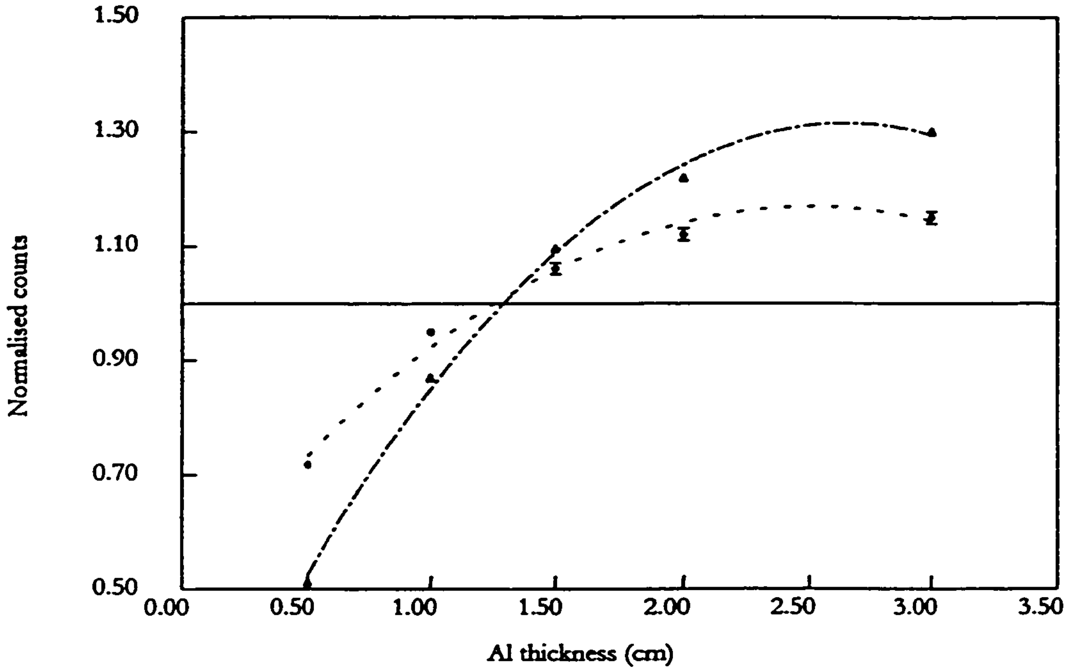

Figure 5.13: Increase in signal (solid dots) and background (open triangles) with increasing polariser thickness. Note that the values have been normalised to a mean of unity in order to display both signal and background changes on the same scale.

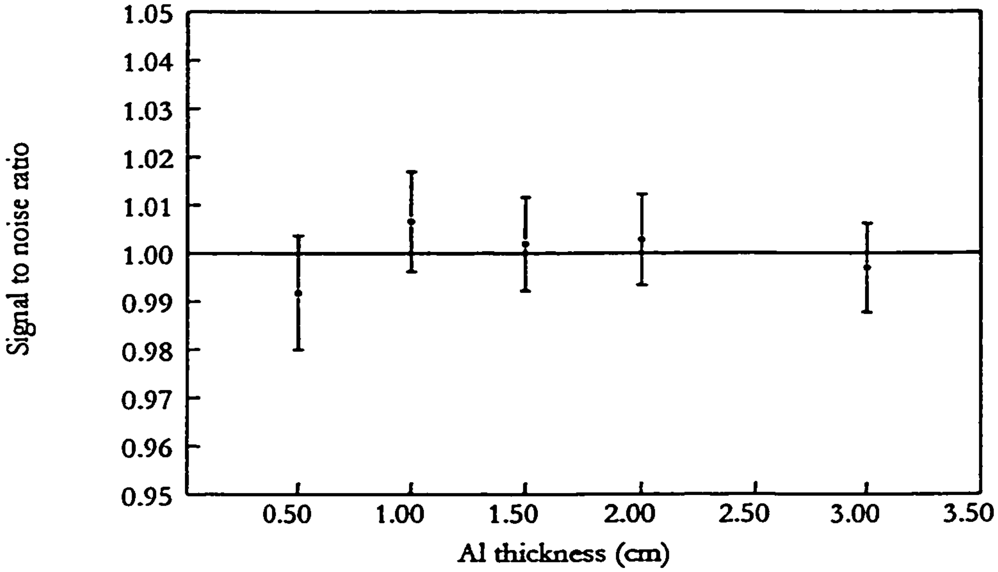

Figure 5.14: Sensitivity (signal to square root of background) as a function of aluminium thickness. It is clear that there is not much effect overall, however, the 1 cm thick polariser gives rise to the best sensitivity.

c) Filtration

Filtration is a means of optimising the energy distribution incident on the sample. Through filtration, the dose to the subject can be reduced with minimal loss in sensitivity, as filters will preferentially remove the low energy photons that do not contribute to characteristic x-ray production. However, regardless of the filter material used, simulations and experiment showed that there is some loss in sensitivity when the beam is filtered. This phenomenon can be understood by a simple analytical examination of the effects of filtration on the intensity of characteristic x-rays and background in the detected spectrum.

The characteristic x-rays are produced by photons with energy greater than 115.6 keV. In addition, the background under the characteristic x-rays is generated by the photons from the polariser in the energy range between 115 and 130 keV. Therefore, it is worth considering the relative effect of filtration on the incident spectrum in two energy regions. If filtration can reduce the photons in the 115 to 130 keV range while a significant number of photons greater than 130 keV remain in the spectrum, it is conceivable then that sensitivity could be improved by decreasing the background more than the corresponding loss in signal. So, consider a simplified model in which the signal is generated by two incident intensities, I_1 and I_2, corresponding to photons between 115 and 130 keV, and 130+ keV. Similarly, the background is generated by I_1 only. This can be represented as:

$$s_1 = k_1 \cdot I_1 + k_2 \cdot I_2 \qquad [5.2]$$

$$b_1 = c \cdot I_1 \qquad [5.3]$$

where s_1 is the x-ray signal generated, b_1 is the background produced, and k_1, k_2, and c are proportionality constants. When filtration is applied before the sample, I_1 and I_2 are reduced, however, as the attenuation coefficients are energy dependent, the fractions by which these terms decrease differ. The filtered signal and background can be written as:

$$s_2 = k_1 \cdot I_1 \cdot \exp(-\mu_1 \cdot x) + k_2 \cdot I_2 \cdot \exp(-\mu_2 \cdot x) \qquad [5.4]$$

$$b_2 = c \cdot I_1 \cdot \exp(-\mu_1 \cdot x) \qquad [5.5]$$

where μ_1 is the attenuation coefficient for the 115 keV to 130 keV energy range, μ_2 is the corresponding value for energies greater than 130 keV, and x is the thickness of filter used.

As discussed previously, the detection limit is proportional to the square root of the background, and inversely proportional to the signal. Therefore:

$$MDL_1 = A \cdot \frac{\sqrt{b_1}}{s_1} \qquad [5.6]$$

And $$MDL_2 = A \cdot \frac{\sqrt{b_2}}{s_2} \qquad [5.7]$$

In order for filtration to result in improved sensitivity, MDL_2 must be less than MDL_1. Or:

$$\frac{\sqrt{b_2}}{s_2} < \frac{\sqrt{b_1}}{s_1} \qquad [5.8]$$

Substituting equations 5.2 to 5.5 into equation 5.8, this can be re-written as:

$$\frac{c \cdot I_1 \cdot \exp(-\mu_1 \cdot x)}{\left(k_1 \cdot I_1 \cdot \exp(-\mu_1 \cdot x) + k_2 \cdot I_2 \cdot \exp(-\mu_2 \cdot x)\right)^2} < \frac{c \cdot I_1}{\left(k_1 \cdot I_1 + k_2 \cdot I_2\right)^2} \qquad [5.9]$$

With some rearranging and further simplifying, the filter thickness x required for the sensitivity to be improved by filtration will only be positive when μ_1 is greater than twice the value of μ_2. Table 5.3 summarises the attenuation coefficients of a number of possible filter materials at 122 keV, to represent the 115 to 130 keV range, and 145 keV, to represent the 130+ keV range.

Element	μ_1 [cm^{-1}]	μ_2 [cm^{-1}]	μ_1/μ_2
Al	0.41	0.38	1.1
Cu	2.8	2.1	1.3
Sn	7.4	4.8	1.5
Pb	38.	25.	1.5
U	81.	53.	1.5

Table 5.3: Attenuation coefficients for various possible filter materials at two photon energies. The ratio of these two values, in the last column, needs to be greater than 2 in order to result in an increase in sensitivity with filtration.

Based on table 5.3, and this simplified assessment of the effects on signal and background when filtering the incident beam, it is clear that conventional filtration is not expected to result in an improved sensitivity for the uranium polarised system. As mentioned above, this has also been observed with simulations and experiments.

When considering the use of these systems for *in vivo* measurements, filtration may be required to reduce the dose to an acceptable level. However, for the purposes of assessing the performance of this system relative to the source-excited measurements reported in section 5.2, the detection limit was investigated with no filtration as the best possible system set-up based on simulations, experiments, and the simplified analytical calculations summarised here.

5.3.2 Phantom measurements

With the tube voltage at 250 kV, a current of 13 mA, an aluminium polariser 1 cm thick, a secondary collimator with a 0.05 radian aperture, and no added filtration, the system was ready for sensitivity testing. In order to compare sensitivity to that achieved with the ^{57}Co-based source-excited system, the same uranium doped plaster of Paris phantoms were irradiated. Spectra from these phantoms, ranging in concentration from 0 to 100 ppm, were acquired for 1 hour (live time) each. The spectra, see figure 5.15, were then analysed for x-ray peak intensities. From figure 5.15, it is clear that the beta peaks are not evident, even for the 100 ppm phantom. It is also clear that there is no coherent scatter peak evident, as the incident photons used with the polarised system are not monoenergetic, unlike the source-excited based system. Therefore, the spectra were divided into two regions only for analysis, the α_1, from 95.9 to 102.2 keV, and the α_2 region, from 89.6 to 95.9 keV.

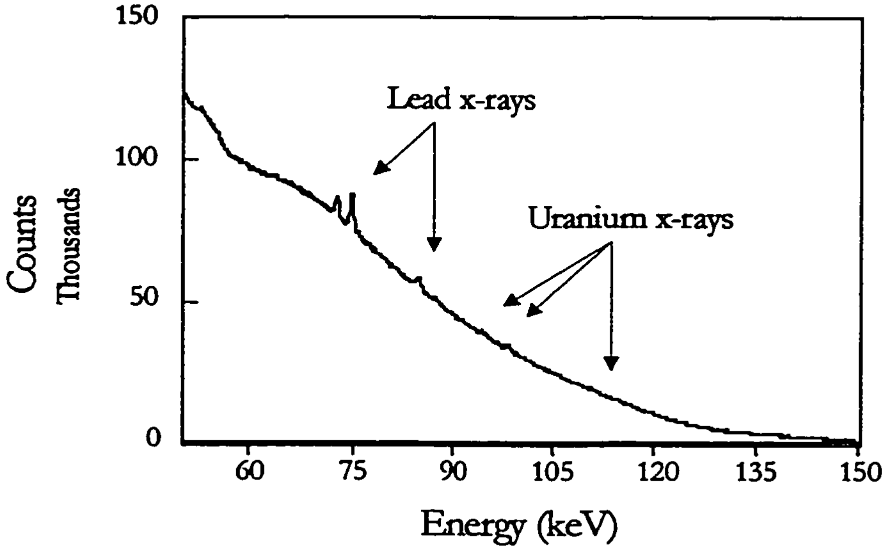

Figure 5.15: Spectrum detected during a one hour (live time) measurement of the 100 ppm uranium-doped plaster of Paris phantom using the polarised system described in section 5.3.1. Note the obvious presence of lead peaks; these arise from photon interactions with the lead shielding around the tube and polariser.

Both alpha regions were fit with a straight line background and one Gaussian of variable amplitude and centroid position. The α_1 and α_2 intensities were plotted against concentration; table 5.4 contains the results of regression analysis of these calibration lines. It should be noted that the x-ray intensities can no longer be normalised to the coherent intensity to eliminate various confounding factors, as the photon source is polyenergetic.

X-ray	Slope ± σ(slope) [counts/ppm]	Intercept ± σ(intercept) [counts]	r^2 value
Kα_1	14.2 ± 2.1	105 ± 157	0.96
Kα_2	10.1 ± 1.1	47 ± 79	0.98

Table 5.4: Summary of regression analysis of 2 calibration lines for the polarised uranium bone system.

As before, the minimum detectable limit (MDL) based on each x-ray calibration line can then be calculated using equation 5.1. With the slopes listed above and the uncertainties in the x-ray intensities for the blank phantom spectra, this gives a combined MDL of 9 ± 1 ppm, for a one hour live time measurement, with the polarised system described above. In order to compare this with the source-excited system, the combined MDL's should not be directly compared, as this term includes contributions from both α and β peaks for the source-excited value, and contributions from the α_1 and α_2 peaks only for the polarised value. Therefore, a fair comparison is the MDL achieved from the α x-rays only. The MDL from the source-excited α features, in a one hour live time measurement, is 4.2 ± 0.1 ppm, while the corresponding value for the polarised system is 9 ± 1 ppm, as stated above.

5.3.3 Dosimetry

In order further to compare source-excited and polarised-based XRF measurements of uranium, preliminary dose measurements were made with the polarised system. For this purpose, a set of 30 Panasonic UD-806 AS personnel dosimeters was used, along with the associated reader. Each dosimeter is comprised of 4 elements arranged in a line, with 0.85 cm between the centres of adjacent elements. These $Li_2B_4O_7$ thermoluminescent dosimeters were used since the response of these badges as a function of photon energy (relative to ^{60}Co) has been well characterised prior to this work. Therefore, by calibrating each dosimeter with a known exposure from ^{60}Co, the exposure from the polarised system can be determined based on the energy distribution of the incident spectrum.

Several preliminary dosimeter readings were done to assess the variability of background accumulation in a fixed time period. When stored between measurements, the dosimeters can accumulate significant background readings due to continuous exposure to background radiation. In order to determine accurately the exposure due to the irradiation procedure, it is necessary to ensure that the background exposure is reasonably constant over a given time period so that comparisons between readings from the irradiation and calibration are made fairly. From these preliminary investigations, 10 dosimeters were rejected, as the background accumulation varied to an unacceptable degree.

First, the dosimeters were read in order to clear residual background exposure. These dosimeters were then irradiated for 1 hour with a calibrated ^{60}Co source. They were then left for 28 hours, at which point each element was read again. The calibration exposure for each element, y, was then corrected for the background accumulation exposure over a 29 hour period, y', based on the preliminary investigations. Before irradiation with the polarised system, each element was again cleared by the reader. The dosimeters were then arranged on the surface of a tissue-equivalent phantom and irradiated for 5 hours. They were then left for 24 hours, at which point each element was read again. The irradiation exposure for each element, x, was then corrected for the background accumulation exposure over a 29 hour period, x', as before.

Knowing the exposure rate associated with the ^{60}Co source, X_{Co}, the exposure of each element due to the polarised system X_{pol} is then given as:

$$X_{pol} = X_{Co} * \frac{x'}{y'} \qquad [5.10]$$

In order to determine X_{pol} accurately, X_{Co} must be known. Therefore, the exposure rate of the ^{60}Co source was measured with a 600 cc ionisation chamber, calibrated at the ^{60}Co photon energy. The source strength was measured five times over the course of two days, at a distance of 132.6 cm from the source to ensure both field uniformity and the validity of the $1/r^2$ field dependence, with the chamber arranged in a low scatter configuration. Each measurement was corrected for atmospheric pressure and temperature since the chamber contains vented air, and therefore the volume of irradiated gas depends on these variables. Based on these measurements, it was determined that the ^{60}Co has a source strength of 86.2 mR/hr at 30 cm from the source, the distance used in the dosimeter calibration procedure. The uncertainty on this value is on the order of 5% based on the uncertainties cited by the National Research Council, Canada (Ottawa, ON), when the chamber was originally calibrated.

With the source strength known, X_{Co} is given and the expression above can be used to determine the exposure due to the irradiation with the polarised system, X_{pol}. However, this X_{pol} is the effective exposure associated with a ^{60}Co source, and does not account for the energy dependence of the elements. The energy response of these elements, relative to ^{60}Co, has been well documented (Heinmiller, 1988), and these data were used to correct the effective exposure to the true exposure recorded from the polarised system irradiation. These data were fit to a polynomial as a function of energy, and this polynomial was then used with the Monte Carlo generated incident energy spectrum as the weighting function to generate a weighted mean relative response of these elements. In addition, the true exposures must then be converted to absorbed dose, through the standard expression relating air exposure, *X*, and dose to a material m, D_m, given as:

$$D_m = 34 \cdot \frac{\left(\mu/\rho\right)_m}{\left(\mu/\rho\right)_{air}} \cdot X \qquad [5.11]$$

where $(\mu/\rho)_m$ and $(\mu/\rho)_{air}$ are the mass energy absorption coefficients of the two media. These mass energy absorption coefficients are also a function of photon energy, so the weighted average ratio of these coefficients was used to convert exposure to dose. This weighted average ratio is also calculated using the normalised Monte Carlo generated spectrum of incident photon energies as the probability density function of the weighting values.

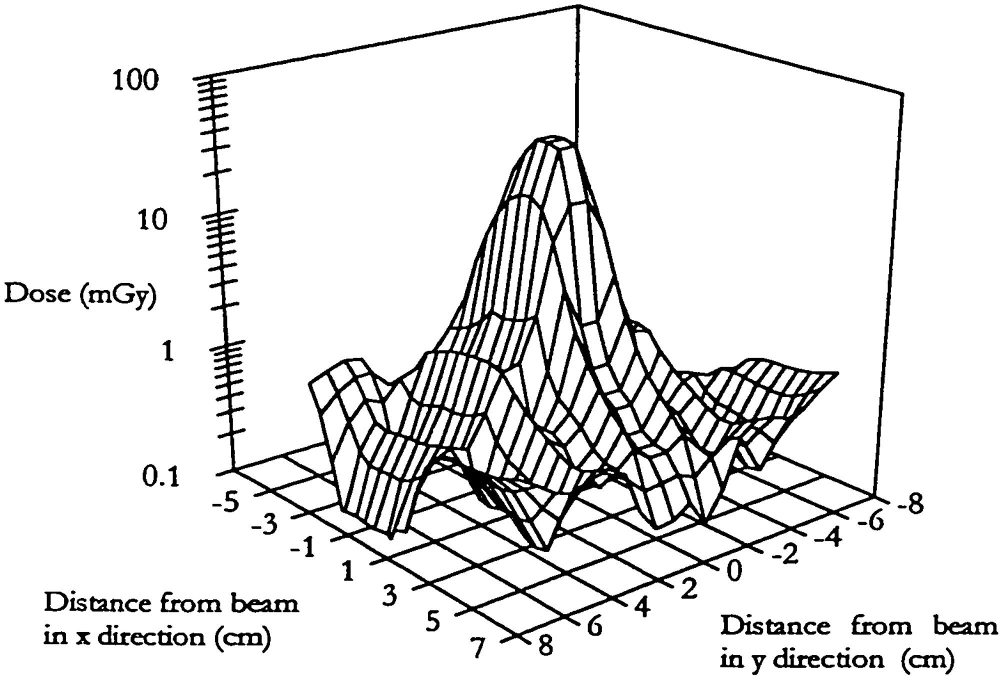

Figure 5.16: Mesh plot of the dose distribution on the surface of the tissue-equivalent phantom. These doses were measured with the Panasonic UD-806 TLD's as described above, for a 5 hour period.

Figure 5.16 shows the dose distribution of the surface of the phantom for a 5 hour irradiation period. Note the log scale used to indicate absorbed skin dose on the z axis in figure 5.16. It is clear that the beam is well collimated, as the dose decreases rapidly away from the centre of the beam; for example, the dose is 50% of its maximum 1.3 cm from the centre, 3% of the maximum at 2 cm from the centre, and a mere 1.6% of the maximum at 3 cm from the centre of the beam.

In order to quantify the total dose delivered to the skin due to this measurement, the dose distribution, as a function of radial distance *r* from the beam centre, was fit empirically to the expression:

$$Dose = a_0 + \frac{a_1}{1+\left(\frac{r}{a_2}\right)^{a_3}} + a_4 * r \qquad [5.12]$$

Figure 5.17 demonstrates the agreement between the experimentally measured dose as a function of radial distance and the best fit to equation 5.12. This expression could then be integrated over the irradiated area to determine the average skin dose delivered. For an area described by a 3 cm radius circle, the average skin dose in a 1 hour period is on the order of 3 mSv.

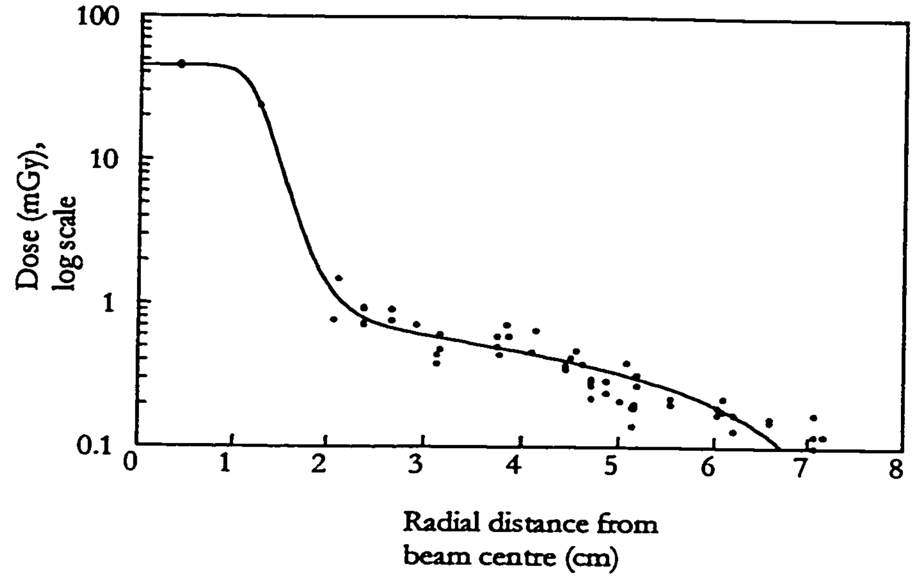

Figure 5.17: Comparison of data and fit to equation 5.12. The data are shown as solid circles, while the fit is represented by the straight line. Note that the y axis is a log scale, and that the dose has not been divided by the irradiation time (5 hours).

For comparison with the source-excited skin dose, the dosimetry assessment of the ^{109}Cd Pb measurement system, by Todd *et al.*, 1992, can again be used as a guide. As argued in section 5.2.7, the skin dose measured for the ^{109}Cd/Pb system can be scaled to a corresponding value for the ^{57}Co/U system based on relative source activities and accounting for the different photon energies. Todd *et al.* measured a skin dose of 220 μSv in a half hour measurement for the ^{109}Cd/Pb system. Therefore, the skin dose associated with the ^{57}Co uranium measurement is on the order of 250 ± 40 μSv for a one hour measurement. It is evident that the skin dose associated with the polarised system is significantly higher than that of the source-excited XRF measurement of uranium.

5.3.4 Clinical Implications

In addition to giving rise to a significantly larger skin dose, the polarised system clearly does not have an improved sensitivity compared with the source-excited based system. Furthermore, adding filtration to reduce the polarised dose is expected to result in an even lower sensitivity than that achieved with ^{57}Co. It is worthwhile investigating the details of this comparison in order to determine the cause of this somewhat unexpected result. The two factors influencing the MDL are signal strength and the square root of the background in the spectral region of concern. These parameters are compared in table 5.5.

	Signal strength per unit concentration	Background	$\text{Signal}/\sqrt{\text{Background}}$
Source-excited	1.3×10^4	3×10^5	23
Polarised	1.8×10^4	3×10^6	10

Table 5.5: A comparison of the performance of source-excited based and polarised based XRF measurements of uranium in bone.

From table 5.5, the source-excited and polarised systems have similar uranium signal generated per unit concentration, with the polarised system resulting in a slightly favourable measurement. However, the background under the α_1 region of the spectrum is a full order of magnitude larger in the polarised system. Initially, this may seem somewhat surprising, as polarised photons are used as a means of reducing the Compton scatter into the detector. The difference mainly arises from the relative geometries used. The polarised system is constrained to a 90° geometry to make use of the reduced scatter, however, this results in a non-ideal position of the Compton distribution relative to the uranium x-rays. Although there is reduced scatter detected with polarised relative to non-polarised photons, the source-excited system results in a better sensitivity. This arises from the better spectral separation between the peak in the scatter distribution and the uranium x-rays achieved with the 180° backscatter geometry in the source-excited system. Furthermore, the monoenergetic γ-rays emitted by the ^{57}Co source give a much narrower energy distribution of scatter, which, coupled with the backscatter geometry, allows for the uranium x-rays to be positioned in a region of relatively low background. Even if the scatter geometry was a variable to optimise with the polarised system, increasing the scatter angle would result in a relatively small reduction in the background due to the broad energy distribution of scatter from this polyenergetic source.

Given that the skin dose is an order of magnitude larger than the source-excited system, and the sensitivity is more than a factor of 2 worse, the clinical prospects are currently not promising for uranium bone assessments with polarised XRF. As discussed in section 5.2.8, the detection limit must be reduced considerably in order to be able to measure levels expected in either occupational workers or survivors of "Friendly Fire" incidents. Future improvements may be achieved through the use of a higher energy tube voltage, as this would provide a greater number of photons above the K edge of uranium, and an overall increase in tube output, as discussed in section 5.3.1 a). With optimal filtration, this increase in voltage may lead to a polarised detection limit that is less than that achieved with the ^{57}Co system. Other means for future improvements in sensitivity will be discussed in more general terms, with respect to all metals investigated in this thesis, in chapter 7.

Chapter 6

Hg INVESTIGATIONS

6.1 Motivation of study

As discussed in chapter 1, a non-invasive method of assessing kidney-mercury levels would be useful for the occupational monitoring of exposure to the inorganic form of this element, as it would serve as a direct probe of toxin levels in a critical organ. Such a tool would also aid in establishing whether there is a clear, quantitative relationship between biological-fluid levels and mercury content in the kidneys. Furthermore, *in vivo* XRF measurements of Hg-kidney levels would provide valuable information to help researchers improve the understanding of the kinetics of this toxic element.

To address these issues, a polarised XRF system to measure Hg in the kidneys of occupationally-exposed individuals has previously been reported (Börjesson *et al.*, 1995). Twenty workers, from both the chloralkali and thermometer-manufacturing industries, were measured. In this group, the measured mercury concentration in the kidney was greater than the minimum detection limit in roughly half of the subjects. Conversely, none of the controls (n=12), with no known occupational mercury exposure, had detectable levels (Börjesson, 1996). It was suggested that an increased tube voltage would further decrease the detection limit, resulting in an *in vivo* polarised XRF system that is capable of more precise assessments of mercury content in occupationally-exposed subjects. This work has investigated the suggestion of improved performance at higher voltage, by assessing the detection limit achieved at 250 kV, compared with 160 kV as reportedly used by Börjesson *et al.*, 1995. Furthermore, extensive Monte Carlo simulations were conducted to establish the optimal design parameters for this target element, as discussed in chapter 5 for the polarised XRF measurements of uranium. The results of these simulations, as well as the minimum detectable limit of the optimal configuration, will be discussed in the following sections.

6.2 System description

A further modification to the x-ray tube was required before the system could be optimised for the measurement of mercury. This modification arose from the use of lead as the shielding material. Lead is frequently used to shield x-rays, as it has a high density and has relatively large cross sections for photon absorption at the energies involved in these studies. However, it was observed experimentally that there was a significant intensity of lead x-rays detected when irradiating samples that did not contain measurable quantities of this element, as is evident in figure 5.15. It was determined that these lead x-rays were arising from the shielding material rather than the irradiated samples, with the vast majority of these x-rays produced by backscatter of the beam from the sample onto the lead box.

The problem with these detected lead x-rays is two-fold; first, there is the concern that these photons will cause the detector and electronics to operate at higher than necessary count rates. Second, the close proximity in energy to the K x-rays of mercury (72.8 keV to 87.3 keV for lead compared to 68.9 keV to 82.5 keV for mercury) results in the detection of lead x-rays from the shielding material unnecessarily complicating spectral analysis when measuring mercury. Therefore, it was proposed that 4 mm of tin, mounted over the front side of the lead box, would be sufficient to reduce the detected lead x-rays from the shielding box to negligible levels. Tin is sufficiently lower in atomic number than the elements of interest that the characteristic x-rays from this material will not result in complicated spectral analysis. This layer of tin is also shown schematically in figure 5.9, as the dotted surface on the front face.

a) Tube current and voltage

As discussed in chapter 5, the maximum tube current will result in the best system sensitivity. In addition, since the motivation of this work was the suggestion that a voltage greater than 160 kV may give rise to a more sensitive device, the optimal voltage is also readily determined. As the Phillips RT 250 (III) Depth Therapy Generator only has four possible operating voltages, namely 75 kV, 125 kV, 175 kV and 250 kV, the best setting to test this hypothesis is a tube voltage of 250 kV. Therefore, the ideal tube parameters for measuring renal mercury with polarised XRF are 250 kV and ~ 15 mA, the maximum current possible at this voltage with the Phillips RT 250.

b) Polariser material, thickness, and collimation

In section 5.3.1 b), the selection of the polariser material, thickness and collimation was discussed in detail with respect to the measurement of uranium. The optimal polariser material was selected by considering the photon yield, energy distribution, and the degree of polarisation of the beam incident on the sample. Based on its high photon yield, reasonably high photon energy distribution and polarisation, aluminium was used for the uranium polarised system. As this optimal choice of polariser material was essentially independent of the target element, it was decided that aluminium would be used in the case of mercury as well.

In the case of uranium, element-specific simulations were conducted to assess the optimal polariser thickness, in order to gain the greatest photon yield while maintaining high polarisation. Figure 5.14 demonstrated the ratio of the uranium x-rays detected to the square root of the background as a function of aluminium thickness. Although there was not much effect overall, it was deemed worthwhile to conduct similar investigations for the case of mercury.

Figure 6.1 shows the effect of increasing the polariser thickness on both the mercury x-rays detected and the background in this spectral region. With the greater photon yield from a thicker polariser, there is an increase in the characteristic x-rays produced and detected. However, as the aluminium thickness increases, there is a resulting decrease in polarisation. This gives rise to a greater background fluence in the spectrum, as shown in figure 6.1. Since the sensitivity is inversely proportional to the square root of the background and directly proportional to the signal, figure 6.2 plots the ratio of these variables with increasing thickness. It is clear that there is little change in this ratio over the range of polariser thicknesses simulated. In fact, it is interesting to note that the signal to noise ratio only varies by ~ 2% over a 0.5 to 3 cm thickness range. Therefore, a 1 cm polariser, as used with the uranium system, was deemed adequate for the measurement of mercury *in vivo*.

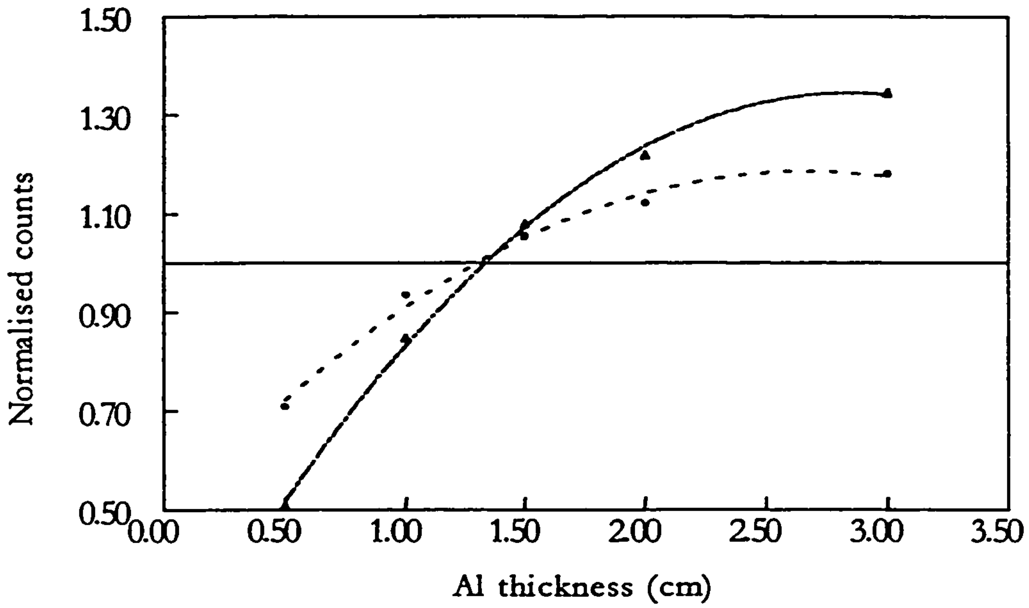

Figure 6.1: Increase in signal (solid dots) and background (open triangles) with increasing polariser thickness. The values have been normalised as in figure 5.13.

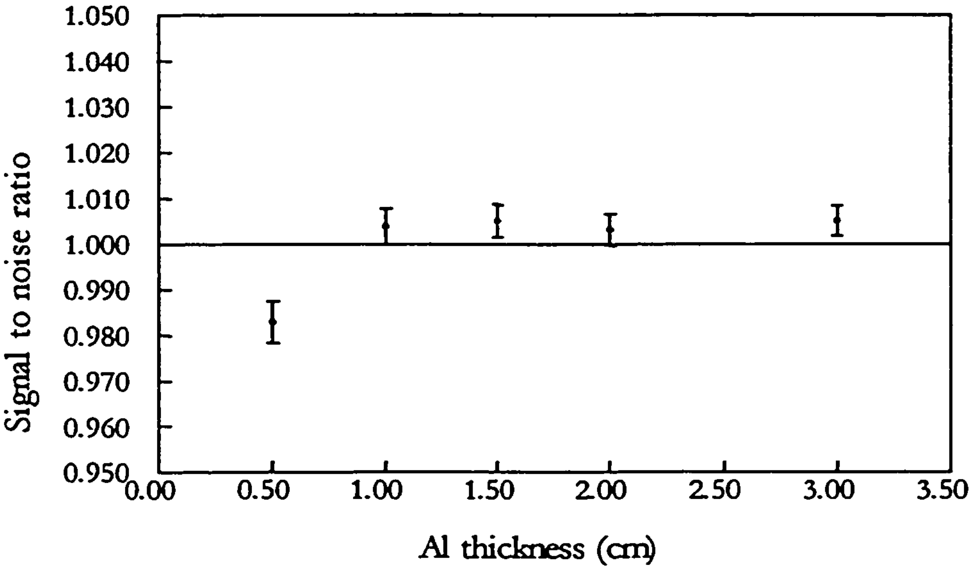

Figure 6.2: Sensitivity (signal to square root of background) as a function of aluminium thickness. It is clear that there is not much effect overall, therefore the same polariser was used for both the uranium and mercury measurements.

Since the logistics of changing the aperture angle by changing the collimation dimensions are decidedly non-trivial, the 20 cm long, 2 cm inner diameter copper collimator discussed in section 5.3.1 b) was also adopted here.

c) Filtration

Filtration is the main parameter that will differ significantly from the optimal settings used in the uranium system. As discussed in section 5.3.1 c), any degree of filtration is expected to result in a reduction in the sensitivity of the system. Recall that in order to compare with the corresponding source-excited system, the uranium system was tested with no filtration to determine the best sensitivity possible. Since even this configuration did not lead to an improvement in system sensitivity relative to the ^{57}Co-based system, the need to filter in order to reduce patient dose was immaterial in the polarised uranium measurements. However, in order for the mercury system to be clinically accepted, the dose is an important consideration.

In addition to concerns for subject dose, filtration may be necessary to reduce the incident photon fluence rate on the detector to levels that are manageable by the associated electronics. As the incident fluence rate increases, the actual throughput rate in the electronics begins to saturate, as there is a finite rate at which the events can be amplified and digitised. As this saturation level is approached, the dead time in the system increases, and the resolution of the system rapidly degrades. It is clearly preferable to run the system such that the throughput rate is less than this saturation level, in order to ensure that the resolution is not compromised and the total acquisition time for a given pre-set live time is not unacceptably long.

Data provided by Dr. I. M. Stronach (Department of Physics and Astronomy, McMaster University) illustrate the relationship between incident photon fluence, actual throughput rate, and the resolution of the system, for the particular HPGe detector and electronics used in this study. Figure 6.3a) demonstrates that as the incident fluence rate increases, the throughput rate also increases, until it appears to saturate at approximately 42 kHz. Figure 6.3 b) demonstrates that the resolution of the system, monitored through the FWHM of the 88 keV line from the ^{109}Cd source used in these experiments, is relatively constant for most fluence rates. However, the FWHM rapidly degrades at the highest incident photon fluence rates. Therefore it is important to limit the incident fluence to ensure that resolution is maintained. The fluence rate can be monitored directly by measuring the throughput rate and the system resolution with the associated software. Based on the data shown in figure 6.3, if the throughput approaches ~ 40 kHz and the resolution of any particular line is degraded relative to a low fluence rate scenario, then the system must be further modified.

The optimal filtration must be selected by considering both the dose and throughput rate limitations. The best filter is the material and thickness that results in the minimum reduction in signal to noise ratio in a fixed time, but satisfies the required reduction in dose and throughput. Clearly, in practice, the greater of the two constraints will be the influential factor in filtration selection. Therefore it is necessary to assess the throughput rate and the dose of the unfiltered system separately in order to determine the degree to which these parameters must be reduced. Once the limiting factor has been identified, simulations of a variety of filters can be used to select the optimal configuration.

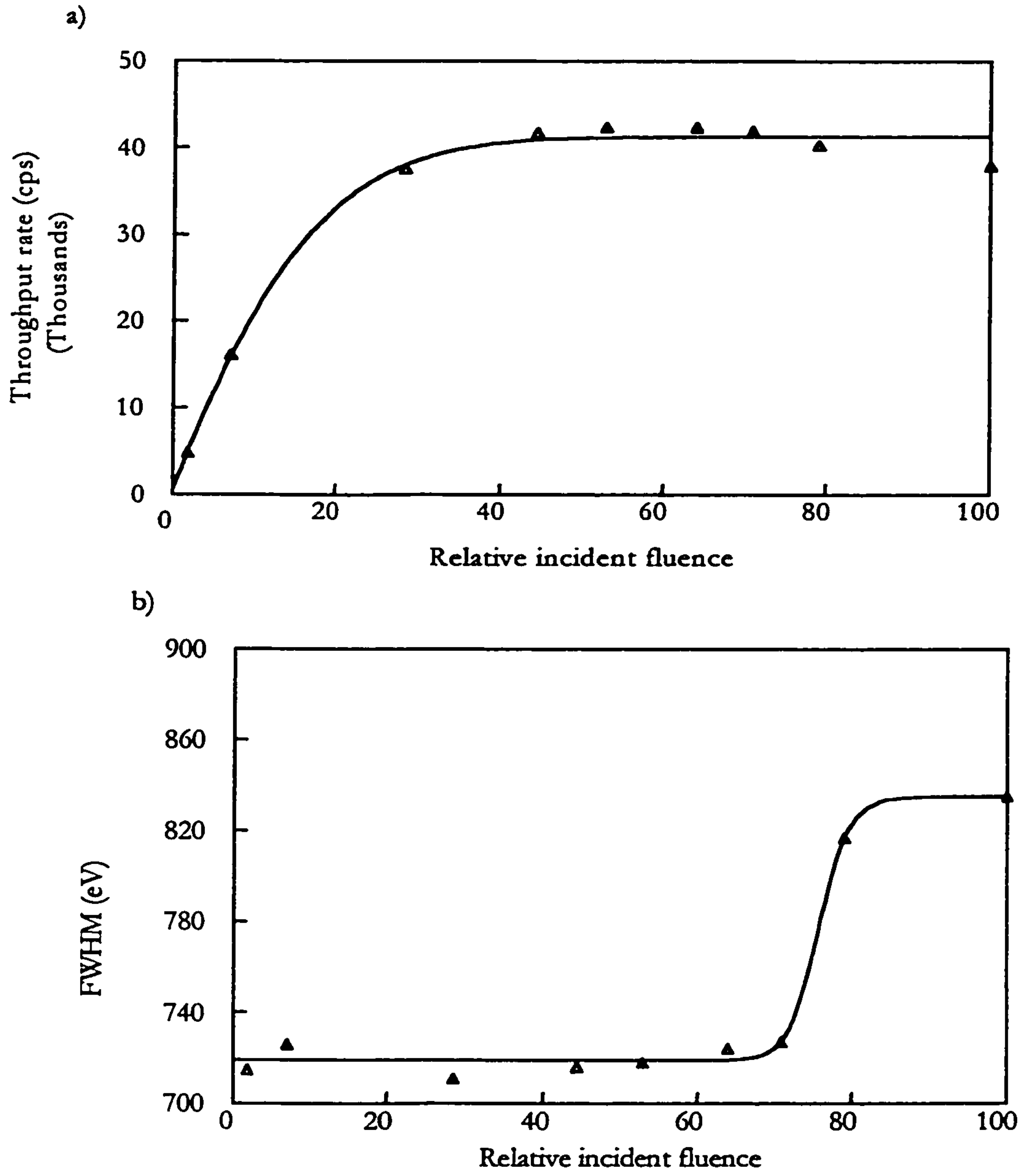

Figure 6.3: a) A plot of throughput versus the relative incident fluence (x axis scale is arbitrary), as assessed with a ^{109}Cd source positioned at various distances on axis from the detector. This graph demonstrates the saturation of throughput as the incident fluence increases. b) A plot of the FWHM as a function of the relative incident fluence. As the incident fluence rate increases, the FWHM will rapidly increase after some point. Data from Dr. I. M. Stronach.

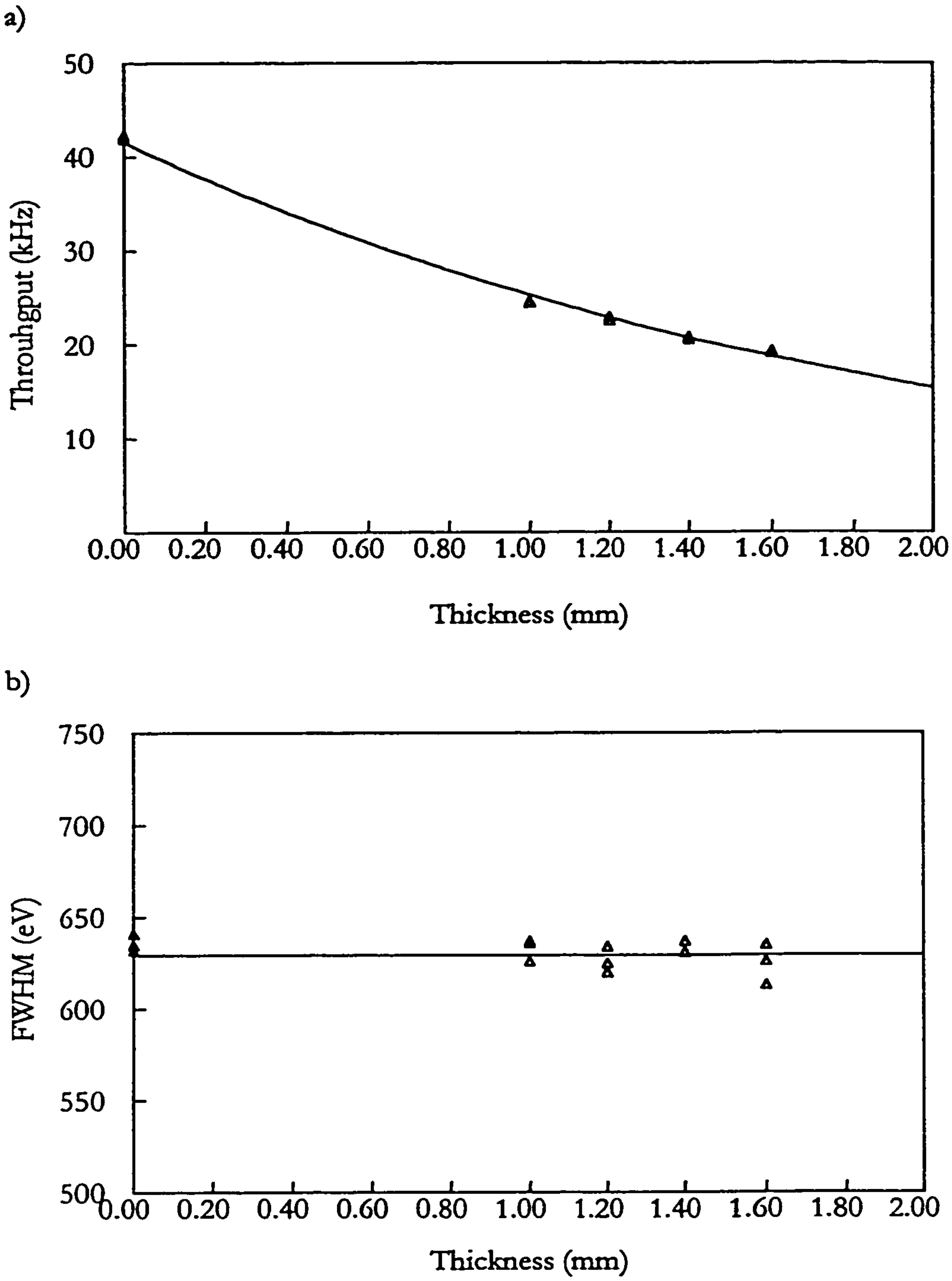

Figure 6.4: a) throughput rate for 250 kV, 12.5 mA waterbath set-up, as a function of copper filter thickness. The rate at 0 mm thickness is in the range at which FWHM degradation was observed in figure 6.3. However, b) demonstrates that the FWHM is not significantly degraded when the beam is unfiltered. Therefore, it does not appear that the system is operating at an unacceptably high incident fluence rate when no filter is used.

Preliminary measurements were made with the water bath arrangement that would ultimately be used to assess the detection limit as a function of kidney depth. Figure 6.4 demonstrates the observed throughput rate (a) and resolution (b) as a function of copper filter thickness. These measurements were made with the filter in the collimator between the polariser and the water bath, and the tube set at 250 kV and 12.5 mA. In these experiments, the resolution was monitored through the FWHM of the K α line of tin, arising from the tin shield used on the front face of the lead shielding box. Note that the resolution of the system is such that the α_1 and α_2 lines are not resolved (at 25.271 and 25.044 keV respectively).

The throughput rate with no filter was observed to be on the order of 42 kHz. This is the level at which the detector throughput was found to saturate (see figure 6.3 a)), and therefore is potentially higher than ideal. However, there is little indication that the resolution is larger with no filter than that observed at the reduced incident fluence rates with filters in place. Therefore, it does not appear that the system is operating at an unacceptably high incident fluence rate when no filter is used.

In order to determine whether filtration is necessary to reduce dose, recall that the dosimetry of the unfiltered system was discussed in section 5.3.3. The preliminary measurements reported in section 5.3.3 detail the skin dose rate associated with the tube operating at 250 kV, with a current of 12.5 mA. Based on these measurements, the maximum skin dose rate from this system is approximately a factor of two greater than that considered acceptable for such a diagnostic tool. Therefore, it was necessary to filter the beam such that a reduction in dose by a factor of two was observed, in order to achieve a feasible clinical measurement system.

Since there was no apparent need to filter the beam in order to obtain an acceptable throughput rate, the limiting factor is clearly the dose rate of the system. Therefore, Monte Carlo simulations were conducted to assess the optimal filter material and position, such that the best configuration corresponded to a factor of two decrease in dose with little reduction in sensitivity, relative to no filtration. The filtered polariser output spectrum was used as the weighting factor for the calculation of the weighted mean mass energy absorption coefficient of tissue (Berger, 1987). This mean mass energy absorption coefficient was used as a measure of the relative dose imparted, with all comparisons between no filtration and filtered output made per unit measurement time (*i.e.* corrections were made for the reduced count rate associated with filtered output, rather than comparing the systems with the same number of photons incident on the subject).

Although dose is the main consideration, it is also important to assess the relative system sensitivity with Monte Carlo. In order to quantify sensitivity, the filtered polariser output spectrum was used as the weighting factor for the calculation of the total probability of K x-ray excitation from mercury, by multiplying the spectral intensity by the K shell photoelectric cross section for this element. Again, corrections were made for the variations in incident photon fluence rate, and comparisons were made per unit measurement time. This estimate of signal strength was then divided by the square root of the estimate of the background under the mercury x-rays in order to compare the relative system sensitivities. While an ideal comparison of the various systems would have included the final stage of the Monte Carlo simulation described in section 3.3.3, it was felt that the approximations made in order to reduce computation time were valid when only relative performances were being investigated.

Simulations were run for elemental filters ranging in atomic number from 13 (Al) to 92 (U). In total, nine different elements were investigated as potential filters. Samples were run such that all filters had the same g/cm^2 thickness. For all nine elements, the effect of positioning between the tube and the polariser (referred to as position 1) as well as positioning between the polariser and the sample (referred to as position 2) were assessed. Combinations of filters were also modelled, for example the relative performance of a system with a gadolinium filter in position 1 and a uranium filter in position 2 was investigated, among other combinations.

Based on these simulations, a titanium filter, 1.6 mm thick, in position 1, or an aluminium filter, 3 mm thick, in either position, gives rise to a dose reduction on the order of a factor of two and the least reduction in the signal to square root background ratio. The titanium filter is the better choice here, as it provides a slightly greater reduction in dose with a similar reduction in sensitivity. Therefore, a 1.6 mm titanium filter in position 1 was selected as the optimal filter for the measurement of mercury.

Since these simulations were run with a fixed g/cm^2 thickness, the reduction in dose achieved was observed to increase with increasing atomic number. In hindsight, a more fair comparison may have been to run all filters with thickness such that there is a constant number of electrons per cm^2, as this would be a more accurate way to account for the relative photon interaction coefficients for the various elements. It was deemed worthwhile to assess that this bias in the Monte Carlo samples did not adversely influence the conclusions reached with respect to the optimal filter material. Specifically, it was important to determine whether a thinner filter of a higher Z element would result in better sensitivity than that of the titanium filter, when only a reduction of a factor of 2 is achieved in the dose rate.

In order to account for the decreasing dose rate with increasing atomic number, the ratio of the sensitivity to the dose was compared for all elements, in both positions, as well as all combinations, relative to the ratio obtained with no filter, *i.e.*:

$$\frac{\left(\mathrm{SNR}/\mathrm{Dose}\right)_{\mathrm{FIL}}}{\left(\mathrm{SNR}/\mathrm{Dose}\right)_{\mathrm{NF}}} \qquad [6.1]$$

or:

$$\frac{\mathrm{SNR}_{\mathrm{FIL}}/\mathrm{SNR}_{\mathrm{NF}}}{\mathrm{Dose}_{\mathrm{FIL}}/\mathrm{Dose}_{\mathrm{NF}}} \qquad [6.2]$$

Therefore, for a given reduction in dose rate, the denominator in [6.2], the ideal filter is one in which the sensitivity ratio, the numerator in [6.2], is as close to unity as possible. Since the sensitivity will always decrease with filtration, the numerator in [6.2] has a maximum value of 1. This suggests that the optimal filter may be the configuration that gives rise to the highest value when taking the ratio shown in [6.1]. From the simulations, a tungsten filter in position 2 resulted in the highest relative sensitivity per unit dose, compared with no filtration.

Tungsten in position 2 was then simulated with a range of thicknesses less than the original value used, in order to assess whether this material would truly result in better sensitivity than the titanium filter, when only a factor of two reduction in dose is achieved. Figure 6.5 demonstrates the results of these simulations. It is clear from figure 6.5 that, by increasing the thickness of filter, the sensitivity of the system relative to no filtration (solid triangles) deteriorates. Figure 6.5 also demonstrates the expected decrease in dose (open triangles), relative to that of no filtration, as the filter thickness increases. These simulations indicated that a thickness on the order of 0.002 cm of tungsten, in position 2, would be expected to decrease the dose by a factor of two, marked in figure 6.5 by the dotted vertical line. The corresponding decrease in sensitivity is comparable to that observed with the aluminium filter in position 1, which was the second choice of optimal filter after titanium in position 1. Therefore, although titanium in position 1, aluminium in either position, and tungsten (of reduced thickness) in position 2 all result in similar effects on the dose and sensitivity, titanium in position 1 was chosen for these experiments.

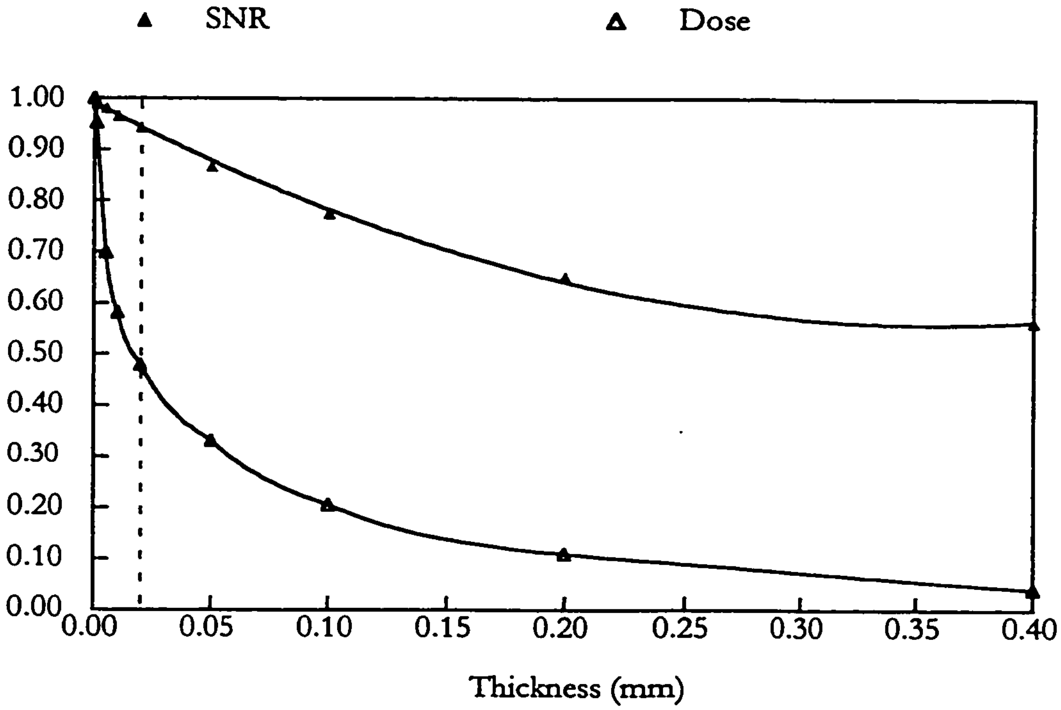

Figure 6.5: The effect of increasing filtration thickness on the relative sensitivity (represented by the SNR), and the effect on the relative dose, compared to no filter. These simulations were run with tungsten to determine the reduction in sensitivity for a reduction of dose by a factor of two. As shown at the vertical dotted line, the sensitivity is reduced by roughly 6% when the dose is reduced by a factor of two.

6.3 Phantom measurements

With the optimal system configuration established, measurements were conducted to assess the minimum detectable limit. Before a full set of spectra was run, preliminary experiments were conducted to verify the conclusions of the simulations. The kidney was represented by a 4.8 cm diameter, 8 cm high Perspex bottle, which contained a range of aqueous mercury solutions. These bottles were then submerged in a water tank, at specific depths, to simulate the kidney within the torso. Spectra were acquired in 30 minutes (live time) from 200 ppm, 100 ppm, and 20 ppm phantoms positioned 2 cm from the tank wall in both the dorsal and lateral directions. Three sets of phantom spectra were acquired; one with no filter, one with a 1.6 mm thick titanium filter in position 1, and the third with a 3 mm aluminium filter in position 2. The tube was set at 250 kV and 12.5 mA for all runs.

These spectra were analysed in three sections to determine the α_1, α_2, and β_1 intensities separately. The α_1 peak was modelled with a Gaussian of variable amplitude on a single exponential background, from 69.8 keV to 73.2 keV. The α_2 peak was fit with a Gaussian in the region from 66.9 to 70.3 keV, and the β_1 peak was fit in the region from 78.4 to 81.8 keV, both with single exponential backgrounds. The β_1 peak was fit with two Gaussians, as the β_3 x-ray is only 400 eV lower in energy, therefore resulting in an unresolved double peak in the spectrum. The β_3 Gaussian is modelled with a linked amplitude and position relative to the β_1, based on the known relative emission rates and energies of these x-rays.

Once the spectra were analysed, the peak intensities were plotted against the phantom concentration and the slopes of these calibration lines were then used, with equation 5.1, to determine the MDL for each particular filter configuration. As predicted by the simulations, the lowest detection limit was achieved with no filtration (16 ± 0.8 ppm), and the titanium filter in position 1 resulted in a similar sensitivity (17.3 ± 0.7 ppm) to that of the aluminium filter in position 2 (17.5 ± 0.6 ppm). The increase in MDL observed in adding these filters is consistent with the simulated effect; Monte Carlo predicted a 5 to 6 % decrease in sensitivity and these experimental data indicate 7 ± 6 % and 9 ± 6 % decreases respectively.

Since these experiments confirmed the Monte Carlo results, a full set of spectra was then obtained with the titanium filter in position 1. The tube was set at 250 kV and 12.5 mA, and six phantom concentrations were used to establish calibration lines at a range of dorsal and lateral depths. Each phantom was run at each depth three times, hence the calibration line at the each depth was comprised of 18 data points. Two lateral depths were assessed, 2 cm and 6 cm, and samples were run at four dorsal depths for each lateral depth (2 cm, 4 cm, 5 cm, and 7 cm). Therefore, calibration lines were obtained at eight locations in the water tank, and detection limits were determined with equation 5.1. Figure 6.6 illustrates the resulting detection limits as a function of depth. As expected, as overlying tissue thickness increases, the detection limit increases.

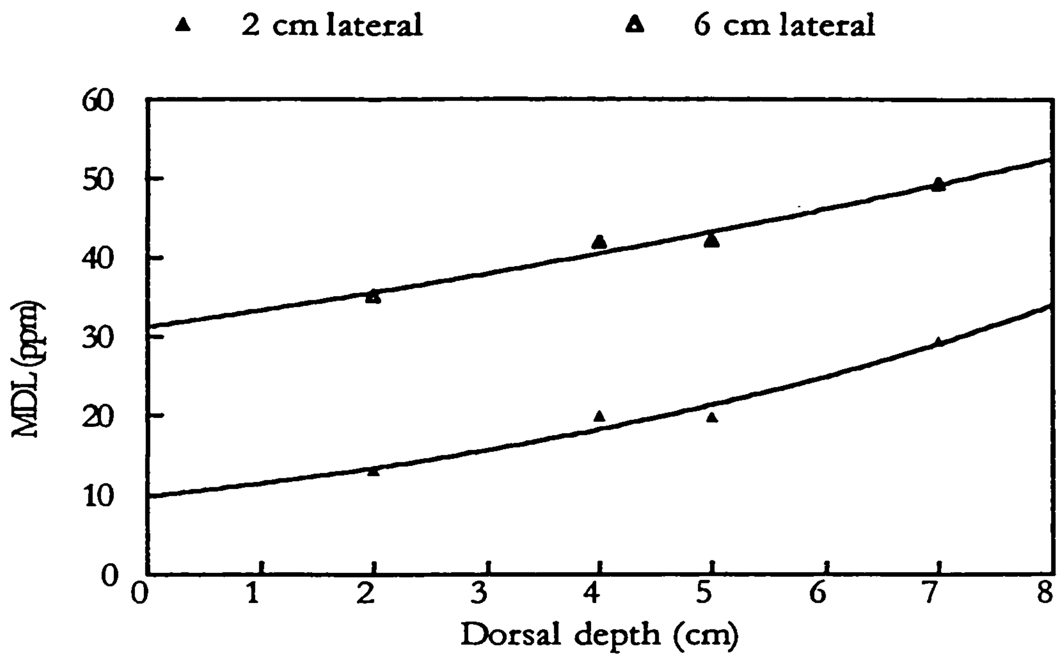

Figure 6.6: Detection limits as a function of dorsal depth in the water tank. Two separate sets of data are shown, one obtained at 2 cm lateral depth and the second at 6 cm lateral depth. Clearly the sensitivity decreases as the depth of the kidney increases.

Since there is such significant variation in signal strength per unit mercury concentration with kidney depth, the conversion of an *in vivo* mercury spectrum to the corresponding concentration must be done with the calibration line associated with the kidney position of the particular patient measured. Therefore, the location of an individual kidney, as assessed by ultrasound, must be used to determine the particular concentration present based on the detected spectrum. Calibration lines at additional locations may be necessary before routine occupational monitoring is conducted with such a system. Table 6.1 summarises the calibration data for the eight kidney positions investigated.

	α_1		α_2		β_1	
Position	Slope (intensity/ ppm)	Intercept (intensity)	Slope (intensity/ ppm)	Intercept (intensity)	Slope (intensity/ ppm)	Intercept (intensity)
2 cm (lateral) 2 cm (dorsal)	7.74 ± 0.33	42 ± 31	4.73 ± 0.19	40 ± 18	1.83 ± 0.22	2 ± 20
2 cm (lateral) 4 cm (dorsal)	4.95 ± 0.28	26 ± 26	2.63 ± 0.25	49 ± 24	1.18 ± 0.20	-9 ± 19
2 cm (lateral) 5 cm (dorsal)	4.68 ± 0.25	44 ± 24	2.84 ± 0.28	5 ± 26	1.06 ± 0.15	-8 ± 14
2 cm (lateral) 7 cm (dorsal)	2.85 ± 0.27	-19 ± 25	1.64 ± 0.13	28 ± 12	0.77 ± 0.16	-25 ± 15
6 cm (lateral) 2 cm (dorsal)	3.10 ± 0.36	54 ± 34	1.69 ± 0.34	22 ± 33	0.62 ± 0.20	-2 ± 19
6 cm (lateral) 4 cm (dorsal)	2.30 ± 0.32	36 ± 30	1.55 ± 0.16	3 ± 15	0.75 ± 0.20	-25 ± 19
6 cm (lateral) 5 cm (dorsal)	2.47 ± 0.35	-14 ± 33	1.26 ± 0.25	52 ± 23	0.37 ± 0.15	-16 ± 14
6 cm (lateral) 7 cm (dorsal)	1.77 ± 0.26	19 ± 24	0.94 ± 0.28	34 ± 26	0.47 ± 0.13	-2 ± 12

Table 6.1: Calibration data for the eight kidney positions investigated. These lines can then be used in conjunction with the *in vivo* spectrum and the ultrasound assessment of kidney position to determine the mercury concentration of a particular subject.

In order to assess whether the increased tube voltage results in improved sensitivity, the detection limit was also measured at 175 kV and 12.5 mA at two locations in the water tank, with the titanium filter in position 1. In addition, a set of spectra was acquired at one location only with a tube voltage of 175 kV and current of 12.5 mA, using a 0.3 mm uranium filter in position 2. Simulations predict that the uranium filter is not ideal, however, this is a similar system to that reported by Börjesson *et al.*, 1995 (160 kV and 20 mA, with a 0.35 mm uranium filter in position 2). Table 6.2 summarises these findings.

Location in tank	175 kV, with U filter	175 kV, with Ti filter	250 kV, with Ti filter
2 cm (lateral), 5 cm (dorsal)	64 ± 6 ppm	39 ± 4 ppm	26 ± 1 ppm
6 cm, 5 cm	n/a	86 ± 12 ppm	54 ± 6 ppm

Table 6.2: The detection limits achieved with various tube voltages and filters, all with 12.5 mA current and acquired in 30 minutes (live time). Clearly the 250 kV with titanium filter system is the best configuration.

From table 6.2, it is clear that the lowest detection limit is achieved at 250 kV, using the titanium filter. These results support the hypothesis that an increased tube voltage improves system sensitivity, since the detection limit at 250 kV is better than that obtained at 175 kV when the same filtration, current, and acquisition time are used. Furthermore, based on table 6.2, the use of a uranium filter is non-ideal, as suggested by the Monte Carlo simulations. From these data, the 250 kV with titanium filter configuration is 2.5 ± 0.2 times better than the 175 kV with uranium filter set-up, when all other design features are kept constant. These results are consistent with simulations, as Monte Carlo predicted that the 250 kV titanium filter set-up gives rise to 3.4 times better sensitivity than the 160 kV with (0.35 mm) uranium filter configuration. One would expect these simulated results to be an overestimate of the experimental performance of 250 kV with titanium filter relative to that of the 175 kV with 0.3 mm uranium filter system; the lower voltage (160 *vs.* 175 kV) and the thicker filter (0.35 *vs.* 0.3 mm) run in the simulation will both serve to exaggerate the observed effect. Experiments and simulations are therefore in reasonable agreement as to the magnitude of the effect of increasing tube voltage and optimising system filtration, when current and acquisition time are fixed.

It should be noted that the 175 kV with uranium filter data set can not directly be used as a reflection of the preceding mercury system reported by Börjesson *et al.*, 1995. The preceding system was operated at 160 kV and 20 mA, and the uranium filter was slightly thicker than that used here, 0.35 mm *cf.* 0.3 mm. In addition, the detection limits given in table 6.2 were based on acquisition times of 30 minutes (live time), while the Swedish system is typically run for 40 or 50 minutes (live time). A direct comparison of the two systems is difficult, since Börjesson *et al.* (1995) do not report both lateral and dorsal depths when citing a detection limit for their system. However, in personal communications, Dr. Börjesson (Department of Radiation Physics, Malmö University Hospital, Malmö, Sweden) has indicated that the Swedish system performs significantly better than our 175 kV uranium filter data suggest. For example, Dr. Börjesson reports a detection limit of 22 ppm at 7 cm lateral depth and 5 cm dorsal depth. This is clearly better than the capabilities suggested by the results in table 6.2, for either the 175 kV uranium filter set or the 250 kV titanium filter data set. The cause of this discrepancy is not clear. It may be that there is/are some design feature(s) (x-ray tube output, polariser thickness, distance between water tank and detector, *etc.*) that are not reproduced in our set-up. If the cause of this discrepancy can be identified and rectified in the McMaster system, the data in table 6.2, in combination with Dr. Börjesson's results, suggest that the 250 kV titanium filter configuration should be capable of a detection limit on the order of 10 ppm at 7 cm lateral depth and 5 cm dorsal depth.

6.4 Dosimetry

In order to determine the clinical feasibility of measuring mercury *in vivo* with polarised XRF, the effective dose associated with this system was assessed. For this purpose, a set of 20 Panasonic UD-806 AS personnel dosimeters was used, along with the associated reader, as described in section 5.3.3.

First, the dosimeters were read in order to clear residual background exposure. These dosimeters were irradiated for 1 hour with a calibrated ^{60}Co source. They were left for 28 hours, at which point each element was read again. The calibration exposure for each element, y, was corrected for the background accumulation exposure over a 29 hour period, y', based on previous assessments. Before irradiation with the polarised system, each element was again cleared by the reader. The dosimeters were arranged in the phantom (to be described below) and irradiated for 6 hours. They were then left for 23 hours before being read again. The irradiation exposure for each element, x, was corrected for the background accumulation exposure over a 29 hour period, x', as before.

Since the exposure rate X_{Co} associated with the ^{60}Co source was measured as 86 ± 4 mR/hr at 30 cm, the exposure of each element due to the polarised system X_{pol} is then given by equation [5.10]. The values of X_{pol} must then be corrected for the energy response of the dosimeters, relative to ^{60}Co, and these exposure values were then converted to absorbed dose with equation [5.11], as described in section 5.3.3.

In order to measure the effective dose of the system rather than just the associated skin dose, the dosimeters were irradiated in a tissue-equivalent phantom, at fixed locations within the beam field. In order to position dosimeters accurately, the phantom consisted of a Perspex container filled with rice. Table 6.3 summarises the photon interaction coefficients of this material at the energies relevant to this study, as well as some physical characteristics.

Bulk density	0.88 ± 0.04 g/cm^3
Relative mass attenuation coefficient	0.96
Relative mass energy absorption coefficient	0.93
Relative electron mass stopping power	0.96

Table 6.3: Characteristics of the phantom material used in dose measurements. The bulk density was measured directly, while the photon and electron interaction coefficients are taken from White, 1978. The coefficients and stopping power values are given for 100 keV, relative to the corresponding values for soft tissue.

From table 6.3, it is clear that this phantom material is a reasonable representation of soft tissue, and provides a sufficiently stabilising medium in which the dosimeters could be accurately positioned.

Seventeen dosimeters were positioned throughout the simulated torso at various distances along and off the beam axis, while three were used to assess skin dose at the point of beam entry. Since each dosimeter consists of four elements arranged in a line vertically, the dose dependence in this direction (z in figure 6.7) was also determined. Figure 6.7 demonstrates the arrangement of dosimeters in the tissue-equivalent dosimetry phantom.

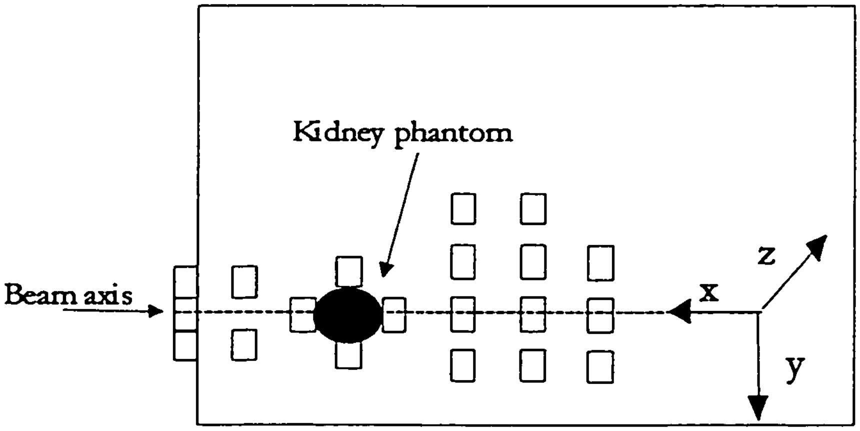

Figure 6.7: Schematic of the arrangement of dosimeters in the tissue-equivalent phantom used to determine the effective dose associated with the polarised XRF measurement of renal mercury.

Once the readings were converted to absorbed dose, as described above, further analysis was required to determine the effective dose of the system. First, a three dimensional function was fit to the data, to describe the dose distribution in the torso mathematically. Equation 6.3 demonstrates the empirically-determined function used for this purpose. This expression was chosen based on the expected beam shape and behaviour in an attenuating medium.

$$D(x,y,z) = a_0 \cdot \left(1 - \frac{1}{1 + \exp\left[\dfrac{-(\sqrt{y^2 + z^2} - 1.5)}{a_1 \cdot x} \right]} \right) \cdot \exp(-a_2 \cdot x) \cdot \exp(-a_3 \cdot \sqrt{y^2 + z^2})$$

[6.3]

Figure 6.8 demonstrates a contour plot of the dose distribution in the x,y plane from the measurements obtained with the 250 kV titanium filter configuration.

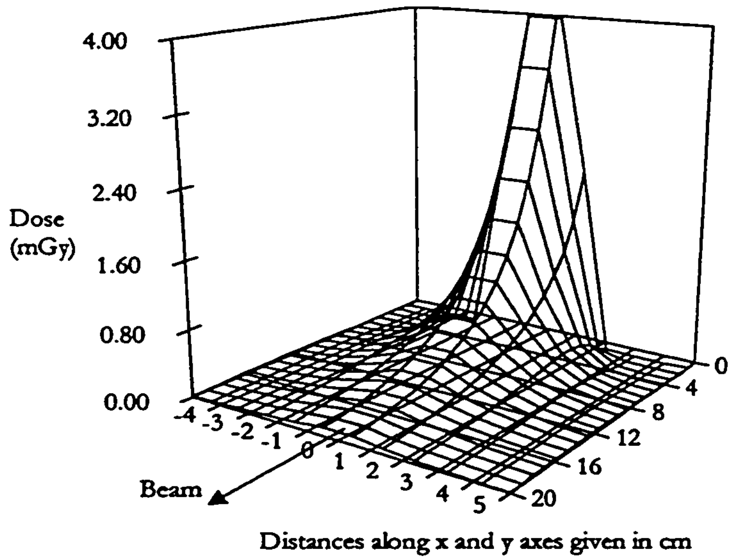

Figure 6.8: Dose distribution for a 6 hour irradiation with the 250 kV titanium filter setup. The dose decreases rapidly as the beam penetrates the attenuating medium.

Equation 6.3 was then used to determine the dose to each organ within the dose field, by integrating over the volume occupied by a given organ. The mean absorbed dose to each organ was then multiplied by the appropriate tissue weighting factor, see for example Turner, 1995, and the sum of these products is then the effective dose to the subject. Table 6.4 summarises the dose measurements for the three systems discussed in section 6.3, that of 250 kV with no filtration, 250 kV with a titanium filter in position 1, and 175 kV with a uranium filter in position 2.

Configuration	Skin dose rate (mGy/hr)	Effective dose rate (μSv/hr)
250 kV, no filter	14 ± 2	28 ± 4
250 kV, Ti filter in position 1	8 ± 1	15 ± 2
175 kV, U filter in position 2	1.0 ± 0.2	1.0 ± 0.2

Table 6.4: Measured dose rates for all systems discussed in section 6.3.

From table 6.4, the use of the titanium filter in position 1 results in the desired factor of two decrease in dose rate, relative to that of the unfiltered system. Table 6.4 also indicates that the dose rate associated with operating at 175 kV with a uranium filter in position 2 is considerably lower than that obtained with the 250 kV titanium filter configuration. Therefore, although the 250 kV with titanium filter system results in a 2.5 ± 0.2 times improvement in sensitivity per unit measurement time, it is worthwhile to compare the performance of these systems per unit dose as well.

For these purposes, a figure of merit can be defined as:

$$\varsigma = \mathrm{MDL} \cdot \sqrt{\mathrm{Dose}} \qquad [6.4]$$

The better system is that which has the lower figure of merit ς. Based on the values in tables 6.2 and 6.4, the corresponding values of ς are 100 for the 250 kV, titanium filter configuration, and 64 for the 175 kV, uranium filter set-up. Therefore, based on per unit dose, the latter system has better sensitivity. However, while this is an interesting observation to note, it should be stressed that at these dose rate levels, the system dose is not the significant point of comparison. As discussed earlier in this chapter, the dose of the 250 kV titanium filter system was chosen as an acceptable level at which to operate. While a lower dose is ideally preferred, the cost of reduced sensitivity is not considered worthwhile when operating at such already low doses. The comparison of sensitivity per unit measurement time, as reported in section 6.3, is the more legitimate point of reference since such systems are usually limited in practice by the time over which the patient can be expected to sit comfortably without significant movement, rather than the dose delivered per examination.

6.5 Clinical Implications

Based on the dose rates reported in table 6.4, the 250 kV with titanium filter configuration results in an acceptable dose rate for this procedure, as this filter provides the desired factor of two decrease in the dose associated with the unfiltered system. Furthermore, the relative sensitivities summarised in table 6.2 are promising. When all other design parameters are the same, increasing the tube voltage from 175 kV to 250 kV results in a 1.5 ± 0.1 times improvement in sensitivity. The system is further improved by using a titanium filter in position 1 rather than a uranium filter in position 2, as used by Börjesson *et al.*, 1995. These experiments indicate that the 250 kV titanium filter system is 2.5 ± 0.2 times better than the 175 kV uranium filter system, when the systems are operated with the same tube current for a fixed acquisition time. Therefore, the new system should be a significant improvement on the preceding configuration reported by Börjesson *et al.*, 1995, when comparing the two devices per unit measurement time. However, more research is required to identify the cause of the discrepancy noted in section 6.3 between the sensitivity of our 175 kV uranium system and the Swedish system. It should be noted that Börjesson (1996) reports a maximum skin dose rate of 6 mGy/hr operating at 160 kV, 20 mA, with a 0.35 mm uranium filter. This is a factor of six larger than the value measured here operating at 175 kV, 12.5 mA, with a 0.3 mm uranium filter. This dose rate discrepancy indicates that tube output may be a factor in the observed differences in sensitivity noted above.

Given the autopsy values of kidney-mercury levels summarised in table 1.3, and the observation that roughly half of the occupational workers in the study reported by Börjesson *et al.* (1995) had kidney levels below the detection limit, the preceding system was not sufficiently sensitive for routine occupational monitoring. The potential factor of 2.5 improvement in detection limit reported here could have profound clinical implications, both in terms of the accuracy of occupational monitoring and in assessing whether there is a clear, quantitative relationship between levels in biological fluids and mercury content in this critical organ. Furthermore, this significant predicted improvement in sensitivity indicates that such a system may provide valuable information to improve the understanding of the kinetics of this toxic element.

Chapter 7

CONCLUSIONS

7.1 Lead

Chapter 4 discussed the investigation of a means of improving one of the first *in vivo* XRF measurement systems of a toxic heavy metal. Based on Monte Carlo simulations and experiments, the absolute number of x-rays detected per unit concentration was found to be a strong function of bone radius when measuring Pb in finger-bone with the ^{57}Co-based XRF system. However, these investigations also demonstrated that the ratios of x-ray to coherent peak areas over an anatomically relevant range of bone radii were all within 5 to 10% of the mean ratio, within uncertainty. This suggests that a calibration procedure similar to that used in the ^{109}Cd-based Pb measurement system could be implemented to relate the number of x-rays detected to the concentration of lead present. Furthermore, the x-ray to coherent ratio has less variability with tissue thickness compared with the absolute number of x-rays detected, although this observation may arise from the ratio eliminating variations in x-rays detected due to slight changes in geometry between experiments. Therefore, both experiments and simulations indicate that the coherent normalisation procedure is feasible for correcting the observed net counting rate of lead x-rays in the ^{57}Co-based XRF *in vivo* measurements to account for interpatient variations in bone size, and to some extent, overlying tissue thickness and geometry.

This normalisation procedure could replace the existing calibration method, which is based on the assessment of the bone dimensions of each subject through the acquisition of two planar x-ray images of the measurement site. The normalisation procedure thereby reduces subject dose, potentially by a factor of two, and improves the transportability of the complete measurement system. Also, this method eliminates the subjectivity currently required in calculations based on such images. From these investigations, it can be concluded that the use of the coherent normalisation procedure may indeed be an improvement to the measurement of Pb *in vivo* with the ^{57}Co-based XRF system.

7.2 Uranium

7.2.1 Source-excited XRF

a) Bone-U measurements

Section 5.2 described the process involved in designing the optimal source-excited *in vivo* XRF system for measuring bone uranium. It was determined that ^{57}Co in a backscatter geometry, with a HPGe detector and fast nuclear electronics, was the best configuration for achieving the highest sensitivity. It was determined that such a system has a detection limit on the order of 15 to 20 μg U per gram of bone mineral, with an associated effective dose of 30 ± 5 nSv for a 45 minute measurement.

Based on autopsy data of bone-uranium concentrations in both occupational and non-occupational groups, the expected concentrations in all individuals are beyond the current capabilities of the *in vivo* XRF system reported here. It is difficult to conclude whether such a system is sufficiently precise for the particular application of measuring bone-uranium concentrations arising from "Friendly Fire" incidents during Operation

Desert Storm. Very little is known about the kinetics of subcutaneous uranium fragments. However, based on the kinetic models described in section 1.2 b) and the typical urinary-U excretion levels observed in this cohort, it is unlikely that bone-U concentrations in this group will exceed the higher end of the range of values observed in workers having several years of occupational exposure. This is consistent with the observation that three measurements of one of the members of the "Friendly Fire" cohort were not above the detection limit of the system. Therefore, it seems that the expected bone-U levels are currently beyond the capabilities of the *in vivo* XRF system reported here, in both workers exposed to uranium through conventional means and the Operation Desert Storm cohort.

b) U shrapnel measurements

The first measurement of a member of the "Friendly Fire" group illustrated that ^{57}Co-based XRF is capable of qualitatively identifying the presence or absence of uranium in subcutaneous fragments. However, the phantom work reported in section 5.2.5 indicated that there is no straight-forward method of calibration for assessing the amount of uranium present in the fragment, as there is no clear relationship between x-ray intensity and fragment mass. Future work may involve determining the extent to which calibration is feasible for determining an effective mass per unit surface area based on x-ray intensity and an estimate of fragment depth.

The benefits of such a system are not obvious. There is no feasible means of using such a device to screen the afflicted cohort in order to identify locations of uranium fragments, as this would be far too time-intensive. The only potential application is in assessing whether or not specific radio-opaque structures contain uranium. It is unclear whether such an examination would lead to clinical action, as surgical removal appears to be rarely pursued with this group. Therefore, although there are avenues to investigate in order to improve the quantitative potential of this system, there is little motivation to continue this research at this time.

7.2.2 Polarised XRF

Section 5.3 described the optimal system configuration for measuring bone-uranium concentrations with polarised XRF. In order to compare the sensitivity of the polarised with the source-excited system, the detection limit was measured with plaster of Paris phantoms with the tube set at 250 kV and 12.5 mA, with no filtration and a 1 cm thick aluminium polariser. It was found that the MDL with such a polarised system is 9 ± 1 ppm, while the corresponding value for the source-excited system is 4.2 ± 0.1 ppm. Furthermore, the entrance skin dose rate for the polarised system is 3.0 ± 0.4 mSv/hr, compared to only 250 ± 40 μSv/hr when measuring bone uranium with the ^{57}Co-based system.

Given that the skin dose is an order of magnitude larger than the source-excited system and the sensitivity is worse by more than a factor of two, the clinical prospects are not promising for bone-uranium measurements with polarised XRF. The detection limit must be reduced considerably in order to be able to measure the expected levels in either occupational workers or survivors of "Friendly Fire" incidents. Future improvements may be achieved through the use of a higher energy tube voltage, as this would provide a greater number of photons above the K edge of uranium. With optimal filtration, a system with higher operating voltage may lead to a polarised detection limit that surpasses that achieved with the ^{57}Co-based measurement, potentially approaching the typical values anticipated in uranium-exposed subjects.

7.3 Mercury

As reported in chapter 6, the optimal system configuration for the polarised XRF measurement of renal mercury consisted of a tube voltage of 250 kV, a current of 12.5 mA, a 1 cm thick aluminium polariser, and a 1.6 mm thick titanium filter positioned between the tube and the polariser. Such an arrangement resulted in the desired factor of two reduction in the dose rate associated with the unfiltered system, while only a 7 ± 6 % loss in sensitivity was observed. Calibration lines were established with the kidney phantoms positioned at eight different locations within the water bath, in order to assess the variation in x-ray signal strength with changes in the attenuation path of the incoming and outgoing photon beams. Figure 6.6 clearly demonstrates that the sensitivity of the system decreases as the depth of the kidney increases. The variation in signal strength with attenuation path length results in a significant variation in the calibration line best fit coefficients, as evident in table 6.1. Therefore, the position of an individual kidney must be identified with ultrasound in order to determine the particular concentration present based on the detected spectrum and the appropriate best fit coefficients. Calibration lines at additional positions within the torso may be necessary before routine occupational monitoring is conducted with such a system.

Experiments confirmed that an increased tube voltage results in improved sensitivity. When all other design parameters are the same, increasing the tube voltage from 175 kV to 250 kV resulted in a 1.5 ± 0.1 times improvement in sensitivity. The system was further improved by using a titanium filter between the tube and the polariser, rather than a uranium filter between the polariser and the sample, as used by Börjesson *et al.*, 1995. These experiments indicated that the 250 kV titanium filter system is 2.5 ± 0.2 times better than the 175 kV uranium filter system, when the same tube current and acquisition time are used.

Therefore, the new system should be a significant improvement on the preceding configuration reported by Börjesson *et al.*, 1995, when comparing the two devices per unit measurement time.

Given the autopsy values of kidney-mercury levels summarised in table 1.3, and the observation that roughly half of the occupational workers in the study reported by Börjesson *et al.* (1995) had kidney levels below the detection limit, the preceding system was not sufficiently sensitive for routine occupational monitoring. The potential factor of 2.5 improvement in sensitivity reported here could have profound implications, specifically in assessing whether there is a clear, quantitative relationship between levels in biological fluids and mercury content in this critical organ, and, more generally, in the field of occupational monitoring. Furthermore, this significant predicted improvement in sensitivity indicates that such a system may ultimately provide valuable information to improve the understanding of the kinetics of this toxic element.

7.4 Potential advances

7.4.1 New photon sources

In the case of source-excited XRF, there is little room for improvement in the optimal source for the excitation of characteristic x-rays from Pb, U, or Hg. When such systems were designed, the ideal radionuclide was selected based on the γ-ray energy emitted, as well as the magnitude of the background in the characteristic x-ray energy region of the detected spectrum. Factors such as price, availability, radioisotopic half-life, and emissions of other, non-contributing, γ-rays were also considered. Therefore, it is unlikely that system improvements could be achieved with alternative radionuclides.

However, the case of polarised XRF is somewhat different. For example, as found in chapter 6 for the case of mercury, a higher operating voltage on the x-ray tube should result in improved sensitivity. In particular, therapeutic x-ray machines exist that are capable of operating at up to 500 kV and higher, and these may prove useful for increasing the sensitivity of measuring uranium with polarised XRF. The application of such devices in the measurement of toxic heavy metals would require extensive investigations of both leakage shielding and subject dose.

As an alternative to the use of a higher operating voltage, some research into the utilisation of the direct tube output, appropriately filtered, may yield improved sensitivity, again particularly with respect to measuring uranium. A higher energy photon distribution would be incident on the subject by exciting with the direct beam, rather than after 90° scatter in order to obtain a polarised system. Filtration should be optimised to reduce dose, and the angle of scatter should also be considered in order to minimise the background under the characteristic x-ray energy region in the detected spectrum. The elimination of the polarisation stage does imply that the angle of scatter and the spectral shape after filtration will be crucial to maximising system sensitivity by minimising background. However, as observed in chapter 5, even when polarisation is used to minimise Compton contribution to the spectrum, the constraint of a 90° source-sample-detector geometry results in an unacceptably high background under the x-rays relative to that observed with the source-excited backscatter geometry. Therefore, there may be some gain in sensitivity achieved by replacing a polarised x-ray tube system with one based on a filtered tube in a backscatter configuration.

Ideally, the optimal source of photons for the excitation of characteristic x-rays is a monoenergetic, polarised, beam. Such a photon source should have an energy that is just above the K edge of the element in question, and results in acceptable separation between the Compton scatter peak and the characteristic x-rays when arranged in the mandatory 90° source-sample-detector geometry of polarised systems. There are two possible immediate avenues to investigate in order to achieve such a photon source for *in vivo* XRF. First, Royal Philips Electronics N.V. (The Netherlands) has recently developed a new x-ray tube, called the Fluorex system (Harding *et al.*, 1991). This tube is designed as a near mono-energetic x-ray source, by maximising the emission of the characteristic lines from the anode material. Figure 3.4 depicts the typical emission spectra of a tungsten anode tube, operated at a variety of voltages. The characteristic x-rays from tungsten are evident in all spectra, and while they are a significant component, there is still considerable bremsstrahlung radiation as well. However, with the Fluorex system, the characteristic x-rays comprise a larger fraction of the spectrum than that seen in a conventional device. Currently Dr. J. Börjesson and colleagues (Department of Radiation Physics, Malmö University Hospital, Malmö, Sweden) are investigating the performance of a polarised Fluorex system with a tantalum anode, for the measurement of cadmium. It is hoped that Philips will soon make a uranium anode Fluorex tube available for assessing the feasibility of measuring mercury with this polarised XRF apparatus. The characteristic x-rays from uranium (94.7 to 114.5 keV) will be reduced to energies around the K edge of mercury (83.1 keV) after 90° scatter in the polariser, and therefore could give rise to significant signal improvement per unit dose. However, while the signal is expected to increase, there may also be a substantial increase in the background, since the energy of the Compton scatter peaks in the detected spectrum will be quite close to that of the mercury x-rays. Further research in this area will indicate whether the gain in signal sufficiently outweighs the gain in background to result in an overall improvement in system sensitivity.

The second possible means of generating a mono-energetic polarised photon beam is through the use of synchrotron radiation. Synchrotron facilities generate intense photon beams by accelerating electrons (or positrons) contained in a storage ring. When the electrons undergo centripetal acceleration, as they are deflected around the ring by bending magnets, they emit electromagnetic radiation. Since the electrons are moving at relativistic speeds, the emissions are well collimated, tangential to the ring and linearly polarised in the plane of the ring. The Doppler phenomenon results in the radiation along the direction of motion having wavelengths in the x-ray region of the electromagnetic spectrum. The photon emission of each beam-line at such a facility is typically tailored for particular applications, and can be broadband radiation or mono-energetic through the use of insertion devices and monochromators. Until recently, synchrotron radiation has typically been too low in energy for the excitation of K shell x-rays from the toxic heavy metals. However, several third generation facilities now have beamlines in the 100 keV range. For example, the Advanced Photon Source at Argonne National Laboratory (Argonne, Illinois) operates one line that makes use of the higher energy component of the emitted spectrum. Synchrotron facilities could therefore be an interesting new means of exciting characteristic x-rays for *in vivo* XRF, since such beams are intense, well collimated, highly linearly polarised, and readily tuneable in energy. By selecting the appropriate beam energy, signal strength could be increased while ensuring that the Compton scatter distribution at 90° is sufficiently removed from the characteristic x-ray region of the detected spectrum. While this could be an ideal photon source for *in vivo* XRF, the need to measure subjects at such a specialised facility substantially reduces the clinical feasibility of such a tool. Extensive research is necessary to determine whether the improvement in sensitivity makes such a clinical inconvenience acceptable. Furthermore, much work is needed, if *in vivo* synchrotron XRF is deemed worthwhile, in establishing a comfortable environment for human subjects at such a multi-user international research facility.

7.4.2 New detection systems

While system sensitivity may be improved through the use of alternative photon sources, research into new detection systems may also enhance performance. One such advance in detection systems has recently been reported by Silver *et al.*, (1996), at lower energies than those relevant to this thesis. Silver *et al.* (1996) demonstrated the use a microcalorimeter detector made of tin, operated at 80 mK, capable of detecting photons with 95% efficiency at 6 keV and a resolution of 7 eV over the energy range of 0.2 to 20 keV. This represents a 20-fold increase in resolution compared to the standard semi-conductor crystal used for high-resolution photon detection.

Calorimetry is not an entirely new mechanism for photon detection. This technique is based on the increase in temperature associated with the energy absorbed by a substance when exposed to photons. Instruments known as bolometers have been used for many years for the detection of thermal or infrared radiation, where the incident flux on a target is measured through the temperature rise as sensed by a thermistor. However, the temperature rise associated with ionising radiation is typically too small to be measured unless the sample is exposed to a very high flux of radiation (Knoll, 1989). Therefore, calorimetric measurements in which the temperature rise in a thermally isolated sample is measured have traditionally been limited to relatively intense radiation fields.

Recent research advances have done much to change this tradition. It has been demonstrated that the sensitivity of such calorimetric methods can be increased by orders of magnitude if the temperature rise is measured in miniature samples of material maintained at very low temperatures (Knoll, 1989). What is unique about such systems is that the pulse associated with each photon detected is not comprised of discrete charges (such as ion pairs or electron-hole pairs) but rather is only a change in the thermal state of the absorber. Therefore, the conventional limits on energy resolution set by charge carrier statistics in virtually all other radiation detectors are avoided. Resolution limits are now set by thermodynamic fluctuations at the phonon level, and since phonon energies are typically several orders of magnitude below the energy required to create an electron-hole pair in a semiconductor, the theoretical resolution is many times better for a microcalorimeter (Knoll, 1989). With the promising results reported by Silver *et al.*, (1996), considerable interest has been generated in the potential application of microcalorimeters at higher photon energies, in particular, the use of microcalorimeters for *in vivo* XRF.

The main concern regarding the application of such devices to *in vivo* XRF is poor efficiency. With the exception of the measurement of cadmium, *in vivo* XRF relies on the detection and quantification of K x-rays in the energy range of 70 to 115 keV. While potentially useful in assessing cadmium levels, the small tin samples used by Silver *et al.* (1996) would not be expected to absorb many of these higher energy photons; the ratio of the total peak area to the events depositing fractions of the full energy is expected to be quite small. Therefore, in order to apply these detectors to higher energy photon systems, the trade-off between resolution and efficiency must be such that there is an overall system improvement from the current *in vivo* XRF spectra collected with HPGe.

One means of improving the efficiency of microcalorimeters for higher photon energies is the use of a superconducting material that has a higher interaction cross section at these energies. For example, in order to detect K x-rays from uranium, the use of lead, a superconductor at 7.19 K, could be investigated. The K shell binding energy of lead is 88.005 keV, therefore, there is a peak in the interaction cross section of lead at this energy. This results in an overall increased probability of photons with this energy and higher interacting in a small sample. However, there is a high probability that the interaction of photons of energies greater than or equal to the binding energy will result in the emission of lead K x-rays. These photons, being of energies less than the binding energy, have a much smaller probability of subsequently interacting, and therefore may result in a significant fraction of events depositing only partial energy in the detector. The overall peak to total ratio may be such that the increased resolution does not result in a dramatic improvement in the detection limits currently attainable with Ge detectors. In order to investigate this further, Monte Carlo simulation was used to determine the expected spectrum of energy deposited in pieces of lead with various dimensions, given an input spectrum of photon energies incident on the detector face. This was then used in a preliminary fashion to compare the expected performance of the lead detector with the current Ge-detected spectra, for source-excited *in vivo* XRF measurements of uranium.

The simulation described in section 3.2 was used to generate the energy distribution of photons incident on a circular detector face, of variable radius, in the backscatter geometry. This spectrum was then used as input to the second program, which models the interactions of these photons in either a germanium crystal or a piece of lead foil of variable dimensions. The second simulation records the spectrum of energies deposited in the sample in an attempt to simulate efficiencies and peak to total area ratios that reflect the corresponding expected experimental results. In the case of the lead sample, the simulation allowed for the generation of K lead x-rays, which are then followed in the sample, in order to investigate the effect of lead x-ray escape on the final spectrum of energies deposited.

Two different simulations of lead detectors were run. The first simulation modelled photon interactions in a detector that has a radius of 300 μm and a thickness of 10 μm, for a total mass of 32 μg of lead. The second simulation modelled interactions in a detector of radius 100 μm and thickness of 100 μm, for a total mass of 36 μg. These were simulated in order to investigate the effect of changing the aspect ratio on the fraction of energy deposited and overall efficiency, with a fixed mass of lead used. A simulation of the spectrum of energies deposited in a Ge crystal was also run with the same spectrum of incident photons used in the lead foil runs.

Figures 7.1, 7.2 and 7.3 demonstrate the results from the first simulation, the spectrum of photon energies incident on the detector face. These plots also demonstrate the simulated spectrum of energies deposited in a Ge crystal, having dimensions that are typical of the crystals used in this thesis. It is evident from figure 7.2 that there is some escape of photon energy from the Ge crystal, but this represents a small fraction of the total spectrum. Overall, the two spectra shown in figures 7.1, 7.2, and 7.3 are quite similar in shape. The spectrum of energies deposited in the Ge crystal has been convolved with a Gaussian to simulate the finite resolution of the detector. This results in considerable broadening of the uranium x-rays, as evident in figure 7.3, and results in a reduction in the signal to noise ratio. (Note: all figures comparing two spectra are normalised to unit area for scaling purposes)

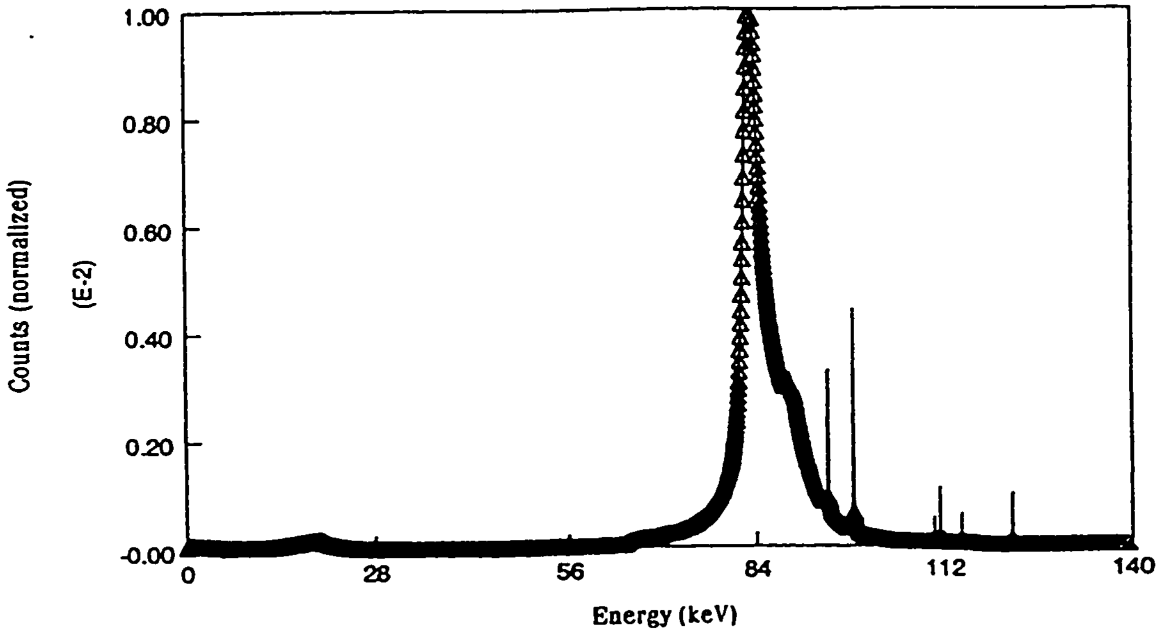

Figure 7.1: The full energy range of the incident (solid line) and Ge detected (triangles) spectra. Note the broadening of the uranium x-ray peaks in the 94 to 115 keV range.

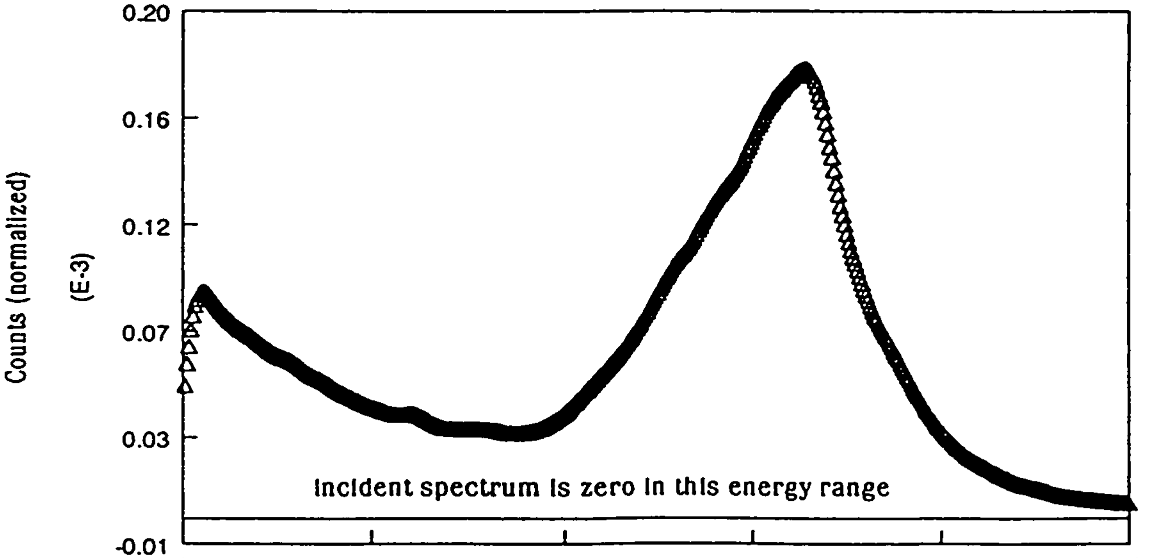

Figure 7.2: Expansion of the 0 to 30 keV region of figure 7.1. This energy range demonstrates the partial energy deposition in the Ge crystal, however, note the different y scales used in figures 7.1 and 7.2. Symbols as in figure 7.1.

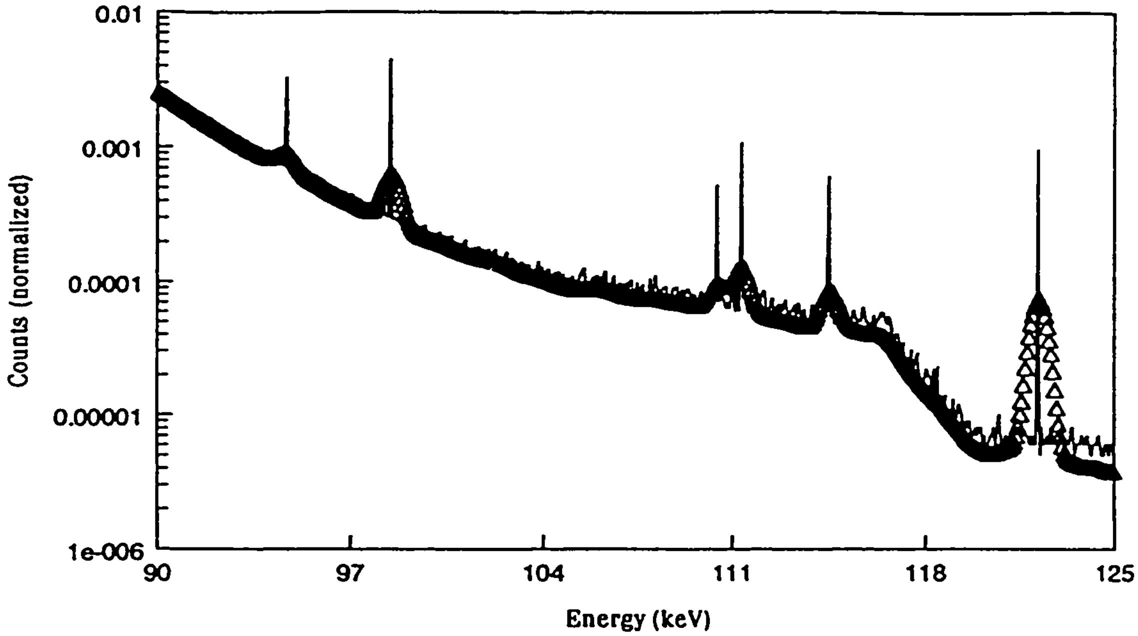

Figure 7.3: Expansion of the uranium x-ray energy region of figure 7.1. Note the broadening of these features due to the resolution of the detector. Symbols as in 7.1.

Figures 7.4 and 7.5 demonstrate the simulated results from photons detected in a 300 μm radius, 10 μm thick piece of lead. Also shown for comparison is the spectrum of energies deposited in the Ge crystal. Note the difference in the widths of the full energy uranium x-rays due to the theoretically superior resolution of the lead detector, figure 7.4. Figure 7.5 clearly demonstrates the problems associated with using a small lead sample for high-energy photon detection. This portion of the spectrum, representing events that result in only partial energy deposition, is clearly a large fraction of the total spectrum in the lead detector compared with the Ge crystal.

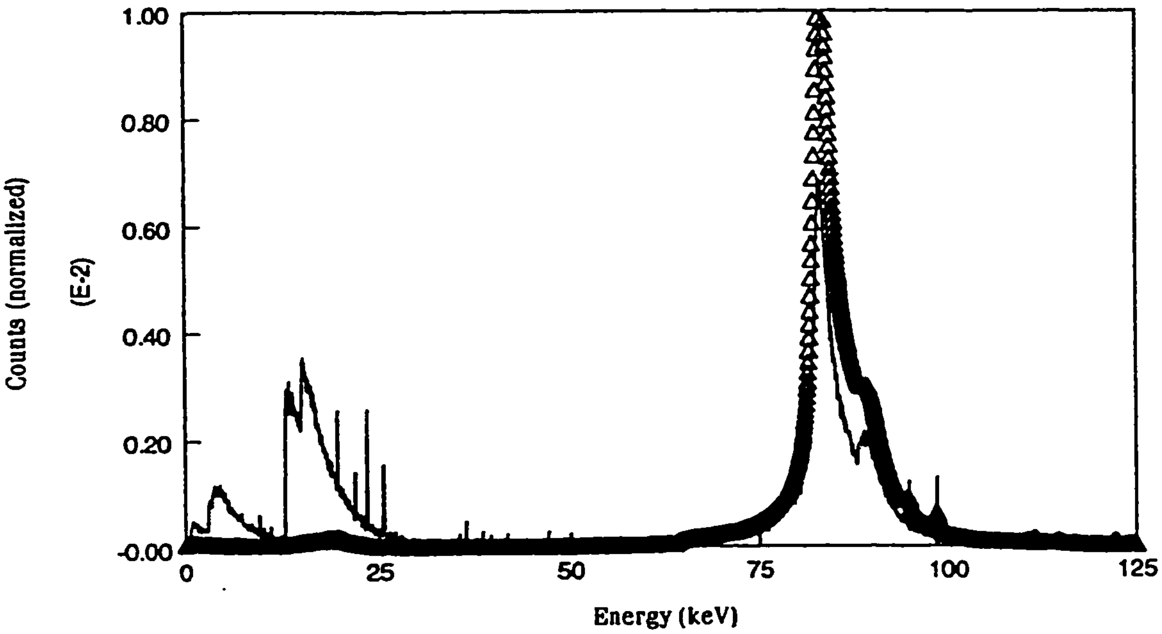

Figure 7.4: The full energy range of the detected spectra for Ge (triangles) and Pb (solid line). Note the differences between the two in the 0 to 30 keV range, and the resolution of the uranium x-rays in the 90 to 125 keV range.

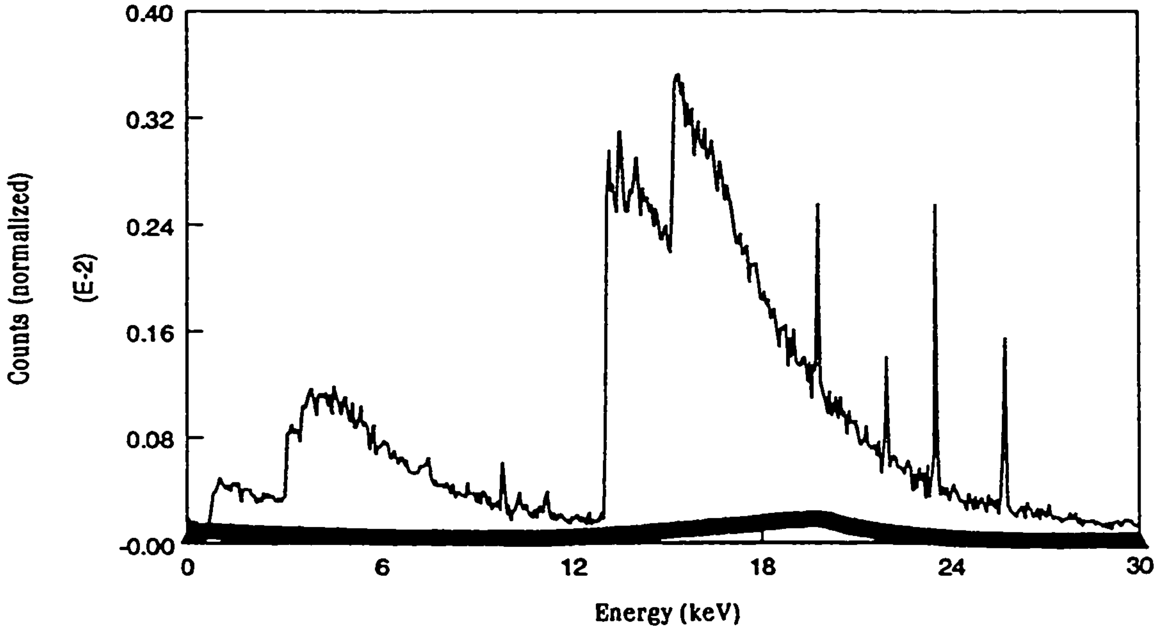

Figure 7.5: The 0 to 30 keV range of figure 7.4. Note the difference in the fraction of the total spectrum detected that is comprised of partial energy deposition in Pb *versus* Ge. Symbols as in figure 7.4.

The simulations of these two different detectors have resulted in marked differences in efficiencies. The 300 μm radius, 10 μm thick detector resulted in only 2% of photons depositing their full energy, with 96.5% of photons depositing no energy at all in the sample. However, the Ge detector simulations resulted in 94% of photons depositing their full energy and only 3.5% of photons depositing no energy at all in the crystal. Clearly the efficiency of the larger Ge crystal is vastly superior to that of the lead foil.

Figures 7.6, 7.7, and 7.8 demonstrate the comparison of the two lead detectors simulated. The aspect ratio was decreased from the initial run of 30 to 1 in the second case (the ratio of the radius to the thickness) in order to reduce the loss of the isotropically produced lead x-rays through the front and back of the detector. Clearly the more "spherical" aspect ratio of 1 results in more of the photons depositing their full energy in the foil, as the lower energy region in figure 7.6 is higher for the aspect ratio of 30. The model predicts that the second simulated lead foil has almost 19% of photons depositing their full energy, with only 72% of all incident photons depositing no energy. This is a marked improvement on the results of the first simulation. Furthermore, the simulations showed that only 5% of lead x-rays produced in the first case resulted in the full energy deposited in the sample, whereas 16% of lead x-rays produced in the second case resulted in full deposition.

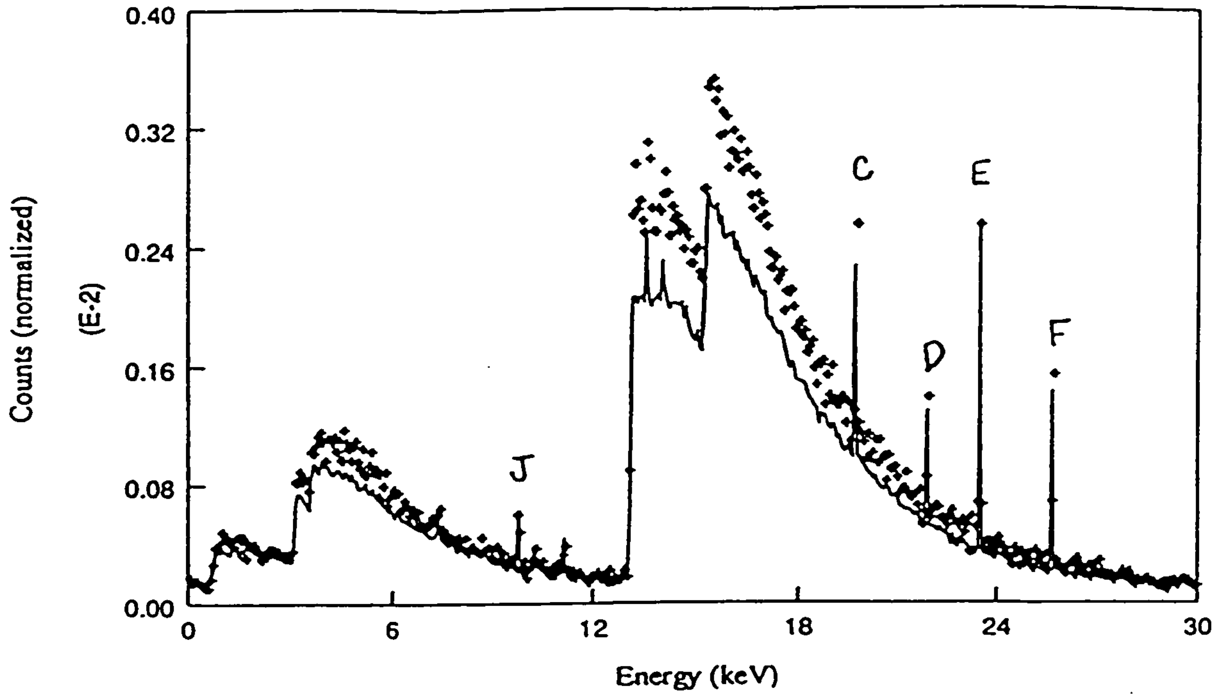

Figure 7.6: Comparing the two Pb detectors simulated. This energy range shows features arising from uranium K α x-rays producing Pb K α and K β x-rays, which subsequently escape. See table 7.1 for details on the various features identified here. Solid line – aspect ratio of 1; plus symbol – aspect ratio of 30.

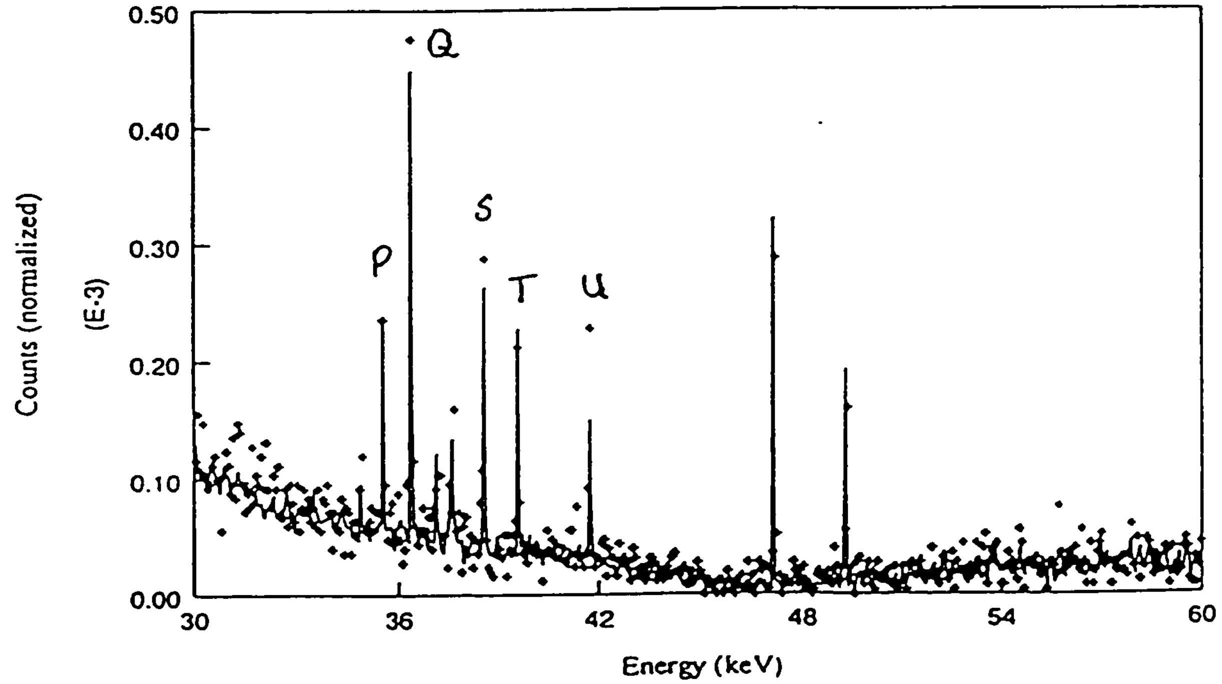

Figure 7.7: A comparison of the two Pb detectors simulated. This energy range corresponds to uranium K β x-rays producing lead K α x-rays, which subsequently escape. Symbols as in figure 7.6.

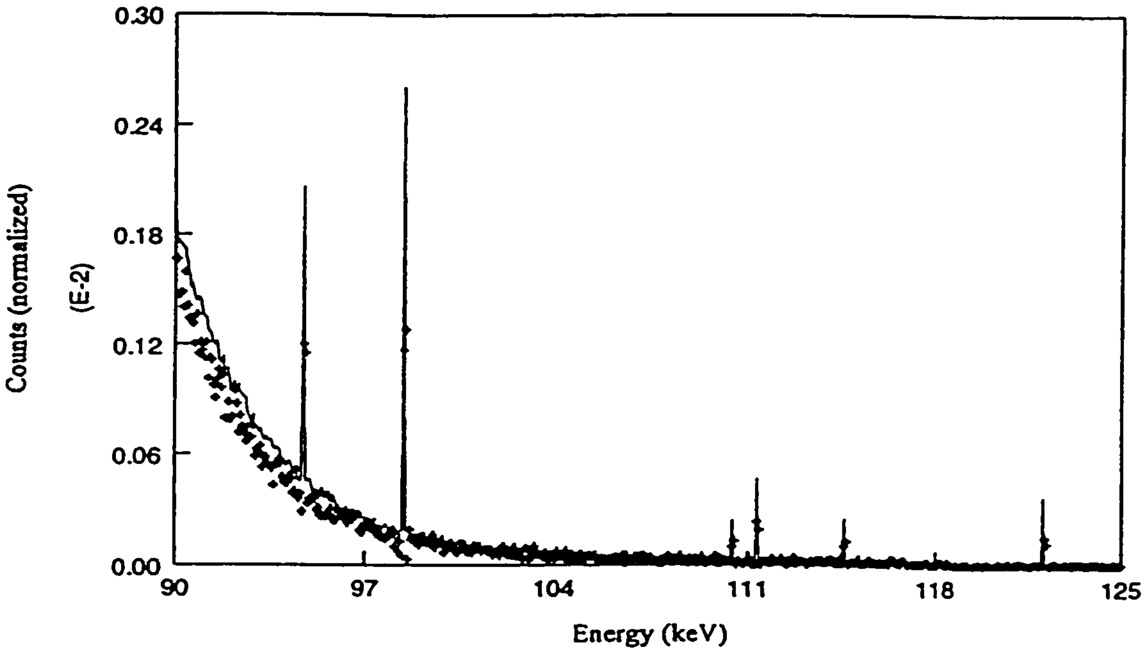

Figure 7.8: Comparing the two Pb detectors simulated. Shown here is the full energy deposition of uranium x-rays. Symbols as in figures 7.6 and 7.7.

A quantitative comparison of the three systems is possible by comparing the signal strengths and background under the uranium features in each spectrum. In the Ge spectrum, the uranium features are the full energy K x-ray peaks observed in the 94 to 115 keV range. However, the lead detector spectra have considerably more uranium features due to the uranium x-rays producing lead x-rays that subsequently escape. Since there are five x-rays from each heavy metal, these combine to give an expected 25 escape features. For example, feature C shown in figure 7.6 corresponds to an incident uranium $K\alpha_2$ x-ray producing a lead $K\alpha_1$ x-ray that then escapes the lead sample. Table 7.1 summarises the signal strengths and backgrounds for each of the more intense features, given as the ratio of signal to square root of background. Table 7.1 also indicates the combinations of U and Pb x-ray energies that give rise to the lettered features in figures 7.6 and 7.7.

Feature	Energy of feature (keV)	Ge detector	Pb detector – case 1	Pb detector – case 2
K α_1 peak	98.434	113.4	71.7	240.0
K α_2 peak	94.665	42.2	28.2	99.2
K β_1 peak	111.298	59.5	34.6	106.5
K β_2 peak	114.5	34.1	17.8	60.9
K β_3 peak	110.406	27.8	15.2	44.5
ESCAPE PEAKS:				
C (U α_2 – Pb α_1)	19.696		19.9	55.2
D (U α_2 – Pb α_2)	21.861		14.9	47.0
E (U α_1 – Pb α_1)	23.465		37.6	154.3
F (U α_1 – Pb α_2)	25.630		41.6	107.7
J (U α_2 – Pb β_1)	9.729		12.8	27.0
P (U β_3 – Pb α_1)	35.427		9.7	30.9
Q (U β_1 – Pb α_1)	36.329		18.9	69.3
S (U β_1 – Pb α_2)	38.494		16.7	43.4
T (U β_2 – Pb α_1)	39.531		10.3	39.1
U (U β_2 – Pb α_2)	41.696		16.0	26.5

Table 7.1: Summary of the ratios of net signal to the square root of background under each feature. Note the improvement in system performance when the aspect ratio is changed from 30 to 1, case 1 lead detector *versus* case 2.

In order to compare the Ge system with the lead detectors, it is necessary to assess the effect of the additional peaks in the lead spectra. This can be achieved by converting all signals in each spectra to an effective Kα_1 signal through the ratios of peak areas, and then taking the inverse variance weighted mean Kα_1 peak area for each detector. When converting peak signal to an effective Kα_1 area, the square root of background was used as a measure of uncertainty in the resulting value. Table 7.2 summarises the mean Kα_1 area and its uncertainty for each detector. The useful quantity for comparison is the ratio of the mean to its uncertainty. Note that the 1:1 aspect ratio detector simulation gave the best mean Kα_1

to uncertainty ratio, of $368 \cdot \sigma$.

System	Mean $K\alpha_1$ area	Mean $K\alpha_1$/uncertainty
Ge	$(24.3 \pm 0.2) \times 10^3$	142
Pb – case 1	$(0.553 \pm 0.005) \times 10^3$	119
Pb – case 2	$(4.44 \pm 0.01) \times 10^3$	368

Table 7.2: Comparing lead and Ge detectors in terms of the ratio of the mean $K\alpha_1$ to its uncertainty. The 1:1 aspect ratio lead detector results in a factor of 2.6 increase in signal sensitivity compared to that of the Ge detector.

It should be noted that the values given in table 7.2 are for roughly the same number of photons incident on each detector. Therefore, the lead simulations represent a considerably longer measurement time, as these detectors subtend a significantly smaller solid angle. However, this table can also be interpreted as the expected improvement in detection of uranium signal using an array of lead detectors, each of dimensions previously mentioned for the two cases, having a total surface area equal to the 2000 mm^2 surface of the Ge detector simulated.

Much work is needed to investigate further the feasibility of applying microcalorimeters to heavy metal *in vivo* XRF measurements. The next step is the optimisation of the aspect ratio for maximum full energy deposition in the lead sample. However, there is still some question as to the maximum mass of lead that can be used in this application. There are two potential constraints on the mass of lead used, heat capacity and count rate. Using the source, sample, and geometry of the present *in vivo* XRF system, the projected count rate for a 35 μg lead detector is on the order of 1 Hz. From Silver *et al.* (1996), it is clear that a count rate on the order of 100 Hz would produce few problems of pulse pile-up. Once an estimate of this mass limit is established that satisfies both constraints, the aspect ratio optimisation can proceed.

Another issue that must be investigated is the temperature at which this detector must operate. Silver *et al.* (1996) demonstrated that much of the heat capacity of the tin-based detector was associated with the germanium thermistor and the electrical leads. For preliminary investigations, operating at 300 mK is readily achieved with existing equipment, however, operating at a higher temperature than the tin sample investigated will result in an increase in the heat capacity of the thermistor and leads. For metals at low temperatures, the heat capacity is dominated by the electronic component, which varies linearly with absolute temperature. However, insulators at low temperatures exhibit heat capacities that vary with T^3. Therefore, the electrical leads would likely have a heat capacity that varies linearly with temperature, while the heat capacity of the germanium thermistor may vary more like T^3 at these temperatures. This implies that the overall dependence on temperature will be dictated by which of these two components has the larger heat capacity. It is expected, then, that the factor of four increase in operating temperature will result in somewhere between a factor of 4 and 64 increase in heat capacity. This, however, may not be a disastrous result, as the excellent resolution of 7 eV obtained by Silver *et al.* (1996) is better than the inherent line width of the K x-rays produced by uranium, given by the CRC Handbook of Chemistry and Physics to be on the order of 100 eV. This implies that an order of magnitude loss in resolution is acceptable for our application purposes, which allows for higher heat capacity in the sample and associated thermistor and leads.

Further avenues to investigate include the modelling of interactions in the lead sample that incorporate the tracking of the electrons generated in order to assess energy losses due to electron escapes. The feasibility of using coincidence methods to enhance the spectral appearance also could be explored. Since a significant fraction of interactions involving photons with energies greater than the K edge result in the emission of a K x-ray from the microcalorimeter, an annular detector could be used to identify those events. If only coincident events are recorded, there will be a substantial reduction in the number of photons with energies less than the K edge in the resulting spectrum. However, if only coincident events are used, any uranium x-rays that deposit full energy will be lost, which, based on these simulations, could amount to as much as 20% of such photons incident on the detector. Clearly there is a trade-off to consider. An additional possibility for the application of microcalorimeters for *in vivo* XRF measurements of heavy metals would be the use of tantalum (K absorption edge of 67.4 keV and T_c of 4.48 K) for detecting K x-rays from lead or mercury. As mentioned previously, tin may be useful in the detection of cadmium x-rays.

Overall, these preliminary simulations have demonstrated that the use of pure lead samples as microcalorimeters shows promise for radiation detection at higher photon energies than the tin samples investigated by Silver *et al.* (1996). The comparisons with the performance of germanium detectors indicate that there is potential for substantial improvement in the sensitivity of *in vivo* XRF measurements of uranium, and experimental investigation of these devices for this application is warranted.

7.4.3 New spectroscopy systems

The use of digital spectroscopy tools is an additional avenue to explore as a means of potentially improving sensitivity by optimising the detection system. Such systems are just now becoming available from manufacturers, and one such unit, DSPEC from EG&G Ortec (Oak Ridge, TN), has recently been tested in our laboratory (Fleming, 1998). Digital electronics are designed to replace the amplifier and analogue to digital converter (ADC) used in the conventional approach. In the particular case of the DSPEC unit, this package also supplies the high voltage to the detector, and is coupled with a multi-channel analyser computer card and associated software from the manufacturer. The main advantages of digital systems are the pulse-shaping properties and the enhanced throughput capabilities.

In an analogue amplifier, the output is typically a Gaussian-shaped pulse. However, the ideal pulse for spectroscopic analysis is one in which there is an exponentially rising edge, followed by a short duration peak, and finishing with an exponentially falling edge (Knoll, 1989). Such a shaped peak is difficult to obtain with linear components, as used in a conventional XRF system, but digital integrated circuits can produce these shapes. Furthermore, there is a lot of flexibility built in to the setting of the shaping parameters, for example the rise time, duration peak width, and the shape factor of the rising edge. The rapid rise and fall of digitally-processed peaks allow for better throughput rates, which, as discussed previously, can be a major limiting factor on the sensitivity of *in vivo* XRF systems. In addition, the highly tuneable shaping parameters ensure that major concessions in resolution are not required for achieving improvements in throughput.

Fleming (1998) has reported on preliminary investigations of the performance of the DSPEC unit. In tests with plaster of Paris phantoms, it was found that the digital system had better energy resolution, and higher throughput rates were possible, while maintaining the enhanced resolution. However, the uncertainty in the coherent peak, a major influence of the precision of the system, was similar to that observed with the conventional analogue system. The system was also tested with resin-based phantoms designed to reflect more accurately the sample sizes encountered in clinical measurements. In this case, there was a much more significant improvement in the performance of the digital system compared to the analogue version. A substantial increase in throughput was observed, as well as superior energy resolution. Furthermore, there was a decrease in the relative uncertainty of the coherent peak detected digitally. The 15% reduction in uncertainty observed in these trials could translate to a 1 μg/g improvement in detection limit in a non-occupationally exposed group of males (Fleming, 1998). The current configuration for the ^{109}Cd/backscatter system has an MDL on the order of 8 μg/g. Therefore, preliminary tests have indicated that the use of digital spectroscopy units could result in a significant improvement in the precision of measuring lead in bone. This observed benefit is not restricted to the measurement of lead, however, and further tests should be conducted to quantify the improvement to the measurement of other heavy metals. It is recommended that digital units be further investigated in order to determine the optimal shaping parameters for all applications. In addition, new units should be assessed as they become available from various manufacturers, and the performance in the field should be determined. This last recommendation is currently underway, as a digital spectroscopic unit is being used in a survey of lead smelter workers in Belledune, New Brunswick.

7.4.4 New analysis methods

A new means of analysing XRF data has recently been proposed, He *et al.*, 1993. This approach compares a Monte Carlo-generated spectrum for a sample of assumed composition to the measured spectrum of the unknown sample. If the elemental amounts calculated for the sample are not sufficiently close to those assumed in the simulation based on this comparison, then another Monte Carlo must be performed for a new assumed composition. Chi-square values are used as an indication that an accurate composition has been identified in this iterative process. He *et al.* (1993) demonstrated that such an approach led to excellent agreement between the calculated and known elemental compositions of standard samples. In most cases, only one iteration was required to converge at the correct elemental composition, when the initial guess was based on the relative intensities of characteristic x-rays present in the sample. However, for trace elements, a second iteration was often needed. It should be noted that this analysis technique may only be applicable to homogeneous samples, in which a general knowledge of the elements present is available. While an approximate understanding of the composition of tissue and bone exists, an *in vivo* sample is not homogeneous, and numerous geometric and physical parameters of the sample would not easily be known for inclusion in the Monte Carlo simulation. Possibly for these reasons He *et al.* (1993) discussed this approach in the context of the XRF analysis of industrial samples, for which geometry can be clearly established and homogeneity can often be assumed. More recently, however, Ao *et al.* (1997) have discussed the feasibility of applying this Monte Carlo Library Least Squares (MCLLS) approach to analysing *in vivo* spectra.

In the application to *in vivo* data, in particular, the analysis of source-excited Pb spectra, Ao *et al.* (1997) have taken a slightly different approach to that reported by He *et al.* (1993). Rather than generating spectra for each element present in the sample and then comparing the weighted sum of these to the experimental spectrum, only two libraries are generated. The first library is the Monte Carlo-generated spectrum from an *in vivo* sample containing no lead, while the second library is generated by subtracting the zero concentration spectrum from a spectrum simulated for a 107 ppm lead sample. This second library is therefore the lead contribution to the total spectrum, when the lead is present at a level of 107 ppm. The unknown Pb concentration can then be determined from an experimental spectrum by comparing the combination of the first library with some fraction of the second library, where the fraction required to reproduce the experimental data indicates the lead content of the sample.

Ao *et al.* (1997) report the use of two variations of the MCLLS method in analysing *in vivo* data. In the first case, all the experimental information in the 60 to 90 keV range, which encompasses the Compton, lead characteristic x-rays, and Rayleigh features, was used to determine the lead concentration present. In the second variation, only the characteristic peaks and their immediate surrounding channels were used, similar to the information included in the conventional analysis method of non-linear least squares utilised in this thesis. It was anticipated that the inclusion of additional spectral information in the first case would be an improvement over the second method and the conventional peak area analysis technique. While there was little difference between the second MCLLS method and the conventional peak area analysis, as expected, the anticipated improvement with the first MCLLS approach was not observed. Based on these investigations, Ao *et al.* (1997) concluded that the Compton scatter peak is affected by changes from sample to sample in measurement geometry, bone density changes, and potentially other, unknown, factors. It can therefore be concluded that a number of experimental parameters must be well known and reproduced in the simulations in order to generate accurately the libraries needed for analysis. In addition, a more accurate Monte Carlo simulation is required for this approach to be feasible, for example the count rate dependent pulse pile-up effect on the detected spectrum must be included. Furthermore, a careful assessment of the feasibility of using MCLLS for analysing *in vivo* data clearly must determine how accurate this technique can be without extensive knowledge of the sample geometry and physical characteristics. It is not clear that MCLLS will be practical in the clinical analysis of spectra from geometrically and physically ill-defined *in vivo* samples, however, the possibility of improving sensitivity by including more spectral information in the analysis is worth investigating.

References

Ahlgren L, Lidén K., Mattsson S., and Tejning S. (1976) X-ray fluorescence analysis of lead in human skeleton *in vivo*. *Scand. J. Work Environ. & Health* **2** 82-6.

Ahlgren L. and Mattsson S. (1979) An x-ray fluorescence technique for *in vivo* determination of lead concentration in a bone matrix. *Phys. Med. Biol.* **24** 136-45.

Ahlgren L, Haeger-Aronsen B, Mattsson S, and Schütz A. (1980) *In-vivo* determination of lead in the skeleton after occupational exposure to lead. *Br J Ind Med* **37** 109-113.

Ao Q., Lee S. H., and Gardner R. P. (1997) Optimization of *in vivo* x-ray fluorescence analysis methods for bone lead by simulation with the Monte Carlo code CEARXRF. *Appl. Radiat. Isot.* **48** 1413-1423.

Armstrong R. (1991) Studies relating to the *in vivo* measurement of cadmium and mercury. Ph.D. Thesis, University of Birmingham, Birmingham, U.K.

Arnold D. L., Bore P. J., Radda G. K., Styles P. and Taylor D. J. (1984) Excessive intracellular acidosis of skeletal muscle on exercise with a patient in a post viral exhaustion/fatigue syndrome. Lancet i 1367-9.

Arnold M. L., McNeill F. E., and Chettle D. R. (1999) The feasibility of measuring manganese concentrations in human liver using neutron activation analysis. *Neurotoxicology* (in press).

Barkla C. G. (1905) Polarised röntgen radiation. *Phil. Trans. Roy. Soc.* **A204** 467-79.

Barregård L. (1993) Biological monitoring of exposure to mercury vapour. *Scand. J. Work Environ. And Health* **19** (suppl 1) 45-9.

Barry P. S. I. (1975) Comparison of concentrations of lead in human tissues. *Br. J. Ind. Med.* **32** 119-139.

Beddoe A. H., and Hill G. L. (1985) Clinical measurement of body composition using *in vivo* neutron activation analysis. *J. Parent. Ent. Nutr.* **9** 504-20.

Berger MJ. 1987 Program XCOM, Version 1.2.

Bevington P. R. (1969) Data Reduction and Error Analysis for the Physical Sciences. McGraw Hill Inc., New York NY.

Biggs F., Mendelsohn L. B., and Mann J. B.(1975) Hartree-Fock Compton profiles for the elements. *At. Data Nucl. Data Tables* **16** 201-309.

Birch R. and Marshall M. (1979) Computation of x-ray bremsstrahlung spectra. *Phys. Med. Biol.* **24** 505-517.

Birch R., Marshall M., and Ardran G. M. (1979) Catalogue of Spectral Data for Diagnostic X-rays. Hospital Physicists' Association, London, U.K.

Börjesson J., Barregård L., Sällsten G., Schütz A., Jonson R., Alpsten M., and Mattsson S. (1995) *In vivo* x-ray fluorescence analysis of mercury: the relation between concentrations in the kidney and in the urine. *Phys. Med. Biol.* **40** 413-26.

Börjesson J. (1996) Studies of cadmium, mercury, and lead in man: The value of x-ray fluorescence measurements *in vivo.* Ph.D. Thesis, Lund University, Malmö, Sweden.

Börjesson J, Gerhardsson L, Schütz A, Mattsson S, Skerfving S, and Österberg K. (1997) *In vivo* measurements of lead in finger-bone in active and retired lead smelters. Int Arch Occup Environ Health **69** 97-105.

Bowman W. W. and MacMurdo K. W. (1974) Radioactive-decay gammas: Ordered by energy and nuclide. *Atomic Data & Nucl Data Tables* **13** 89-292.

Canberra (1991) Germanium detectors: User's Manual. Canberra Industries Inc., Meriden CT.

Cember H. (1992) Introduction to Health Physics, McGraw-Hill Inc., New York, NY.

Chan H. P. and Doi K. (1988) Monte Carlo simulation in diagnostic radiology in Monte Carlo Simulation in the Radiological Sciences ed. R.L. Morin, CRC Press, Boca Raton, FL

Chase G. R. (1989) Correlation between airborne uranium exposure and uranium urinalysis results at Bear Creek Uranium. *Health Phys.* **56** 195-9.

Chettle D. R., and Fremlin J. H. (1984) Techniques of *in vivo* neutron activation analysis. *Phys. Med. Biol.* **29** 1011-43.

Christoffersson J-O and Mattsson S. (1983) Polarized x-rays in x-ray fluorescence analysis for improved *in vivo* detectability of cadmium in man. *Phys. Med. Biol.* **28** 1135-44.

Christoffersson J-O, Schütz A, Ahlgren L, Haeger-Aronsen B, Mattsson S, and Skerfving S. (1984) Lead in finger-bone analysed *in vivo* in active and retired lead workers. *Am J Ind Med* **6** 447-457.

Christoffersson J-O, Ahlgren L, Mattsson S, Schütz A, and Skerfving S. (1986) Decrease of skeletal lead levels in man after end of occupational exposure. *Arch Environ Health* **41** 312-318.

Cohn S. H., and Parr R. M. (1985) Nuclear based techniques for the *in vivo* study of human body composition. *Clin. Phys. Physiol. Meas.* **6** 275-301.

Dang H. S., Pullat V. R., and Sharma R. C. (1995) Distribution of uranium in human organs of an urban Indian population and its relationship with clearance half-lives. *Health Phys.* **68** 328-31.

Epstein I. R., Williams B. G., and Cooper M. J. (1973) Studies in molecular Compton scattering. II. The Compton profile of $C_4H_8O_2$ – dioxane, isobutyric and *n*-butyric acids. *J. Chem. Phys.* **58** 4098-103.

Fleming D. E. B. (1998) Human lead metabolism: Chronic exposure, bone lead and physiological models. Ph.D. Thesis, McMaster University, Hamilton, Canada.

Gerhardsson L, Börjesson J, Mattsson S, Schütz A, and Skerfving S. 1998 Chelated lead in relation to lead in bone and ALAD genotype. *Environ Res*; in press.

Gonsior B. and Roth M. (1983) Trace element analysis by particle and photon-induced x-ray emission spectroscopy. *Talanta* **30** 385-400.

Goulding F. S., and Jaklevic J. M. (1977) XRF analysis – some sensitivity comparisons between charged-particle and photon excitation. *Nucl. Instrum. Methods* **142** 323-32.

Goulding F. S., Jaklevic J. M., Jarrett B. V. and Landis D. A. (1971) Detector background and sensitivity of semiconductor x-ray fluorescence spectrometers. *Adv. X-Ray Anal.* **15** 470-82.

Halton J. H. (1970) A retrospective and prospective survey of the Monte Carlo method. *SIAM Rev.*, **12**, 1.

Harding G., Jordan B., and Kosanetzky J. (1991) A new fluorescent x-ray source for photon scattering investigations. *Phys. Med. Biol.* **36** 1573-83.

He T., Gardner R. P., and Verghese K. (1993) The Monte-Carlo library least-squares approach for energy-dispersive x-ray fluorescence analysis *Appl. Radiat. Isot.* **44** 1381-8.

Health and Welfare Canada (1987) Bioassay Guideline 4: Guidelines for uranium bioassay, Environmental Health Directorate, Health Protection Branch, Health and Welfare Canada, Ottawa, Canada.

Heath R. L. (1971) The application of high-resolution solid state detectors to x-ray spectrometry – a review. *Adv. X-Ray Anal.* **15** 1-35.

Heckel J. (1995) Using Barkla polarised x-ray radiation in energy dispersive x-ray fluorescence analysis (EDXRF). *J Trace Microprobe Tech* **13** 97-108.

Heinmiller B. (1988) Photon response of $Li_2B_4O_7$:Cu thermoluminsecent dosimeters. M.Sc. Thesis, McMaster University, Hamilton, Canada.

Hugtenburg R. P., Turner J. R., Mannering D. M., and Robinson B. A. (1998) Monte Carlo methods for the *in vivo* analysis of cisplatin using x-ray fluorescence. *Appl. Radiat. Isot.* **49** 673-676.

ICRP (1975). Publication 23, Report of the Task Group on Reference Man. Oxford: Pergamon Press.

ICRP (1979) Publication 30, Part 1, Annals of the ICRP, Vol 2, Nos. 3 & 4. Limits for intakes of radionuclides by workers. Pergamon Press, Oxford, U.K.

Jacobson B. (1964) *Am. J. of Roentgenology* **91** 202-210.

Jonson R., Mattsson S., and Unsgaard B. (1988) A method for *in vivo* analysis of platinum after chemotherapy with cisplatin. *Phys. Med. Biol.* **33** 847-57.

Karpas Z., Lorber A., Elish E., Marcus P., Roiz Y., Marko R., Kol R., Brikner D., and Halicz L. (1998) Uranium in urine – normalization to creatinine. *Health Phys.* **74** 86-90.

Kaufman L. and Camp D. C. (1974) Polarised radiation for x-ray fluorescence analysis. *Adv. X-ray Anal.*, **18**, 247-58.

Kaufman L., Shosa D., Arbel A. and Zender M. (1982) Improved quantitation of low level tracers in x-ray fluorescent excitation analysis *Nucl. Instrum. Methods Phys. Res.* **193** 105-10.

Knoll G. F. (1989) Radiation Detection and Measurement, 2nd Edition. John Wiley & Sons Inc., New York.

Kosta L, Byrne A. R., Zelenko V. (1975) Correlation between selenium and mercury in man following exposure to inorganic Hg. *Nature* **254** 238-9.

Laird E. E. (1983) Factors affecting *in vivo* x-ray fluorescence measurements of lead in bone. Ph.D. Thesis, University of Birmingham, Birmingham, U.K.

Leach M. O. (1988) "Spatially localised nuclear magnetic resonance" in: The Physics of Medical Imaging, Ed.: S. Webb. IOP Publishing Ltd., Bristol, U.K.

Lederer C. M. and Shirley V. S. (1978) Table of Isotopes, 7th Edition. John Wiley & Sons Inc., New York.

Leggett R. W. (1989) The behaviour and chemical toxicity of uranium in the kidney: A reassessment. *Health Phys.* **57** 365-83.

Leggett R. W. (1994) Basis for the ICRP's age-specific biokinetic model for uranium. *Health Phys.* **67** 589-610.

Lewis D. G. (1994) Optimization of a polarized source for in vivo x-ray fluorescence analysis of platinum and other heavy metals. *Phys. Med. Biol.* **39** 197-206.

Lewis D. G., Kilic A., and Ogg C. A. (1995) Adaptation of the EGS4 Monte Carlo code for the design of a polarized source of x-ray fluorescence analysis of platinum and other heavy metals *in vivo Adv. X-Ray Anal.* **38** 579-585.

Lewis D. G., Kilic A., and Ogg C. A. (1998) Computer aided design of a polarised source for *in vivo* x-ray fluorescence analysis. *Appl. Radiat. Isot.* **49** 707-709.

Lux I. And Koblinger L. (1991) Monte Carlo Particle Transport Methods: Neutron and Photon Calculations. CRC Press Inc., Boca Raton, U.S.A.

Matsuo N., Suzuki T., and Akagi H. (1989) Mercury concentrations in organs of contemporary Japanese. *Arch. Environ. Health* **44** 298-303.

McCallum R. I., Day M. J., Underhill J., and Aird E. G. A. (1970) Measurement of antimony oxide dust in human lungs *in vivo* by x-ray spectrophotometry. *Proc. of 3rd Int. Symp. On Inhaled Particles*, London, Sept. 1970.

Meixner C. H. (1974) A Monte Carlo program for the calculation of γ-ray spectra for germanium detectors. *Nucl. Instrum. Methods Phys. Res.* **119** 521-6.

Namito Y., Ban S., and Hirayama H. (1993) Implementation of linearly-polarized photon scattering into the EGS4 code. *Nucl. Instrum. Methods Phys. Res. A* **332** 277-283.

Nilsson U, Attewell R, Christoffersson J-O, Schütz, Ahlgren L, Skerfving S, and Mattsson S. (1991) Kinetics of lead in bone and blood after end of occupational exposure. *Pharmacol Toxicol* **68** 477-484

Nordberg G. F. and Skerfving S. (1972) "Metabolism" in: Mercury in the Environment, Ed. L. Friberg and J. Vostal, CRC Press Inc., Cleveland, Ohio, U.S.A.

O'Meara J. M., Chettle D. R., McNeill F. E., and Webber C. E. (1997) The feasibility of measuring bone uranium concentrations *in vivo* using source excited K x-ray fluorescence. *Phys. Med. Biol.* **42** 1109-1120.

O'Meara J. M, Chettle D. R., and McNeill F. E. (1998a) The validity of the coherent scatter peak normalization of x-ray intensities detected during *in vivo* XRF measurements of metals in bone *Advances in X-Ray Analysis* **41**

O'Meara J. M., Chettle D. R., McNeill F. E., W. V. Prestwich, and Svensson C. E. (1998b) Monte Carlo simulation of source-excited *in vivo* x-ray fluorescence measurements of heavy metals. *Phys. Med. Biol.* **43** 1413-28.

O'Meara J. M., Chettle D. R., McNeill F. E., and Webber C. E. (1998c) *In vivo* x-ray fluorescence (XRF) measurement of depleted uranium. AFRRI (Armed Forces Radiobiology Research Institute, U.S.A.) Special Publication **98-3** 33-37.

O'Meara J. M., Börjesson J., Chettle D. R., and Mattsson S. (1999) Normalisation with coherent scatter signal: improvements in the calibration procedure of the ^{57}Co-based *in vivo* XRF bone-lead measurement. Submitted to the *Appl. Rad. Isot.*

Pejović-Milić A., McNeill F. E., Prestwich W. V., Waker A. J., and Chettle D. R. (1998) Development of an accelerator based determination of aluminum burden in peripheral bone by neutron activation analysis. *Appl. Radiat. Isot.* **49** 717-9.

Price J, Baddeley H, Kenardy JA, Thomas BJ, and Thomas BW. (1984) *In vivo* x-ray fluorescence estimation of bone lead concentrations in Queensland adults. *Br J Radiol* **57** 29-33.

Price J, Grudzinski AW, Craswell PW, and Thomas BJ. (1992) Repeated bone lead levels in Queensland, Australia - previously a high lead environment. *Arch Environ Health* **47** 256-262.

Rindby A., Selin E., Berggren K.-F. and Ribberfors R. (1982) Experimental and theoretical distributions of inelastically scattered radiation from aluminum in an EDXRF spectrometer (letter) *Nucl. Instrum. Methods Phys. Res.* **196** 569-71.

Rosen J. F., Markowitz M. E., Bijur P. E., Jenks S. T., Wielopolski L., Kalef-Ezra J. A., and Slatkin D. N. (1989) L-line x-ray fluorescence of cortical bone lead compared with the $CaNa_2$ EDTA test in lead-toxic children: Public health implications. *Proc. Natl. Acad. Sci.* **86** 685-9.

Ryon R. W., Zahrt J. D., Wobrauschek P., and Aiginger H. (1982) The use of polarised x-rays for improved detection limits in energy dispersive x-ray spectrometry. *Am Lab* **14** 38-49.

Sällsten G., Barregård L., and Järvholm B. (1990) Mercury in the Swedish chloralkali industry – An evaluation of the exposure and preventive measures over 40 years. *Ann. Occup. Hyg.* **34** 205-14.

Schütz A, Skerfving S, Christoffersson J-O, Ahlgren L, and Mattsson S. (1987a) Lead in vertebral bone biopsies from active and retired lead workers. *Arch Environ Health* **42** 340-346.

Schütz A, Skerfving S, Christoffersson J-O, and Tell I. (1987b) Chelatable lead versus lead in human trabecular and compact bone. *Sci Tot Environ* **61** 201-209.

Seltzer S. M. (1981) Calculated response of intrinsic germanium detectors to narrow beams of photons with energies up to ≈300 keV. *Nucl. Instrum. Methods Phys. Res.* **188** 133-51.

Shakeshaft J., and Lillicrap S. (1993) Technical note: an x-ray fluorescence system for the determination of gold *in vivo* following chrysotherapy. *Br. J. Radiol.* **66** 714-7.

Silver E., LeGros M., Madden N., Beeman J., and Haller E. (1996) High-resolution, broad-band microcalorimeters for x-ray microanalysis. *X-Ray Spectrom.* **25** 115-22.

Smith J. R., Athwal S. S., Chettle D. R., and Scott M. C. (1982) On the *in vivo* measurement of Hg using n capture and x-ray fluorescence. *Int. J. Appl. Rad. & Isot.* **33** 557-61.

Somervaille L. J., Chettle D. R., and Scott M. C. (1985) *In vivo* measurement of lead in bone using x-ray fluorescence. *Phys. Med. Biol.* **30** 929-43.

Spitz H. B., Simpson J. C., and Aldridge T. L. (1984) Analysis of uranium urinalysis and *in vivo* measurement results from 11 participating uranium mills. Batelle Pacific Northwest Laboratory, Washington D.C., USNRC (NUREG/CR-2955).

Sutcliffe J. F. (1996) A review of *in vivo* experimental methods to determine the composition of the human body. *Phys. Med. Biol.* **41** 791-833.

Tartari A., Fernandez J. E., Casnati E., Baraldi C. and Felsteiner J. (1993) EDXRS modelling for *in vivo* trace element analysis by using the SHAPE code. *X-Ray Spectrom.* **22** 323-7.

Tartari A., Casnati E., Baraldi C., Giganti M., De Rosa E., Gregorio P., and Brito J. (1997) *In vivo* monitoring of bone-Pb and retrospective exposure: an assessment in occupationally exposed subjects. *J. Trace Elements Med. Biol.* **11** 179-181.

Taylor D. J., Bore P. J., Styles P., Gadean D. G., and Radda G. K. (1983) Bioenergetics of intact human muscle: a ^{31}P NMR study. *Mol. Biol. Med.* **1** 77-94.

Tell I, Somervaille LJ, Nilsson U, Bensryd I, Schütz A, Chettle DR, Scott MC, and Skerfving S. (1992) Chelated lead and bone lead. *Scand J Work Environ Health* **18** 113-119.

Thomas B. J., Harvey T. C., Chettle D. R., McLellan J. S., and Fremlin J. H. (1979) A transportable system for the measurement of liver cadmium *in vivo*. *Phys. Med. Biol.* **24** 432-7.

Todd A. C., Chettle D. R., Scott M. C. and Somervaille L. J. (1991) Monte Carlo modelling of *in vivo* x-ray fluorescence of lead in the kidney *Phys. Med. Biol.* **36** 439-48.

Todd A. C., McNeill F. E., Palethorpe J. E., Peach D. E., Chettle D. R., Tobin M. J., Strosko S. J., and Rosen J. C. (1992) *In vivo* x-ray fluorescence of lead in bone using K x-ray excitation with ^{109}Cd sources: radiation dosimetry studies. *Environ. Res.* **57** 117-132.

Tucker D. M., Barnes G. T., Wu X. (1991) Molybdenum target x-ray spectra: A semi-empirical model. *Med. Phys.* **18** 402-407.

Turner J. E. (1995) Atoms, Radiation, and Radiation Protection, 2nd Edition. John Wiley & Sons, Inc., New York.

Varley B. J., Kitching J. E., Leo W., Miskin J., Moore R. B., Wunsch K. D., Decker R., Wollnik H., and Siegert G. (1981) Investigations of the response of germanium detectors to monoenergetic electron, positron and γ-ray beams. *Nucl. Instrum. Methods Phys. Res.* **190** 543-54.

Vartsky D., Ellis K. J., Hull D. M., and Cohn S. H. (1979) Nuclear resonant scattering of γ-rays – a new technique for *in vivo* measurement of body iron stores. *Phys. Med. Biol.* **24** 689-701.

Wallace J. D. (1994) The Monte Carlo modelling of *in vivo* x-ray fluorescence measurement of lead in tissue. *Phys. Med. Biol.* **39** 1745-56.

White D. R. (1978) Tissue substitutes in experimental radiation physics. *Med. Phys.* **5** 467-479.

Wielopolski L., Rosen J. F., Slatkin D. N., Vartsky D., Ellis K. J., and Cohn S. H. (1983) Technical notes: Feasibility of noninvasive analysis of lead in human tibia by soft x-ray fluorescence. *Med. Phys.* **10** 248-51.

Wielopolski L., Rosen J. F., Slatkin D. N., Zhang R., Kalef-Ezra J. A., Rothman J. C., Maryanski M. and Jenks S. T. (1989) *In vivo* measurement of cortical bone lead using polarized x-rays. *Med. Phys.* **16** 521-8.

Woodard H.Q. (1962) The elementary composition of human cortical bone. *Health Phys* **8** 513-7.

World Health Organization (1976) Environmental Health Criteria I: Mercury. Published under the joint sponsorship of the United Nations Environment Programme and the World Health Organization, Geneva, Switzerland.

Wrenn M. E., Durbin P. W., Howard B., Lipsztein J., Rundo J., Still E. T., and Willis D. L. (1985) Metabolism of ingested U and Ra. *Health Phys.* **48** 601-33.